UC Riverside
UC Riverside Electronic Theses and Dissertations

Title

A Lipid Biomarker and Stable Isotopic Investigation of Ediacaran and Modern Marine Microbial Communities and Carbon Cycling

Permalink

https://escholarship.org/uc/item/8gm644zx

Author

Lee, Carina

Publication Date

2016

Peer reviewed|Thesis/dissertation

UNIVERSITY OF CALIFORNIA
RIVERSIDE

A Lipid Biomarker and Stable Isotopic Investigation of Ediacaran and Modern Marine
Microbial Communities and Carbon Cycling

A Dissertation submitted in partial satisfaction
of the requirements for the degree of

Doctor of Philosophy

in

Geological Sciences

by

Carina Lee

June 2016

Dissertation committee:
Professor Gordon D. Love (Chairperson)
Professor Mary L. Droser
Professor Timothy W. Lyons

The Dissertation of Carina Lee is approved:

_____

_____

_____

Committee Chairperson

University of California, Riverside

ACKNOWLEDGEMENTS

ABSTRACT OF THE DISSERTATION

A Lipid Biomarker and Stable Isotopic Investigation of Ediacaran and Modern Marine
Microbial Communities and Carbon Cycling

by

Carina Lee

Doctor of Philosophy, Graduate Program in Geological Sciences
University of California, Riverside, June 2016
Professor Gordon D. Love, Chairperson

Lipid biomarkers and stable carbon isotopes can track the evolution of microbial
communities and carbon cycling, respectively, in preserved organic matter. Traditionally,
carbon isotopes are measured in bulk materials, though technological advances allow us
to measure the carbon isotope composition of individual hydrocarbon molecules,
providing direct insights into the carbon source and microbial metabolism used for
biosynthesis. During sedimentary diagenesis, lipids are incorporated into a complex
macromolecular matrix—(proto)-kerogen. Lipids associated with or tightly bound within
the kerogen matrix are not routinely analysed, thus a large repository of geochemical
information relating to mode of binding and preservation remains unexplored.

Presented here are two studies of marine organic matter preservation and cycling,
from the enigmatic late Ediacaran Shuram excursion of South Oman and from the
modern hypersaline microbial mats of Guerrero Negro, Baja California, Mexico.

From South Oman, we present the first detailed bulk isotope, lipid biomarker, and
compound-specific carbon isotope compilation from an organic-rich, deeper water facies

that captures the unique 'Shuram excursion'—a carbon isotope excursion in carbonate (down to -12‰) that is not paralleled in magnitude by the coeval organic carbon phases. Our results definitively demonstrate that preserved organic matter is syngenetic and marine-derived and has two distinct organic carbon isotopic sources. The extractable alkane hydrocarbons preserve a smaller overall magnitude carbon isotope excursion in phase with a primary surface seawater origin.

From Guerrero Negro, we investigated kerogen-bound lipid biomarker profiles from two cores of different salinity and compare them to lipids extracted using conventional techniques. Additionally, to investigate the mode of binding and incorporation of sterols and hopanoids into kerogen during diagenesis, we extracted kerogen-bound lipids of pre-extracted microbial mat residues that were subjected to three selective chemical degradations. Our findings indicate a suite of lipid biomarkers, including sterols and hopanoids, are rapidly incorporated into kerogen *via* strong covalent linkages and preserved during sedimentary diagenesis. The absence of sterols or other polycyclic biomarker compounds classes is unlikely the result of taphonomic bias in periods of Earth history where benthic organic matter source inputs are pronounced.

TABLE OF CONTENTS

Chapter Three: Marine organic matter cycling during the Ediacaran Shuram excursion

Chapter Four: Incorporation of lipid biomarkers in microbial mat proto-kerogens during sedimentary diagenesis

Chapter Five: Investigating the nature of covalent bonding of bound lipids in microbial mat proto-kerogens *via* sequential chemolysis and hydropyrolysis

x

LIST OF FIGURES

LIST OF TABLES

CHAPTER ONE

Introduction

1.1 Lipid biomarker geochemistry

Ancient and modern marine ecosystems throughout geologic time preserve organic lipid biosignatures with varying levels of biological specificity. Biological markers (herein referred to as biomarkers) are the hydrocarbon molecular fossil remains of formerly functioning lipid molecules of living organisms—predominantly a component of cellular membranes that—under suitable conditions, can be preserved in the sedimentary rock record on timescales of hundreds of millions to billions of years (Brocks & Summons, 2003). An important feature that makes lipids appropriate biomarkers is the ability to withstand the increasing temperature and pressures associated with deep burial during degradation to structurally stable hydrocarbon molecules that have recognisable biological precursors derived from known source organisms.

In the marine realm, primary organic matter is mainly produced in the surface ocean by photoautotrophs. After death, a large proportion (>99.9%) of organic matter is recycled and remineralised by heterotrophic organisms living in the water column and at the sediment-water interface. Certain recalcitrant molecules (e.g., lipids and pigments) escape the recycling and remineralisation process and eventually become buried deep within the sediment where they are subjected to post-depositional processes. The three main stages of alteration to organic matter with increasing time and temperature are

known as diagenesis, catagenesis, and metagenesis (Peters & Moldowan, 1993; Figure 1.1).
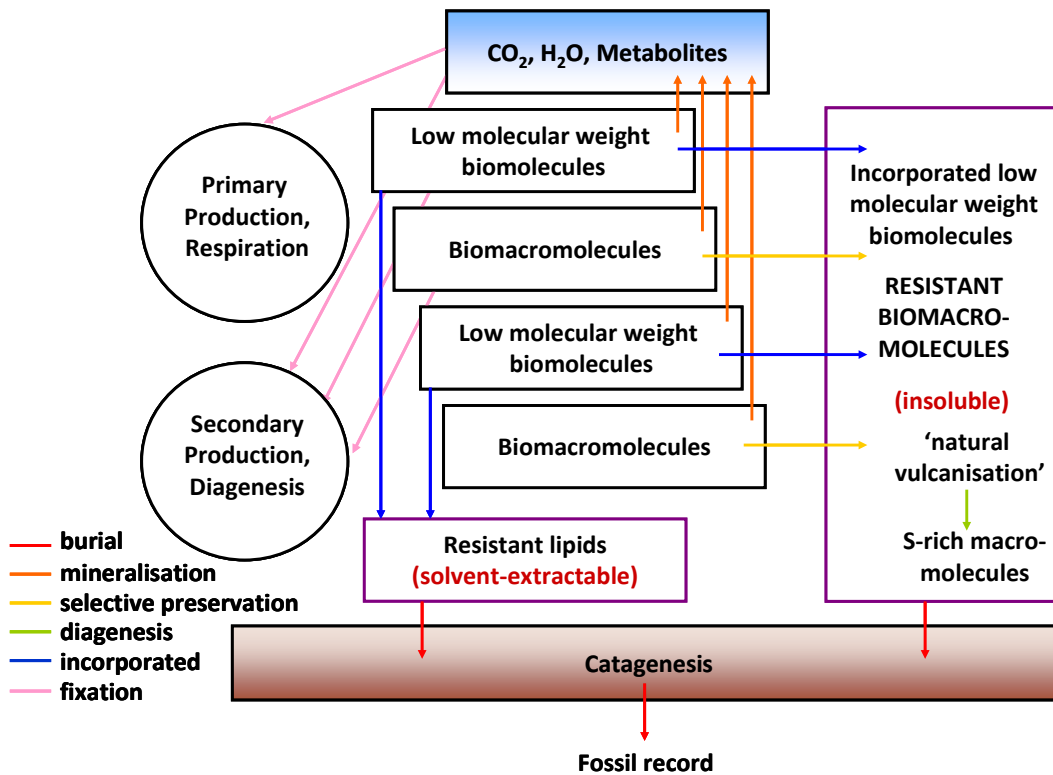
Figure 1.1. Schematic representation of the key reactions involved in the formation, transformation, and fate of mainly cyanobacterial-derived microbial mat organic matter. The coloured arrows correspond to the processes listed to the left. The purple outlined boxes represent different repositories that sequester organic matter; resistant lipids (solvent-extractable) represent the bitumen fractions and resistant bio-macromolecules (insoluble) represent the kerogen fraction.

Diagenesis is defined as the initial physical, chemical, and biological alterations that occur in the water column and during shallow burial in unconsolidated sediment. This involves changes to molecular structures that can occur at low temperature. Advanced sedimentary evolution of organic matter is characterised by increases in temperature (50-150°C) and pressure (Kissin, 1990). During burial, organic matter will become chemically altered and may coalesce to a macromolecular aggregate called kerogen. Kerogen is a complex mixture of degradation-resistant biopolymers cross-linked with smaller molecular units (Brocks & Pearson, 2005). It is, by definition, insoluble in normal organic solvents (Vandenbroucke & Largeau, 2007).

Catagenesis involves thermally-induced structural rearrangements (Peters & Moldowan, 1993) and cracking of stronger covalent bonds such as C—C and C—O. These reactions will start to crack individual free molecules off the macromolecular kerogen yielding mobile bitumen. Continued burial of organic matter accumulated in sediments at the onset of low-grade metamorphic temperatures (*ca.* 200°C) results in metagenesis (Brocks & Summons, 2003).

Metagenetic reactions involve cracking of residual bitumen into dry gas (>98% methane) and solidified pyrobitumen. The residual kerogen will turn into amorphous black carbon that is strongly aromatic as a result of the elimination of side groups (Brocks & Summons, 2003). Hydrocarbons generated up to the metagenetic stage include gas and short-chained hydrocarbons and have lost all structural characteristics that make them diagnostic biomarkers.

The most informative biomarkers are compounds or compound classes that have high taxonomic specificity, though more commonly biological communities or environmental conditions are best characterised by the biomarker assemblages with both compound ratios and presence/absence molecular indicators from a large suite of biomarker analytes being used to assess the assemblage contents. Additionally, lipid biomarkers can provide information about the thermal history of preserved organic matter as they progressively isomerise to the most thermodynamically stable stereochemical configuration during thermal maturation. The following compound classes, accompanied by brief descriptions, are mentioned throughout the thesis.

Alkanes. Alkanes are saturated hydrocarbons that are stable and ubiquitous compounds in organic matter preserved in the geological record and sedimentary alkanes encompass a diverse array of linear, branched, and cyclic structures. Alkanes are the hydrocarbon equivalents of *n*-alkyl lipids derived from the acetogenic pathway of lipid biosynthesis, from functionalised precursors such as *n*-alkanoic acids and *n*-alkanols. Linear normal alkanes (*n*-alkanes; C_{11}-C_{45}), iso- (2-methyl), anteiso- (3-methyl) alkanes, mono- and di- methylalkanes are also preserved in ancient and modern organic matter (e.g., Pawlowska *et al.,* 2013). *N*-alkanes can have a variety and mixture of sources in samples. They can be derived from eukaryotes or prokaryotes in aquatic (marine and lacustrine) environments as well as from the epicuticular leaf waxes of terrestrial higher plants (long-chain *n*-alkanes $>C_{24}$ with odd-over-even carbon number predominance). It has been shown that many bacterial species produce linear hydrocarbons with less than

22 carbon atoms in total, while archaeal lipid structures are dominated by acyclic isoprenoidal cores (Love *et al*., 2005).

Acyclic isoprenoids. Isoprenoids, which form the base structure of thousands of natural products, are methyl-branched linear alkanes that are synthesised from condensation of C_5 isoprene (C_5H_8; 2-methyl-1,3-butadiene) monomer units *via* the isoprenoidal pathway of lipid biosynthesis. Isoprenoids can be biosynthesised in nature through one of two different ways—the isopentenyl diphosphate (IPP) intermediate of the mevalonate pathway (MEP) or deoxyxylulose 5-phosphate (DXP – also known as non-mevalonate pathway, Eisenreich *et al.,* 2004). Most isoprenoids in the natural environment are regular (C_{14}-C_{25}) with 1,4 head-to-tail (e.g., regular iC_{40}) isoprene linkages however they can have irregular structures with either 1,1 head-to-head (e.g., biphytane) or 4,4 tail-to-tail (e.g., lycopane) linkages (Figure 1.2).

_i_C$_{40}$, irregular head-to-head (biphytane)

_i_C$_{40}$, irregular, tail-to-tail (lycopane)

_i_C$_{40}$, regular, head-to-tail (regular _i_C$_{40}$)
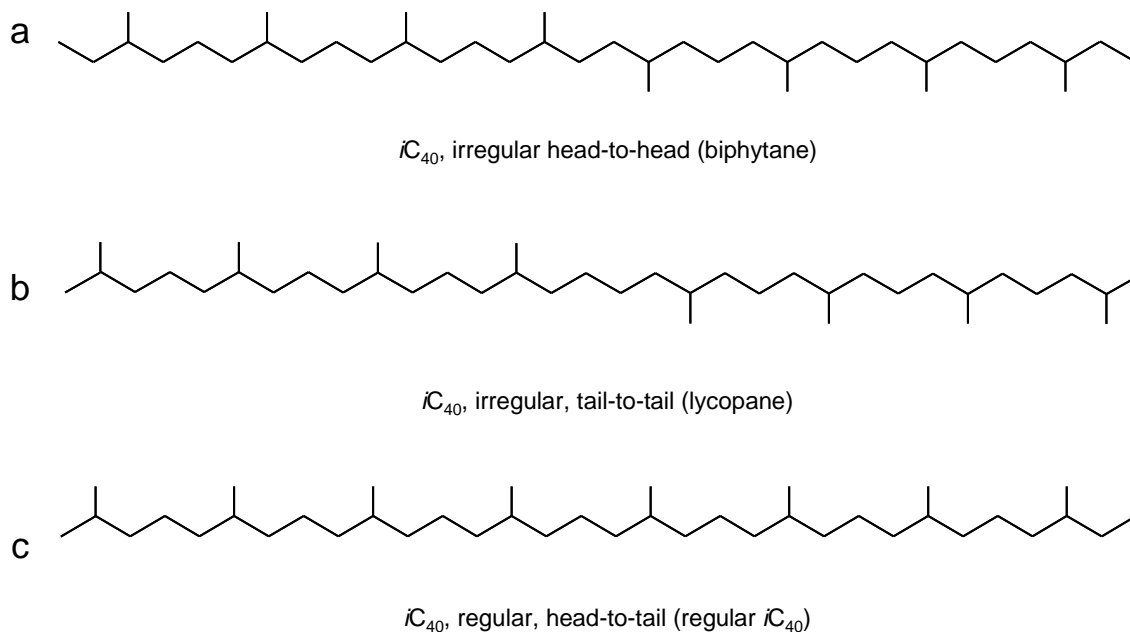
Figure 1.2. Chemical structures of C$_{40}$ isoprenoids with regular and irregular isoprenoid linkages. A) Acyclic biphytane with irregular head-to-head; b) Lycopane with irregular tail-to-tail; and c) C$_{40}$ isoprenoid with regular head-to-tail.

Cyclic isoprenoids: carotenoids. Carotenoids are pigment terpenoids with irregular isoprenoid linkages that can be differentiated into carotenes (hydrocarbons) or xanthophylls (containing oxygen). They are accessory pigments in some photosynthesising organisms and their preservation in the geological record is rare due to their high chemical reactivity (e.g. Koopmans *et al.,* 1997). Under certain conditions, their saturated hydrocarbon equivalents—carotanes—and their breakdown products (Lee & Brocks, 2011) and aromatic hydrocarbon equivalents and their breakdown products— aryl isoprenoids—can be preserved in ancient sediments (e.g. Brocks *et al.,* 2005, Brocks & Schaeffer, 2008). A comprehensive temporal study of C$_{40}$ sedimentary carotenoids can be found in French *et al.,* 2015.

Terpenoids: Tetracyclic (steranes) and pentacyclic (hopanes) terpanes are the polycyclic hydrocarbon remains of the isoprenoid-derived sterols and hopanoids, respectively. They provide a first order assessment of the bulk contribution of eukaryotic (steranes) versus bacterial (hopanes) biomass to preserved organic matter. Sterols are present in the membrane of eukaryotes to provide rigidity and regulate membrane fluidity. The biosynthesis of sterols requires the presence of molecular oxygen (specifically the epoxidation of squalene) and proceeds through pathways including synthesis and activation of isoprene, mevalonate, and squalene. There are three main sterol pseudohomologues that are common in organisms, sterols with 27 (C_{27}, cholesterol), 28 (C_{28}, ergosterol), and 29 (C_{29}, stigmasterol) carbon numbers (Figure 1.3).

C_{27} cholestane   **C_{28} ergostane**   **C_{29} stigmastane**

C_{30} *n*-propylcholestane (npc)   **C_{30} *iso*-propylcholestane (ipc)**
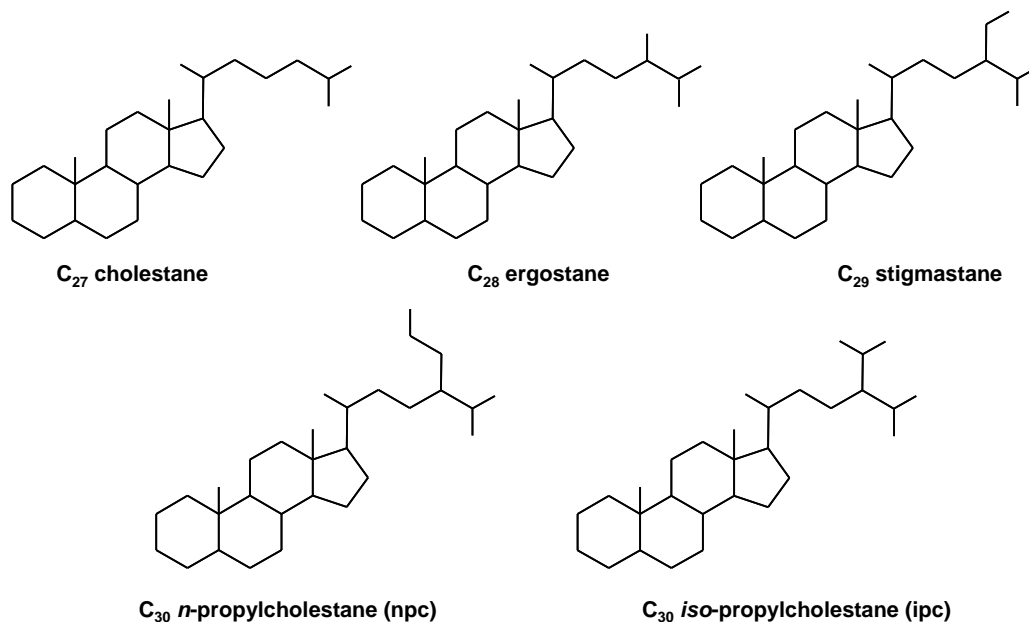
Figure 1.3. Chemical structures of sterane hydrocarbon homologues; C_{27} – cholestane; C_{28} – ergostane; C_{29} – stigmastane; C_{30} structural isomers *n*-propylcholestane and *iso*-propylcholestane.

The side-chain of cholesterol (at C-17) can be alkylated *via* the s-adenosyl-L-methionine-dependent C-24 sterol methyltransferase (SMT) enzyme at the C-24 position to produce the C_{28}, C_{29}, and even C_{30} sterol homologues. Sterane homologues are not diagnostic of single biological groups, but their abundance (relative to other sterane homologues) and changes through geological time reflects the succession of primary producers in the ocean (Schwark and Empt, 2006; Love *et al.,* 2009; Rohrssen *et al.,* 2015)—C_{27} (red algae), C_{28} (phytoplankton and fungi), C_{29} (green algae and higher plants), and C_{30} (pelagophytes and sponges). Hopanoids (Figure 1.4), as bacteriohopanepolyol (BHP), are mainly biosynthesised by bacteria and are similarly structured compounds to eukaryotic sterols, probably possessing similar functions. Their diagenetic products (geohopanoids) can be preserved in sample extracts and oils ranging from norhopanes (C_{27}-C_{29}) and extended homohopane series (C_{31}-C_{35}). Similarly with steranes, isomer distributions in hopane epimers can provide information regarding the thermal history of the sample. Methylated hopane homologues, such as 2α-methylhopane and 3β-methylhopanes (Figure 1.4), have been purported as biomarkers for cyanobacteria (Summons *et al.,* 1999) and type I microaerophilic methanotrophic bacteria, respectively. The taxonomic link between 2α- methylhopanes and cyanobacteria has been questioned, in terms of both source (Rashby *et al.,* 2007) and their mechanistic links to oxygenic photosynthesis (Doughty *et al.,* 2009; Welander *et al.,* 2010).
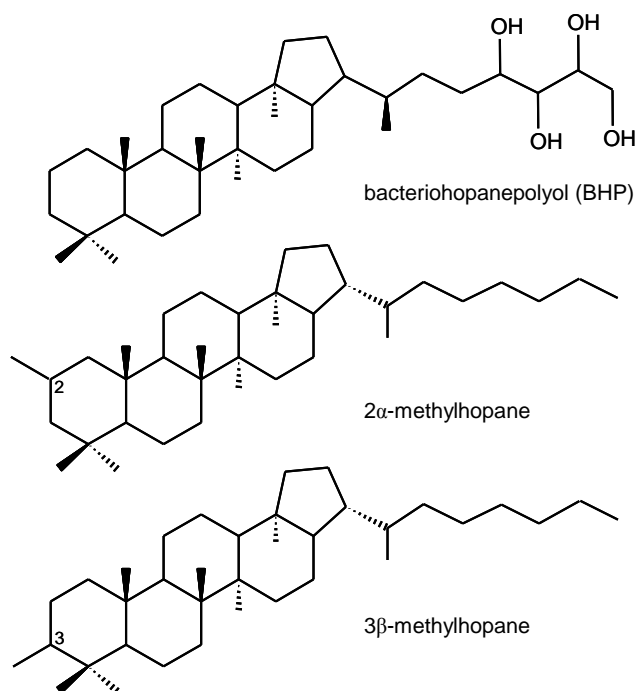
Figure 1.4. Chemical structures of bacteriohopanepolyol (BHP) and methylhopane hydrocarbons; 2α-methylhopane, and 3β-methylhopane.

1.2 Stable carbon isotope geochemistry

Measuring the two stable isotopes of carbon—[12]C (98.93% abundance) and [13]C (1.07% abundance) in the natural environment can be used to infer the budget, flow, and processing of carbon within the global carbon cycle (Figure 1.5). Carbon isotopes have been used to document local and global changes within the carbon inventory and have become staple geochemical stratigraphic correlation tools (Saltzman & Thomas, 2012).

Carbon dioxide dissolved into surface seawater dissociates into the inorganic aqueous species $CO_{2(aq)}$, HCO_3^- (bicarbonate ion), and CO_3^{2-} (carbonate ion), with minor contributions of H_2CO_3 (carbonic acid) (Zeebe, 2012). The resulting species can be fixed organically or inorganically to produce organic matter and calcium carbonate ($CaCO_3$),

respectively. A kinetic isotope effect is associated with the isotopic fractionation of inorganic and organic carbon, where biological processes such as photosynthesis enrich the light isotope (^{12}C) of carbon leaving the remaining inorganic pool enriched in the heavy isotope (^{13}C). Excursions in carbon isotope (^{13}C/^{12}C) trends can track perturbations to the global carbon cycle and can indicate the addition (negative ^{13}C excursion) or removal (positive ^{13}C excursion) of light ^{12}C carbon in to or from the system.
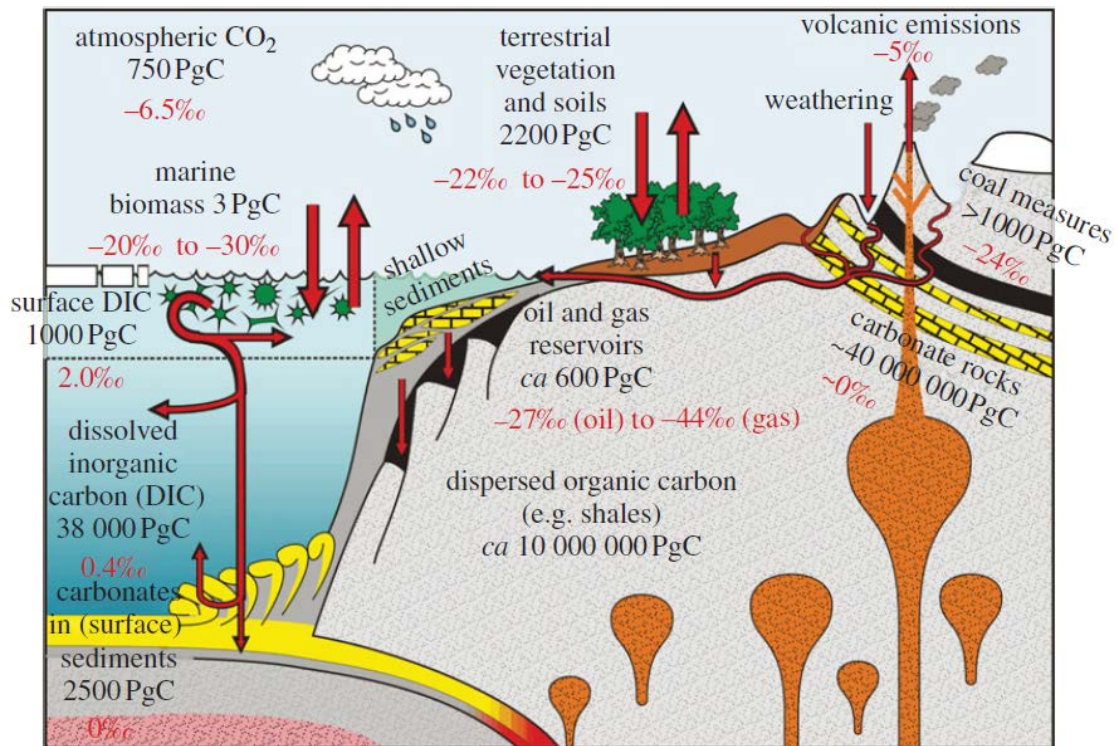
Figure 1.5. Graphical representation of the global long-term carbon cycle (Ridgwell & Zeebe, 2005; Zeebe, 2012; Saltzman & Thomas, 2012), showing the flow of carbon from different reservoirs (Dunkley Jones *et al.,* 2010). Numbers in red indicate average δ^{13}C isotopic composition (in ‰VPDB) and numbers in black indicate average size of reservoir in PgC (10^{15} grams – petagrams of carbon).

As early as carbon isotope measurements were being made, distinctive patterns emerged, allowing geochemists to utilise carbon isotopes as a proxy for studying the carbon cycle. The first comprehensive measurement of stable carbon isotopes ($^{13}C/^{12}C$) was carried out in a study published by Craig (1953), looking at the $^{13}C/^{12}C$ isotope ratios in 14 different carbon-bearing materials (Figure 3 in Craig, 1953). Results from these analyses show interesting patterns diagnostic of (biological) source and respective carbon utilisation pathways (Craig, 1953).

In addition to the use of lipid biomarkers to track biological source organisms, we can go one step further and track the source of utilised carbon by investigating the carbon isotopic composition ($\delta^{13}C$) of bulk organic matter as well as individual lipids (Hayes *et al.,* 1999). For example, analyses of the carbon isotopic composition of individual lipids in the Messel shale (Freeman *et al.,* 1990) reveals a diverse range of $\delta^{13}C$ values. Bulk values of ~-28 to -29‰ (Hayes *et al.,* 1987) accompanied by relatively ^{13}C-enriched lipids (-21‰) to heavily ^{13}C-depleted lipids (-73‰).

1.3 Overview of the thesis

There are four main chapters that make up the two parts of this thesis. They centre on the use of a variety of complimentary organic geochemical techniques such as traditional lipid biomarkers and bulk stable carbon isotopes as well as more novel and advanced applications including kerogen-bound lipid biomarkers and compound-specific carbon isotopes to probe questions pertaining to the source, preservation, and diagenesis

11

of benthic organic matter in Ediacaran and modern marine microbial mat ecosystems. The use of biomarkers has become an important tool in complimenting more conventional paleontological studies, especially in environments where body fossils are not well preserved. Although most biomarkers only have specificity to domain, phyla, or class level, they can provide biological information about groups of organisms which otherwise do not provide recognisable fossil remains in the sedimentary record. In the Precambrian (>541 Ma) body- and trace- fossil preservation is rare compared with the Phanerozoic. Therefore, with the prevalence of microscopic, unicellular, unmineralised bacterial and archaeal organisms in the Precambrian, biomarkers are the ideal tool to study early life and ecology.

The first part (Chapters 2 and 3) of this thesis is focussed on a period in Earth history that experienced intensive climatic perturbations and biological innovation. In addition to being bracketed by severe glaciations that were potentially global in scope and the evolution of large and complex biomineralising multicellular animals, this unique period in Earth history (~635 – 541 Ma; Ediacaran), hosts one of the largest negative carbonate carbon isotope excursions ever recorded—the 'Shuram excursion'—captured in marine carbonates. The origin, timing, and duration of the Shuram excursion continues to elude geochemists, as it has for over two decades, and garners a wide range of interpretations—including, but not limited to ideas expressed in Rothman *et al.,* 2003; Fike *et al.,* 2006; Kaufman *et al.,* 2007; Derry, 2010; Knauth & Kennedy, 2009; Bjerrum & Canfield, 2011; Johnston *et al.,* 2012; Young, 2013; Schrag *et al.,* 2013; Oehlert & Swart, 2014). Chapter 2 investigates bulk geochemical features of a thermally well-

preserved drillcore (TM-6) that is part of a deeper water, organic-rich facies. We present results for carbon (total carbonate minerals and bulk organic) content as well as stable isotope data for carbonate carbon and oxygen, bulk organic carbon, pyrite and carbonate-associated sulfate (Fike & Grotzinger, 2008), and organic nitrogen. In addition to presenting the first detailed biomarker profiles traversing the Shuram excursion, we address some important theories and models regarding Neoproterozoic carbon cycling, especially those that make predictions for the composition (e.g., quality or quantity) and behaviour of preserved organic matter. The majority of Chapter 2 was published in the peer-reviewed journal *Geobiology* (Lee *et al., 2013*) with the addition of organic nitrogen data post-publication.

A continuation of the aims of Chapter 2 to better understand source biota and carbon cycling through the Shuram excursion, Chapter 3 explores the carbon isotopic composition of individual hydrocarbons constituents from rock bitumens through the same TM-6 drillcore section capturing the Shuram excursion. We present the first stratigraphically-continuous δ^{13}C values from the adductable saturated hydrocarbon fraction (including C_{20}-C_{28} *n*-alkanes and an unusual series of mid-chain monomethyl alkanes) as well as the non-adductable saturated hydrocarbon fraction (including branched and polycyclic compounds and the unresolved complex mixture; UCM). We also investigate possible mechanistic scenarios and mass balance calculations that may help explain the extremely diverse δ^{13}C signals within preserved organic matter during the Shuram excursion. We define at least two isotopically distinct organic carbon pools (a surface autotrophic pool from primary phototrophs and a large seepage flux of petroleum

fluids generated from older sedimentary packages of rocks in the subsurface) that were decoupled from one another during the Shuram excursion and drove the unusual carbon cycle dynamics. The organic carbon source from subsurface petroleum seepage likely pervaded into multiple basins around the world, explaining the global decoupling of organic and inorganic carbon isotopic signatures. Importantly, the 5-7‰ excursion seen in the two major extractable alkane series confirms a perturbation to the Neoproterozoic carbon cycle of significant size, thus it is more likely recording a primary perturbation to seawater DIC than post-depositional diagenetic alteration. The majority of Chapter 3 is an extension of the manuscript published in the peer-reviewed journal *Geology* (Lee *et al.,* 2015).

The second part of this thesis—Chapters 4 and 5—moves into the modern marine realm, specifically targeting the preservation and modification of lipid biosignatures deposited in benthic hypersaline microbial mats. To investigate the processes which ultimately result in the consolidation of sedimentary organic matter and the transformations to key lipid biosignatures during these stages, pyrolysis techniques have proven to be beneficial. Kerogen hydropyrolysis provides a window into potential early diagenetic sequestration by covalent binding into high molecular weight macromolecular organic matter along with other transformations. The application of this and other complimentary techniques and the results they generate serve as insights into the evolution of preserved sedimentary organic matter as well as the intermediate stages individual molecules may experience during and post-burial.

Chapter 4 investigates 1) compositional differences between traditional intact polar lipid (IPL) extraction of the solvent-extractable lipids (bitumen) compared with novel solvent non-extractable lipids (kerogen-bound) through catalytic hydropyrolysis (HyPy)—and how these similarities and/or differences change with depth; and 2) the effect of microbial community structure and depositional environmental conditions (e.g., water salinity) on lipid preservation and modification in both the free and bound lipid fractions and with depth. Through these analyses, we find that the polycyclic hydrocarbon biomarker equivalents, steranes and hopanes, are rapidly incorporated into proto-kerogen at the very earliest stages of diagenesis dominated by the biological isomer and bind through strong covalent linkages. Molecular profiles are also able to capture subtle variations associated with changes in biological source inputs from even small increases in salinity.

Chapter 5 investigates the effect of different chemical treatments (chemolysis) on the composition of lipids released by catalytic hydropyrolysis from pre-extracted residues and how these are related to the timing and mode of (covalent) binding within the kerogen matrix during diagenesis. This chapter investigated two layers from two different cores, the first layer (layer 4 in both cores) is representative of active microbial processes, and the second layer (layer 7 in both cores) is representative of a sedimentary layer, defined mineralogically as the transition from a gelatinous matrix to a coarser, sandy/gravelly texture. The chemical treatments were designed to target specific chemical linkages within the kerogen matrix, with a range of degrees of chemical aggressiveness, from zero (untreated control) and least aggressive (trichloroacetic acid

and acid methanolysis) to most aggressive (periodate treatment). Additionally during acid methanolysis an emulsion formed during extraction, yielding a white fibrous material that makes up almost 50% of the extract residue, by (dry) weight. This material is probably sheath material or remnant accumulated sheath material from the microbial mats and constitutes a 'hydrophobic layer', however more detailed structural analyses to understand its origin is required. The results from this study provide strong additional evidence that polycyclic biomarkers (terpenoids) are rapidly incorporated into microbial mat proto-kerogen and get transformed during sedimentary diagenesis. The addition of this new data compliments existing data from this extensively well-studied natural laboratory, adding to a rich database with over two decades of compilations that track the physical, biological, geochemical processes of this unique environment.

Chapter 6 contains a synthesis and summary of the main data and conclusions presented in this thesis and contains some ideas and applications for ongoing, as well as future, research.

References

Bjerrum, C. J., and Canfield, D. E. 2011. Towards a quantitative understanding of the late Neoproterozoic carbon cycle. *Proceedings of the National Academy of Sciences of the United States of America*, **108**(14), 5542-5547.

Brocks, J. J., and Pearson, A. 2005. Building the biomarker tree of life. *Reviews in Mineralogy and Geochemistry* **59**(1), 233-258.

Brocks, J. J., and Schaeffer, P. 2008. Okenane, a biomarker for purple sulfur bacteria (Chromatiaceae), and other new carotenoid derivatives from the 1640 Ma Barney Creek Formation. *Geochimica et Cosmochimica Acta* **72**(5), 1396-1414.

Brocks, J. J., and Summons, R. E. 2003. Sedimentary hydrocarbons, biomarkers for early life. In: *Treatise on Geochemistry*. (eds. Holland, H. D., and Turekian, K. K.). Elsevier, 63-115.

Craig, H. 1953. The geochemistry of the stable carbon isotopes. *Geochimica et Cosmochimica Acta* **3**(2-3), 53-92.

Derry, L. A. 2010. A burial diagenesis origin for the Ediacaran Shuram-Wonoka carbon isotope anomaly. *Earth and Planetary Science Letters*, **294**, 152-162.

Doughty, D. M., Hunter, R. C., Summons, R. E., and Newman, D. K. 2009. 2 Methylhopanoids are maximally produced in akinetes of *Nostoc punctiforme*: geobiological implications. *Geobiology* **7**, 524-532.

Dunkley Jones, T., Ridgwell, A. J., Lunt, D. J., Maslin, M. A., Schmidt, D. N., and Valdes, P. J. 2012. A Paleogene perspective on climate sensitivity and methane hydrate stability. *Philosophical Transactions of the Royal Society A* **368**, 2935 2415.

Eisenreich, W., Bacher, A., Arigoni, D., and Rohdich, F. 2004. Biosynthesis of isoprenoids via the non-mevalonate pathway. *Cellular and Molecular Life Sciences* **61**(12), 1401-1426.

Fike, D. A., Grotzinger, J. P., Pratt, L. M., and Summons, R. E. 2006. Oxidation of the Ediacaran Ocean. *Nature*, **444**, 744-747.

Fike, D. A., and Grotzinger, J. P. 2008. A paired sulfate-pyrite δ^{34}S approach to understanding the evolution of the Ediacaran-Cambrian sulfur cycle. *Geochimica et Cosmochimica Acta* **72**(11), 2636-2648.

Freeman, K, H., Hayes, J. M., Trendel, J-M., and Albrecht, P. 1990. Evidence from carbon isotope measurements for diverse origins of sedimentary hydrocarbons. *Nature* **343**, 254-256.

French, K. L., Rocher, D., Zumberge, J. E., and Summons, R. E. 2015. Assessing the distribution of sedimentary C_{40} carotenoids through time. *Geobiology* **13**, 139 151.

Hayes, J. M., Takigiku, R., Ocampo, R., Callot, H. J., and Albrecht, P. 1987. Isotopic compositions and probable origins of organic molecules in the Eocene Messel shale. *Nature* **329**, 48-51.

Johnston, D. T., Macdonald, F. A., Gill, B. C., Hoffman, P. F., Schrag, D. P. 2012. Uncovering the Neoproterozoic carbon cycle. *Nature*, **483**, 320-324.

Kaufman, A. J., Corsetti, F. A., and Varni, M. A. 2007. The effect of rising atmospheric oxygen on the carbon and sulfur isotope anomalies in the Neoproterozoic Johnnie Formation, Death Valley, USA. *Chemical Geology* **237**(1-2), 47-63.

Kissin, Y. V. 1990. Catagenesis of light cycloalkanes in petroleum. *Organic Geochemistry* **15**(6), 575-594.

Lee, C., and Brocks, J. J. 2011. Identification of carotenoid breakdown products in the geological record. *Organic Geochemistry* **42**(4), 425-430.

Lee, C., Fike, D. A., Love, G. D., Sessions, A. L., Grotzinger, J. P., Summons, R. E., and Fischer, W. W. 2013. Carbon isotopes and lipid biomarkers from organic-rich facies of the Shuram Formation, Sultanate of Oman. *Geobiology* **11**(5), 406-419.

Lee, C., Love, G. D., Fischer, W. W., Grotzinger, J. P., and Halverson, G. P. 2015. Marine organic matter cycling during the Ediacaran Shuram excursion. *Geology* **43**(12), 1103-1106.

Love, G. D., Bowden, S. A., Jahnke, L. L., Snape. C. E., Campbell, C. N., Day, J. G., Summons, R. E. 2005. A catalytic hydropyrolysis method for the rapid screening of microbial cultures for lipid biomarkers. *Organic Geochemistry* **36**, 63-82.

Love, G. D., Grosjean, E., Stalvies, C., Fike, D. A., Grotzinger, J. P., Bradley, A. S., Kelly, A. E., Bhatia, M., Meredith, W., Snape, C. E., Bowring, S. A., Condon, D. J., and Summons, R. E. 2009. Fossil steroids record the appearance of Demospongiae during the Cryogenian Period. *Nature*, **457**, 718-722.

Oehlert, A. M., and Swart, P. K. 2014. Interpreting the carbonate and organic carbon isotope covariance in the sedimentary record. *Nature Communications* **5**, 1-7.

Peters, K. E., and Moldowan, J. M. 1993. The Biomarker Guide: Interpreting molecular fossils in petroleum and ancient sediments. Prentice Hall, pp. 363.

Rashby, S. E., Sessions, A. L., Summons, R. E., and Newman, D. K. 2007. Biosynthesis of 2-methylbacteriohopanepolyols by an anoxygenic phototroph. *Proceedings of the National Academy of Sciences of the United States of America* **104**, 15099 15104.

Ridgwell, A. J., and Zeebe, R. E. 2005. The role of the global carbonate cycle in the regulation and evolution of the Earth system. *Earth & Planetary Science Letters* **234**, 299-315.

Rohrssen, M., Gill, B. C., and Love, G. D. 2015. Scarcity of the C_{30} sterane biomarker, 24-*n*-propylcholestane, in Lower Paleozoic marine paleoenvironments. *Organic Geochemistry* **80**, 1-7.

Rothman, D. H., Hayes, J. M., and Summons, R. E. 2003. Dynamics of the Neoproterozoic carbon cycle. *Proceedings of the National Academy of Sciences of the United States of America* **100**(14), 8124-8129.

Saltzman, M. R., and Thomas, E. 2012. Carbon isotope stratigraphy. In: *The Geologic Time Scale*. (eds. Grandstein, F. M., Ogg, J. G., Schmitz, M., and Ogg, G.). Elsevier, 207-232.

Schrag, D. P., Higgins, J. A., Macdonald, F. A., and Johnston, D. T. 2013. Authigenic carbonate and the history of the global carbon cycle. *Science* **339**, 540-543.

Schwark, L., and Empt, P. 2006. Sterane biomarkers as indicators of Palaeozoic algal evolution and extinction events. *Palaeogeography, Palaeoclimatology, Palaeoecology* **240**, 225-236.

Summons, R. E., Jahnke, L. L., Hope, J. M., and Logan, G. A. 1999. 2-Methylhopanoids as biomarkers for cyanobacterial oxygenic photosynthesis. *Nature* **400**, 554-557.

Vandenbroucke, M., and Largeau, C. 2007. Kerogen origin, evolution, and structure. *Organic Geochemistry* **38**(5), 719-833.

Welander, P. V., Coleman, M. L., Sessions, A. L., Summons, R. E., and Newman, D. K. 2010. Identification of a methylase required for 2-methylhopanoid production and implications for the interpretation of sedimentary hopanes. *Proceedings of the National Academy of Sciences of the United States of America* **107**, 8537-8542.

Young, G. M. 2013. Evolution of Earth's climatic system: Evidence from ice ages, isotopes, and impacts. *GSA Today* **23**(10), 4-10.

Zeebe, R. E. 2012. History of seawater carbonate chemistry, atmospheric CO_2 and ocean acidification. *Annual Reviews in Earth & Planetary Sciences* **40**, 141-165.

CHAPTER TWO

Bulk chemostratigraphic profiles traversing organic-rich facies from the Nafun Group, South Oman Salt Basin, Sultanate of Oman

ABSTRACT

The largest recorded carbon isotopic excursion in Earth history is observed globally in carbonate rocks of middle Ediacaran age (*ca*. 580 Ma). Known from the Sultanate of Oman as the 'Shuram excursion', this event records a dramatic, systematic shift in $\delta^{13}C_{carbonate}$ ($\delta^{13}C_{carb}$) values to *ca*. -12‰. Attempts to explain the nature, magnitude, and origin of this excursion include *i)* as a primary signal resulting from the protracted oxidation of a large dissolved organic carbon (DOC) reservoir in seawater, release of methane from sediment-hosted clathrates, or water column stratification; and *ii)* a secondary signal from diagenetic processes. The compositions and isotope ratios of organic carbon phases during the excursion are critical to evaluating these ideas, however previous work has focused on localities that are low in organic carbon, hindering straightforward interpretation of the observed time series trends. We report carbon isotope data from bulk organic carbon, extracted bitumen and kerogen, in addition to detailed lipid biomarker stratigraphy, from a subsurface well drilled on the eastern flank of the South Oman Salt Basin, Sultanate of Oman. This section captures Nafun Group strata through the Ediacaran-Cambrian boundary (541 Ma) in the Ara Group, and includes an organic-rich, deeper water facies of the Shuram Formation. Despite the high organic matter contents, the carbon isotopic compositions of carbonates—which record a

negative $\delta^{13}C$ isotope excursion similar in shape and magnitude to sections elsewhere in Oman—do not covary with those of organic phases (bulk total organic carbon (TOC), bitumen, and kerogen). Paired inorganic and organic $\delta^{13}C$ data only display coupled behaviour during the latter part of the excursion's recovery. Furthermore, lipid biomarker data reveal that organic matter composition and source inputs varied stratigraphically, reflecting biological community shifts in non-migrated, syngenetic organic matter deposited during this interval.

1. Introduction

The rock record of the late Neoproterozoic Era (*ca*. 800-541 Ma) captures a period of dynamic and global environmental change in Earth history, marked by large magnitude perturbations to the global carbon cycle (Grotzinger *et al*., 2011), several global low-latitude glaciations (Hoffman *et al*., 1998), increasing and widespread oxygenation of Earth's atmosphere and deep oceans (Knoll *et al*., 1986; Fike *et al*., 2006; Scott *et al*., 2008), and the evolution and diversification of Metazoa (Knoll & Carroll, 1999). Subsequent to the Cryogenian global glaciations yet prior to the evolution of bilateria near the Ediacaran-Cambrian boundary, middle Ediacaran-aged successions host the largest negative carbon isotopic excursion observed in the geologic record, with values of $\delta^{13}C_{carbonate}$ ($\delta^{13}C_{carb}$) as low as -12‰ (summarised in Grotzinger *et al*., 2011). This excursion was first observed in the Wonoka Formation of South Australia (Jansyn, 1990; Urlwin *et al*., 1993; Pell *et al*., 1993). Burns and Matter (1993) were the first to detail the

unusual excursion in Oman and link these carbon cycle dynamics to animal evolution. In addition to Oman (e.g., Le Guerroué *et al*., 2006a,b,c) and Australia (e.g., Calver, 2000), negative excursions displaying similar characteristics have been observed in many Ediacaran sedimentary successions, including the Doushantuo Formation of South China (e.g., McFadden *et al*., 2008), the Johnnie Formation of the western United States (e.g., Kaufman *et al*. 2007; Bergmann *et al*., 2011), as well as other potentially correlative strata around the world.

If primary, the striking pattern observed in the Shuram excursion makes it difficult to interpret the historical behaviour of the carbon cycle using commonly applied assumptions in an isotope mass balance framework. Fundamentally, explanations must invoke carbon fluxes (inputs) into the fluid Earth with isotope ratios lower than -5 to -6‰–values commonly assumed for outgassing and weathering. Alternatively, it has been hypothesised that the Shuram excursion does not record the primary isotopic composition of marine dissolved inorganic carbon (DIC), but was caused rather by secondary, diagenetic processes—perhaps global in scope (Bristow & Kennedy, 2008; Knauth & Kennedy, 2009; Derry, 2010a; Grotzinger *et al*., 2011; Schrag *et al*., 2013). Several observations fuel diagenetic hypotheses—including the widely observed positive correlation between the carbon and oxygen isotopic composition of carbonates—but another critical part of the Shuram puzzle is that the isotopic composition of coeval organic matter does not record the same time series pattern, but is instead largely invariant (e.g., Fike *et al*., 2006; McFadden *et al*., 2008). This feature might be most simply explained if the excursion were diagenetic in origin (e.g., Derry, 2010b), but two

23

different hypotheses have been developed to explain the pattern as a consequence of primary sedimentary and carbon cycle processes.

Focussing on the pattern of decoupled $\delta^{13}C_{carb}$ and $\delta^{13}C_{org}$ values in Neoproterozoic successions, Rothman *et al*. (2003) formulated a generic carbon cycle scenario in which both the negative excursions in $\delta^{13}C_{carb}$ values and the invariant organic matter $\delta^{13}C$ values ($\delta^{13}C_{org}$) were caused by the slow oxidation of a large dissolved organic carbon (DOC) seawater pool (Rothman *et al*., 2003). A large DOC reservoir, much larger than the mass of inorganic carbon in DIC, allows $\delta^{13}C_{org}$ to be buffered against isotopic variation, while its progressive and eventual remineralisation would have produced ^{13}C-depleted isotope ratios observed in carbonate (Rothman *et al*., 2003). Fike *et al*. (2006) subsequently invoked this hypothesis to explain the Shuram excursion, and this idea has seen broad application to explain decoupled carbonate-organic datasets from other sections (e.g., McFadden *et al*., 2008) and Neoproterozoic intervals (e.g., Swanson-Hysell *et al*., 2010), and has been integrated into new modelling approaches (Bjerrum & Canfield, 2011). A reasonable concern with the decoupling argument comes from the quality of the organic carbon isotope data, much of which comes from organic-lean sections (Calver, 2000; Fike *et al*., 2006; Swanson-Hysell *et al*., 2010)—with TOC wt% values of <0.05, perhaps approaching analytical blanks. Recently it was proposed that throughout Neoproterozoic time, $\delta^{13}C_{org}$ values should record an expected ^{13}C-depleted linear translation of DIC trends and that the reason organic-lean samples do not mirror the expected trends is because the $\delta^{13}C_{org}$ of these samples is instead controlled by admixtures of fossil detrital or migrated organic carbon (Johnston *et al*., 2012). In order

to test these different hypotheses, it is important to examine the isotopic systematics of strata that capture the Shuram excursion that are rich in organic carbon and derived from unweathered materials.
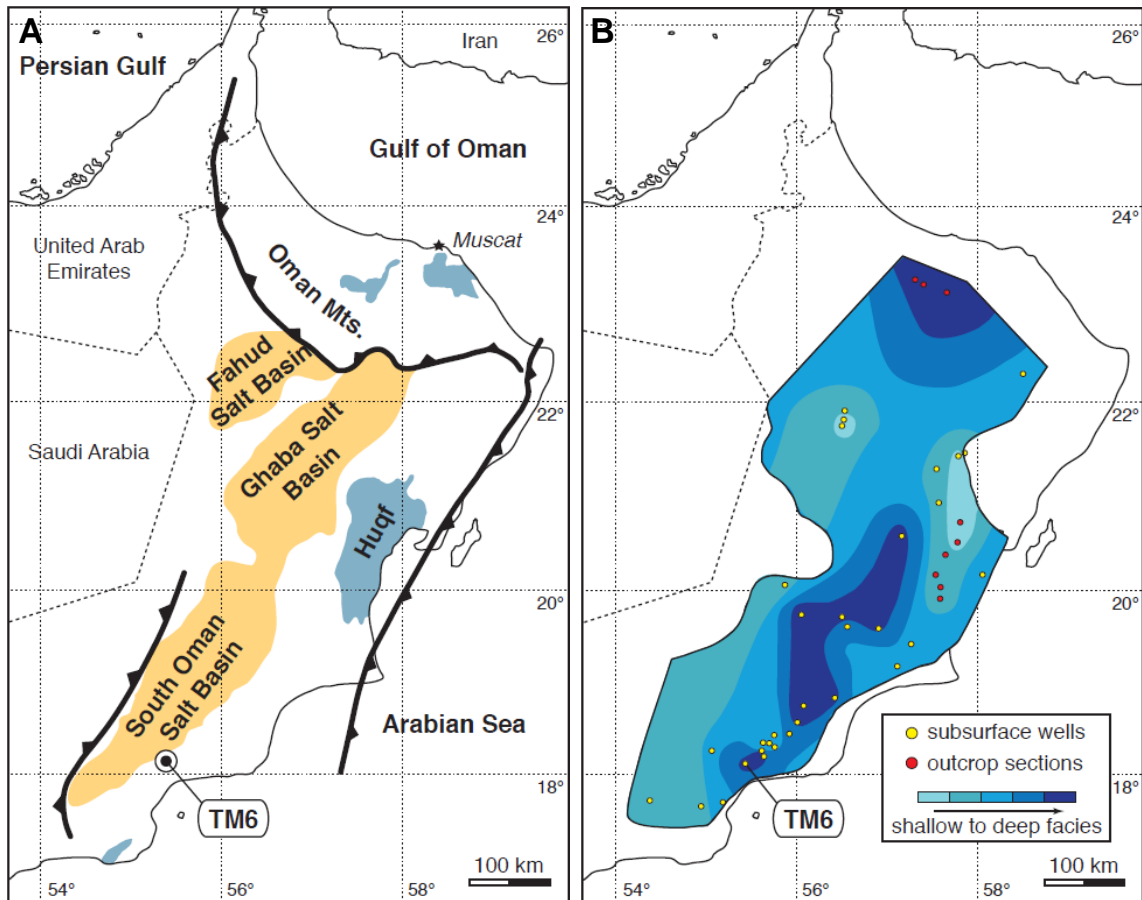
Figure 2.1: Left panel (A): Geologic map of the sub-basins containing Huqf Supergroup strata throughout the Sultanate of Oman. Outcrop localities are shown in dark blue, subsurface salt basins are shown in orange. The location of the subsurface well TM-6 on the eastern flank of the South Oman Salt Basin is marked. Right panel (B): Bathymetric facies map of the Shuram Formation in Oman (data from Petroleum Development Oman and Le Guerroué *et al*., 2006a).

Much of the Shuram Formation studied thus far is organic-lean in both outcrop and subsurface strata, but in certain areas of the basin, petroliferous and fossiliferous strata are preserved. The eastern flank of the South Oman Salt Basin (Figure 2.1A) contains extremely thermally well-preserved molecular fossils (e.g., Love *et al*., 2008; Grosjean *et al*., 2009; Love *et al*., 2009) as well as a suite of sphaeromorphic acritarchs and filamentous microfossil assemblages in the Nafun Group (Butterfield & Grotzinger, 2012). Here we report isotopic and lipid biomarker data from an eastern flank locality in Oman that captures a deeper water (Figure 2.1B), organic-rich facies of the Shuram and overlying Buah formations, in order to better understand carbon cycle processes and biological community dynamics through the Shuram excursion.

2. Geology: The South Oman Salt Basin, Sultanate of Oman

The Huqf Supergroup of the Sultanate of Oman provides one of the best-preserved, most continuous late Neoproterozoic to early Cambrian (*ca*. 713-540 Ma; Allen, 2007; Bowring *et al*., 2007) successions globally. Outcrop exposures of Huqf strata are limited to the Oman Mountains in the north, Mirbat area in the south, and the Huqf area, but a substantial amount of knowledge and materials exist from numerous petroleum exploration and production wells throughout the subsurface, particularly the South Oman Salt Basin (Schröder *et al*., 2004) (Figure 2.1).

The Huqf Supergroup is composed of three groups that show broadly similar stratigraphic patterns between the sub-basins. The lowest group—the Abu Mahara—is composed of clastics, including Cryogenian-age, glacially-derived sediments (Allen, 2007). The overlying Nafun Group begins with the Marinoan (*ca.* 630 Ma) Hadash cap carbonate and then records two overall clastic-to-carbonate shallowing upward trends defined by the Masirah Bay clastics and overlying Khufai Formation carbonate ramp, and the Shuram Formation mixed clastics and carbonates with the overlying Buah Formation carbonate ramp (McCarron, 2000; Grotzinger *et al*., 2002; Cozzi *et al*., 2004; Le Guerroué *et al*., 2006a). The Shuram excursion nearly covers one of these first order cycles, beginning in the uppermost Khufai Formation (Osburn *et al*., 2014) with the recovery finishing in the lower Buah Formation (Burns & Matter 1993; Le Guerroué *et al*., 2006a). Finally, the Ara Group records an evaporite basin with several successive carbonate platform stringers (Gorin *et al*., 1982; Schröder *et al*., 2004). Despite similar overall stratigraphic patterns between basins, facies differences between regions record striking gradients in paleoenvironment; and Nafun Group strata exemplify this.

The Shuram Formation exhibits significant facies changes across Oman. In outcrop, it is well known that shallow shelf platform facies in the Huqf outcrop region pass downdip into sub-wave base deposits (McCarron, 2000; Le Guerroué *et al*., 2006a,b). The depositionally updip deposits include wave-rippled to hummocky cross-stratified siltstones and fine sandstones, interstratified with trough cross-stratified ooid grainstones and intraclast conglomerates. Characteristically these upper shoreface

27

deposits form shallowing-upward cycles in which the siliciclastic-dominated facies pass upward into the carbonate-dominated facies (Le Guerroué *et al*., 2006b).

In contrast, downdip facies are expressed as interbedded siliciclastic mudstones and siltstones, with zones of carbonate cementation and concretion development (Figure 2.1). Convolute bedding and slump structures are present, along with current ripples. Uncommonly, small scale hummocky cross-stratification is observed. References to "organic-rich" facies in outcrop have been noted (e.g., Le Guerroué *et al*., 2006a) though these have not been confirmed through measurement of organic carbon concentrations.

Due to the lack of surface oxidative weathering, the subsurface record of Shuram Formation facies variability provides the best indicator of how primary concentrations of organic content vary spatially and temporally throughout the formation. Well data collected by Petroleum Development Oman over the past 40 years was examined by Le Guerroué *et al*. (2006a) who reproduced their facies map for the Shuram Formation (Figure 2.1B). Figure 2.1B shows these lateral facies changes in the Shuram, illustrating the presence of deeper water facies trending NE-SW, shallowing to the east along the Huqf area outcrop belt, a long-lived topographic high. The western limit of the deeper water facies belt is uncertain due to uplift and erosion along the Western Deformation Front (Loosveld *et al*., 1996; Grotzinger *et al*., 2002). Paleogeographic trends suggest it would have continued to deepen in a westerly direction (see Allen, 2007, Figure 10).

Only a small fraction of the Shuram Formation has been cored. Fortunately, it is standard industry practice to analyse cuttings for information regarding lithology, including primary sedimentology, diagenesis, and the detection of organic-rich facies. Wireline logs additionally provide a wealth of petrophysical data that can provide important constraints on organic content. The presence of organic matter can be confidently detected with a combination of increasing gamma ray values, sonic transit time, neutron porosity, resistivity, and with reduction in the formation bulk density (Meyer & Nederlof, 1984; Mann *et al.*, 1986; Herron & Le Tendre, 1990). Based on analysis of wireline logs and organic geochemical analyses of cuttings, the Shuram Formation was recognised to contain organic-rich source rocks in deeper water paleogeographic settings (Le Guerroué *et al.*, 2006a; Grosjean *et al.*, 2009). We examined materials from the TM-6 well located within this organic-rich, deeper water facies belt (Figure 2.1B).

3. Methods

3.1 Sample preparation and bitumen extraction

Samples from TM-6, collected as cm-sized drill cuttings, were initially soaked and rinsed 3× in distilled deionised (DI) water, then rinsed with 3x methanol (MeOH), 3× dichloromethane (DCM), and 3× *n*-hexane to remove residual surface contamination. The cuttings were milled to fine powder using a SPEX 8510 Shatterbox with an alumina

ceramic container. The mill was cleaned with pre-combusted (850°C; 9 h) sand between each sample, as well as rinsed with water, MeOH, and DCM.

Rock powders (typically 1.5 – 3 g) were extracted in 20 ml of DCM:MeOH (9:1 v/v) using either Mars5 or MarsXpress (CEM) microwave extraction system at 100°C for 15 mins with constant stirring. One blank consisting of pre-combusted silica sand (850°C; 9 h) was extracted with each batch of samples. After cooling, sample extracts were filtered and solvent was evaporated under a stream of pure N_2 into pre-tared vials. To ensure complete extraction, the remaining sediment was re-extracted – up to eight times – until the extract contained no more measurable (by weight) bitumen. Fraction yields reported in Appendix Table A2.1.

3.2 Kerogen isolation and Total Organic Carbon (TOC)

To isolate kerogen, solvent-extracted rock powder was acidified at room temperature using concentrated hydrochloric acid (HCl; 1 N) for 48 h to remove carbonate minerals. The powders were rinsed repeatedly with DI water until a pH in the range of 4 – 5 was achieved. To prepare samples for TOC measurements, whole rock power was acidified as described above. Samples were dried overnight and loaded into tin capsules for analysis.

3.3 Isotope ratio analyses

3.3.1 Carbonate carbon and oxygen isotopes ($\delta^{13}C_{carb}$ and $\delta^{18}O_{carb}$)

Carbonate carbon ($\delta^{13}C_{carb}$) and oxygen isotopes ($\delta^{18}O_{carb}$) were measured on CO_2 after reaction with anhydrous phosphoric acid by gas-source mass spectrometry according to standard methods previously described in Ostermann and Curry (2000). Data are reported in the conventional $\delta^{13}C$ notation as parts per thousand (permil; ‰) deviations from the Vienna Pee Dee Belemnite (VPDB) standard.

3.3.2 Sulfur isotopes (pyrite and carbonate-associated sulfate (CAS); $\delta^{34}S_{pyr}$, $\delta^{34}S_{CAS}$)

The sulfur isotopic composition of pyrite ($\delta^{34}S_{pyrite}$; $\delta^{34}S_{pyr}$) was determined by extraction as chromium-reducible sulfur, described in detail in Fike *et al*., 2006 and Fike & Grotzinger, 2008. Briefly, crushed and cleaned powders were extracted under N_2 gas by acidifying with 6 N HCl and reduced by a 0.4 M chromium chloride ($CrCl_3$) solution. Silver sulfide precipitates were collected, rinsed, filtered, and dried and combined with vanadium oxide (V_2O_5). The sulfur isotopic composition of carbonate-associated sulfate (CAS) was determined by dissolution of carbonate and precipitation of barite, followed by combustion to SO_2 and analysis by gas-source mass spectrometry; the details of the method are outlined in Fike and Grotzinger (2008). Briefly, CAS was obtained by dissolving powered sample in 6 N HCl for either 2 h at 60°C under nitrogen gas or 12 – 24 h at room temperature. Samples were filtered to eliminate insoluble residues and excess barium chloride was added to the filtrate to precipitate barium sulfate for

subsequent analysis. $\delta^{34}S_{pyr}$ and $\delta^{34}S_{CAS}$ isotopes were measured on a Finnigan MAT 252 gas source mass spectrometer fitted with a peripheral elemental analyser (EA), performed at Indiana University. Sulfur isotope ratio data are reported in permil relative to the Vienna-Canyon Diablo Troilite (V-CDT) standard. Samples were calibrated using the international standards NBS-127 (20.3‰) and S3 (-31.5‰), as well as four internal standards: silver sulfide (ERE-Ag$_2$S: -4.3‰), chalcopyrite (EMR-CP: 0.9‰), and two barium sulfate standards (BB4-18: 39.5‰; PQB: 38.0‰) (Fike & Grotzinger, 2008).

3.3.3 Organic carbon isotopes ($\delta^{13}C_{org}$)

TOC and kerogen fractions were loaded into tin capsules (Costech) as powder. Bitumen dissolved in DCM was pipetted into tin capsules and the solvent was evaporated to dryness prior to analysis. Samples for bitumen and kerogen were flash combusted in a 1000°C furnace using a Costech Analytical Technologies Elemental Analyser (EA). The resulting CO_2 gas was analysed by continuous flow using a Finnigan MAT Delta-S Isotope Ratio Mass Spectrometer (IRMS). Calibration of $\delta^{13}C_{org}$ values was accomplished by comparison with system blanks (empty tin capsules) and two working standards, acetanilide ($C_6H_5NH(COCH_3)$) and urea (CH_4N_2O). Blanks and standards were run after every 10 sample measurements (including replicates). Sample $\delta^{13}C$ values were repeatable to a standard error of 0.26‰ (TOC), 0.32‰ (bitumen), and 0.54‰ (kerogen). Blanks and standards were repeatable to an average standard error of 0.62‰ (system blank; n = 19), 0.02‰ (acetanilide standard; n = 20), and 0.04‰ (urea standard; n = 23). Samples for TOC were flash combusted at 1060°C in a Carlo Erba NA1500

Elemental Analyser fitted with an AS200 autosampler. The resulting CO_2 gas was analysed by a Finnigan DELTAplusXP (Thermo Fisher Scientific) IRMS. Organic carbon isotope ratios are reported in the conventional delta notation as permil variations relative to the VPDB standard. $\delta^{13}C_{org}$ values were calibrated against the two international standards sucrose (IAEA-CH-6) and mineral oil (NBS-22) and the two in-house reference standards acetanilide ($C_6H_5NH(COCH_3)$) and Penn State Kerogen (Fike, 2007).

3.3.4 Organic nitrogen isotopes ($\delta^{15}N_{org}$)

Nitrogen isotopes were obtained on the total lipid extract fraction by dissolving in DCM, transferring to tin capsules (Costech) and allowing the solvent to evaporate to dryness prior to analysis. Samples were flash combusted at 1,020°C on a Costech Analytical Technologies ECS 4010 CHNSO Nitrogen/Protein Elemental Analyser (EA) fitted with a sealed Zero Blank autosampler. The resulting gas was analysed by continuous flow on a DELTA V Advantage (Thermo Fisher Scientific) IRMS. Organic nitrogen isotope ratios are reported in the conventional delta notation as permil variations relative to air. Calibration of $\delta^{15}N_{org}$ was accomplished by system blanks and two standard reference materials; peach leaves (SRM 1547) and USGS40 (L-glutamic acid; SRM 8573). Samples were repeatable to an average standard error of 0.10‰.

3.4 Lipid biomarkers

Traces of elemental sulfur were removed from bitumen extracts using acid- (6 N HCl, 6× MilliQ water) and solvent-washed (6× MeOH, 6× DCM, 6x *n*-hexane) activated copper granules (Alfa Aesar). The extract was separated into three fractions by columns filled with pre-combusted (450°C; 9 h) dry-packed silica gel (Geduran EMD, Grade 60). The saturates fraction was eluted with *n*-hexane, the aromatic fraction with *n*-hexane:DCM (1:1 v/v), and the polar fraction with DCM:MeOH (3:1 v/v). A deuterated C_{29} sterane standard (d4-ααα-24-ethylcholestane (20R), Chiron Laboratories AS) was added to the saturate fraction prior to biomarker quantification through GC-MS. Typically 50 ng of internal standard was added to a 1 mg aliquot of saturates.

3.5 Gas Chromatography-Mass Spectrometry (GC-MS) and Metastable Reaction Monitoring (MRM)

Saturated hydrocarbons were analysed by gas chromatography-mass spectrometry (GC-MS) in full scan mode on a Micromass Autospec Ultima equipped with a HP6890 gas chromatograph (Hewlett Packard). Sterane and hopane biomarkers were analysed on the Autospec instrument in Multiple Reaction Monitoring (MRM) mode. Details of the run conditions and uncertainties in the biomarker ratios are the same as in Love *et al*., 2009. Samples were run in full scan mode according to Rohrssen *et al*., 2013 supplemental information. Uncertainties in polycyclic biomarker ratios determined from multiple analyses of a saturated hydrocarbon fraction from AGSO (Australian Geological Survey Organisation) standard oil are ± 8%.

4. Results & Discussion

Figure 2.2 contains a compilation of geochemical and isotope ratio profiles spanning ~1,000 m of Huqf Supergroup strata, ranging from the lower Masirah Bay siliciclastics into Ara Group carbonates (Appendix Table A2.2a, A2.2b). This TM-6 section captures the Shuram excursion in the Shuram Formation and the Ediacaran-Cambrian boundary in the A4 unit. Each profile is described in detail below. Isotope ratios reported throughout this chapter are defined as:

$$\delta^n X_{fraction} = (R_{sample}/R_{standard}) - 1) \times 1,000$$

where:

X = C, O, S, or N; n = 13 (C), 18 (O), 34 (S), 15 (N); R = $^{13}C/^{12}C$, $^{18}O/^{16}O$, $^{34}S/^{32}S$, $^{15}N/^{14}N$

with units in parts per thousand (permil; ‰) (Table 2.1).

Table 2.1. Delta notation for measured carbon, oxygen, sulfur, and nitrogen isotope ratios.

Isotope ratios

Carbonate carbon	$\delta^{13}C_{carb}$	=	$(^{13}C/^{12}C_{sample}/^{13}C/^{12}C_{standard})$	− 1)	×1,000	‰ *vs.* VPDB
Carbonate oxygen	$\delta^{18}O_{carb}$	=	$(^{18}O/^{16}O_{sample}/^{18}O/^{16}O_{standard})$	− 1)	×1,000	‰ *vs.* VPDB
Organic carbon	$\delta^{13}C_{org}$	=	$(^{13}C/^{12}C_{sample}/^{13}C/^{12}C_{standard})$	− 1)	×1,000	‰ *vs.* VPDB
CAS	$\delta^{34}S_{CAS}$	=	$(^{34}S/^{32}S_{sample}/^{34}S/^{32}S_{standard})$	− 1)	×1,000	‰ *vs.* VCDT
Pyrite sulfur	$\delta^{34}S_{pyr}$	=	$(^{34}S/^{32}S_{sample}/^{34}S/^{32}S_{standard})$	− 1)	×1,000	‰ *vs.* VCDT
Organic nitrogen	$\delta^{15}N_{org}$	=	$(^{15}N/^{14}N_{sample}/^{15}N/^{14}N_{standard})$	− 1)	×1,000	‰ *vs.* air
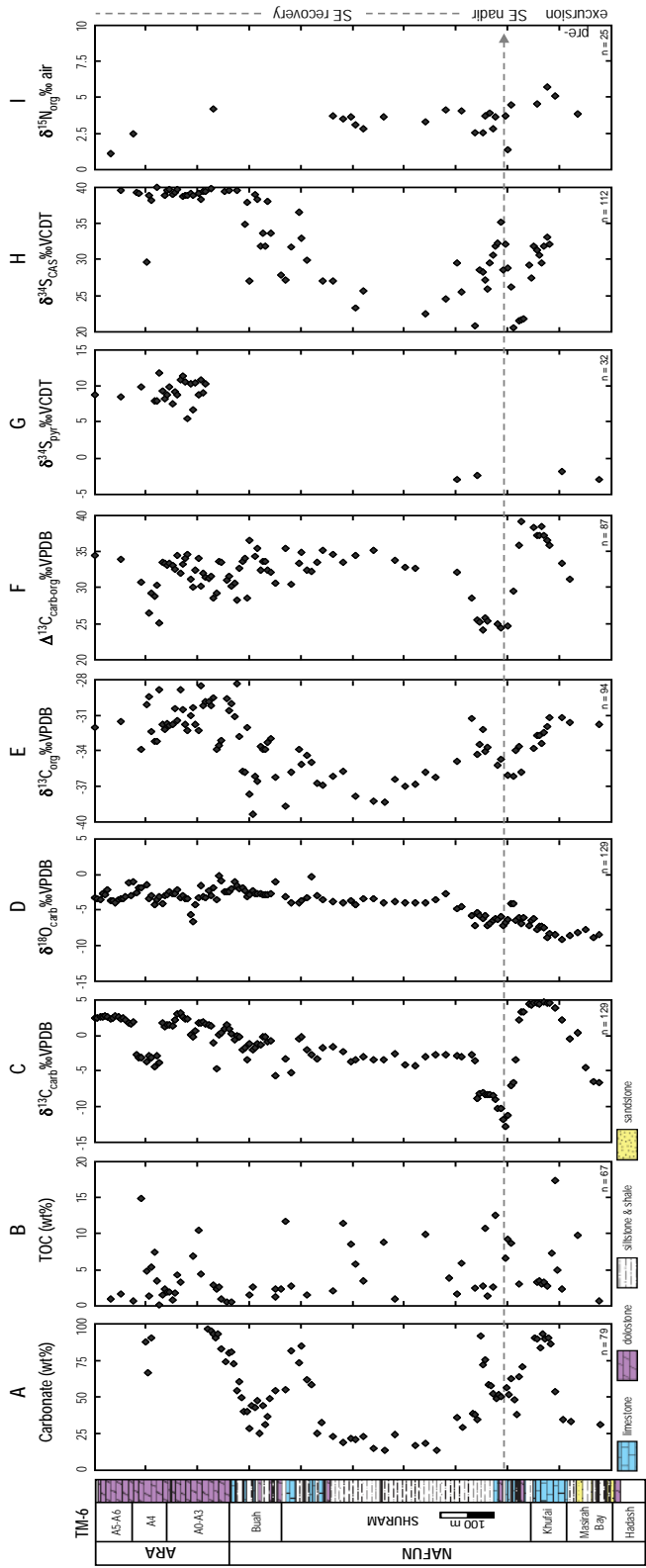
Figure 2.2. Isotopic and geochemical profiles from TM-6 plotted alongside stratigraphy. Lithologic log and group and formation names are along the left. (A) Carbonate content measured in weight percent (wt%). Note all well cuttings mix the interbedded siliciclastic and carbonate lithologies typical of the Shuram Formation. (B) Total organic carbon (TOC) content measured in weight percent (wt%). (C) Carbon isotopic composition ($\delta^{13}C_{carb}$) of carbonate, both dolomite and limestone in ‰VPDB. (D) Oxygen isotopic composition ($\delta^{18}O_{carb}$) of carbonate in ‰VPDB. (E) Carbon isotopic composition ($\delta^{13}C_{org}$) of bulk organic carbon in ‰VPDB. (F) $\Delta^{13}C_{carb-org}$, calculated as the difference between $\delta^{13}C_{carb}$ and $\delta^{13}C_{org}$ values in ‰VPDB. (G) Sulfur isotopic composition ($\delta^{34}S_{pyr}$) of pyrite in ‰VCDT (Fike & Grotzinger, 2008). (H) Sulfur isotopic composition ($\delta^{34}S_{CAS}$) of carbonate-associated sulfate (CAS) in ‰VCDT (Fike & Grotzinger, 2008). (I) Nitrogen isotopic composition ($\delta^{15}N_{org}$) of bulk organic matter in ‰ vs. air. Dashed grey lines and labels to the right define the pre-excursion, SE nadir, and the excursion's recovery.

36

Carbon content

Carbonate wt%

The carbonate content through the Nafun and Ara Groups display a trend that is consistent with the described lithology; high carbonate contents (>80 wt%) are observed in the Khufai and leading up to the Buah carbonate ramps of the Nafun Group and in the Ara Group (Figure 2.2A). Lower carbonate contents are observed in the most of the Shuram Formation and the middle Buah Formation reflecting mixed carbonate-siliciclastic material, with minima at 20-25 wt% through these sections.

Total Organic Carbon (TOC) wt%

The total organic carbon content (TOC) is high yet variable, with an average of 4.4 wt% and maximum values reaching 17.4 wt% in the Khufai Formation (Figure 2.2B). Lower values are observed in the Ara carbonates but there is no significant trend in TOC with stratigraphy. The range of TOC values, observed in the A0-A3 unit, in the Ara Group are 0.18-14.86 wt%, whereas the Nafun Group exhibits a range from 0.56-17.41 wt%, with the Shuram Formation averaging 5.61 wt%.

4-1: Carbonate carbon. $\delta^{13}C_{carb}$ values display two well-defined negative excursions (Figure 2.2C). The first begins near the contact of the Khufai and Shuram formations, with $\delta^{13}C_{carb}$ values dropping from +5‰ to -12‰ over ~70 m of stratigraphy with the recovery taking place over the overlying ~400 m into the Buah Formation. Even in this deeper depositional environment with far higher sedimentary organic carbon

loadings, this $\delta^{13}C_{carb}$ excursion is very similar in shape and magnitude to the observations presented in Burns and Matter (1993), and elsewhere in Oman (Fike *et al.*, 2006; Le Guerroué *et al.*, 2006a,c). A second excursion occurs step-wise in the A4 unit of the Ara Group, is smaller in magnitude, and has been interpreted to mark the Ediacaran-Cambrian boundary at 541 Ma (Amthor *et al.*, 2003; Schröder *et al.*, 2004; Bowring *et al.*, 2007). Both carbonate carbon isotope excursions do not correlate with wt% carbonate (Figure 2.2A,C, Figure 2.7B).

4-2: Carbonate oxygen. $\delta^{18}O_{carb}$ reveals a wide range of values (from 0 to -9‰) characteristic of differential alteration during carbonate diagenesis (Figure 2.2D). $\delta^{18}O_{carb}$ values generally decline with stratigraphic depth suggesting carbonate recrystallisation during burial, though this interpretation is non-unique without independent constraints on recrystallisation temperatures or fluid compositions. It is notable, however, that we do not observe the strong covariation of ^{13}C and ^{18}O isotope ratios in carbonates observed elsewhere in Oman through the Shuram excursion (e.g., Burns & Matter 1993; Fike *et al.*, 2006; Fike, 2007), similar to observations from Le Guerroué and Cozzi, (2010) and potentially other correlative sections (e.g., Bergmann *et al.,* 2011; Loyd *et al.*, 2013). This result suggests the operation of a different combination of diagenetic processes in the carbonates deposited in this deeper water paleoenvironment, and is not readily explained by existing diagenetic hypotheses for the Shuram carbon isotope excursion (e.g., Bristow & Kennedy, 2008; Knauth & Kennedy, 2009; Derry, 2010a).

4-3: Organic carbon. Bulk organic carbon isotope ratios ($\delta^{13}C_{org}$) (Figure 2.2E) show a wide range of values from -28 to -39‰, and several systematic trends within the stratigraphy. A broad negative excursion covers much of the Nafun Group strata, beginning in the lower Khufai Formation and ending at the top of the Buah Formation. Superimposed on this trend is a smaller positive excursion in the lower Shuram Formation. Neither $\delta^{13}C_{org}$ nor $\delta^{13}C_{carb}$ data show significant relationships with organic carbon concentrations (TOC wt%) ($\delta^{13}C_{org}$ m = -1.6; $R^2 = 0.05$ and $\delta^{13}C_{carb}$ Figure 2.7D), which are generally high throughout the stratigraphy (4.4 wt% ± 3.8 wt%; Figure 2.2B).

4-4: $\Delta^{13}C_{carb-org}$. The trends observed in $\delta^{13}C_{org}$ do not directly mirror those of $\delta^{13}C_{carb}$ (Figure 2.7C). The fractionation between carbonate and organic carbon ($\Delta^{13}C_{carb-org}$; Figure 2.2F) is not constant but rather exhibits a clear systematic pattern that mimics the Shuram excursion in carbonate carbon. Typical average marine values during the last 800 Ma for $\Delta^{13}C_{carb-org}$ are in the range of 28-32‰ (Hayes *et al*., 1999; Ader *et al*., 2009). $\Delta^{13}C_{carb-org}$ values from TM-6 show a range between 24-39‰ and an average value of 32‰ ± 3.5‰. During the nadir of the Shuram excursion, $\Delta^{13}C_{carb-org}$ values are 25‰ ± 0.6‰, whereas from the middle Shuram to upper Buah and A4 units in the Ara, average $\Delta^{13}C_{carb-org}$ values are 33‰ ± 1.9‰. Finally, we do not observe the relationship between $\Delta^{13}C_{carb-org}$ and TOC values hypothesised by Johnston *et al*., (2012).

4-5: Sulfur. The sulfur isotopic composition of pyrite has been previously reported for Shuram excursion-containing sections, though the published $\delta^{34}S_{pyr}$ record of TM-6 is limited to the Ara Group (Figure 2.2G; Fike & Grotzinger, 2008). Average

$\delta^{34}S_{pyr}$ values for the Ara Group are 9.2‰ ± 1.5‰ (n = 25), which are enriched relative to Nafun Group values (Fike & Grotzinger, 2008). The sulfur isotopic composition of sulfate substituted in the crystal lattice of calcium carbonate (i.e. carbonate-associated sulfate (CAS); $\delta^{34}S_{CAS}$) is a proxy for tracking the sulfur isotopic composition and broadly inferring sulfate concentrations of ancient seawater (Burdett *et al*., 1989; Marenco *et al*., 2008; Fike & Grotzinger, 2008; Gill *et al.*, 2008), although sulfate concentrations can be affected by diagenesis (Gill *et al*., 2008). The $\delta^{34}S_{CAS}$ profile from TM-6 shows an overall general positive trend from a nadir in the middle Shuram Formation to high $\delta^{34}S$ values (up to 40‰) in the Ara Group (Figure 2.2H), observed throughout Oman (Fike & Grotzinger, 2008). The lower Nafun Group strata reveal high $\delta^{34}S_{CAS}$ values in the lower Khufai Formation, which subsequently drop by approximately 10‰, reversing course briefly with a small positive trend at the onset of the Shuram excursion. Superimposed on these trends are ^{34}S-depleted values that stand out from the trend and might reflect alteration by secondary processes (Fike & Grotzinger, 2008), possibly including contamination by coexisting pyrite during CAS extraction (e.g., Marenco *et al*., 2008). Overall, the $\delta^{34}S_{CAS}$ trends associated with the Shuram excursion in TM-6 are similar to those observed by Fike *et al*. (2006) from shallower paleoenvironments north of the Huqf area.

  4-6: Nitrogen. Nitrogen isotopes reveal information about biological source and marine nutrient cycling in preserved sedimentary organic matter and have been used as a proxy to track these processes (e.g., Bauersachs *et al*., 2009; Higgins *et al*., 2011; Tsao *et al*., 2012). Nitrogen isotope fractionation can capture both internal and external nitrogen

cycling, e.g., nitrogen assimilation, diazotrophic nitrogen fixation, nitrification, and de-nitrification/anammox (Robinson *et al*., 2012). A study by Bauersachs and colleagues (2009) found negative $\delta^{15}N_{org}$ values from the Holy Cross Mountains (average $\delta^{15}N_{extract}$ -0.9‰) and Bardzkie Mountains (average $\delta^{15}N_{extract}$ -0.13‰) characteristic of biological N_2 fixation from cyanobacteria, as N_2 fixation produces ^{15}N values slightly depleted relative to atmospheric nitrogen (Wada & Hattori, 1978). Compound-specific nitrogen isotope studies, such as those performed by Higgins and colleagues, investigate the nitrogen isotopes of individual chlorophyll pigments and find them to be depleted relative to biomass (the difference between the isotopic composition of biomass and chloropigment; $\delta^{15}N_{biomass} - \delta^{15}N_{chloropigment}$). Freshwater species of cyanobacteria have more ^{15}N-depleted isotopic values compared with marine cyanobacteria; which are even more depleted relative to the ^{15}N-enriched values found in algae (Higgins *et al*., 2011). Compound-specific nitrogen isotopes of chloropigments may be able to discern environmental (freshwater *vs.* marine) as well as source inputs (cyanobacterial *vs.* algal) into sedimentary organic matter. The bulk organic nitrogen isotope trend through Ara and Nafun Group strata shows a general increase in $\delta^{15}N$ values with depth, with an absolute range from ~1‰ through to ~5‰ (Figure 2.2I). From the Khufai and Masirah Bay section, $\delta^{15}N_{org}$ values are enriched, between +4-5‰, and exhibit a negative >4‰ excursion coincident with the Shuram excursion in $\delta^{13}C_{carb}$ and consequently $\Delta^{13}C_{carb-org}$, with paired $\delta^{15}N_{org}$-$\delta^{13}C_{carb}$ and $\delta^{15}N_{org}$-$\Delta^{13}C_{carb-org}$ showing moderate (R^2 = 0.44; 0.45, respectively) coupling during the excursion from upper Masirah Bay through to mid-Shuram Formation. This is followed by steady values between +3-3.5‰ with a second

broad negative excursion beginning in the mid- to upper- Shuram Formation, reaching ~1‰ in the Ara Group. These values fall within the range of expected nitrogen isotopes of marine bitumen, with kerogen $\delta^{15}N$ values being slightly lighter (e.g., Williams *et al*., 1995), and the increase to more positive values with depth likely reflect a slight burial trend (e.g., Williams *et al*., 1995; Robinson *et al*., 2012). The systematics of the nitrogen cycle and nitrogen isotopes are complex and not well characterised (review in Handley & Raven, 1992; Altabet, 2006). The $\delta^{15}N$ values through this section fall in the range where it is difficult to interpret significant nitrogen inputs into bulk organic matter. We observe $\delta^{15}N_{org}$ values through Ara and Nafun Groups in the range that is expected for marine organic matter but we cannot attribute these to specific source inputs. Cross-plots of $\delta^{15}N_{org}$ show no obvious relationship, at least in our TM-6 section in Oman, to either $\delta^{18}O_{carb}$, $\delta^{13}C_{org}$ (bitumen and kerogen), or $\delta^{34}S_{CAS}$, with only moderate covariation during the Shuram excursion to $\delta^{13}C_{carb}$ and $\Delta^{13}C_{carb-org}$.

Figure 2.3 contains a compilation of organic geochemical features (Appendix Table A2.3), including key lipid biomarker ratios (Appendix Table A2.4a-b), spanning the same depths and intervals as defined in Figure 2.2. Organic matter source and characteristics as well as the general trends for each proxy are described individually and in detail below. A comprehensive table of lipid biomarker ratios, as well as those not presented in figures, can be viewed in Appendix Table A2.4a, A2.4b.
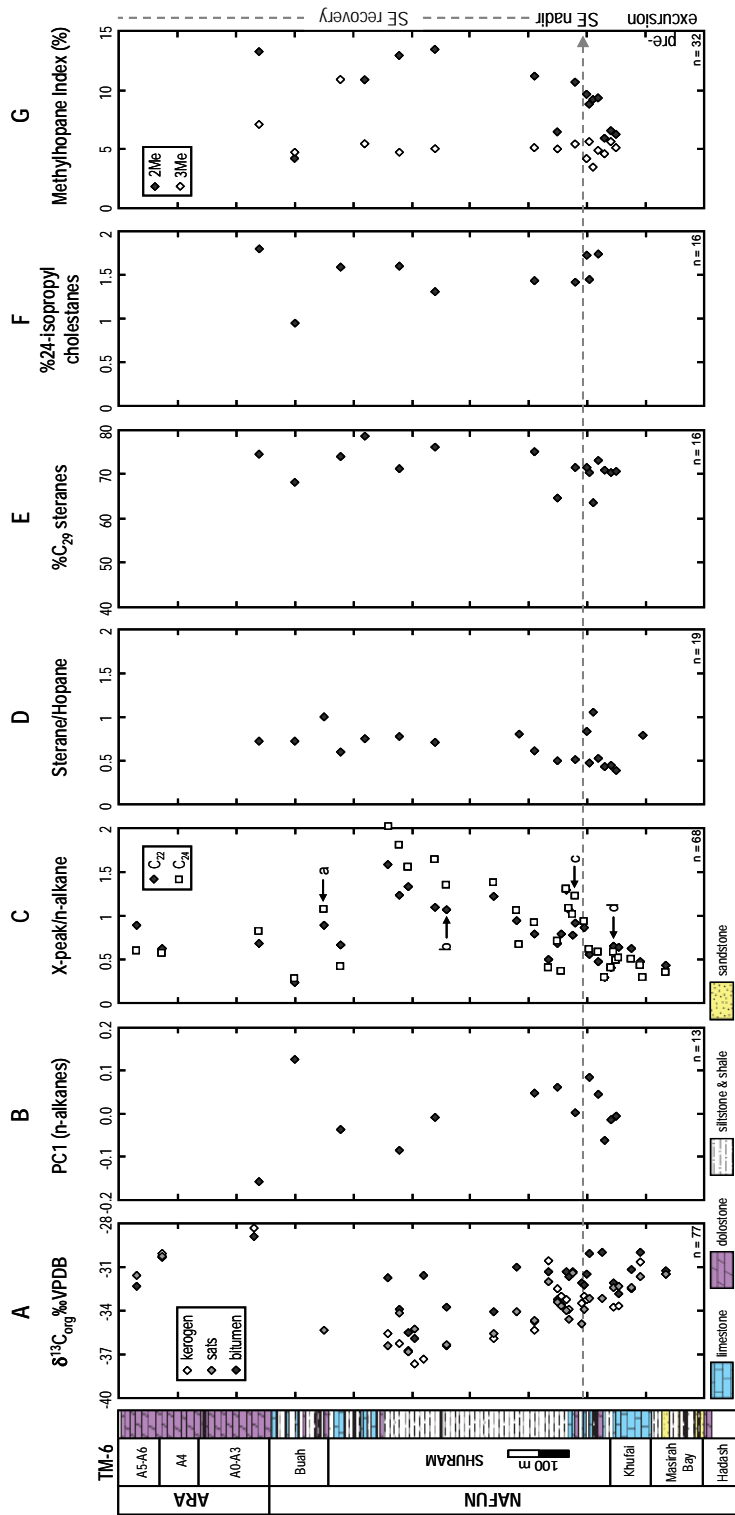
Figure 2.3. Carbon isotopic and lipid biomarker stratigraphic profiles from the TM-6 drill well. (A) $\delta^{13}C_{org}$ values for bitumen (filled diamonds), kerogen (open diamonds), and saturated hydrocarbon fraction (sats; grey diamonds). (B) First principle component (PC1) from principle component analysis of C_{19}-C_{26} n-alkane abundances (sats). (C) Relative X-peak mid-chain monomethyl alkane abundances measured by X-peak/n-alkane for representative C_{22} (filled diamonds) and C_{24} (open squares) homologues. Lower case letters indicate stratigraphic position of samples with chromatograms in Figure 1.5. (D) Sterane/hopane (using 2 isomers of diasteranes and 4 isomers of C_{27}-C_{29} regular steranes/19 isomers of C_{27}-C_{35} hopanes (Cao et al., 2009). (E) Relative abundance of C_{29} steranes to total C_{27}-C_{29} steranes, in percent (4 isomers of C_{29} regular steranes/4 isomers of C_{27}-C_{29} regular steranes × 100). (F) Relative abundance of 24-isopropylcholestane to total C_{27}-C_{29} steranes in percent (24-isopropylcholestane/2 isomers of diasterane and 4 isomers of C_{27}-C_{29} regular steranes × 100). (G) Methylhopane indices for 2α-methylhopane (filled diamonds) [(2-methyl C_{30} hopane/2-methyl C_{30} hopane + C_{30} αβ hopane) × 100)] and 3β-methylhopane (open diamonds) [C_{31} 3β-methylhopane/(C_{30} αβ methylhopane + C_{31} 3β-methylhopane) × 100)]. Dashed grey lines define the pre-excursion, SE nadir, and the excursion's recovery.

43

4-7: Organic matter. Organic geochemical data through the Shuram excursion in TM-6 show a range of features typical of the Huqf Supergroup throughout Oman. Characteristic features of organic matter from source rocks throughout the Huqf Supergroup include conspicuous ^{13}C-depletions (δ^{13}C *ca.* -36‰), high sulfur content, low pristane/phytane, high relative abundance of C_{29} steranes, lack of rearranged diasteranes, presence of 24-isopropylcholestane, and an abundant series of mid-chain monomethylalkanes (MMAs)—sometimes termed X-peaks or X-compounds (Grantham *et al.*, 1987; Höld *et al.*, 1999; Love *et al.*, 2008; Grosjean *et al.*, 2009). Oils, in particular from the Eastern Flank Play, are early expulsion crudes with wide ranges of densities (generally high) and viscosities and very low gas-oil ratios (Al-Marjeby & Nash, 1986; Alsharhan, 1997). Oils with the same properties and of similar age are also known from successions in Pakistan, Eastern Siberia, India, and the Eastern European Platform (Höld *et al.*, 1999).

Bitumen, kerogen, and the saturated hydrocarbon fraction

In TM-6, bitumen, kerogen, and the saturated hydrocarbon fraction solvent-extracted from whole rock powder have similar δ^{13}C values and show comparable δ^{13}C trends with stratigraphic height (Figure 2.3A). Kerogen, in general, is slightly ^{13}C-depleted relative to coexisting bitumen (Figure 2.3A) in Nafun Group samples—a feature observed in Neoproterozoic-age strata globally, but largely reversed by late Ediacaran time (Logan *et al.*, 1995; Höld *et al.*, 1999; Kelly, 2009). The largest fractionation between bitumen and kerogen is 6.3‰ and occurs in the middle of the Shuram Formation, whereas latest Ediacaran and early Cambrian samples from the Ara Group

44

show similar values for bitumen and kerogen (within the reproducibility). In general, the carbon isotopic composition of bitumen and kerogen shows a very similar trend to the bulk organic carbon values (Figure 2.2E); neither tracks the negative carbon isotope excursion observed in carbonates (Figure 2.2C).

4-8 Lipid biomarkers. Lipid biomarker data from TM-6 bitumens exhibit characteristics similar to Nafun strata and oils studied in TM-6 and elsewhere in Oman (e.g., Grosjean *et al*., 2009; Love *et al*., 2009), but also show intraformational differences and trends with stratigraphic height. Each group of biomarkers will be discussed in detail below.

4-8.1 Saturated hydrocarbons

Alkanes and isoprenoids

The abundances of C_{19}-C_{26} *n*-alkanes provide insight into bacterial *versus* eukaryotic contributions to sedimentary organic matter. These larger alkanes are not strongly affected by evaporative losses during sample handling; and although they can be modified by biodegradation, this process did not substantially impact the biomarker composition of pre-salt oils (Grosjean *et al*., 2009). The relative abundances of C_{19}-C_{26} *n*-alkanes, statistically reduced to the first principle component (which explains 91% of the data variance) using principle component analysis, highlights fundamental differences in the organics preserved within the stratigraphy (Figure 2.3B). Variable loadings for C_{19}-C_{26} *n*-alkanes are C_{19} (0.6328), C_{20} (0.3610), C_{21} (0.2050), C_{22} (0.0446), C_{23} (-0.1698),

C_{24} (-0.2820), C_{25} (-0.3537), and C_{26} (-0.4379). The low molecular weight end of the spectrum receives strong positive loadings on PC1, whereas the higher molecular weight alkanes receive negative loadings. Consequently, decreasing PC1 values imply greater contributions of algal biomass to sedimentary organic matter—an inference weakly supported by sterane to hopane ratio data (discussed below).

The pristane/phytane (Pr/Ph) ratio is often used in conjunction with other molecular parameters to assess oxic or anoxic conditions of sedimentary deposition, but can be influenced by source. Pr ($C_{19}H_{40}$; 2,6,10,14-tetramethylpentadecane) and Ph ($C_{20}H_{42}$; 2,6,10,14-tetramethylhexadecane) are regular acyclic isoprenoid hydrocarbons. They can be derived from the degradation of chlorophyll pigments although there are other potential sources of these isoprenoids, such as tocopherols, archaeal ether lipids, or methyl trimethyl tridecylchromans (MTTCs) (e.g., Volkman & Maxwell, 1986; Rontani & Bonin, 2011). When derived from chlorophyll, under oxic conditions the phytyl side chain of chlorophyll is oxidised from phytol to phytenic acid, decarboxylated to pristene, and then reduced to pristane (Pr/Ph > 1). However, under reducing conditions the phytyl side chain is cleaved to yield phytol and reduced to dihydrophytol, then phytane (Pr/Ph < 1). All Pr/Ph values throughout the TM-6 core do not exceed 0.8 (Figure 2.4A), indicating that sediments were probably deposited under reducing conditions, also supported by the high organic carbon content. The base of the Masirah Bay Formation shows higher (~0.65) Pr/Ph, followed by a drop to lower values of around 0.2 in the middle Khufai Formation. An increase in Pr/Ph to ~0.5 is observed heading into the Shuram excursion followed by a drop back to baseline values of 0.2 in the excursion's

immediate recovery. Another, smaller, positive excursion is observed with values reaching 0.4 before recovery to baseline values (Figure 2.4A). Values remain at their baseline values of 0.2 throughout the Shuram Formation of the Nafun Group and into the Ara Group, with an outlier at 0.74 in the upper Buah Formation. Plots of Pr/nC_{17} and Ph/nC_{18} show generally similar profiles ($R^2 = 0.6$). Cross plots of Ph/nC_{18} and Pr/nC_{17} a log scale place these samples in a reducing environment of marine Type II kerogen. Both plots show a steady baseline of values throughout, with Pr at ~0.4 and Ph at ~1.0. A notable spike in the Pr/nC_{17} (to ~0.9) and Ph/nC_{18} (to ~2.5) occurs during the nadir of the Shuram excursion (Figure 2.4B,C). Similar profiles and similarly depleted $\delta^{13}C$ values (see Section 3.1.1 of Chapter 2) indicate that these compounds derive from the same source, probably an autotrophic one.
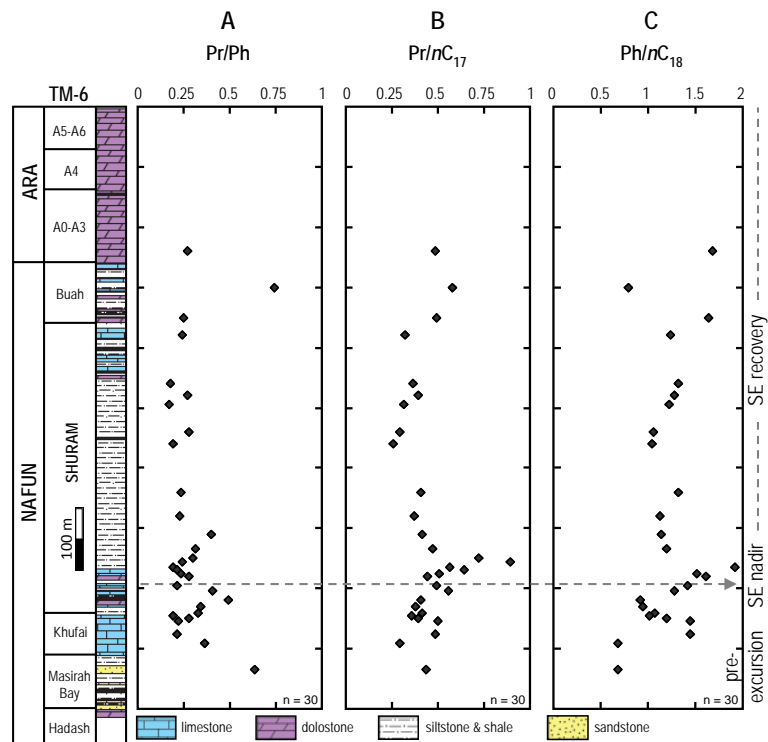
Figure 2.4. Stratigraphic profiles of (A) Pristane (Pr)/Phytane (Ph); (B) Pr/nC_{17}; and (C) Ph/nC_{18}.

Mid-chain branched monomethyl alkanes (MMAs) – X-peaks

X-peaks are an unusual series of C_{14}-C_{30} mid-chain monomethyl branched alkanes, but with greatest abundance in the C_{20}-C_{26} range, which have been detected before in Huqf oils and sedimentary rocks (Klomp, 1986; Höld *et al*., 1999; Grosjean *et al*., 2009, 2012) as well as in other late Proterozoic-early Cambrian samples. These include heavy petroleum from Pakistan (Grantham *et al*., 1988), source rocks and oils from the Eastern European (Russian) Platform (Bazhenova & Arefiev, 1996), and oils from the Eastern Siberian Platform (Fowler & Douglas, 1987). Ratios of mid-chain branched monomethyl alkanes to *n*-alkanes (*n*-C_x) show very high values throughout the Nafun and Ara groups and several systematic excursions with local maxima recorded in the lower and middle Shuram Formation and local minima in the middle Buah Formation, respectively (Figure 2.3C, Figure 2.5). In general, MMAs are much less abundant (ratios <0.1 relative to *n*-alkane with the same carbon number) in Phanerozoic rocks (Peters *et al*., 2005). However, the observation of the C_{20}-C_{26} pattern (X-peaks) with a slight even-over-odd carbon number preference is only prominent in late Neoproterozoic- to early Cambrian-age sedimentary rocks and oils (Love *et al*., 2008). For typical Phanerozoic strata, the methylalkane abundance tracks *n*-alkane abundance, where small amounts of methylalkanes are partially derived from diagenesis of linear alkanes. Patterns in late Neoproterozoic and early Cambrian samples with prominent X-peaks, do not simply record *n*-alkane abundance patterns (Figure 2.3C, Figure 2.5), implying a specific and significant biological source input for these compounds.

The biological sources of X-peak compounds remain unconfirmed at present. Though rare, elevated concentrations of mid-chain monomethyl branched alkanes observed in unusually organic sulfur-rich Jurassic rocks (e.g., van Kaam-Peters & Sinninghe Damsté, 1997) and suggest these compounds might be derived from organisms living in benthic microbial mats associated with stratified bottom waters, perhaps sulfur-oxidising chemoautotrophic bacteria (Love *et al*., 2008). If correct, this implies a substantial contribution to sedimentary organic matter from organisms that would have fractionated carbon isotopes quite differently than expectations from ribulose-1,5-bisphosphate carboxylase oxygenase in the Calvin-Benson-Bassham cycle of embryophytes (e.g., Scott *et al*., 2004). Compound-specific measurements of X-peak compounds reveal a ^{13}C-depletion by an average of 3.7‰ (up to 6.5‰ for C_{24}) when compared to *n*-alkanes in Huqf bitumens (Höld *et al*., 1999), implying that the source organisms either fractionated carbon isotopes to a greater degree or were benthic and consumed ^{13}C-depleted bottom water DIC (Love *et al*., 2008). X-peak/*n*-C_x ratios correlate with the δ^{13}C values of bulk organic carbon, kerogen, and to a lesser degree, bitumen. It is interesting, however that they do not correlate well with $\Delta^{13}C_{carb-org}$. Uncertainty about sources aside, the high X-peak abundances observed in TM-6 strata (up to 60% more abundant than the similar *n*-alkane) are exotic and imply a specific and significant source input. These data also highlight the ever more apparent prevalence of these compounds in the late Neoproterozoic stratigraphic record globally.
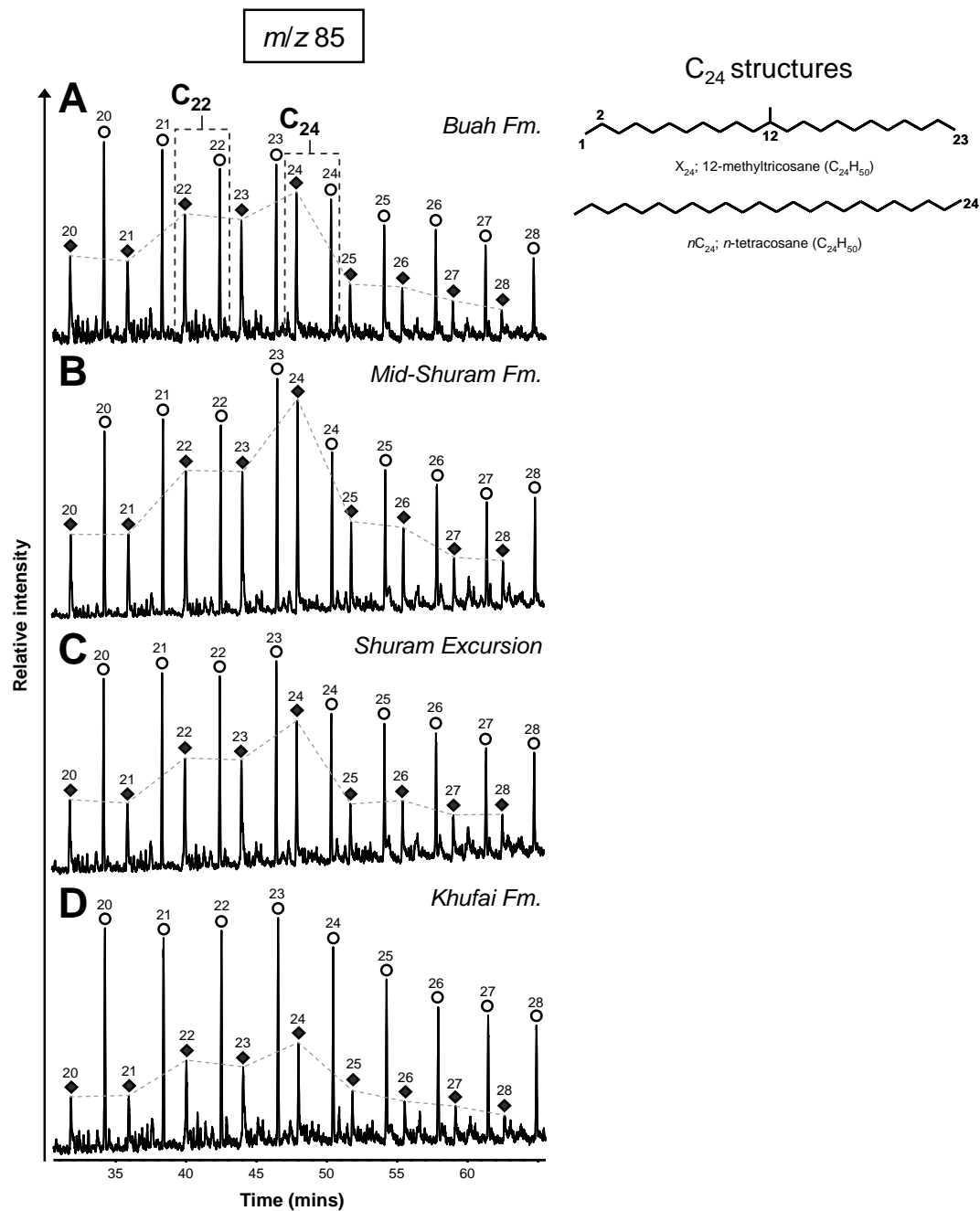
Figure 2.5. *M/z* 85 partial ion chromatograms showing the distribution of *n*-alkane (open circles) and X-peak (filled diamonds) homologues from C_{20}-C_{28} for representative samples from (A) Buah Formation; (B) Mid-Shuram Formation; (C) Shuram excursion; and (D) Khufai Formation. Dashed lines show the changing X-peak pattern with stratigraphy and highlight the compounds used in the X-peak/*n*-alkane ratio. Example structures for *n*C_{24} and X_{24} (note: additional unresolvable structural isomers for X-peak homologues) are presented on the top right).

50

Terpenoids

Steranes and hopanes

Sterane (C_{27}-C_{29}) to hopane (C_{27}-C_{35}) ratios provide a coarse proxy for the relative contributions of bacterial and eukaryotic biomass to preserved sedimentary organic matter. Generally, sterane/hopane ratios increase upsection, but also show significant variability with several notable outliers at the top of the Masirah Bay Formation and within the lower Shuram Formation (Figure 2.3D). The ranges in sterane/hopane ratios observed here (between ca. 0.4 and 1) imply significant changes in the autotrophic communities through the Shuram excursion, which coincide with the facies and environmental changes observed upsection. These values still remain within the second quartile of the typical range (0.5 to 2.0) observed in Phanerozoic marine sedimentary rocks and oils (Peters *et al*., 2005). Although bacteria and eukaryotes can fractionate carbon isotopes differently (due to differences in cell size and physiology; as discussed in Close *et al*., 2011), we do not observe relationships between sterane/hopane and the isotopic composition of total organic carbon, bitumen, kerogen, or $\Delta^{13}_{carb-org}$.

Sterane homologues

Sterane patterns in TM-6 bitumens are dominated by C_{29} isomers (relative average abundances of >70%; Figure 2.3E and Figure 2.6), hydrocarbons derived from sterols typical of green algae (Volkman, 1986). This feature is also characteristic of Proterozoic and Paleozoic bitumens and supports the notion that green algae were important primary producers prior to the Mesozoic marine revolution of higher order

51

endosymbiotic clades (e.g., Grantham & Wakefield, 1988; Schwark & Empt, 2006; Knoll *et al.*, 2007). These observations may also provide some additional context into the possible taxonomic identities of the leiosphaerid acritarchs observed throughout Nafun Group strata (Butterfield & Grotzinger, 2012).
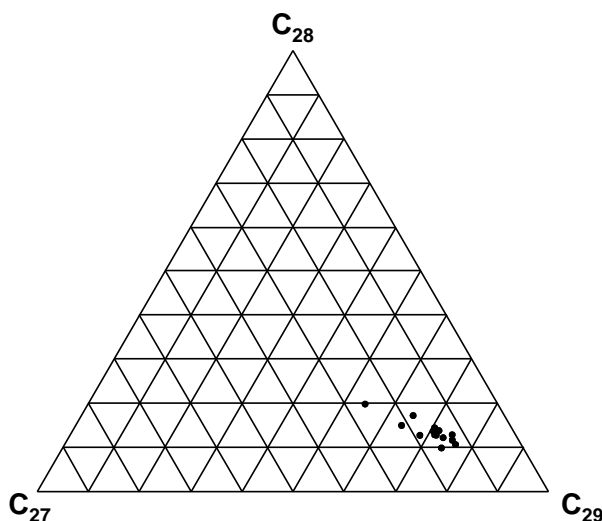
Figure 2.6. Ternary diagram of regular C_{27}, C_{28}, and C_{29} sterane isomers showing C_{29} as the dominant sterane homologue in organic matter preserved in TM-6. % sterane is calculated as 4 regular isomers/(4 regular isomers of $C_{27}+C_{28}+C_{29}$) $\times$ 100.

C_{30} steranes: 24-isopropylcholestane

Finally, we observe variable but significant abundances of 24-isopropylcholestanes (from 1-3% of summed C_{27}-C_{29} abundances, typical for South Oman oils and rocks) throughout the Nafun Group and Ara Group stratigraphy (Figure 2.3F). These biomarkers are thought to reflect the diagenetically-stabilised equivalents of C_{30} sterols produced by marine demosponges, and extend into the Cryogenian-age Abu Mahara Group elsewhere in Oman, constituting the oldest observations of Metazoa (Love *et al.*, 2009). From comparative biology it was recognised that early sponges had an

aerobic metabolism (e.g., Berkner & Marshall, 1965; Towe, 1970; King *et al*., 2008)—anaerobic metazoans appear evolutionarily-derived (Danovaro *et al*., 2010). The facies and source-rock characteristics of this deep water paleoenvironment suggest that the seafloor in this sub-basin was anoxic through much of Nafun Group time. If 24-isopropylcholestanes were produced by adult benthic organisms with similar growth habits and ecology to modern demosponges (e.g., Sperling *et al*., 2011), then these molecules were likely advected to deeper sites from organisms living on the shelf. Alternatively, these observations could be explained by the broadcast spawning of planktonic larval stages, or an early-evolved sponge group with a largely planktonic life cycle. If the latter is correct, the sedimentary context observed here provides some support for the hypothesis that the evolution and development of sponge larvae may have been an important waypoint in the evolution of higher metazoan taxa (Nielsen, 2008).

Methylhopanes

Methylhopane indices show stratigraphic variability through the Shuram excursion. 2α-methylhopane indices, describing the relative abundance of compounds largely derived from cyanobacteria and α-proteobacteria (Summons *et al*., 1999; Welander *et al*., 2010), vary with depth but are high throughout much of TM-6 and can exceed 15% (Figure 2.3G). These values are consistent with previous observations of microfossils and lipid biomarkers from Proterozoic strata that suggest overall proportionally higher amounts of primary production from bacteria during Neoproterozoic time than is observed from the late Paleozoic through today (Summons *et*

al., 1999; Knoll *et al*., 2007). The 2α-methylhopane index is highly correlated to X_{22} (R^2 = 0.71) and X_{24} (R^2 = 0.92) (X-peak compound with 22 and 24 carbons, respectively), perhaps pointing to a source relationship. The relative abundance of 3β-methylhopanes, compounds largely produced by microaerophilic type 1 methanotrophic proteobacteria and acetic acid bacteria (Farrimond *et al*., 2004), also vary with depth exhibiting similar overall pattern to 2α-methylhopanes. Despite the stratigraphic variability, the lack of a major secular change in the relative abundance of methylhopanes through the Shuram excursion suggests the absence of extreme temporal shifts in local environmental conditions, e.g., temperature, salinity, and sedimentary methane fluxes (Rohrssen *et al*., 2013).

Thermal maturity

Thermal maturity is assessed *via* a combination of molecular proxies such as Rock Eval pyrolysis parameters, vitrinite reflectance, and maturity-sensitive biomarkers to evaluate the degree to which preserved organic matter has been exposed to post-depositional heating conditions. Rock Eval pyrolysis performed on samples from the South Oman Salt Basin shows hydrogen indices (HI) values of >400 mg/g TOC (Grosjean *et al*., 2009) in the immature to peak oil-window range. Maturity-sensitive biomarkers Ts (18α(H)-22,29,30-trisnorhopane) and Tm (17α(H)-22,29,30-trisnorhopane) are pentacyclic triterpane hydrocarbons likely derived from formerly functionalised hopanoids. Tm is less stable than Ts, therefore with increasing maturity the

value of Ts/Ts + Tm increases. Throughout TM-6, Ts/Ts + Tm values are consistently low, with an average of 0.32 ± 0.06.

5. Implications for carbon cycle function through the Shuram excursion

The Shuram excursion presents a suite of challenges to our understanding of the limits of the operation of the Neoproterozoic carbon cycle. This has engendered hypotheses that range from the existence of a large DOC reservoir (Rothman *et al*., 2003; Fike *et al*., 2006), to the alteration *via* known (Knauth & Kennedy, 2009; Derry, 2010a; Schrag *et al.,* 2013) and unknown (Grotzinger *et al*., 2011) diagenetic processes. Though diagenetic hypotheses for the Shuram excursion provide a simple explanation for decoupled carbonate and organic carbon isotope records, we do not observe the covariation of ^{13}C and ^{18}O isotope ratios in TM-6 carbonates through the Shuram excursion (Figure 2.7A) anticipated by these diagenetic hypotheses (Knauth & Kennedy, 2009; Derry, 2010a). Although both the absolute values and variation seen in δ^{18}O throughout the section point to significant water-rock interaction, this alteration does not appear to have significantly affected the δ^{13}C isotope composition.

It is also important to note that the overall magnitude and shape of the Shuram excursion is the same across Oman—from TM-6 in the south to the Huqf area to the Oman Mountains (Burns & Matter, 1993; Le Guerroué *et al*., 2006c)—despite the dramatic differences in depositional environment (e.g., water depth), sedimentary organic carbon input, and burial history between these regions. The differences in burial history

of Huqf strata across Oman are substantial; this is suggested by the varying $\delta^{18}O_{carb}$ values across Oman, but not reflected in the $\delta^{13}C_{carb}$ values (Burns & Matter 1993, Le Guerroué *et al*., 2006c). This pattern is inconsistent with burial diagenesis hypotheses for the $\delta^{13}C_{carb}$ excursion (e.g., Derry, 2010a). Further, it was recently hypothesised that the Shuram excursion record (and the Neoproterozoic carbon isotope more broadly) reflects the local influence of DIC and alkalinity derived from anaerobic respiration metabolisms driven by the biological pump and sedimentary organic matter inputs (Schrag *et al*., 2013). We note that despite the high sedimentary organic carbon loadings present in this part of the basin (which is markedly different than other Oman sections; e.g., Fike *et al*., 2006), the $\delta^{13}C_{carb}$ excursion is similar (Figure 2.7D)—observations that do not support the hypothesis of Schrag *et al*. (2013) for the Shuram excursion. For these reasons we tentatively regard the carbonate carbon isotope excursion as representative of the time-varying behaviour of marine DIC.
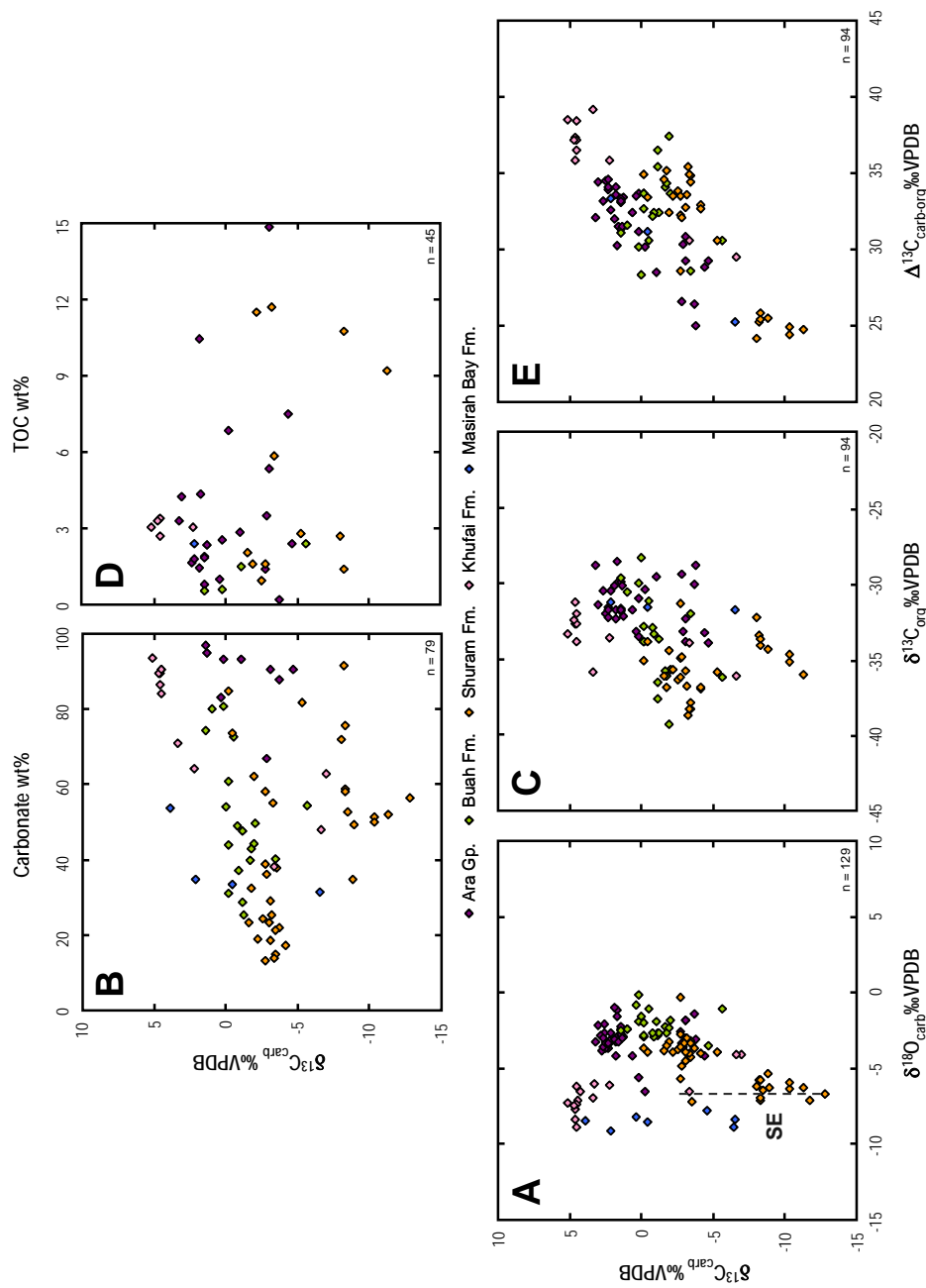
Figure 2.7. TM-6 carbonate carbon isotope ratio ($\delta^{13}C_{carb}$ ‰ VPDB) cross-plots plotted against (A) Carbonate oxygen isotope ratios ($\delta^{18}O_{carb}$ ‰ VPDB); $R^2 = 0.2$ for data points through the Shuram excursion as indicated by the dashed grey line. (B) Carbonate abundance in wt%; $R^2 = 0.09$. (C) Organic carbon isotope ratios ($\delta^{13}C_{org}$ ‰ VPDB); $R^2 = 0.2$. (D) Total organic carbon in wt%; $R^2 = 0.08$. (E) $\Delta^{13}C_{carb-org}$ ‰ VPDB. The only significant relationship in the cross-plots shown occurs in panel E ($R^2 = 0.55$). The Buah, Shuram, Khufai, and Masirah Bay formations are part of the Nafun Group.

57

Examining the time series of $\Delta^{13}C_{carb\text{-}org}$, it is clear that during the onset of the Shuram excursion, carbonate and organic phases were decoupled with regard to their isotopic composition (Figure 2.2F). However from the middle Shuram Formation through the Buah Formation and into the Ara Group—through the latter part of the Shuram excursion recovery—$\delta^{13}C_{carb}$ and $\delta^{13}C_{org}$ show coupled behaviour (Figure 2.2F). This is similar to shallower sections in Oman (Fike *et al*., 2006), and was also observed in Doushantuo unit IV sections from South China (McFadden *et al*., 2008). These observations (including organic carbon isotope ratios as low as -39‰) support the idea that the Shuram excursion records a primary carbon cycle signal, as the stratigraphic coherence of this covariation is unlikely to occur simply by chance.

In general, the disparity between the paired inorganic and organic datasets has been a focal point for hypotheses regarding the nature of Neoproterozoic sedimentary organic matter, suggesting that organic matter could be low in concentration (Jiang *et al*., 2012; Johnston *et al*., 2012), buffered by a large, metastable, DOC reservoir (Rothman *et al*., 2003), or have mixed (Melim *et al*., 2004; Swart, 2008), multiple (Oehlert *et al*., 2012) or exogenous (Kaufman *et al*., 2007; Johnston *et al*., 2012) carbon sources.

Lipid biomarker and bitumen data from TM-6 supports hypotheses that the bulk isotopic composition of sedimentary organic matter reflects multiple syngenetic sources. Organic matter composition and source inputs show stratigraphic variation through the Shuram excursion. In addition, the carbon isotopic composition of kerogen and bitumen display remarkably similar stratigraphic patterns. This discounts hypotheses wherein the organic matter was derived from either a large isotopically homogenous DOC reservoir

(e.g., Rothman *et al*., 2003) or exogenous, migrated or detrital fossil carbon sources. The isotopic compositions of organic phases (bitumen and kerogen) from TM-6 vary stratigraphically, but not as a function of organic carbon concentrations. Furthermore, the difference between $\delta^{13}C_{carb}$ and $\delta^{13}C_{org}$ (here $\Delta^{13}C_{carb-org}$, Figure 2.2F) does not vary as a function of organic carbon content (TOC wt%)—two variables that Johnston *et al*. (2012) hypothesised should show a hyperbolic relationship due to compositional mixing of syngenetic and fossil detrital organic carbon sources in sections with decoupled carbonate-organic records. Thus we can effectively rule out the hypotheses that specify inputs from weathering of fossil detrital carbon sources (Kaufman *et al*., 2007; Johnston *et al*., 2012) to explain this excursion.

Strong evidence for non-migrated, syngenetic organic matter is demonstrated by two critical observations. First, we report a combination of variable magnitude and distinctive biomarker characteristics (e.g., abundance of distinct X-peak mid-chain methylalkane series and high C_{29} (green algal) and C_{30} (marine demosponge) steranes) in TM-6 samples, as found in all Huqf Supergroup oils and rocks from the South Oman Salt Basin. Similar compositional characteristics were observed from late Neoproterozoic-age eastern Siberian oils (Kelly *et al*., 2011). Second, the strong relationship between bitumen and kerogen is observed compositionally through comparisons between bitumen and kerogen hydropyrolysates (Love *et al*., 2008; Grosjean *et al*., 2009; Love *et al*., 2009). This is also reflected in the similarity of their $\delta^{13}C$ values ($m = 1.1$; $R^2 = 0.61$); which is congruent with non-migrated marine-derived organic matter.

Models of the Neoproterozoic carbon cycle that predict the isotopic composition of sedimentary organic matter as a linear translation of carbonate carbon isotope time series data probably are too simple to accurately describe the carbon cycling at this time, particularly during large perturbations. Organic carbon isotope ratios need not provide a global proxy, and can show idiosyncratic local differences depending on the diversity of biological communities and their respective carbon utilisation pathways (Pancost & Sinninghe Damsté, 2003). Consequently, organic carbon isotopic trends can appear strongly decoupled from trends in carbonate carbon for primary biogeochemical and ecological reasons (e.g., Pancost *et al*., 1998). The clear shifts in organic matter source contributions is evidenced by the notable variations in a wide range of lipid biomarker abundances through the Nafun Group of TM-6, particularly during the Shuram excursion. This underscores the biological richness underlying stratigraphic organic carbon isotope ratio data through the largest carbon isotope excursion in the geologic record.

If primary, the Shuram excursion provides an important isotope mass balance constraint on the middle to late Ediacaran carbon cycle. But in considering mechanisms for the excursion it is useful to evaluate the quality of the assumptions commonly made in these interpretations. Most isotope mass balance frameworks for the geological carbon cycle make three assumptions (often implicitly) to solve for the burial fraction of organic carbon: steady state (where inputs and outputs are equal), the isotopic composition of the inputs, and the isotopic difference between coeval carbonates and organic matter (Hayes *et al*., 1999). Although dynamics are required by the excursion itself, the long timescales suggested by the substantial stratigraphic thickness of the Shuram excursion support

quasi-static interpretations of the data (e.g., Rothman *et al*., 2003). The isotopic composition of historical carbon cycle inputs cannot be directly observed and is often set between -5 to -7‰. But it is important to note that mantle carbon is highly variable and bimodal (one mode at -25‰ and another at -6‰) in its isotopic composition (Deines, 2002), nearly displaying the range observed in sedimentary rocks. In addition to the variable isotopic composition of outgassing, the likelihood of changes in the isotopic composition of the inputs is assured by the weathering of pre-existing sedimentary rocks (e.g., Halevy *et al*., 2012). The Shuram excursion requires input values lower than -12‰. But values this low for historical carbon inputs are, in principle, reasonable. Isotopic differences between carbonates and organic carbon are often set between 25-30‰, and assumed to be constant. In principle, however, this difference (as $\Delta^{13}C_{carb-org}$) is observable in sedimentary rocks. As stated above, organic carbon isotope ratios need not record global trends. Nevertheless, several Shuram-age sections with paired records capture a secular increase in the observed $\Delta^{13}C_{carb-org}$ (e.g., Calver, 2000; Fike *et al*., 2006; McFadden *et al*., 2008), suggesting a need to examine a different hypothesis for the origin of this excursion—one wherein the $\delta^{13}C_{carb}$ values were largely controlled and driven by global changes in carbon isotope fractionations between coeval carbonate and organic carbon (e.g., Rothman *et al*., 2003). Mass balance can be satisfied with multiple combinations of lower input values, reduced organic carbon burial fluxes, and lower fractionations. But if the observed changes in $\Delta^{13}C_{carb-org}$ are indeed global in scope, mechanisms behind why these fractionations might change so systematically remain unclear.

6. Conclusions

Paired datasets of $\delta^{13}C_{carb}$ and $\delta^{13}C_{org}$ are largely decoupled during the Shuram excursion, even in highly organic-rich strata that characterise deeper water paleoenvironments of the Nafun Group in Oman. Though the well-defined $\delta^{13}C_{carb}$ decline at the beginning of the Shuram excursion is not recorded in the carbon isotopic composition of any of the organic phases (TOC, bitumen, and kerogen), these materials show systematic trends that define a broad negative excursion, the onset of which occurs within the Khufai Formation and ends with a recovery that matches $\delta^{13}C_{carb}$ in the middle to upper Shuram Formation. Neither the carbon isotopic composition of the organic phases nor the difference between $\delta^{13}C_{carb}$ and $\delta^{13}C_{org}$ vary as a function of organic concentration. Lipid biomarker data reveal substantial changes in the biological communities and organic matter source inputs through the Shuram excursion in this sedimentary basin, but within the ranges expected of Neoproterozoic sedimentary rocks. Together these observations imply that carbonate-organic isotopic decoupling during the Shuram excursion is not a result of mixing of fossil or exogenous carbon sources (either DOC, detrital, or migrated) with syngenetic organic matter, though differential mixing of distinct syngenetic sources may have played an important role in the observed differences between inorganic and organic carbon isotope ratios. Ultimately, these results highlight the possibility that systematic global changes in the fractionations between organic and inorganic carbon provided a driving mechanism for the Shuram excursion.

References

Ader, M., Macouin, M., Trindade, R. I. F., Hadrien M-H., Yang, Z., Sun, Z., and Besse, J. 2009. A multilayered water column in the Ediacaran Yangtze platform? Insights from carbonate and organic matter paired δ^{13}C. *Earth and Planetary Science Letters*, **288**, 213-227.

Allen, P. A. 2007. The Huqf Supergroup of Oman: Basin development and context for Neoproterozoic glaciation. *Earth-Science Reviews*, **84**, 139-185.

Al-Marjeby, A., and Nash, D. F. 1986. A summary of the geology and oil habitat of the Eastern Flank hydrocarbon province of South Oman. *Marine and Petroleum Geology*, **3**, 306-314.

Alsharhan, A. S. 1997. The hydrocarbon habitat of the Oman Basin. In: *Sedimentary Basins and Petroleum Geology of the Middle East*. (eds. Alsharhan, A.S., and Nairn, A. E. M.). Elsevier, **13**, 737-773.

Altabet, M. A. 2006. Isotopic tracers of the marine nitrogen cycle: Present and past. In: *Marine Organic Matter: Biomarkers, Isotopes and DNA* (ed. Volkman, J.K.). Springer Berlin Heidelberg, **2N**, 251-293.

Amthor, J. E., Grotzinger, J. P., Schröder, S., Bowring, S. A., Ramezani, J., Martin, M. W., and Matter, A. 2003. Extinction of *Cloudina* and *Namacalathus* at the Precambrian-Cambrian boundary in Oman. *Geology*, **31**(5), 431-434.

Bauersachs, T., Kremer, B., Schouten, S., and Sinninghe Damsté, J. S. 2009. A biomarker and δ^{15}N study of thermally altered Silurian cyanobacterial mats. *Organic Geochemistry* **40**, 149-157.

Bazhenova, O. K., and Arefiev, O. A. 1996. Geochemical peculiarities of Precambrian source rocks in the East European Platform. *Organic Geochemistry* **25**(5-7), 341 351.

Bergmann, K. D., Zentmyer, R. A., and Fischer, W. W. 2011. The stratigraphic expression of a large negative carbon isotope excursion from the Ediacaran Johnnie Formation, Death Valley. *Precambrian Research* **188**, 45-56.

Berkner, L. V., Marshall, L. C. 1965. On the origin and rise of oxygen concentration in the Earth's atmosphere. *Journal of Atmospheric Science*, **22**, 225–261.

Bjerrum, C. J., and Canfield, D. E. 2011. Towards a quantitative understanding of the late Neoproterozoic carbon cycle. *Proceedings of the National Academy of Sciences of the United States of America*, **108**(14), 5542-5547.

Bowring, S. A., Grotzinger, J. P., Condon, D. J., Ramezani, J., Newhall, M. J., and Allen, P. A. 2007. Geochronologic constraints on the chronostratigraphic framework of the Neoproterozoic Huqf Supergroup, Sultanate of Oman. *American Journal of Science*, **307**, 1097-1145.

Bristow, T. F., and Kennedy, M. J. 2008. Carbon isotope excursions and the oxidant budget of the Ediacaran atmosphere and ocean. *Geology*, **36**(11), 863-866.

Burdett, J. W., Arthur, M. A., and Richardson, M. 1989. A Neogene seawater sulfur isotope age curve from calcareous pelagic microfossils. *Earth & Planetary Science Letters* **94**(3-4), 189-198.

Burns, S. J., and Matter, A. 1993. Carbon isotopic record of the latest Proterozoic from Oman. *Eclogae Geologicae Helvetiae*, **86**, 595-607.

Butterfield, N. J., and Grotzinger, J. P. 2012. Palynology of the Huqf Supergroup, Oman. In: *Geology and Hydrocarbon Potential of Neoproterozoic-Cambrian Basins in Asia* (eds. Bhat, G. M., Thurow, C. J., Thusu, J. W., and Cozzi, A.). Geological Society, London, Special Publications, **366**, 1-13.

Calver, C. R. 2000. Isotope stratigraphy of the Ediacaran (Neoproterozoic III) of the Adelaide Rift Complex, Australia, and the overprint of water column stratification. *Precambrian Research*, **100**(1-3), 121-150.

Cao, C., Love, G. D., Hays, L. E., Wang, W., Shen, S., and Summons, R. E. 2009. Biogeochemical evidence for euxinic oceans and ecological disturbance presaging the end-Permian mass extinction event. *Earth and Planetary Science Letters*, **281**, 188-201.

Close, H. G., Bovee, R., and Pearson, A. 2011. Inverse carbon isotope patterns of lipids and kerogen record heterogeneous primary biomass. *Geobiology*, **9**(3), 250-265.

Cozzi, A., Allen, P. A., Grotzinger, J. P. 2004. Understanding carbonate ramp dynamics using $\delta^{13}C$ profiles: examples from the Neoproterozoic Buah Formation of Oman. *Terra Nova*, **16**(2), 62-67.

Danovaro, R., Dell'Anno, A., Pusceddu, A., Gambi, C., Heiner, I., and Kristensen, R. M. 2010. The first metazoan living in permanently anoxic conditions. *BMC Biology*, **8**(30), 1-10.

Deines, P. 2002. The carbon isotope geochemistry of mantle xenoliths. *Earth-Science Reviews*, **58**, 247-278.

Derry, L. A. 2010a. A burial diagenesis origin for the Ediacaran Shuram-Wonoka carbon isotope anomaly. *Earth and Planetary Science Letters*, **294**, 152-162.

Derry, L. A. 2010b. On the significance of $\delta^{13}C$ correlations in ancient sediments. *Earth and Planetary Science Letters*, **296**, 497-501.

Farrimond, P., Talbot, H. M., Watson, D. F., Schulz, L. K., and Wilhelms, A. 2004. Methylhopanoids: molecular indicators of ancient bacteria and a petroleum correlation tool. *Geochimica et Cosmochimica Acta* **68**(19), 3873-3882.

Fike, D. A., Grotzinger, J. P., Pratt, L. M., and Summons, R. E. 2006. Oxidation of the Ediacaran Ocean. *Nature*, **444**, 744-747.

Fike, D. A. 2007. Carbon and sulfur isotopic constraints on Ediacaran biogeochemical processes, Huqf Supergroup, Sultanate of Oman. PhD dissertation, Massachusetts Institute of Technology.

Fike, D. A., and Grotzinger, J. P. 2008. A paired sulfate-pyrite $\delta^{34}S$ approach to understanding the evolution of the Ediacaran-Cambrian sulfur cycle. *Geochimica et Cosmochimica Acta*, **72**, 2636-2648.

Fowler, M. G., and Douglas, A. G. 1987. Saturated hydrocarbon biomarkers in oils of Late Precambrian age from Eastern Siberia. *Organic Geochemistry* **11**(3), 201 213.

Gorin, G. E., Racz, L. G., and Walter, M. R. 1982. Late Precambrian-Cambrian sediments of Huqf Group, Sultanate of Oman. *The American Association for Petroleum Geologists Bulletin*, **60**(12), 2609-2627.

Gill, B. C., Lyons, T. W., and Frank, T. D. 2008. Behaviour of carbonate-associated sulfate during meteoric diagenesis and implications for the sulfur isotope proxy. *Geochimica et Cosmochimica Acta* **72**, 4699-4711.

Grantham, P. J., Lijmbach, G. W. M., Posthuma, J., Hughes Clarke, M. W., and Willink, R. J. 1988. Origin of crude oils in Oman. *Journal of Petroleum Geology*, **11**(1), 61-80.

Grantham, P. J., and Wakefield, L. L. 1988. Variations in the sterane carbon number distributions of marine source rock derived crude oils through geological time. *Organic Geochemistry*, **12**(1), 61-74.

Grosjean, E., Love, G. D., Stalvies, C., Fike, D. A., and Summons, R. E. 2009. Origin of petroleum in the Neoproterozoic-Cambrian South Oman Salt Basin. *Organic Geochemistry*, **40**, 87-110.

Grosjean, E., Love, G. D., Kelly, A. E., Taylor, P. N., and Summsons, R. E. 2012. Geochemical evidence for an Early Cambrian origin of the 'Q' oils and some condensates from north Oman. *Organic Geochemistry* **45**, 77-90.

Grotzinger, J. P., Al-Siyabi, A. H., Al-Hashimi, R. A., and Cozzi, A. 2002. New model for the tectonic evolution of Neoproterozoic-Cambrian Huqf Supergroup basins, Oman. *GeoArabia*, **7**, 241.

Grotzinger, J. P., Fike, D. A., and Fischer, W. W. 2011. Enigmatic origin of the largest known carbon isotope excursion in Earth's history. *Nature Geoscience*, **4**, 285 292.

Halevy, I., Peters, S. E., and Fischer, W. W. 2012. Sulfate burial constraints on the Phanerozoic sulfur cycle. *Science*, **337**, 331-334.

Handley, L. L., and Raven, J. A. 1992. The use of natural abundance of nitrogen isotopes in plant physiology and ecology. *Plant, Cell and Environment* **15**, 965-985.

Hayes, J. M., Strauss, H., and Kaufman, A. J. 1999. The abundance of ^{13}C in marine organic matter and isotopic fractionation in the global biogeochemical cycle of carbon during the past 800 Ma. *Chemical Geology*, **161**, 103-125.

Herron, S. L., and Le Tendre, L. 1990. Wireline source-rock evaluation in the Paris Basin. In: *Deposition of Organic Facies* (ed. Huc, A.), American Association of Petroleum Geologists, Special Studies in Geology, **30**, 57-71.

Higgins, M. B., Wolfe-Simon, F., Robinson, R. S., Qin, Y., Saito, M. A., and Pearson, A. 2011. Paleoenvironmental implications of taxonomic variation among δ^{15}N values of chloro-pigments. *Geochimica et Cosmochimica Acta* **75**, 7351-7363.

Hoffman, P. F., Kaufman, A. J., Halverson, G. P., Schrag, D. P. 1998. A Neoproterozoic Snowball Earth. *Science*, **281**, 1342-1346.

Höld, I. M., Schouten, S., Jellema, J., Sinninghe Damsté, J. S. 1999. Origin of free and bound mid-chain methyl alkanes in oils, bitumens and kerogens of the marine, Infracambrian Huqf Formation (Oman). *Organic Geochemistry*, **30**, 1411-1428.

Jansyn, J. 1990. Strato-tectonic evolution of a large subsidence structure associated with the late Proterozoic Wonoka Formation at Wilpena Pound, central Flinders

Ranges, South Australia. B.Sc. Honours thesis, University of Adelaide (unpublished).

Jiang, G. Q., Wang, X., Shi, X., Xiao, S., Zhang, S., and Dong, J. 2012. The origin of decoupled carbonate and organic carbon isotope signatures in the early Cambrian (*ca*. 542-520 Ma) Yangtze platform. *Earth and Planetary Science Letters*, **317 318**, 96-110.

Johnston, D. T., Macdonald, F. A., Gill, B. C., Hoffman, P. F., and Schrag, D. P. 2012. Uncovering the Neoproterozoic carbon cycle. *Nature*, **483**, 320-324.

Kaufman, A. J., Corsetti, F. A., Varni, M. A. 2007. The effect of rising atmospheric oxygen on the carbon and sulfur isotope anomalies in the Neoproterozoic Johnnie Formation, Death Valley, USA. *Chemical Geology* **237**(1-2), 47-63.

Kelly, A. E. 2009. Hydrocarbon biomarkers for biotic and environmental evolution through the Neoproterozoic-Cambrian transition. PhD dissertation, Massachusetts Institute of Technology.

Kelly, A. E., Love, G. D., Zumberge, J. E., and Summons, R. E. 2011. Hydrocarbon biomarkers of Neoproterozoic to Lower Cambrian oils from eastern Siberia. *Organic Geochemistry* **42**(6), 640-654.

King, N., Westbrook, M. J., Young, S. L., Kuo, A., Abedin, M., Chapman, J., Fairclough, S., Hellsten, U., Isogai, Y., Letunic, I., Marr, M., Pincus, D., Putnam, N., Rokas, A., Wright, K. J., Zuzow, R., Dirks, W., Good, M., Goodstein, D., Lemons, D., Li, W., Lyons, J. B., Morris, A., Nichols, S., Richter, D. J., Salamov, A., JGI Sequencing, Bork, P., Lim, W. A., Manning, G., Miller, W. T., McGinnis, W., Shapiro, H., Tjian, R., Grigoriev, I. V., and Rokhsar, D. 2008. The genome of choanoflagellate *Monosiga brevicollis* and the origin of metazoans. *Nature*, **451**(7180), 783-788.

Klomp, U. C. 1986. The chemical structure of a pronounced series of iso-alkanes in South Oman crudes. *Organic Geochemistry* **10**(4-6), 807-814.

Knauth, L. P., and Kennedy, M. J. 2009. The late Precambrian greening of the Earth. *Nature* **460**(6), 728-732.

Knoll, A. H., Hayes, J. M., Kaufman, A. J., Swett, K., Lambert, I. B. 1986. Secular variation in carbon isotope ratios from Upper Proterozoic successions of Svalbard and East Greenland. *Nature*, **321**, 832-838.

Knoll A. H., and Carroll, S. B. 1999. Early animal evolution: emerging views from comparative biology and geology. *Science*, **284**, 2129-2137.

Knoll, A. H., Summons, R. E., Waldbauer, J. R., and Zumberge, J. E. 2007. The geological succession of primary producers in the oceans. In: *The Evolution of Primary Producers in the Sea* (eds. Falkowski, P,. and Knoll, A. H.). Burlington, Elsevier, 133-163.

Le Guerroué, E., Allen, P. A., and Cozzi, A. 2006a. Chemostratigraphic and sedimentological framework of the largest negative carbon isotopic excursion in Earth history: The Neoproterozoic Shuram Formation (Nafun Group, Oman). *Precambrian Research*, **146**, 68-92.

Le Guerroué, E., Allen, P. A., and Cozzi, A. 2006b. Parasequence development in the Ediacaran Shuram Formation (Nafun Group, Oman): High resolution stratigraphic test for primary origin of negative carbon isotopic ratios. *Basin Research*, **18**, 205-220.

Le Guerroué, E., Allen, P. A., Cozzi, A., Etienne, J. L., and Fanning, M. 2006c. 50 Myr recovery from the largest δ^{13}C excursion in the Ediacaran ocean. *Terra Nova*, **18**(2), 147-153.

Le Guerroué, E., and Cozzi, A. 2010. Veracity of Neoproterozoic negative C-isotope values: The termination of the Shuram negative excursion. *Gondwana Research* **17**(4), 653-661.

Lee, C., Fike, D. A., Love, G. D., Sessions, A. L., Grotzinger, J. P., Summons, R. E., and Fischer, W. W. 2013. Carbon isotopes and lipid biomarkers from organic-rich facies of the Shuram Formation, Sultanate of Oman. *Geobiology* **11**(5), 406-419.

Logan, G. A., Hayes, J. M., Hieshima, G. B., and Summons, R. E. 1995. Terminal Proterozoic reorganisation of biogeochemical cycles. *Nature*, **376**, 53-56.

Loosveld, R. J. H., Bell, A., and Terken, J. J. M. 1996. The tectonic evolution of interior Oman. *GeoArabia*, **1**, 28-50.

Love, G. D., Stalvies, C., Grosjean, E., Meredith, W., Snape, C. E. 2008. Analysis of molecular biomarkers covalently bound within Neoproterozoic sedimentary kerogen. In: *From Evolution to Geobiology: Research Questions Driving Paleontology at the Start of a New Century*. (eds. Kelley, P. H., and Bambach, R. K.). Paleontological Society Papers, Paleontological Society Short Course, October **4**, 14.

Love, G. D., Grosjean, E., Stalvies, C., Fike, D. A., Grotzinger, J. P., Bradley, A. S., Kelly, A. E., Bhatia, M., Meredith, W., Snape, C. E., Bowring, S. A., Condon, D.

J., and Summons, R. E. 2009. Fossil steroids record the appearance of Demospongiae during the Cryogenian Period. *Nature*, **457**, 718-722.

Loyd, S. J., Marenco, P. J., Hagadorn, J. W., Lyons, T. W., Kaufman, A. J., Sour-Tovar, F., and Corsetti, F. A. 2013. Local δ^{34}S variability in ~580 Ma carbonates of northwestern Mexico and the Neoproterozoic marine sulfate reservoir. *Precambrian Research* **224**, 551-569.

Mann, U., Leythaeuser, D., and Muller, P. J. 1986. Relation between source rock properties and wireline log parameters: An example from lower Jurassic Posidonia shale, NW Germany. *Advances in Organic Geochemistry*, **10**, 1105 1112.

Marenco, P. J., Corsetti, F. A., Hammond, D. E., Kaufman, A. J., and Bottjer, D. J. 2008. Oxidation of pyrite during extraction of carbonate associated sulfate. *Chemical Geology*, **247**, 124-132.

McCarron, G. M. E. 2000. The sedimentology and chemostratigraphy of the Nafun Group, Huqf Supergroup, Oman. PhD dissertation, Oxford University, p175.

McFadden, K. A., Huang, J., Chu, X., Jiang, G., Kaufman, A. J., Zhou, C., Yuan, X., and Xiao, S. 2008. Pulsed oxidation and biological evolution in the Ediacaran Doushantuo Formation. *Proceedings of the National Academy of Sciences of the United States of America*, **105**(9), 3197-3202.

Melim, L. A., Swart, P. K., and Eberli, G. P. 2004. Mixing-zone diagenesis in the subsurface of Florida and the Bahamas. *Journal of Sedimentary Research*, **74**(6), 904-913.

Meyer, B. L., and Nederlof, M. H. 1984. Identification of source rocks on wireline logs by density/resistivity and sonic transit time/resistivity crossplots. *American Association of Petroleum Geologists Bulletin*, **68**, 121-129.

Nielsen, C. 2008. Six major steps in animal evolution: are we derived from sponge larvae? *Evolution and Development*, **10**(2), 241-257.

Oehlert, A. M., Lamb-Wozniak, K. A., Devlin, Q. B., Mackenzie, G. J., Reijmer, J. J. G., and Swart, P. K. 2012. The stable carbon isotopic composition of organic material in platform derived sediments: implications for reconstructing the global carbon cycle. *Sedimentology*, **59**, 319-335.

Osburn, M. R., Grotzinger, J. P., Bergmann, K. D. 2014. Facies, stratigraphy, and evolution of a middle Ediacaran carbonate ramp: Khufai Formation, Sultanate of

Oman. *The American Association for Petroleum Geologists Bulletin* **98**(8), 1631 1667.

Ostermann, D. R., and Curry, W. B. 2000. Calibration of stable isotopic data: An enriched $\delta^{18}O$ standard used for source gas mixing detection and correction. *Paleoceanography*, **15**, 353-360.

Pancost, R. D., Freeman, K. H., Patzkowsky, M. E., Wavrek, D., and Collister, J. W. 1998. Molecular indicators of redox and marine phytoplankton composition in the late Middle Ordovician of Iowa, U.S.A. *Organic Geochemistry*, **29**, 1649-1662.

Pancost, R. D., and Sinninghe Damsté, J. S. 2003. Carbon isotopic compositions of prokaryotic lipids as tracers of carbon cycling in diverse settings. *Chemical Geology*, **195**, 29-58.

Pell, S. D., McKirdy, D. M., Jansyn, J., and Jenkins, R. J. F. 1993. Ediacaran carbon isotope stratigraphy of South Australia. *Transactions of the Royal Society of South Australia* **117**, 153-161.

Peters, K. E., Walters, C. C., Moldowan, J. M. 2005. The Biomarker Guide, 2nd edition: Cambridge University Press, Cambridge. pp. 1132

Robinson, R. S., Kienast, M., Albuquerque, A. L., Altabet, M., Contreras, S., De Pol Holz, R., Dubois, N., Francois, R., Galbraith, E., Hsu, T-C., Ivanochko, T., Jaccard, S., Kao, S-J., Kiefer, T., Kienast, S., Lehmann, M., Martinez, P., Ryabenko, E., Schmittner, A., Schneider, R., Schneider-Mor, A., Shigemitsu, M., Sinclair, D., Somes, C., Studer, A., Thunell, R., Yang, J-Y. 2012. A review of nitrogen isotopic alteration in marine sediments. *Paleoceanography* **27**, 1-13.

Rohrssen, M., Love, G. D., Fischer, W. W., Finnegan, S., Fike, D. A. 2013. Lipid biomarkers record fundamental changes in the microbial community structure of tropical seas during the Late Ordovician Hirnantian glaciation. *Geology* **41**(2), 127-130.

Rontani, J-F., and Bonin, P. 2011. Production of pristane and phytane in the marine environment: role of prokaryotes. *Research in Microbiology* **162**, 923-933.

Rothman, D. H., Hayes, J. M., and Summons, R. E. 2003. Dynamics of the Neoproterozoic carbon cycle. *Proceedings of the National Academy of Sciences of the United States of America*, **100**(14), 8124-8129.

Schrag, D. P., Higgins, J. A., Macdonald, F. A., and Johnston, D. T. 2013. Authigenic carbonate and the history of the global carbon cycle. *Science* **339**, 540-543.

Schröder, S., Schreiber, B. C., Amthor, J. E., and Matter, A. 2004. Stratigraphy and environmental conditions of the terminal Neoproterozoic-Cambrian period in Oman: evidence from sulfur isotopes. *Journal of the Geological Society London*, **161**, 489-499.

Schwark, L., and Empt, P. 2006. Sterane biomarkers as indicators of Palaeozoic algal evolution and extinction events. *Palaeogeography, Palaeoclimatology, Palaeoecology*, **240**, 225-236.

Scott, K. M., Schwedock, J., Schrag, D. P., and Cavanaugh, C. M. 2004. Influence of Form IA RubisCO and environmental dissolved inorganic carbon on the ^{13}C of the clam-chemoautotroph symbiosis *Solemya Velum*. *Environmental Microbiology*, **6**(12), 1210-1219.

Scott, C., Lyons, T. W., Bekker, A., Shen, Y., Poulton, S. W., Chu, X., and Anbar, A. D. 2008. Tracing the stepwise oxygenation of the Proterozoic ocean. *Nature*, **452**, 456-459.

Sperling, E. A., Peterson, K. J., and Laflamme, M., 2011. Rangeomorphs, *Thectardis* (Porifera?) and dissolved organic carbon in the Ediacaran oceans. *Geobiology*, **9**, 24-33.

Summons, R. E., Jahnke, L. L., Logan, G. A., and Hope, J. M. 1999. 2-Methylhopanoids as biomarkers for cyanobacterial oxygenic photosynthesis. *Nature*, **398**, 554-557.

Swanson-Hysell, N. L., Rose, C. V., Calmet, C. C., Halverson, G. P., Hurtgen, M. T., and Maloof, A. C. 2010. Cryogenian glaciation and the onset of carbon-isotope decoupling. *Science*, **328**, 608-611.

Swart, P. K. 2008. Global synchronous changes in the carbon isotopic composition of carbonate unrelated to changes in the global carbon cycle. *Proceedings of the National Academy of Sciences of the United States of America*, **105**(37), 13741-13745.

Towe, K. M. 1970. Oxygen-collagen priority and the early metazoan fossil record. *Proceedings of the National Academy of Sciences of the United States of America*, **65**, 781-788.

Tsao, L. E., Robinson, R. S., Higgins, M. B., and Pearson, A. 2012. Nitrogen isotope ratio of cyanobacterial chlorophyll: Chemostat vs. batch culture. *Organic Geochemistry* **49**, 96-99.

Urlwin, B., Ayliffe, D. J., Jansyn, J., McKirdy, D. M., Jenkins, R. J. F., and Gostin, V. A. 1993. A δ^{13}C survey of carbonate in the Early Ediacaran Wonoka Formation. In:

Field guide to the Adelaide Geosyncline and Amadeus Basin, Australia. (eds. Jenkins, R. J. F., Lindsay, J. F., and Walter, M. R.). AGSO Record 1993/**35**, 92 96.

Volkman, J. K. 1986. A review of sterol markers for marine and terrigenous organic matter. *Organic Geochemistry*, **9**, 83-99.

Wada, E., and Hattori, A. 1978. Nitrogen isotope effects in the assimilation of inorganic nitrogenous compounds by marine diatoms. *Geomicrobiology Journal* **1**, 85-101.

Volkman, J. K., and Maxwell, J. R. 1986. Acyclic isoprenoids as biological markers. In: *Biological Markers in the Sedimentary Record*. (ed. Johns, R. B.). Elsevier, 1-46.

Welander, P. V., Coleman, M., Sessions, A. L., Summons, R. E., Newman, D. K. 2010. Identification of a methylase required for 2-methylhopanoid production and implications for the interpretation of sedimentary hopanes. *Proceedings of the National Academy of Sciences of the United States of America*, **107**, 8537-8542.

Williams, L. B., Ferrell Jr., R. E., Hutcheon, I., Bakel, A. J., Walsh, M. M., and Krouse, R. H. 1995. Nitrogen isotope geochemistry of organic matter and minerals during diagenesis and hydrocarbon migration. *Geochimica et Cosmochimica Acta* **59**(4), 765-779.

CHAPTER THREE

Marine organic matter cycling during the Ediacaran Shuram excursion

ABSTRACT

Ediacaran (*ca.* 635–541 Ma) marine carbonates capture a global $\delta^{13}C$ carbon isotope excursion to extremely negative values (*ca.* −12‰)—known as the Shuram excursion (SE)—that cannot be explained by conventional mass balance scenarios. Furthermore, the carbon isotopic variation of bulk organic matter (OM) does not mirror that of carbonate through the excursion, suggesting that the OM reflects a mixture of different sources. To evaluate this hypothesis, we investigated thermally immature marine sedimentary rocks that record the SE from the Sultanate of Oman. Compound-specific carbon isotopic analyses of the extractable hydrocarbons reveal low $\delta^{13}C$ values of long-chain ($>C_{20}$) *n*-alkanes and mid-chain monomethyl alkanes (MMAs) as low as −40‰. Such light signatures are rare in marine rocks of any age and provide evidence that the SE reflects a primary carbon cycle perturbation. The magnitude of the SE recorded in these organic phases is smaller than observed in carbonate and implies that the primary perturbation to dissolved inorganic carbon (DIC) was at least 5−7‰ and more likely 7−12‰ in magnitude when correcting for end-member source mixing. Due to isotopic differences in stratigraphic patterns of the different organic compounds, we propose that bulk organic carbon (both bitumen and kerogen) reflects source mixing between two distinct pools that previously masked the excursion in bulk $\delta^{13}C_{org}$ measurements. OM sources were derived

from both autotrophs fixing ^{13}C-depleted DIC and from a less ^{13}C-depleted heterotrophic microbial biomass feeding on a marine OM pool sustained by petroleum expelled from older sedimentary OM. Expulsion of these sedimentary fluids also helps explain both the duration and magnitude of the SE.

1. Introduction

Much debate surrounds the enigmatic Shuram carbon isotope excursion, which is observed globally in late Neoproterozoic marine carbonates (Grotzinger *et al.,* 2011). Bulk carbon isotope results reveal a large (>12‰) $\delta^{13}C$ excursion in marine carbonates ($\delta^{13}C_{carbonate}$; $\delta^{13}C_{carb}$) with no parallel excursion of equal magnitude in bulk organic carbon ($\delta^{13}C_{organic}$; $\delta^{13}C_{org}$) phases (e.g., Fike *et al.,* 2006; McFadden *et al.,* 2008; Lee *et al.,* 2013; Macdonald *et al.,* 2013). The decoupling of carbonate and organic carbon isotopes during the excursion is unexpected if they are derived from the same source of dissolved inorganic carbon (DIC) with isotopic offset associated with biological fractionation during carbon fixation (Rothman *et al.,* 2003); leading to suggestions that marine carbonates may not record a primary carbon cycle perturbation but rather reflect $\delta^{13}C_{carb}$ values typical of diagenetic processes (e.g., Knauth & Kennedy, 2009; Derry, 2010). For example, the lack of similar excursion in organic carbon has been proposed to be a result of: i) oxidation of a large pool of dissolved organic carbon (DOC) in seawater (Rothman *et al.,* 2003; Fike *et al.,* 2006; McFadden *et al.,* 2008); ii) multilayered ocean stratification (Ader *et al.,* 2009); iii) sedimentary methane clathrate collapse (Bjerrum &

Canfield, 2011); iv) a significant contribution of exogenous organic carbon sources in carbonate samples with low total organic carbon (TOC) content (Johnston *et al.,* 2012); v) post-depositional burial diagenesis of carbonates resulting in alteration of primary $\delta^{13}C_{carb}$ signatures (Derry, 2010; Knauth & Kennedy, 2012); vi) sea level changes associated with a large marine impact (bolide) followed by the return of shallow marine biota (Young, 2013); vii) amplification by authigenic carbonate precipitation (Schrag *et al.,* 2013; Macdonald *et al.,* 2013); and vii) mixed or multiple sources of organic carbon combined with diagenetic alteration of carbonates (Melim *et al.,* 2004; Oehlert *et al.,* 2012; Oehlert & Swart, 2014).

Prior organic carbon isotope records through the SE have focused on bulk organic matter (OM) derived from samples with low TOC content. These records can be difficult to decipher because preserved sedimentary OM can contain a mixture of organic carbon inputs (e.g., Freeman *et al.,* 1990; Johnston *et al.,* 2012). The $\delta^{13}C_{org}$ value that is routinely measured represents the average of all organic compounds proportional to their relative abundance and as such, bulk $\delta^{13}C_{org}$ measurements may not reflect the diverse range of carbon source inputs, especially in Proterozoic samples with large unresolved complex mixtures (UCMs), which are difficult to assess in terms of their ^{13}C isotopic contributions. Compound-specific carbon isotope analyses (CSIA) lend isotopic insights at the molecular level and provide details about the range of biological source organisms and metabolic processes contributing to bulk $\delta^{13}C_{org}$ values as the carbon isotopic signature conferred on the hydrocarbon skeleton lipids during synthesis is retained on geological timescales (e.g., Hayes *et al.,* 1990; Freeman *et al.,* 1990). Thus, CSIA

provides a means of untangling OM records and interrogating more directly isotopic signatures of primary OM production.

Here we present the first attempted deconvolution of the organic carbon isotopic variability of the main hydrocarbon compound series from detailed compound-specific carbon isotopic analyses of hydrocarbon fractions from organic-rich marine facies capturing the build-up, onset, nadir, and recovery of the Shuram excursion in sedimentary strata from a well drilled in the South Oman Salt Basin (Lee *et al.,* 2013). A detailed lipid biomarker investigation as part of this prior study unequivocally demonstrated that the organic matter in these strata is thermally well-preserved and primary. Additionally it contains abundant extractable biomarker assemblages dominated by a marine microbial *n*-alkane signature (Figure 3.1) not significantly affected by contamination (Lee *et al.,* 2013). Moderate to high organic carbon contents are found in the TM-6 rocks (range of 0.2 to 17 wt%; Lee *et al.,* 2013), including in the stratigraphic intervals within and around the SE, indicating that OM production and burial in the ocean did not cease during the SE carbonate minimum.
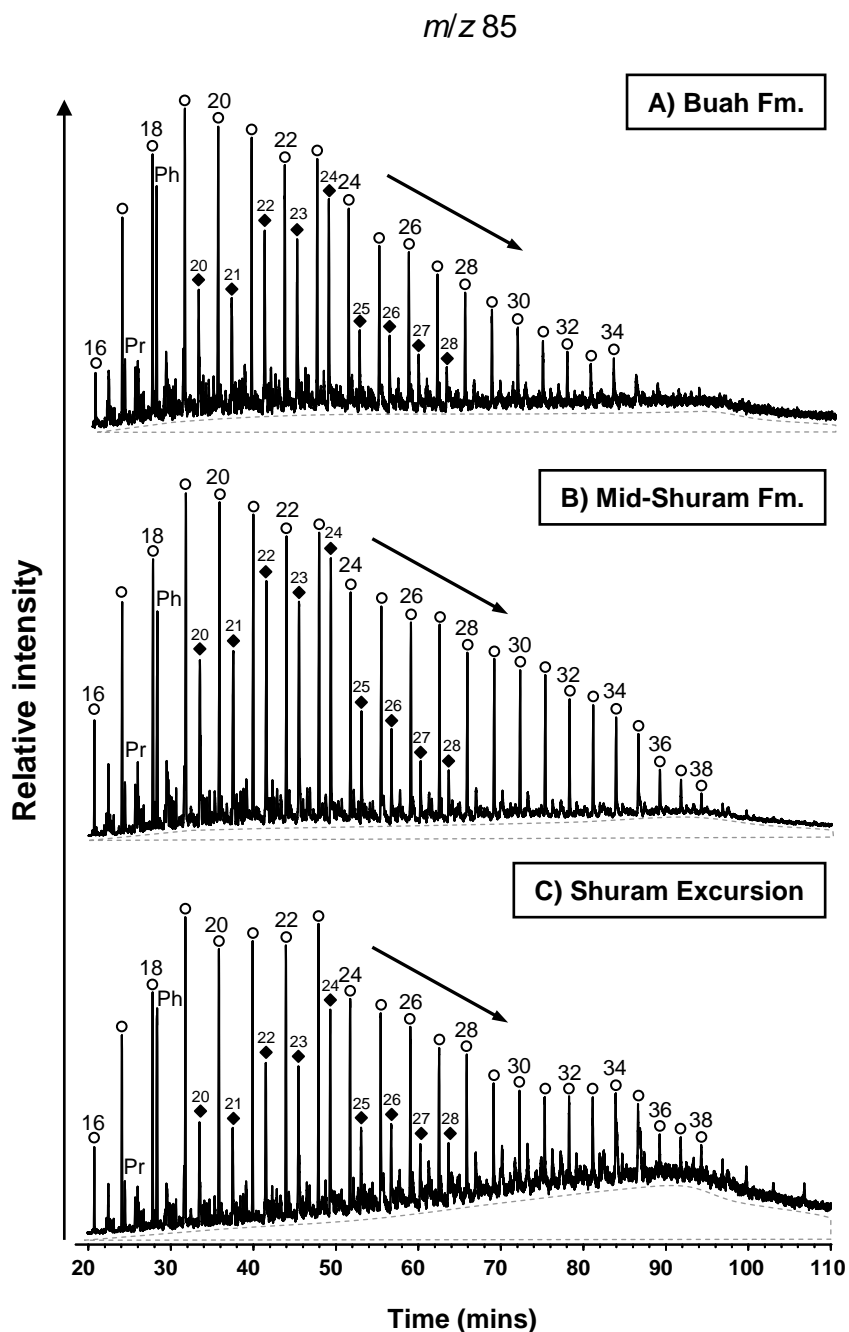
Figure 3.1. *M/z* 85 chromatograms highlight alkane series in representative samples from a) Buah Formation; b) Mid-Shuram Formation; and c) the Shuram excursion. Open circles represent *n*-alkanes with the carbon number indicated above and filled diamonds represent midchain monomethyl alkanes (MMAs) with the carbon number indicated above. The *n*-alkane envelope is typical of marine-sourced organic matter, with higher molecular weight *n*-alkanes tailing off in peak intensity with increasing carbon number (black arrow).

77

2. Materials & Methods

The South Oman Salt Basin (SOSB) is a large, well-studied, salt basin part of an extensive belt of evaporitic basins encompassing Oman, Iran, Pakistan, and the East Himalayas. The Eastern Flank Play of the SOSB is an important oil-bearing locale and contains thermally well-preserved late Neoproterozoic strata (Al-Marjeby & Nash, 1986). Samples were collected as cm-sized drillcore cuttings. The location of these samples and detailed descriptions of the geological setting are previously described in Section 2: Geology of the South Oman Salt Basin of Chapter 2 as it appears in Lee *et al.,* 2013.

2.1 Bulk carbon isotopes

2.1.1 Sample preparation. Bulk branched/cyclic (non-adduct) fractions were separated from the bulk saturated hydrocarbon fraction using a combination of standard 5Å molecular sieves (3-5 mm beads, Alfa Aesar) and a ZSM molecular sieve (zeolite, type ZSM-5, Acros Organics). The sieves were milled to fine powder and activated in a crucible held over a Bunsen burner flame for 10-15 mins. Prior to use, the activated sieves were kept in covered ceramic crucibles in a 110°C drying oven. The sieve columns were plugged with pre-combusted (475°C; 9h) glass wool (Ohio Valley Specialty), 1 mm thick layer of pre-combusted (450°C; 9 h) silica gel (Fisher silica gel sorbent, Grade 40, 35-70 mesh), and 2 cm thick layer of activated molecular sieve. ~1 mg of saturated hydrocarbon sample was pipetted directly on top of the sieve and left to react for up to 1 h. The branched/cyclic fraction was eluted with three column volumes of *n*-pentane

(OmniSolv), and evaporated to dryness. The composition of each fraction was analysed by GC-MS as described below in section 2.2.1.

2.1.2 Isotope analyses. Bulk carbon isotopes (TOC, bitumen, kerogen, bulk saturated hydrocarbons, bulk branched/cyclic hydrocarbons) were prepared and analysed according to methods outlined in Lee *et al.,* 2013. Bulk saturated and branched/cyclic hydrocarbon fractions were dissolved *n*-hexane prior to samples being dried into tin capsules. Samples were flash combusted at 1,000°C on a Costech Analytical Technologies Elemental Analyser (EA) coupled to a Thermo-Fisher Delta-V isotope ratio mass spectrometer (IRMS) *via* the Thermo Conflo-IV interface. $\delta^{13}C$ values were calibrated against CO_2 reference gas. Blank tin capsules and two in-house reference standards were run after every 10 samples (Lee *et al.,* 2013) with average standard errors for saturated hydrocarbons (0.34‰, $n = 24$), bulk branched/cyclic hydrocarbons (0.17‰, $n = 12$), blank (0.30‰, $n = 11$), acetanilide standard (0.05‰, $n = 11$), and urea standard (0.04‰, $n = 11$).

2.2 Compound-specific carbon isotope analysis

2.2.1 Separation of *n*-alkanes and mid-chain monomethyl alkanes (mid-chain MMAs) by urea adduction. Total lipids were extracted and fractionated according to methods outlined in Lee *et al.,* 2013. One procedural blank was run to monitor levels of background contamination with each batch of adductions. 1-2 mg of the saturated hydrocarbon fraction dissolved in 1.5 ml of 2:1 *n*-hexane:dichloromethane (DCM) (v/v) was quantitatively transferred to a 10 ml graduated glass centrifuge tube. 1 ml of a

saturated solution of urea (ultra pure, MP Biomedicals, LLC) in methanol (MeOH) (solubility of urea 167 gL^{-1} in MeOH at room temperature) was added to the sample, instantly precipitating white crystals of urea. The centrifuge tubes were vortexed for 10 s and placed into the freezer for 20 mins. The samples were allowed to thaw at room temperature for 15 mins before centrifuging for 3 mins at 2,500 rpm (Eppendorf 5804) and decanting the supernatant. 3 ml of n-hexane was added to the centrifuge tube, vortexed, and centrifuged for 3 mins at 2,500 rpm. The supernatant was collected into 8 ml vials. This step was repeated 3 times to quantitatively collected the non-adduct (branched/cyclic) fraction. The adduct fraction was collected by dissolving the n-alkane- and methylalkane-bound urea crystals with 3 ml MilliQ water. The trapped hydrocarbons were extracted using 3 ml of 4:1 n-hexane:DCM (v/v) with vortexing and centrifuging as described above. This step was also repeated 3 times with fractions collected in 8 ml vials. Both fractions were passed through pre-combusted (450°C; 9 h) and dry-packed silica gel (Geduran EMD, Grade 60) columns, the non-adduct fraction eluted with DCM and the adduct fraction with n-hexane. The solvent in both fractions were evaporated to dryness and analysed by gas chromatography-mass spectrometry (GC-MS) on an Agilent 7890A GC system coupled to an Agilent 5975C inert MSD mass spectrometer. The GC was equipped with a DB1-MS capillary column (60 m × 0.25 mm, 0.32 μm film thickness) and He was used as the carrier gas. Samples were run in full scan mode and injected into the GC in splitless mode at 60°C for 2 min, heated at 20°C/min to 150°C then 2°C/min to 325°C for 20 mins. Samples that were separated out for Pr and Ph $\delta^{13}C$ measurements were dried onto columns packed with ~1 cm of ZSM-5 (zeolite type,

ZSM-5, Acros Organics) for 30 mins and eluted three times with pentane and analysed in the same way.

2.2.2 Compound-specific carbon isotope analysis by gas chromatography-isotope ratio mass spectrometry (GC-C-IRMS).

Compound-specific carbon isotope values of n-alkanes (C_nH_{2n+2}; $n = 17$-35), mid-chain monomethyl alkanes (X_{20}-X_{28}), pristane (2,6,10,14-tetramethylpentadecane; $C_{19}H_{40}$; Pr), and phytane (2,6,10,14-tetramethylhexadecane; $C_{20}H_{42}$; Ph) were obtained at GB Scientific Incorporated on an Agilent 6890 GC-C-IRMS (GV Instruments Isoprime) equipped with a DB-1 capillary column (60 m x 0.25 mm, 0.25μm film thickness). n-alkanes and MMAs were injected into the GC at 120°C for 1 min, heated at 8°C/min to 200°C then 5°C/min to 320°C for 25 mins. Pristane and phytane were injected into the GC at 120°C for 1 min, heated at 4°C/min to 250°C then 12°C/min to 320°C for 20 mins. Sample replicates were repeatable to an average standard error of 0.22‰ for n-alkanes, 0.16‰ for mid-chain monomethyl alkanes, 0.05‰ for pristane, and 0.09‰ for phytane. The alkane reference standard (B2, Indiana University) containing n-alkanes $nC_{16} – nC_{30}$ was run after every batch. Carbon isotope values are calibrated against a CO_2 reference gas and reported in standard delta notation as $\delta^{13}C$ with units in ‰, relative to the VPDB standard (details in Lee *et al.,* 2013).

All isotope data are reported in units of parts per thousand (permil; ‰), described in Section 3.3.3 of Chapter 2 and Appendix Tables A3.1-3.3.

3. Results & Discussion

3.1 Isotopic composition of sedimentary organic carbon through the Shuram excursion

3.1.1 ^{13}C-depleted compounds: long-chain alkanes. *N*-alkanes and mid-chain monomethyl alkanes (MMAs**;** also known as X-peaks or X-compounds, but herein referred to as MMAs) constitute the two dominant resolvable series of compounds in the saturated hydrocarbon fractions. Long-chain *n*-alkanes ($>nC_{22}$) in sedimentary marine organic matter can have mixed sources—from algae and bacteria—but algal contributions are expected to be higher in proportion because they synthesise lipids containing long chain *n*-alkanes more commonly than prokaryotes (Love *et al.,* 2005). The biological precursor lipids of MMAs, which are long-chain linear methylalkanes containing a single methyl branch in the middle of the chain (e.g., Love *et al.,* 2008 and references therein), have not been unambiguously identified in any modern source organism. However, from independent data it has been speculated they have bacterial origins associated with benthic microbial mats (e.g., Love *et al.,* 2008; Lee *et al.,* 2013).
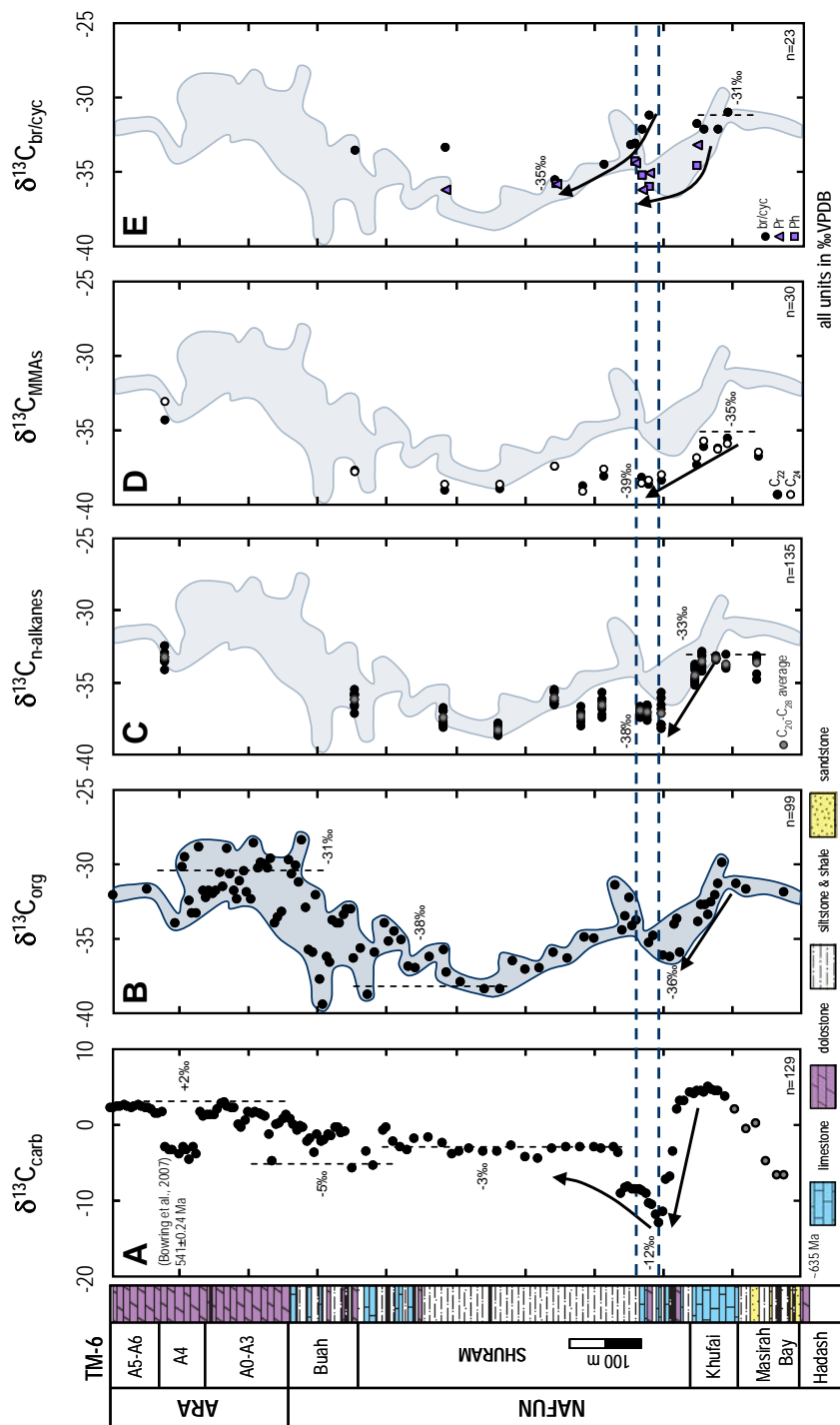
Figure 3.2. Carbon isotope ($\delta^{13}C$) trends through TM-6 (Lee *et al.*, 2013). A) Marine carbonates (grey points in the Masirah Bay Formation are likely influenced by diagenetic processes); b) Bulk organic carbon; c) C_{20}-C_{28} *n*-alkanes, with grey circles indicating the average $\delta^{13}C$; d) C_{22} (filled circles) and C_{24} (open circles) mid-chain monomethyl alkanes (MMAs); and e) Bulk branched/cyclic hydrocarbons, purple triangles and squares are $\delta^{13}C$ pristane and phytane, respectively. Blue dashed lines and black arrows highlight the nadir and immediate recovery of the excursion in $\delta^{13}C_{carb}$ and the response of the organic phases, B through E. Blue shaded region shows the profile of bulk $\delta^{13}C_{org}$. All values have units in ‰ VPDB.

Long-chain (nC_{20}-nC_{28}) n-alkanes (Figure 3.2C) and MMAs (C_{20}-C_{28}) (Figure 3.2D) during the SE display a broad negative excursion in $\delta^{13}C$ spanning hundreds of metres of stratigraphy, with MMA values dropping over a range from −33‰ to −40‰. $\delta^{13}C$ values of C_{20}-C_{28} n-alkanes range from ~ −32‰ to <−38‰ (Fig. 2C) and are similar to n-alkane values previously reported from South Oman (e.g., Höld *et al.,* 1999), but much lower than values from other Early Cambrian–Proterozoic strata (Figure 3.3; n = 432; Logan *et al.,* 1997; Brocks *et al.,* 2003; Li *et al.,* 2003; Williford *et al.,* 2011; Luo *et al.,* 2015). Although n-alkanes and MMAs are ^{13}C-depleted—approaching values of −40‰—they are not sufficiently ^{13}C-depleted to be substantially derived from methanotrophy (Birgel *et al.,* 2008). The 5−7‰ excursion in individual hydrocarbons coincides stratigraphically with the −12‰ $\delta^{13}C_{carb}$ anomaly observed both in this core and throughout Oman (Burns and Matter, 1993; Le Guerroué *et al.,* 2006; Lee *et al.,* 2013). Even more ^{13}C-depleted values for n-alkanes and MMA series in TM-6, as for bulk organic carbon, are found stratigraphically higher than the most ^{13}C-depleted carbonate interval within the Shuram Formation (Figure 3.2C,D). This stratigraphic offset points to a two end-member OM source mixing during the peak of the SE that explains the decoupling of organic and inorganic carbon isotopes and hints that the true magnitude of the excursion in marine DIC might be greater than 5−7‰. Hence, these new data confirm that the SE reflects, at least in part, a primary perturbation to the Neoproterozoic carbon cycle.
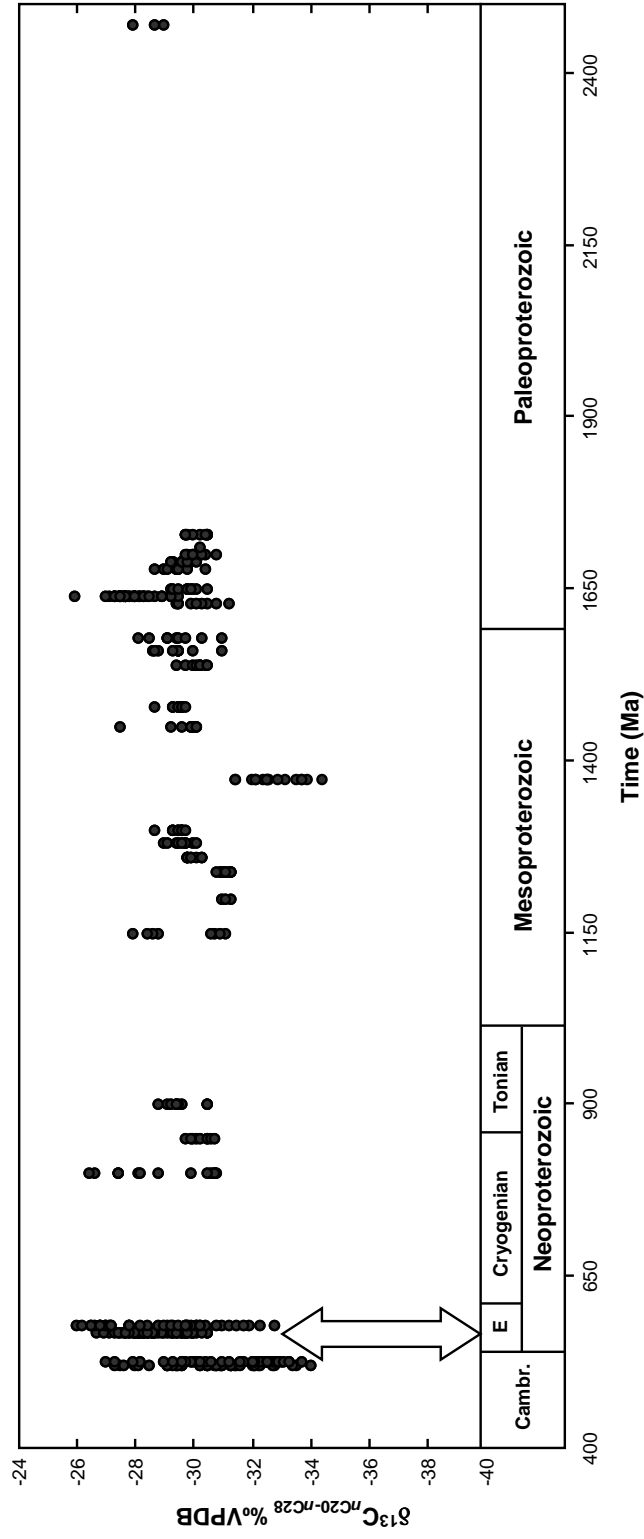
Figure 3.3. Carbon isotopic composition of *n*-alkanes in the C_{20}-C_{28} carbon number range reported from Early Cambrian-Proterozoic strata (Logan *et al.*, 1997; Brocks *et al.*, 2003; Li *et al.*, 2003; Williford *et al.*, 2011; Luo *et al.*, 2015; n = 432). White arrow represents the range of $\delta^{13}C$ values of *n*-alkanes from South Oman in this study.

We also measured the isotopic composition of several additional compounds that likely have autotrophic sources, that are commonly derived from the phytol side chain of chlorophylls: the isoprenoids pristane (2,6,10,14-tetramethylpentadecane; $C_{19}H_{40}$; Pr) and phytane (2,6,10,14-tetramethylhexadecane; $C_{20}H_{42}$; Ph). $\delta^{13}C$ values for Pr and Ph during the SE average $-35.2‰ \pm 0.05‰$ and $-35.3‰ \pm 0.09‰$, respectively, and trend toward heavier $\delta^{13}C$ values with depth below the SE (Figure 3.2E). These values are not as low as those observed in coeval *n*-alkanes and MMAs, but the degree of ^{13}C-depletion is likely underestimated since these compounds were measured on a substantial "heavy" unresolved complex mixture (UCM) baseline (Figure 3.4) even after considerable efforts to cleanly isolate these compounds. We interpret these values as a mixture of ^{13}C-depleted Pr and Ph with ^{13}C-enriched UCMs given that UCMs are the most ^{13}C-enriched alkane components we observed. Thus, Pr and Ph must be more ^{13}C-depleted than the measured $-35‰$—perhaps several permil lighter. Overall the Pr and Ph data support a photoautotrophic input to OM during the SE that is more ^{13}C-depleted than typically observed in marine sedimentary basins of any age.

3.1.2. ^{13}C-enriched compounds: UCM and branched/cyclic hydrocarbons.

UCMs are common features observed in gas chromatograms of extractable hydrocarbon constituents of Proterozoic sedimentary organic matter (e.g., Pawlowska *et al.,* 2013). Proterozoic UCMs are characterised by a substantial rise in the baseline towards the high molecular weight end of a gas chromatogram forming a 'hump-like' feature (Figure 3.4A,C) containing hundreds of largely unidentified branched and polycyclic

hydrocarbons. UCMs are also sometimes features of Phanerozoic samples where they are probably derived from late-stage microbial biodegradation. Previous $\delta^{13}C$ isotopic values of UCMs indicate they are typically ^{13}C-enriched relative to individual saturated hydrocarbons (e.g., Pearson & Eglinton, 2000), even in modern near shore marine samples where these mixtures may derive from fossil carbon sources (e.g., White *et al.,* 2013). Here, and throughout the text, the UCM refers to the non-resolvable mixture of hydrocarbon compounds within the branched and cyclic hydrocarbon fraction (br/cyc), which also contains pristane, phytane, and other acyclic, isoprenoids, tricyclic terpanes, steranes, and hopanes as resolvable constituents (Figure 3.4). Importantly, this whole br/cyc fraction shows a different stratigraphic $\delta^{13}C$ trend than the two alkane series. Khufai carbonates record a small ~1‰ positive excursion in $\delta^{13}C$ br/cyc isotopes, followed by a 4‰ negative excursion that occurs after the Shuram excursion nadir in $\delta^{13}C_{carb}$, with recovery to -33‰.
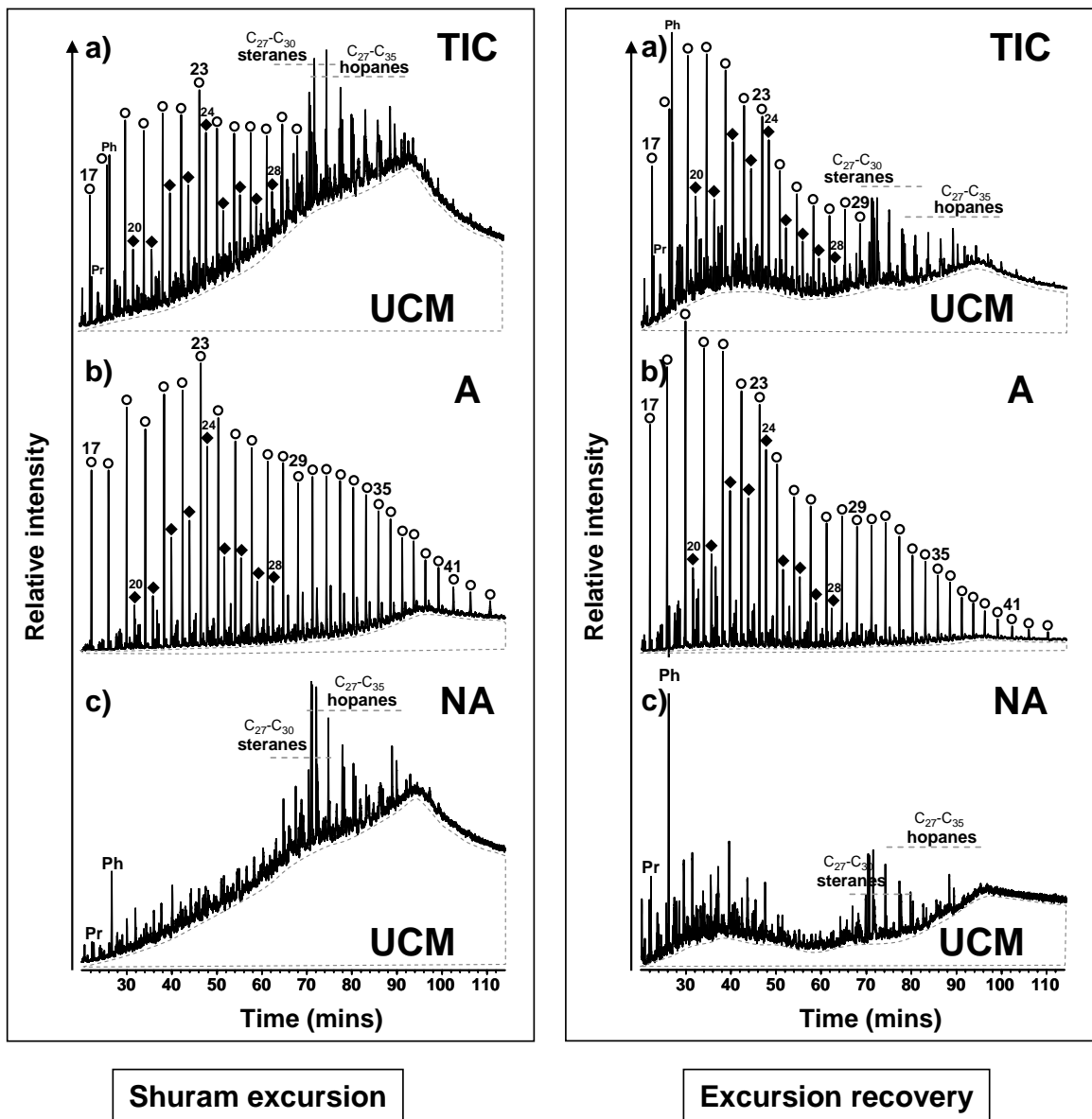
Figure 3.4. Chromatograms depict the saturated hydrocarbon profiles from the Shuram excursion (left) and the recovery (right). In both samples, a) represents the total ion chromatogram (TIC), b) the adduct fraction separated out by urea adduction, and c) the non-adduct fraction separated out by a 5Å molecular sieve. Open circles are *n*-alkanes with carbon numbers indicated; filled diamonds are MMAs with carbon numbers indicated; Pr = pristane; Ph = phytane; UCM = unresolved complex mixture. Despite the high UCM contribution during the Shuram excursion, urea adduction is effective at removing it.

During the Shuram excursion the UCM can constitute a substantial proportion of the total br/cyc fraction. The contribution of the UCM was estimated based on normalising the detector response at peak UCM intensity to the sample mass. These values are only internally comparable but give a rough guide to the contribution of the UCM to each sample. When cross-plotted against the $\delta^{13}C$ value of this fraction, there is a little to no correlation between the two—which is unexpected if the UCM contributes the ^{13}C-enriched end of the spectrum to the sample. The sample displaying the highest UCM contribution is found in the immediate recovery of the Shuram excursion and all samples prior and during the excursion display relatively ^{13}C-enriched values (average -31.6‰ ± 0.5‰, n = 6) with only moderate UCM contributions. One sample from the mid-Shuram Formation during the Shuram excursion recovery has the lightest $\delta^{13}C$ value (-35.5‰) but a relatively high UCM contribution. To reconcile these observations, we examined the entire composition of each $\delta^{13}C_{org}$ fraction in the individual samples. Stratigraphic horizons deposited prior to, during, and in the immediate recovery of the Shuram excursion display broad $\delta^{13}C$ variations between fractions (average variation 5‰ ± 1.6‰, n = 6), whereas the sample with $\delta^{13}C$-depleted UCM values has a very narrow range of $\delta^{13}C$ values (1.6‰). The largest difference between $\delta^{13}C_{MMAs}$ and $\delta^{13}C_{br/cyc}$ (lightest and heaviest organic carbon fractions) occurs during the Shuram excursion, at 8.4‰. In this unusual case, we interpret the heavy end to reflect contributions from heterotrophic biomass feeding on breakdown products from subsurface petroleum seepage and the light end to reflect syngenetic photoautotrophic sources.

4. Organic matter *versus*. carbonates as archives of carbon cycle change

Sedimentary carbonates provide a view of the global carbon cycle through the lens of local environmental and biological processes (e.g., carbonate precipitation mechanisms and mineralogy; Husson *et al.,* 2015)—processes that can impact carbonate isotopic compositions and embellish (or mask) the changes in the isotopic composition of DIC. For the SE, some have argued that the pattern observed in $\delta^{13}C_{carb}$ reflects secular changes in diagenetic processes rather than primary seawater perturbations to carbon cycle mass balance (Knauth and Kennedy, 2009; Derry, 2010; Schrag *et al.,* 2013). While a range of observations suggest that diagenetic processes did not alone account for the trends observed in $\delta^{13}C_{carb}$ (Bergmann *et al.,* 2011; Lee *et al.,* 2013; Husson *et al.,* 2015), the absolute magnitude of the perturbation to DIC remains uncertain. If the SE in TM-6 is interpreted as a perfect reflection of seawater, the $\delta^{13}C_{carb}$ data imply a DIC excursion of 17‰ (Figure 3.2A).

Organic carbon phases also provide a measure of the isotopic composition of DIC, filtered by microbial metabolisms and ecology. CSIA values for alkanes through the SE record at least a ~5−7‰ isotopic excursion that coincides with the main carbonate isotopic excursion. This shift is much smaller than that observed in carbonates, but nevertheless implies that the SE records a carbon cycle perturbation of significant size. Consequently, the isotopic change in DIC through the SE must have been ≥5‰, and perhaps much greater since source mixing appears to have buffered the magnitude of the ^{13}C depletion in the hydrocarbon fractions.

Isotope mass balance approaches to deconvolve the different sources, allowing for small 1–2‰ isotopic fractionations of saturated hydrocarbons from bulk $\delta^{13}C_{org}$ from South Oman rocks (e.g., Grosjean *et al.,* 2009), suggest the true magnitude of the negative SE for autotrophic organic carbon is estimated to be 7–12‰ offset from the baseline pre-Shuram value of −30‰ for bulk OM (Figure 3.5). Using a 10–50% contribution of a heavy end-member composition of −30‰ at the nadir in $\delta^{13}C_{carb}$ and a bulk $\delta^{13}C_{org}$ value of −36‰ gives an estimate of the light end-member OM in the range of −37 to −42‰. Although this solution is not unique, it does imply that the primary carbon isotopic shift associated with the SE is significant and greater than the observed 5–7‰ for individual alkanes and 6‰ for bulk organic carbon. An estimated 7–12‰ range excursion for the autotrophic organic carbon end-member is still substantially lower than the 17‰ excursion in $\delta^{13}C_{carb}$ over SE, requiring other contributing factors to explain the overall carbonate excursion.
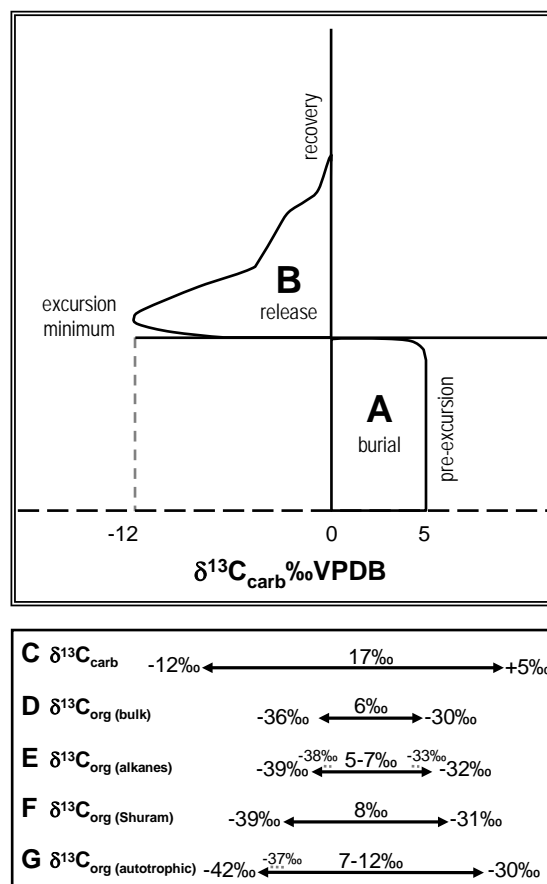
Figure 3.5. Conceptual schematic illustrating the A) burial and B) release of ^{13}C-enriched carbon prior to and during the SE, respectively. The magnitude scenarios on the bottom represent C) observed 17‰ SE magnitude from marine carbonates from TM-6; D) 6‰ δ13C in bulk OM during the SE; E) 5–7‰ excursion in *n*-alkanes; F) during the SE carbonate minimum, the maximum difference in different alkane series in the same sample observed is 8.4‰ between MMAs and br/cyc fraction and G) 7–12‰ perturbation in the light end-member organic carbon pool (autotrophic), taking into account the deconvolution of light and heavy contributions to the organic carbon pools during the SE.

92

Finally, since similar C_{org} isotopic profiles are seen both for rock bitumen and kerogen for TM-6 (Lee *et al.,* 2013) the carbon isotope decoupling between these phases and the compound-specific trends is not due to local oil staining of the rocks but involves a two end-member endogenous biomass input to host sediments at the time of deposition.

5. Assessment of mechanisms driving organic carbon cycle dynamics

Mechanisms driving the carbon cycle during the time period capturing the Shuram excursion are difficult to reconcile due to its unusual geochemical characteristics. Many different hypotheses and analogues have been proposed, but so far none of them are able to unambiguously explain all of the features. Specifically addressing the decoupling of the carbonate and organic carbon isotopes during the excursion, there have been several recent hypotheses that make inferences about sources of organic carbon (Knauth & Kennedy, 2009; Jones *et al*., 2014; Oehlert & Swart, 2014).

Seepage of petroleum from the subsurface into multiple basins worldwide

The SE punctuates a long interval of high $\delta^{13}C_{carb}$ values widely observed in Ediacaran strata (e.g., Husson *et al.,* 2015 and references therein). A reasonable interpretation of these high $\delta^{13}C_{carb}$ values is sustained high relative rates of organic carbon burial in sedimentary basins globally, the duration of which is not well constrained but could be tens of millions of years (Fike *et al.,* 2006; McFadden *et al.,* 2008. This is long enough to build up a substantial pool of ^{13}C-enriched organic-rich source rocks buried and matured to the stage of oil generation in multiple basins around

the world (Figure 3.5), the influence of which may have been magnified by the large number of passive margin basins formed during the break-up of the supercontinent Rodinia (Bradley, 2008).

Enhanced organic carbon burial in newly formed Ediacaran basins was previously proposed (Knoll *et al.,* 1986), and estimates of the global crustal organic carbon pool suggest this reached modern levels for the first time (Des Marais *et al.,* 1992). Thus we hypothesise that the SE reflects an interval of enhanced mass transfer of these hydrocarbon-rich fluids from sedimentary reservoirs to the fluid Earth—a large and dynamic suite of geophysical processes in sedimentary basins (Huuse *et al.,* 2010). The source of the fluids need not reflect a single or specific source, though there could have been multiple global sources with possible tectonic drivers, such as the Pan-African orogenies, playing an important role in synchronising catagenesis and expulsion of petroleum in different basins through the duration of the SE minimum. Furthermore, the middle Ediacaran is thought to be a time of increased tectonic activity (Halverson *et al.,* 2007; McKenzie *et al.,* 2014), and enhanced weathering could increase the oxidant supply needed to drive the oxidation of OM under this subsurface seepage scenario.

This hypothesis explains both the source mixing observed in sedimentary OM in Oman as well as the phase-shift between carbonate and organic isotope trends. In this scenario, a heterotrophic marine OM pool partially decoupled from surface primary production significantly fuelled by seepage of relatively ^{13}C-enriched OM from the subsurface, would produce ^{13}C-depleted DIC through OM oxidation (and a source for the

carbonate excursion), while buffering bulk $\delta^{13}C_{org}$ through the peak and immediate recovery of the SE. As hydrocarbon-rich fluid fluxes drop, this buffering capacity wanes and is exhausted through the mid-Shuram Formation, reflected in the recoupling between the isotopes of carbonate and OM. Additional support for this scenario comes from $\delta^{13}C_{org}$ values of −39‰ in the Buah Formation that match those of the upper Doushantuo Formation (IV) South China (McFadden *et al.,* 2008) at the level where carbonate-OM isotope coupling resumes. The seepage of petroleum from subsurface source rocks as a major source flux of marine carbon expelled over hundreds of thousand to millions of years has been proposed previously to explain significant perturbations to $\delta^{13}C_{carb}$ isotope records for the Paleocene/Eocene transition (Kroeger & Funnell, 2012). The protracted release of a vast pool of reduced carbon into the ocean in the middle Ediacaran may have produced a redox barrier that suppressed the diversification and expansion of Metazoa until the Late Ediacaran. If correct that the SE was driven by enhanced carbon fluxes from sedimentary basins, it suggests that this mechanism was capable of driving substantial carbon cycle perturbations in Earth's past.

6. Conclusions

We report the first detailed record of compound-specific carbon isotopes on the two major resolvable series of hydrocarbon compounds in extracts from thermally well-preserved sedimentary rocks through the Shuram excursion. During the excursion, organic carbon pools are strongly decoupled (by up to 12‰ in separated organic carbon

phases) followed by recovery through the upper Shuram Formation. In light of the partial deconvolution of carbon isotopic signatures of individual organic constituents, we are able to observe two very distinct compositions contributing to $\delta^{13}C_{org}$ as well as a larger absolute magnitude excursion in $\delta^{13}C_{org}$ than previously described, despite the offset in timing between the isotopic excursions in $\delta^{13}C_{carb}$ and $\delta^{13}C_{org}$. We consider the profiles of the light end member of $\delta^{13}C_{org}$ after deconvolution as a reliable record for assessing the magnitude of primary carbon isotope excursions, therefore identifying the major organic matter source inputs is critical toward this evaluation. The excursion in alkanes is at least 5‰ from measured $\delta^{13}C$ values but realistically in the range of 7-12‰ from isotopic fractionations associated with going from bulk $\delta^{13}C$ values to individual saturated hydrocarbons. We propose that a significant contribution of a more ^{13}C-enriched pool of organic matter, possibly reflecting heterotrophic microbial biomass and associated DOM fuelled by sub-surface petroleum seepage, buffered the measured $\delta^{13}C_{org}$ and accounts for the well recognised decoupling of inorganic and bulk organic carbon isotopic signatures during the peak of the Shuram excursion.

References

Ader, M., Macouin, M., Trindade, R. I. F., Hadrien, M-H., Yang, Z., Sun, Z., and Besse, J. 2009. A multilayered water column in the Ediacaran Yangtze platform? Insights from carbonate and organic matter paired δ^{13}C. *Earth and Planetary Science Letters* **288**, 213-227.

Al-Marjeby A., and Nash, D. F.1986. A summary of the geology and oil habitat of the Eastern Flank hydrocarbon province of South Oman. *Marine and Petroleum Geology* **3**, 306-314.

Allan, J., and Matthews, R. 1982. Isotope signatures associated with early meteoric diagenesis. *Sedimentology* **29**, 797-817.

Arthur, M. A., Dean, W. E., and Claypool, G. E. 1985. Anomalous ^{13}C enrichment in modern marine organic carbon. *Nature* **315**(6016), 216-218.

Bergmann, K. D., Zentmyer, R. A., and Fischer, W. W. 2011. The stratigraphic expression of a large negative carbon isotope excursion from the Ediacaran Johnnie Formation, Death Valley. *Precambrian Research* **188**, 45-56.

Birgel, D., Himmler, T., Freiwald, A., and Peckmann, J. 2008. A new constrain on the antiquity of anaerobic oxidation of methane: Late Pennsylvanian seep limestones from southern Namibia. *Geology* **36**, 543-546.

Bjerrum, C. J., and Canfield, D. E. 2011. Towards a quantitative understanding of the late Neoproterozoic carbon cycle. *Proceedings of the National Academy of Sciences of the United States of America* **108**(14), 5542-5547.

Bowring, S. A., Grotzinger, J. P., Condon, D. J., Ramezani, J., Newall, M., and Allen, P. A. 2007. Geochronological constraints on the chronostratigraphic framework of the Neoproterozoic Huqf Supergroup, Sultanate of Oman. *American Journal of Science* **307**, 1097-1145.

Bradley, D. C. 2008. Passive margins through earth history. *Earth-Science Reviews* **91**, 1 26.

Brocks, J. J., Buick, R., Logan, G. A., and Summons, R. E. 2003. Composition and syngeneity of molecular fossils from the 2.78 billion-year-old Mount Bruce Supergroup, Pilbara Craton, Western Australia. *Geochimica et Cosmochimica Acta* **67**(22), 4289-4319.

Buggisch, W., and Mann, U. 2004. Carbon isotope stratigraphy of Lochkovian to Eifelian limestones from the Devonian of central and southern Europe. *International Journal of Earth Sciences* **93**(4), 521-541.

Burns, S. J., and Matter, A. 1993. Carbon isotopic record of the latest Proterozoic from Oman. *Eclogae Geologicae Helvetiae* **86**, 595-607.

Calver, C. R. 2000. Isotope stratigraphy of the Ediacaran (Neoproterozoic III) of the Adelaide Rift Complex, Australia, and the overprint of water column stratification. *Precambrian Research* **100**(1-3), 121-150.

Derry, L.A. 2010. On the significance of $\delta^{13}C$ correlations in ancient sediments. *Earth and Planetary Science Letters* **296**, 497-501.

Des Marais, D. J., Strauss, H., Summons, R. E., and Hayes, J. M. 1992. Carbon isotope evidence for the stepwise oxidation of the Proterozoic environment. *Nature* **359**, 605-609.

Fike, D. A., Grotzinger, J. P., Pratt, L. M., and Summons, R. E. 2006. Oxidation of the Ediacaran Ocean. *Nature* **444**, 744-747.

Freeman, K. H., Hayes, J. M., Trendel, J-M., and Albrecht, P. 1990. Evidence from carbon isotope measurements for diverse origins of sedimentary hydrocarbons. *Nature* **343**, 254-256.

Grosjean, E., Love, G. D., Stalvies, C., Fike, D. A., and Summons, R. E. 2009. Origin of petroleum in the Neoproterozoic-Cambrian South Oman Salt Basin. *Organic Geochemistry* **40**, 87-110.

Grotzinger, J. P., Fike, D. A., and Fischer, W. W. 2011. Enigmatic origin of the largest known carbon isotope excursion in Earth's history. *Nature Geoscience* **4**, 285 292.

Halverson, G. P., Dudás, F. Ö., Maloof, A. C., and Bowring, S. A. 2007. Evolution of the $^{87}Sr/^{86}Sr$ composition of Neoproterozoic seawater. *Palaeogeography, Palaeoclimatology, Palaeoecology* **256**, 103–129.

Hayes, J. M., Freeman, K. H., Popp, B. N., and Hoham, C. H. 1990. Compound-specific isotope analyses: A novel tool for reconstruction of ancient biogeochemical processes. *Organic Geochemistry* **16**(4-6), 1115-1128.

Höld, I. M., Schouten, S., Jellema, J., and Sinninghe Damsté, J. S. 1999. Origin of free and bound mid-chain methyl alkanes in oils, bitumens and kerogens of the marine

Infracambrian Huqf Formation (Oman). *Organic Geochemistry* **30**(11), 1411 1428.

Husson, J. M., Maloof, A. C., Schoene, B., Chen, C. Y., and Higgins, J. A. 2015. Stratigraphic expression of Earth's deepest $\delta^{13}C$ excursion in the Wonoka Formation of South Australia. *American Journal of Science* **315**, 1-45.

Huuse, M., Jackson, C. A-L., Van Rensbergen, P., Davies, R. J., Flemings, P. B., and Dixon, R. J. 2010. Subsurface sediment remobilization and fluid flow in sedimentary basins: an overview. *Basin Research* **22**, 342-360.

Johnston, D. T., Macdonald, F. A., Gill, B. C., Hoffman, P. F., and Schrag, D. P. 2012. Uncovering the Neoproterozoic carbon cycle. *Nature* **483**, 320-324.

Jones, D. S., Creel, R. C., Rios, B., and Santiago Ramos, D. P. 2014. Chemostratigraphy of an Ordovician-Silurian carbonate platform: $\delta^{13}C$ records below glacioeustatic exposure surfaces. *Geology* **43**, 59-62.

Kaufman, A. J., Corsetti, F. A., and Varni, M. A. 2007. The effect of rising atmospheric oxygen on carbon and sulfur isotope anomalies in the Neoproterozoic Johnnie Formation, Death Valley, USA. *Chemical Geology* **237**(1-2), 47-63.

Knauth, L. P., and Kennedy, M. J. 2009. The late Precambrian greening of the Earth. *Nature* **460**(6), 728-732.

Knoll, A. H., Hayes, J. M., Kaufman, A. J., Swett, K., and Lambert, I. B. 1986. Secular variation in carbon isotope ratios from upper Proterozoic successions of Svalbard and east Greenland. *Nature* **321**, 832-838.

Kroeger, K. F., and Funnell, R. H. 2012. Warm Eocene climate enhanced petroleum generation from Cretaceous source rocks: A potential climate feedback mechanism? *Geophysical Research Letters* **39**, 1-6.

Kump, L. R. 2014. Hypothesised link between Neoproterozoic greening of the land surface and the establishment of an oxygen-rich atmosphere. *Proceedings of the National Academy of Sciences of the United States of America* **111**(39), 14062 14065.

Lee, C., Fike, D. A., Love, G. D., Sessions, A. L., Grotzinger, J. P., Summons, R. E., and Fischer, W. W. 2013. Carbon isotopes and lipid biomarkers from organic-rich facies of the Shuram Formation, Sultanate of Oman. *Geobiology* **11**(5), 406-419.

Lee, C., Love, G. D., Fischer, W. W., Grotzinger, J. P., and Halverson, G. P. 2015. Marine organic matter cycling during the Ediacaran Shuram excursion. *Geology* **43**(12), 1103-1106.

Le Guerroué, E., Allen, P. A., and Cozzi, A., 2006. Chemostratigraphic and sedimentological framework of the largest negative carbon isotopic excursion in Earth history: The Neoproterozoic Shuram Formation (Nafun Group, Oman). *Precambrian Research* **146**, 68–92.

Li, C., Peng, P., Sheng, G., Fu, J., and Yan, Y. 2003. A molecular and isotopic geochemical study of Meso- to Neoproterozoic (1.73–0.85 Ga) sediments from the Jixian section, Yanshan Basin, North China. *Precambrian Research* **125**, 337-356.

Logan, G. A., Summons, R. E., and Hayes, J. M. 1997. An isotopic biogeochemical study of Neoproterozoic and Early Cambrian sediments from the Centralian Superbasin, Australia. *Geochimica et Cosmochimica Acta* **61**(24), 5391-5409.

Love, G. D., Bowden, S. A., Summons, R. E., Jahnke, L. L., Snape, C. E., Campbell, C. N., and Day, J. G. 2005. An optimised catalytic hydropyrolysis method for the rapid screening of microbial cultures for lipid biomarkers. *Organic Geochemistry* **36**, 63-82.

Love, G. D., Stalvies, C., Grosjean, E., Meredith, W., Snape, C. E. 2008. Analysis of molecular biomarkers covalently bound within Neoproterozoic sedimentary kerogen. In: *From Evolution to Geobiology: Research Questions Driving Paleontology at the Start of a New Century*. (eds. Kelley, P. H., and Bambach, R. K.). Paleontological Society Papers, Paleontological Society Short Course, October **4**, 14.

Macdonald, F. A., Strauss, J. V., Sperling, E. A., Halverson, G. P., Narbonne, G. M., Johnston, D. T., Kunzmann, M., Schrag, D. P., and Higgins, J. A., 2013. The stratigraphic relationship between the Shuram carbon isotope excursion, the oxygenation of Neoproterozoic oceans, and the first appearance of the Ediacara biota and bilaterian trace fossils in northwestern Canada. *Chemical Geology* **362**, 250-272.

McFadden, K. A., Huang, J., Chu, X., Jiang, G., Kaufman, A. J., Zhou, C., Yuan, X., Xiao, S. 2008. Pulsed oxidation and biological evolution in the Ediacaran Doushantuo Formation. *Proceedings of the National Academy of Sciences of the United States of America* **105**(9), 3197-3202.

McKenzie, N. R., Hughes, N. C., Gill, B. C., and Myrow, P. M., 2014. Plate tectonic influences on Neoproterozoic-early Paleozoic climate and animal evolution. *Geology* **42**, 127–130.

Melim, L. A., Swart, P. K., and Eberli, G. P., 2004. Mixing-zone diagenesis in the subsurface of Florida and the Bahamas. *Journal of Sedimentary Research* **74**(6), 904-913.

Oehlert, A. M., and Swart, P. K. 2014. Interpreting carbonate and organic carbon isotope covariance in the sedimentary record. *Nature Communications* **5**, 1-7.

Oehlert, A. M., Lamb-Wozniak, K. A., Devlin, Q. B., Mackenzie, G. J., Reijmer J. J. G., and Swart, P. K. 2012. The stable carbon isotopic composition of organic material in platform derived sediments: implications for reconstructing the global carbon cycle. *Sedimentology* **59**(1), 319-335.

Pawlowska, M. M., Butterfield, N. J., and Brocks, J. J. 2013. Lipid taphonomy in the Proterozoic and the effect of microbial mats on biomarker preservation. *Geology* **41**(2), 103-106.

Pearson, A., and Eglinton, T. I. 2000. The origin of *n*-alkanes in Santa Monica Basin surface sediment: a model based on compound-specific $\Delta^{14}C$ and $\delta^{13}C$ data. *Organic Geochemistry* **31**(11), 1103-1116.

Rothman, D. H., Hayes, J. M., Summons, R. E. 2003. Dynamics of the Neoproterozoic carbon cycle. *Proceedings of the National Academy of Sciences of the United States of America* **100**(14), 8124-8129.

Scott, R. W., Formolo, M., Rush, N., Owens, J. D., and Oboh-Ikuenobe, F. 2013. Upper Albian OAE 1d event in the Chihuahua Trough, New Mexico, U.S.A. *Cretaceous Research* **46**, 136-150.

Schrag, D. P., Higgins, J. A., Macdonald, F. A., and Johnston, D. T. 2013. Authigenic carbonate and the history of the global carbon cycle. *Science* **339**(6119), 540-543.

White, H. K., Xu, L., Hartmann, P., Quinn, J. G., and Reddy, C. M. 2013. Unresolved complex mixture (UCM) in coastal environments is derived from fossil sources. *Environmental Science & Technology* **47**(2), 726-731.

Young, G. M. 2013. Evolution of Earth's climatic system: Evidence from ice ages, isotopes, and impacts. *GSA Today* **23**(10), 4-10.

CHAPTER FOUR

Incorporation of lipid biomarkers into microbial mat proto-kerogens during sedimentary diagenesis

ABSTRACT

Microbial mat environments—modern analogues for the earliest microbial ecosystems on Earth—host diverse, layered, microbial communities. During diagenesis of organic matter in the water column and at the sediment-water interface, recalcitrant biomolecules such as lipids and pigments get incorporated into a complex, macromolecular matrix known as proto-kerogen (unconsolidated) or kerogen (consolidated) and, methodologically, constitutes the insoluble residual solid after extraction using organic solvents. This is usually the most abundant organic phase in modern sediment and ancient rocks. We performed catalytic hydropyrolysis on pre-extracted IMOM residues from microbial mat cores from two salt ponds of different salinity from Guerrero Negro, Baja California, Mexico. Hydropyrolysates from both mat cores preserve a diverse and abundant suite of hydrocarbon biomarkers with depth and are bound through strong covalent linkages that occur very early during diagenesis. A variety of polycyclic biomarkers classes, such as steranes and hopanes, can be sequestered and preserved within the mat sediment IMOM beneath the extant photosynthetic layers from the earliest stages of sedimentary diagenesis. As these compounds will eventually be regenerated as hydrocarbon equivalents through increasing burial with time, this study provides an

excellent opportunity to investigate actualistic taphonomy in times of geologic past where benthic microbial mat signals made significant contributions to preserved organic matter.

1. Introduction

Benthic microbial mats with diverse prokaryotic communities were prevalent in the Precambrian, particularly prior to the appearance of bilaterian Metazoa in the late Ediacaran. Elucidating the compositional diversity of prokaryotic communities can be difficult due to fossilisation biases based on size and morphology. Characterisation of modern hypersaline microbial communities may provide significant insights into the biological dynamics in past hypersaline ecosystems, e.g., 3.45 Ga Warrawoona Group of western Australia, the 800 Ma Amadeus Basin of the Centralian Superbasin, and the late-Neoproterozoic-Cambrian Salt Ranges of Pakistan. Due to an interest in understanding the diversity and ecology of aquatic Precambrian communities, an abundance of published research on the sedimentology, microbiology and organic geochemistry of modern hypersaline mats exists and allows for comparisons to be made with ancient equivalents. Thus far, only few comprehensive, integrated studies (e.g., Oehler *et al*., 1979; McKirdy & Kantsler, 1980; Schinteie, 2011; Schinteie & Brocks, 2014) have been undertaken to understand the dynamics of hypersaline ecosystems in the Proterozoic to early Cambrian. Hence it is unsurprising the gaps in knowledge that currently exist in microbial community compositions and the associated biogeochemical interactions that occurred during this dynamic period in Earth's history. The Exportadora del Sal, S. A.

(ESSA) saltern in Guerrero Negro (GN), Mexico is an example of one of the most well-studied modern hypersaline microbial ecosystems in the world (e.g., Des Marais, 1991; Des Marais, 2003; Spear *et al.*, 2004; Ley *et al.*, 2006; Orphan *et al.*, 2008). ESSA represents a modern analogue for investigating and understanding ancient hypersaline microbial ecosystem dynamics, as well-preserved evaporitic microbial assemblages and silicified stromatolites have significantly improved our knowledge of Archean and Precambrian paleobiology (e.g., Knoll, 1985; Shen & Buick, 2004). Although GN mats are non-lithifying, characteristics such as salinity and sedimentation rate (Des Marais *et al.*, 1992) offer insights into the production and preserved of organic matter over the course of diagenesis that are directly relevant to the interpretation of fossilised mat counterparts (stromatolites).

Lipid biomarkers (Chapter 1) reflect the enormous compositional and phylogenetic diversity of the GN microbial mat ecosystem including inputs from all three domains of life. Examples of organic molecules from this mat include cyanobacterial hydrocarbons, terpenoids such as eukaryotic sterols and prokaryotic bacteriohopanepolyols (BHPs), chlorophyll and accessory carotenoid pigments from photosynthesising organisms, and archaeal ether lipids such as archaeol. It contains an abundance of lipids from various phototrophic microorganisms found in three distinct layers. Two microbial mats collected from different sites at GN present contrasting salinity regimes. At lower salinity (*ca*. 8-9 wt%), *Microcoleus chthonoplastes* are the dominant cyanobacteria and at higher salinity (*ca*. 13-17 wt%), and switches to halotolerant cyanobacterial communities including *Halospirulina*, *Phormidium*, and

Euhalothece (Des Marais *et al*., 1992; Nübel *et al*., 2000). The surface of the *Microcoleus* mat comprises a *ca*. 0.5 mm orange-brown layer of unicellular cyanobacteria and diatoms; below this layer is a thicker (1 mm) green layer of filamentous cyanobacteria and filamentous anoxygenic phototrophs of green non-sulfur bacteria; followed by a thin (<0.5 mm) purple layer with dominantly anoxygenic purple sulfur phototrophs. A large number of compound classes have been identified in the GN mats, including hydrocarbons, cyclic isoprenoids, pigments, and ether lipids (see Table 4.1 for a summary).

Table 4.1. Summary of the major compounds that contribute to the rich diversity of total lipids in the GN microbial mats of Baja California, Mexico.

Compound	Examples	Precursor(s)	References
Alkanes	Eicosane, 7-hexamethyl decane, 6-heptadecane, octadecane	Cyanobacteria, archaea, methanogens	Jahnke *et al*., 2008; Orphan *et al*., 2008
Sterols	C_{27}-C_{29} unsaturated sterols	Eukaryotes (diatoms)	Conte *et al*., 1994
Hopanols	Bacteriohopanepolyols, C_{32} bishomohopanols	Cyanobacteria, proteobacteria	Jahnke *et al*., 1992; Summons *et al*., 1999
Pigments	Myxoxanthophyll, β-carotene, fucoxanthin, γ-carotene, zeaxanthin, echinenone, bacteriochlorophyll a, c	Diatoms, green sulfur bacteria, cyanobacteria	Palmisano *et al*., 1989
Ether lipids	Mono- and dialkyl glycerol ethers (MAGE-/DAGE), archaeol	Bacteria, archaea	Koga & Morii, 2007; Jahnke *et al*., 2008

The abundance and diversity of lipids in the GN microbial mats allows us to accurately identify the major source inputs into this system. Another advantage of this diversity is that many lipids found in GN mats are excellent biomarkers for a variety of

microorganisms that are well represented in the ancient sedimentary record as identifiable fossil hydrocarbon equivalents.

Here we present a comparison of lipid biomarker profiles from two microbial mat cores sourced from two different salt ponds at Guerrero Negro, with one core representing a lower salinity depositional environment with contrasting microbial populations to a higher salinity core. We compare the extractable lipid biomarkers to the pre-extracted residue compounds associated with proto-kerogen released *via* kerogen hydropyrolysis.

2. Geological setting

The Exportadora del Sal S. A. (ESSA) saltern of Guerrero Negro (Baja California Sur, Mexico) lies within a typical sabhka environment adjacent to Laguna Ojo de Liebre. Figure 4.1 shows the spatial extent of the 13 major ponds of the ESSA system. Precipitation ranges from 1.5-12 mm/year and no groundwater enters the pond system due to lying above the local hydrologic gradient. The GN ponds thrive under well-monitored and stable conditions with steady state accretion and degradation of mat layers (around 0.5 – 1.4 cm per year). Organic mats typically attain up to 10 cm in thickness, depending on the location, which represents about 60 years of growth since these ponds were established. Sedimentation rate is rapid in these non-lithifying and non-mineralising mats, 1-1.5 cm per year (Palmisano *et al*., 1989; Des Marais *et al*., 1992). This environment is ideal for investigating *in situ* lipid preservation and diagenesis without the

influence of constantly changing physical parameters. Unpolluted seawater evaporates and flows through the pond sites, with the numbering of each site corresponding to the direction of brine flow—shown by the red arrows in Figure 4.1. Water temperatures are 22-29°C and vary between 14°C and 22°C for the summer and winter, respectively, and air temperatures are 20-32°C and vary between 8°C and 24°C for the summer and winter, respectively (Des Marais, 2010). The wind blows in the W-NW direction at 5 m/s, though this varies seasonally. Both these sampling sites are on the windward side of their respective ponds, thereby minimising the exogenous microbial debris input and maximising the fraction of organic matter input from local primary productivity. The pond system is fed by seawater from the local laguna and the salinity of each site increases (while temperature increases and pH decreases) with distance from Pond 1— values in blue in Figure 4.1 with units in %. Ponds 4, 5, and 6 are dominated by thick microbial mat communities, thus the focus of this study are cores from Pond 4 near the dike it shares with Pond 5 (P4n5—Pond 4 near 5) and Pond 5A near the dike it shares with Pond 5B (P5AB—Pond 5A near 5B), indicated by black stars in Figure 4.1. Both ponds are about 15 km apart, permanently submerged in 0.5-1 m of overlying brine, and host the thickest microbial mats.
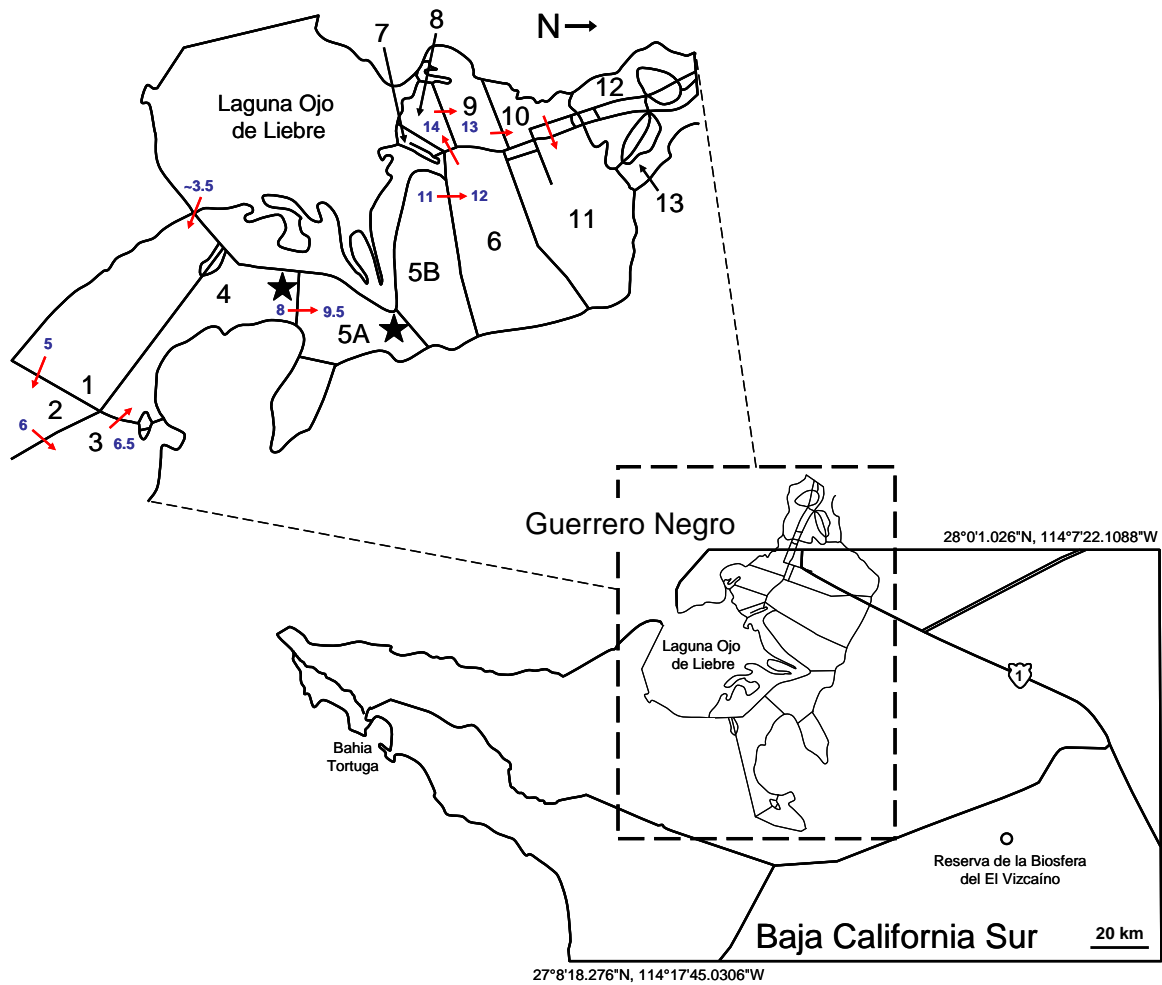
Figure 4.1. Map of Guerrero Negro pond system (inset) located in Baja California Sur, Mexico with ponds numbered 1 through 13. The black stars represent the sampling locations of P4n5 (left star) and P5AB (right star) – see text for description. The red arrows indicate the direction of brine flow and blue numbers show average salinity, with units in %.

3. Materials & Methods

3.1 Sample collection and description

P4n5 and P5AB cores were collected as ~9 cm and 6.5 cm fresh cores, respectively (Figure 4.2), by NASA Ames Research Centre in June 2001 and September 2010, respectively from the ESSA saltern at Guerrero Negro, Baja California Sur, Mexico. The P4n5 core (9-9.1% salinity, water temperature 25°C, pH 8.62) was taken from Pond 4 near 5 (Figure 4.1) and sub-divided into 11 layers (Figure 4.2A and Table 4.2). Layers 1 through 4 range from 2-6 mm in total thickness, whereas layers 7 through 11 are 10 mm thick. The P5AB core (11.2% salinity, water temperature 26.2°C, pH 8.04) was taken from Pond 5A near 5B (Figure 4.1) and sub-divided into 8 layers (Figure 4.2B and Table 4.2). Layers 1 and 2 are 2 mm total thickness and layers 3 through 8 are 10 mm thick. Samples were collected and lyophilised and in preparation of sample residues, mat layers were sectioned, freeze-dried, and powdered. Before analysis, samples were washed using the Klock washing procedure. The Klock washing procedure involves resuspending the mat sediment layer in a solution containing 10 wt% NaCl and homogenising with a Sorvall mixer at high speed for 1 min. The mixture was then centrifuged and the supernatant removed. This procedure typically removes mucilage-like EPS and capsular material, but it does not remove sheath material (Figure 4.3), which is a complex heteropolysaccharide that is more structured than mucilage or slime.
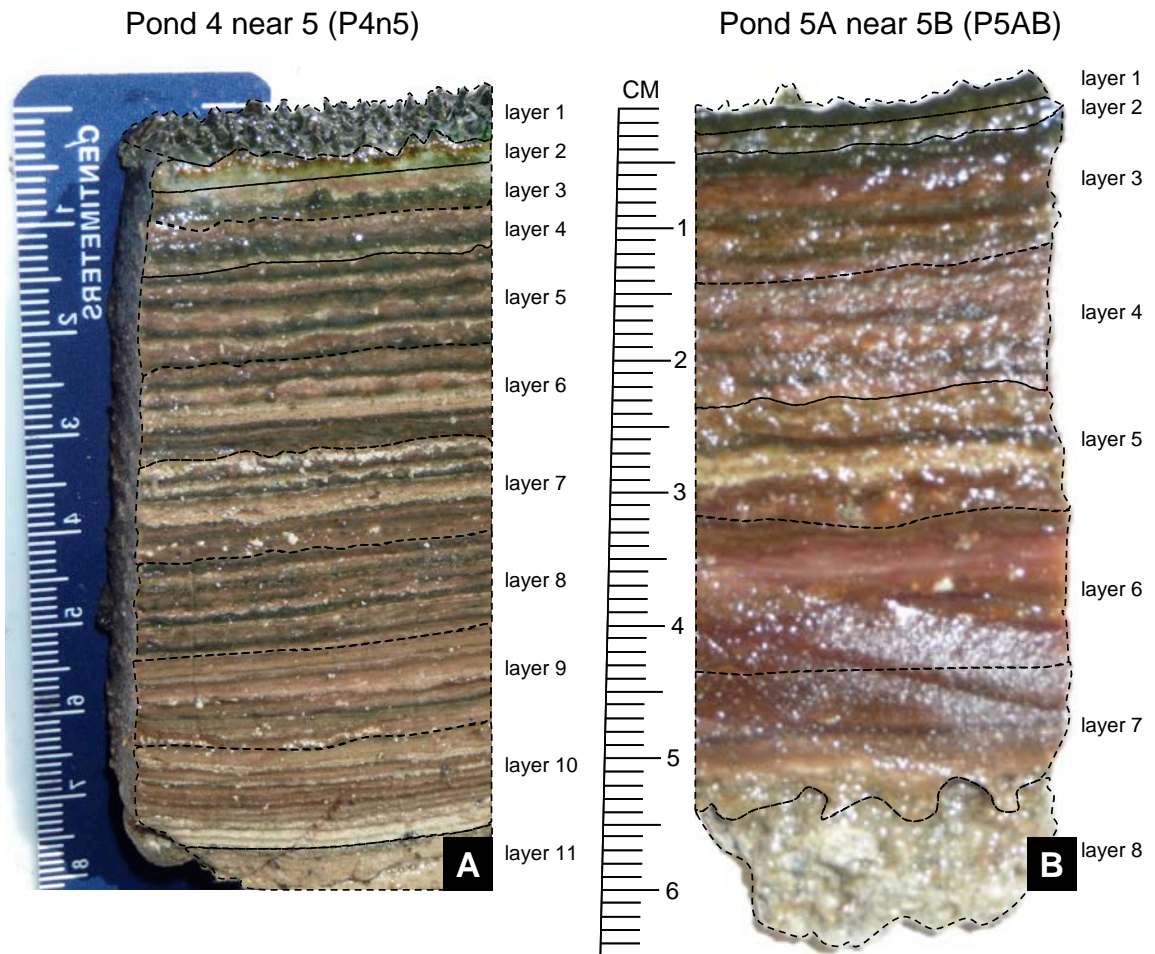
Figure 4.2. Cross section of cores A) Pond 4 near 5 (P4n5) with layers numbered 1 through 11 with blue scale bar on left and B) Pond 5A near 5B (P5AB) with layers numbered 1 through 8 with black scale bar on left. Images courtesy of L. Jahnke and M. N. Parenteau.

110

3.2 Lithological descriptions and chronostratigraphy

The following table lists descriptions of the 11 layers from the P4n5 core and the 8 layers from the P5AB core (Table 4.2). Descriptions are provided based on colour, mineralogical and microbial population assessed from extensive previous analyses (Ley *et al.*, 2006; Des Marais, 2010; Houghton *et al.*, 2014), and textures from visual inspection in hand samples. Additionally, high-resolution images taken with a compound microscope and a dissecting microscope (images courtesy of M. N. Parenteau) to look at the structures in detail, particularly during the treatment to remove EPS (Figure 4.3).
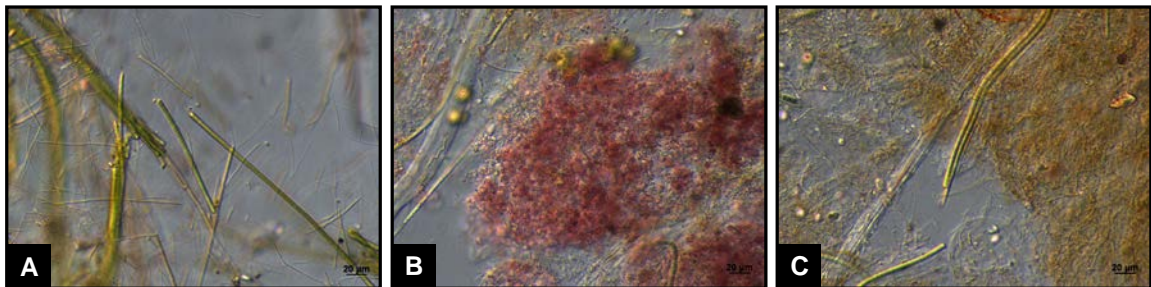
Figure 4.3. P5AB core layers with images taken with a dissecting microscope of A) top layer (layer 1) 1 mm depth; B) upper portion of layer 2 (2-3 mm depth); and C) lower portion of layer 2 (3-4 mm depth). Scale is 20 µm in all images, courtesy of M. N. Parenteau.

Chronostratigraphy

The age of the layers are based on several observations and previous field and laboratory experiments (Des Marais *et al.*, 1992; Canfield & Des Marais, 1993). P4n5 mats dominated by *Microcoleus* were observed to accumulate between 8-12 mm per year,

Table 4.2. Description of each layer analysed in this study. [a]See Section 3.2 for description, age units in years, representing maximum basal age.

Core	Layer	Depth (mm)	Age[a]	Description
P4n5	1	0-2	1	Orange top layer (diatoms), green colour on the underside with gelatinous texture, dominated by filamentous cyanobacteria, *Microcoleus chthonoplastes*
	2	2-5	2	Greenish thin layer, flaky, gelatinous
	3	5-9	4	Orange/beige colour, gelatinous
	4	9-15	8	Darker brown, gelatinous
	5	15-25	13	Orange, brown, and green, gelatinous
	6	25-35	18	Orange/brown colour with collapse laminations, gelatinous
	7	35-45	24	Brown/orange, gelatinous with lower portion first appearance of gravelly texture
	8	45-55	32	Brown/grey, mixed with upper portion (gelatinous), immediate transition to sandy/gravel texture
	9	55-65	42	Darker grey colour, soft sediment, with pyritic sand and some gravel
	10	65-75	Unknown	Grey, soft sediment, pyritic sand, with some gravel
	11	75-85	Unknown	Grey, soft sediment, small pieces of shell material, with some gravel
P5AB	1	0-2	1	Orange/green network, gelatinous, loosely consolidated (Figure 4.4), dominated by filamentous cyanobacteria such as *Halospirulina* and *Phormidium* and coccoid unicellular cyanobacteria *Aphanothece*
	2	2-4	2	Upper portion purple (anoxygenic phototrophs such as purple sulfur bacteria *Chromatium*, forming discrete layers), lower portion green, gelatinous (Figure 4.4)
	3	4-14	5	Beige/brown/tan, gelatinous
	4	14-24	8	Beige/brown/tan, gelatinous
	5	24-34	13	Beige/brown/tan, gelatinous
	6	34-44	18	Brown/tan, gelatinous
	7	44-54	24	Upper portion is beige/light orange and gelatinous, lower portion grey
	8	54-64	Unknown	Grey sediment with lots of gravel

coinciding with a dark green-orange/brown layer pairs typically representing one year of mat accumulation. Lower mat layer experience a thinning with depth which represents mat fabric decomposition as organic diagenesis progresses over time. Mats in pond P5AB accumulated at ~5-10 mm/year and, with increasing salinity, the accumulation rate of organic mat material decreased, e.g., Pond 5 near 6 mats (13% salinity) were recorded to accumulate at 4 mm/year. The age of each layer was based on the above observations and by counting the visible dark green-orange/brown layer pairs in each layer. The ages are uncertain when it comes to layer 9 in P4n5 and layer 7 in P5AB, since layers beneath these are decomposed beyond recognition. The entire sequence of mats is known to growing in these concentration ponds for about 60 years, thus half the original mat layers have been decomposed beyond recognition. The maximum age for P4n5 of the visible layers is approximately 40 years old, and for P5AB, about 25 years old. Although the sedimentation/accumulation rate of organic material is very high, because these mats are non-lithifying, this means the degradation rate is also equally high- more so at the surface due to disruptive wind action. So even though we would expect 10 mm of material to accumulate at the surface in one year, the amount preserved is more likely an order of magnitude lower (1 mm).

3.3 Carbon content and bulk isotopes

Carbon content and bulk carbon isotopes were measured for each layer for both cores, prepared by Mike Kubo at NASA Ames Research Centre. 0.5-1 mg of mat sample

powder was weighed into silver capsules (Costech), wetted with a minimal amount of MilliQ water, fumigated for 6 h with concentrated HCl (Ultrex grade) in a grease-free ground glass desiccator. Samples were dried at 60°C for 12 h and placed into tin capsules. Samples were combusted at 1,000°C on an Elementar vario Micro Cube elemental analyser (EA) coupled to an Isoprime VisION isotope ratio mass spectrometer (irms). All samples were run in triplicate at the Stable Isotope Facility at the University of California, Davis. Four standards (bovine liver SRM 1577b: -21.69‰; Nylon 5: -27.72‰; USGS-41 glutamic acid: -16.65‰; and an artificially-enriched alanine (UCD-Ala): +43.02‰) and blank silver/tin capsules were selected to be compositionally similar to the samples being analysed and run to assess the precision and reproducibility of isotope measurements. TOC was calculated based on the integrated peak area of evolved $CO_{2(g)}$ during the measurement of $\delta^{13}C_{org}$.

3.4 Lipid extraction

3.4.1 Intact Polar Lipids (IPLs)

Bligh-Dyer extraction. All Bligh-Dyer extractions and intact polar lipid separation and analyses were performed by Linda Jahnke in the Exobiology Division laboratories at NASA Ames Research Centre with assistance from Megan Carslon and Niki Parenteau. A schematic of the Bligh-Dyer procedure with subsequent lipid separations is summarised in Figure 4.4. The procedure used is a single phase modification of the Bligh & Dyer procedure (Bligh & Dyer, 1959). In detail, ~1 g of powdered mat layer was

placed into a 10 ml glass centrifuge tube with 4 ml DI H_2O, 10 ml MeOH, and 5 ml of chloroform with mixing and vortexing in between each addition. The sample mixture was sonicated in a warm water bath for 1 h and placed onto a shaker for 1 h. Samples were centrifuged for 10 mins with the supernatant collected in a separate vial. The cell pellet was re-extracted up to three times to ensure complete extraction by repeating the steps mentioned above. 5 ml of chloroform followed by 5 ml of DI H_2O was added to the supernatant extract, capped, and inverted to mix. Samples were placed into the refrigerator and left to settle for a few hours. The organic layer (total lipid extract; TLE) was separated from the aqueous layer and pipetted into a separate vial. The solvent from the TLE was removed under a stream of purified $N_{2(g)}$. The same steps were carried out for all extracts.
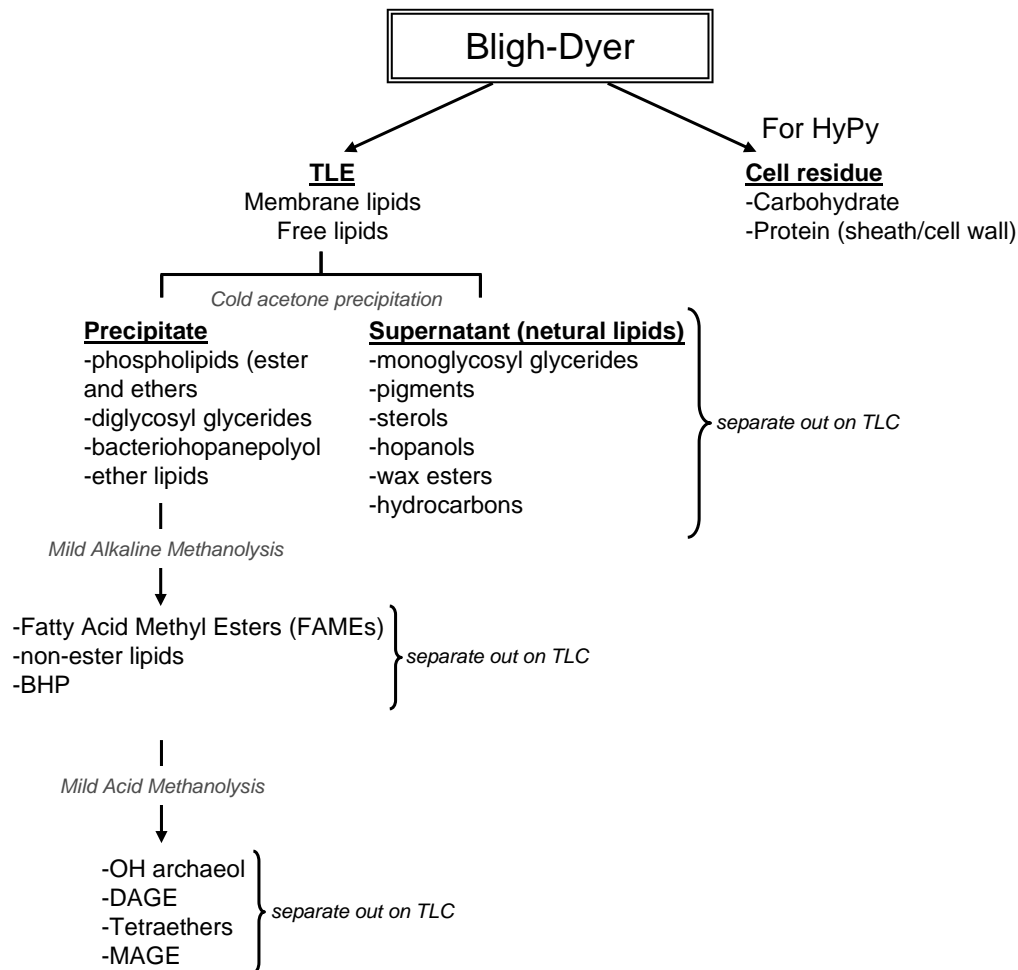
Figure 4.4. Schematic summary different chemical treatments performed on the mat layers outlining the different types of lipids released with each treatment. The Bligh-Dyer treatment is performed on dried mat layer powder, producing a total lipid extract (TLE) and a cell residue portion. Cold acetone precipitation produces a precipitate and a supernatant fraction—with various degrees of chemical treatment available to target specific compound series. BHP = bacteriohopanepolyol, OH archaeol = hydroxyarchaeol, DAGE = dialkyl glycerol ethers, MAGE = monoalkyl glycerol ethers; TLC = thin layer chromatography.

3.4.2 Total lipid extraction and kerogen preparation

~5-10 g of powdered mat sample was extracted by microwave extraction system as described in Section 3.1 of Chapter 2. One layer was re-extracted up to five times until solvent was clear. The residue from this layer was catalyst loaded and pyrolysed with the result being compared to the original pyrolysate residue. There is little compositional difference between the two extraction treatments. Consequently, all samples were extracted once with the microwave extraction system as this proved sufficient.

3.5 Lipid analysis

3.5.1 Analysis of free lipids

All IPL extractions, analyses, and result quantifications were performed at NASA Ames Research Centre in the Exobiology Division laboratories by Linda Jahnke with assistance from Megan Carlson and Niki Parenteau. Polar compounds were analysed on a Waters quadrupole time-of-flight (QTOF) liquid chromatography-mass spectrometry (LC-MS) system in atmospheric pressure chemical ionisation (APCI) mode. Prior to IPL analyses, alcohol and glycerol ethers were derivitised by trimethylsilyl (TMS) by activating 50 µl of 1 : 1 BSTFA (N,O-*bis*(trimethyl-silyl)trifluoroacetamide) : pyridine at 60°C for 1 h, or acetate and run on an HP (5890/5971A) gas chromatograph (GC) coupled to a mass spectrometer (MS). The GC was equipped with a 60 m fused DB-5 ms silica column and He was used as the carrier gas. Compounds were run in full scan mode

and ionised by EI (70 eV). Compounds were quantified using an Agilent 6890 GC interfaced with a flame ionisation detector (FID). Hydrocarbons and fatty acid methyl esters (FAME) were quantified using tricosane and methyltricosanate, respectively, as internal standards and all concentrations are reported in µg/gTOC (ppm TOC).

3.5.2 Analysis of bound lipids *via* kerogen hydropyrolysis (HyPy)

Catalyst synthesis and loading

Catalyst for kerogen hydropyrolysis was synthesised by combining 2 g of ammonium molybdate tetrahydrate $((NH_4)_6Mo_7O_{24} \cdot 4H_2O)$ (Fisher) with 11 ml of ammonium sulfide $((NH_4)_2S)$ (Fisher) in a 40 ml vial. Solution was shaken around to homogenise and then sonicated for 5 mins. Precipitate was filtered under vacuum and rinsed out with DCM, *n*-hexane, and DCM. The dried catalyst was placed into a 4 ml vial and stored in the freezer.

~1-1.5 g of exhaustively pre-extracted mat layer powders were catalyst-loaded with ~4-6 wt% MoS_2 catalyst (Tables A4.1-A4.2). Sample powder was placed into a 500 ml flat-bottomed flask with catalyst dissolved in ~5 ml H_2O : MeOH (4:1, v/v). Capped flat-bottomed flask with catalyst and sample slurry was placed onto the shaker for 40 mins. Solvent was removed from the sample on a RotoVap (Heidolph Laborota 4001 efficient HB digital) with rotation speeds not exceeding 150 rpm and temperatures not exceeding 70°C.

Hydropyrolysis set up

One soxhlet solvent-cleaned (48 h) and pre-combusted (450°C; 2 h) steel wool ball (Grade 1) was placed into a solvent-cleaned steel reactor tube. Catalyst-loaded sample was placed into the reactor. Steel wool twig was placed into the trap with a small amount of pre-combusted (475°C; 9 h) glass wool (Ohio Valley Specialty) and filled with pre-combusted silica gel (Fisher silica gel sorbent, Grade 40, 35-70 mesh).

Experimental conditions

Procedural blanks consisting of silica gel were heated from room temperature to 250°C at 100°C/min up to 450°C at 8°C/min. Microbial mat kerogens were heated from room temperature to 250°C at 100°C/min up to 500°C at 8°C/min. Both blanks and samples were run in a leak-tight (H_2 leak rate not exceeding 5 bar/min at pressure) set up at H_2 pressures not exceeding 150 bars with a flow rate of 4 L/min. For immature sediments, H_2 pressure >100 bars is sufficient for hydrocarbon bond cleavage from kerogen and samples were run in the range of 130-145 bars.

Extraction of kerogen-bound lipids

Pyrolysate was extracted from the trapped silica gel by silica gel column chromatography on large (250 ml) glass columns. The pre-combusted glass columns were plugged with pre-combusted glass wool, ~2 cm thick silica gel (Fisher silica gel sorbent, Grade 40, 35-70 mesh), and topped off with silica gel (Geduran EMD, Grade 60). Sample was poured on to the top of the column and fractionated according to the procedures

outlined previously in Section 3.4 of Chapter 2 to obtain the saturated, aromatic, and polar hydrocarbon fractions, with yields reported in Appendix Table A4.1-A4.2.

Gas Chromatography-Mass Spectrometry (GC-MS)

Samples were analysed using the same methods and run conditions as reported in Section 3.5 of Chapter 2.

Gas Chromatography-Mass Spectrometry Metastable Reaction Monitoring (GC-MS-MRM)

Hopane and sterane biomarkers of the saturated hydrocarbon fractions from P4n5 and P5AB kerogen hydropyrolysates were analysed by GC-MS-MRM on a Micromass AutoSpec Ultima equipped with a HP6890 gas chromatograph and a DB-1MS coated capillary column (60 m × 25 mm i.d., 0.25 µm film thickness) using He as carrier gas. Samples were analysed with a total cycle time of 1.3 s per scan for 24 transitions (Table 4.3). The GC oven was held at 60°C (2 min), heated to 150°C at 10°C/min, further heated to 315°C at 3°C/min and held at final temperature for 24 mins. 50 ng of deuterated C_{29} sterane standard [d_4-ααα-24-ethylcholestane (20R)] was added to quantify the polycyclic biomarker content. Yields assume equal mass spectral response factors between analytes.

Table 4.3. Monitored ion (parent→daughter) channels for steranes and hopanes.

Transition (Da)	Steranes	Transition	Hopanes
358→217	C_{26} steranes	370→191	C_{27}; Tm, 17(β)Tm
372→217	C_{27} steranes	398→191	C_{29} hopanes
386→217	C_{28} steranes	412→191	C_{30} hopanes
400→217	C_{29} steranes	426→205	C_{30} methylhopanes
414→217	C_{30} steranes	426→191	C_{31} homohopanes
414→231	C_{30} methylsteranes	440→205	C_{31} methylhopanes
404→221	d4 internal standard	440→191	C_{32} bishomohopanes
		454→205	C_{32} methylhopanes
		454→191	C_{33} trishomohopanes
		468→205	C_{33} methylhopanes
		468→191	C_{34} tetrakishomohopanes
		482→205	C_{34} methylhopanes
		482→191	C_{35} pentakishomohopanes
		496→205	C_{35} methylhopanes

4. Results & Discussion

4.1 Pond 4 near 5 (P4n5) *versus* Pond 5A near 5B (P5AB)

The following sections describe compositional changes in the carbon isotopes and lipid biomarker profiles from 1) extractable organic matter from intact polar lipid (IPL) analysis from P4n5 and downcore trends between two cores of differing salinity (P4n5 and P5AB). The sections are split into 1) P4n5 IPL results and 2) down core trends for both P4n5 and P5AB cores and a comparison between each. All P4n5 data are represented by light blue diamonds and all P5AB data are represented by orange squares, unless otherwise explicitly stated in the text or in the figure. Fraction yields for P4n5 and P5AB can be found in Appendix Tables A4.1-4.2.

4.1.1 Carbon cycling

4.1.1.1 Total carbon (TC) and total organic carbon (TOC) content

Downcore trends of total organic carbon (TOC) measured in wt% are consistent with the upper layers being the most productive in terms of generating biomass (P4n5: 18.8 wt%; P5AB: 18.1 wt%), with the decreasing trend being a reflection of the remineralisation and/or breakdown during diagenesis over time. Both cores exhibit very similar trends in carbon content with depth (m = 0.94; R^2 = 0.9. Figure 4.5).

4.1.1.2 Carbon isotopes ($\delta^{13}C$)

Carbonate and organic carbon isotopic signatures of marine sediments provide a means to track the cycling of carbon in the ocean, associated with biogeochemical processes such as carbon fixation, respiration, authigenic mineral precipitation, and post-depositional alteration. Bulk total and organic carbon isotopes reported for both cores are similar with depth (Figure 4.5; Appendix Table A4.3) as well as similar to other reports from GN (e.g., Des Marais *et al*., 1989; Bebout *et al*., 2002; Houghton *et al*., 2014), and typically slightly heavier than organic carbon isotope values reported from other well-studied hypersaline microbial mat ecosystems (e.g., Schidlowski *et al*., 1994; Wieland *et al*., 2008). The ^{13}C-enriched values have been invoked to represent $CO_{2(aq)}$ limitation during the formation and deposition of the microbial mat, hence lower fractionations by photosynthesisers, primarily surface cyanobacteria and underlying filamentous

anoxygenic phototrophs (FAPs). P4n5 and P5AB show heavier ^{13}C values for the surface layers (average -9.83‰) and decrease slightly with depth from the decrease in carbon fixation rate going down core. Where the transition between layer 7 and 8 in P4n5 shows a switch to more ^{13}C-enriched values (average -8.66‰ from layers 7-11) likely due to decomposition, the value for layer 8 in P5AB, -12.64‰, follows the decreasing trend.
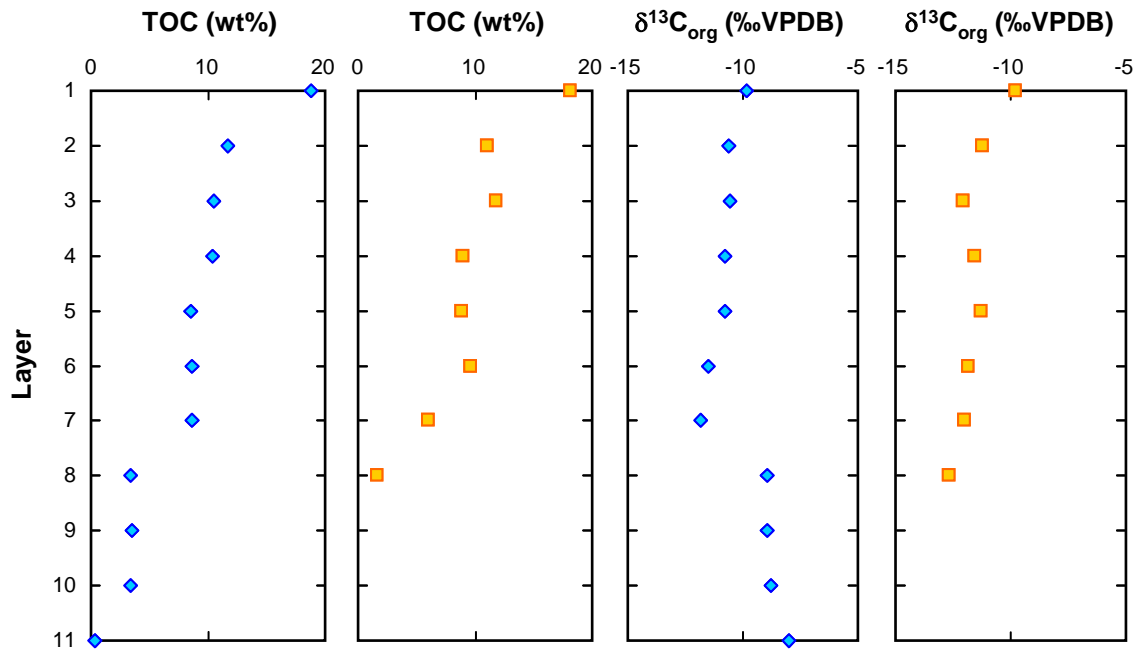
Figure 4.5. Total organic carbon (TOC) in weight percent (wt%) for P4n5 (blue diamonds) and P5AB (orange squares) with depth. Carbon isotope profiles ($\delta^{13}C_{org}$) with depth for P4n5 (blue diamonds) and P5AB (orange squares), with units in ‰ relative to VPDB.

4.1.2 Intact polar lipid (IPL) analyses of P4n5

Cell numbers

In P4n5, cell densities (as measured as cell numbers/volume of sediment in each layer and calculated from the abundance of ester-linked fatty acids (FAs)) decrease exponentially with depth (Figure 4.6; Appendix Table A4.3). Layer 1 contains the highest cell density $(7.6 \times 10^7/\text{mm}^3)$, unsurprisingly as it constitutes the most active layer of microbial activity. Cell densities decrease rapidly going from layer 2 $(4.5 \times 10^7/\text{mm}^3)$, layer 3 $(2.9 \times 10^7/\text{mm}^3)$, up until layer 4 $(1.6 \times 10^7/\text{mm}^3)$. Layers 5 through 11 have low cell counts and range from 0.8 to $0.1 \times 10^7/\text{mm}^3$. Although cell numbers have not yet been measured for the higher salinity P5AB core, the overall cell densities in the surface layer are expected to be high but less so compared to P4n5 due to harbouring a dominantly unicellular cyanobacterial community which have lower cell densities compared with filamentous cyanobacterial populations (Des Marais, 2010).

Cell density (x 10^7/mm³)
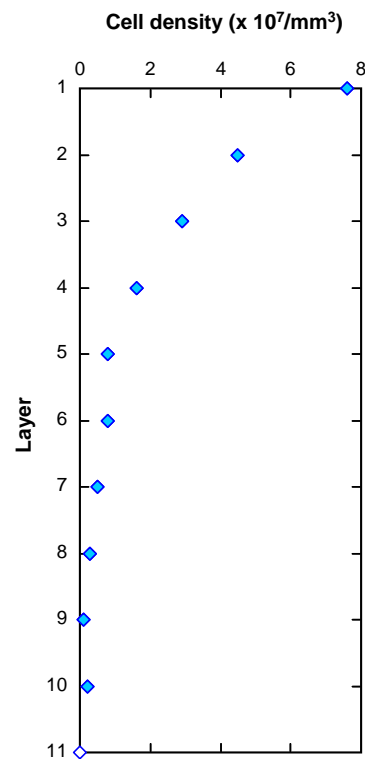
Figure 4.6. Cell densities in P4n5 (calculated from the abundance of extractable ester-linked FAs) with depth. Open symbols represent samples in which cell density was not measured/calculated.

Ester-linked membrane fatty acids (FAs) and fatty acid methyl esters (FAME)

In P4n5, total fatty acid methyl esters (FAME), which include both normal and branched membrane FAs, is highest in layer 1 (20 mg FA ppm TOC) and decreases with depth (Figure 4.7A). The normal monounsaturated FAs (sourced from cyanobacteria) dominate the total amount recovered in layers 1, 2, and 3 (decreasing slightly from ~10

mg FA ppm TOC in layer 1 to 4.4 mg FA ppm TOC in layer 3; Figure 4.7B). Polyunsaturated FAs (sourced from proteobacteria) are the next most abundant compound class in layers 1 and 2, but decreases rapidly after layer 3 to negligible values in layers 9, 10, and 11 (Figure 4.6C). Long chain (nC_{22}-nC_{32}) FAs with even-over-odd predominance (EOP) increase steadily with depth throughout the core, starting with 0.1 mg FA ppm TOC in layer 1, with a marked increase from layer 7 onwards (Figure 4.7D). However, the biological source(s) of LCFAs remains unknown. Branched FAs (Figure 4.7H) recovered include iso- (2-methyl) (Figure 4.7E), anteiso- (3-methyl) (Figure 4.7F), mid-chain (Figure 4.7G), and vinyl ether dimethylacetals. Iso- and anteiso-(*Bacteriodetes*), 10Me16:0 (10-methylhexadecanoic acid), and 10Me18:0 (10-methyloctadecanoic acid from sulfate reducing bacteria, SRB) but increase with depth, possessing maxima at layer 4. 2Me-FAs (Figure 4.7G), which are likely derived from environmental mycobacteria although there are limited literature reports, are ester-linked. C_{17}-C_{24} 2-Me and 2,X-diMe FAs (where X is an unknown methyl branching position in the chain) are absent in the top 3 layers, but increase with depth to a maxima at layer 7, followed by a decrease in layer 8, and onwards to negligible values in layers 9, 10, and 11. Vinyl ether (VE) dimethylacetals are characteristic of Gram positive anaerobes such as *Clostridia* (Goldfine & Panos, 1971). Structurally, dimethylacetals are derived from plasmalogen lipids, hence they possess one ester and one VE linkage. They are low in abundance in the surface layers and throughout most of the core, but begin to increase at layer 9 with maximal concentration in layer 10 (Figure 4.7H).
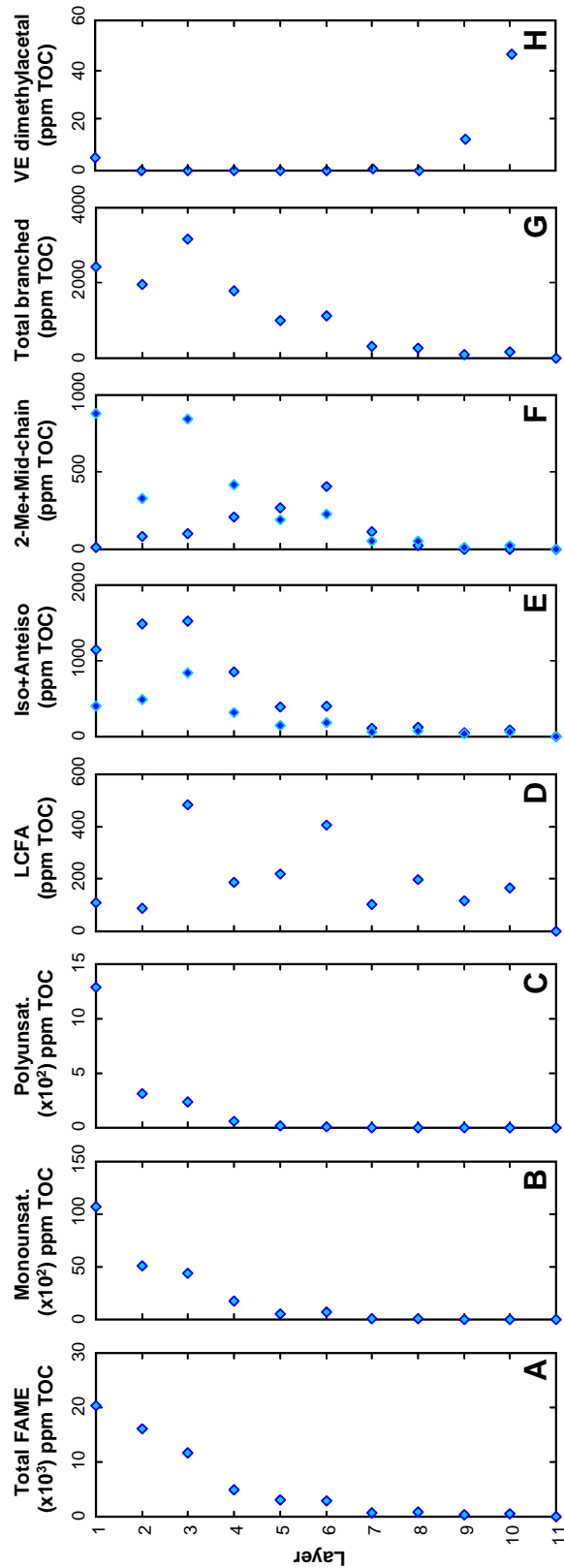
Figure 4.7. P4n5 abundance profiles from extractable IPLs of A) Total fatty acid methyl ester (FAME) concentration in $\times 10^3$ ppm TOC; B) Monounsaturated fatty acids (FA) in $\times 10^2$ ppm TOC; C) Polyunsaturated FAs in $\times 10^2$ ppm TOC; D) Long-chain fatty acids (LCFAs) in ppm TOC; E) Iso (light blue filled) and anteiso (dark blue filled) FAs in ppm TOC; F) 2-methyl FAs (dark blue filled) and mid-chain FAs (light blue filled) in ppm TOC; G) Total branched FAs in ppm TOC; and H) Vinyl ether (VE) dimethylacetals in ppm TOC. Appendix Table A4.4a

126

Alkanes

The mild BBr_3 cleavage procedure releases both normal (*n*) and methyl-branched (Me-) short-chain (nC_{12}-nC_{20}) and long-chain (nC_{21}-nC_{34}) alkanes, though generally in the C_{12}-C_{30} range for *n*-alkanes. Alkane chromatograms are dominated by nC_{17} and $nC_{17:1}$, which are probably sourced from cyanobacteria and surface layers show high nC_{17} and nC_{19}, as expected. Sedimentary layers, e.g., layer 6, shows the characteristic even-over-odd (EOP) predominance with nC_{16} and nC_{18} being the dominant carbon numbers. Additionally, abundant unsaturated, alkylated, branched, cyclic, and acyclic alkane isomers were recovered following mild alkaline methanolysis (solely recovering ester-linked FAs) and acid methanolysis (which methylate any free FAs) treatments. *N*-alkanes are not recovered in layers following layer 7 (i.e., 8-11) and are even not well represented in layer 7 itself. Hydrocarbons in these lower layers are predominantly acyclic isoprenoids.

Isoprenoids

In addition to releasing alkanes, a variety of isoprenoids were released by the BBr_3 method. Examples of isoprenoids isolated include: regular acyclic isoprenoids such as iC_{19} (pristane), $iC_{19:1}$ (pristene) iC_{20} (phytane), $iC_{20:1}$ (phytene), regular iC_{25}, $iC30:1$ and various isomers, iC_{40}, and regular cyclic iC_{40} (Figure 4.8; Appendix Table A4.4b). The concentration of pristane and phytane are low in the surface layer and at the bottom, but exhibit a zone of elevated concentrations in the middle layers (5 and 7; Figure 4.8A; Figure 4.8B). Multiple phytene (4 resolvable) isomers are abundant in the upper layers

but disappear with depth (Figure 4.8C). Hopanoic acids (Figure 4.11) and phytanate (as well as other short-chain isoprenoid acids) were released during the mild alkaline methanolysis treatment followed by a moderate acid methanolysis. Highly branched isoprenoids as C_{20} HBI sourced from diatoms (HBI; Yon's compound) is absent/very low in the surface layer and increases substantially with depth with maximum concentration in layer 7 (Figure 4.8D). Squalene (and its isomers) were detected in surface layers and then decreases with depth (Figure 4.8E) Mono- (MAGE) and dialkyl glycerol ethers (DAGE) were detected (in a 10 : 1 ratio) as well as archaeol (Arc; Figure 4.8F). However, hydroxyarchaeol (OH-Arc) was tentatively identified in the lower layers, but further analysis would be needed to confirm its presence (Figure 4.8F). Pentamethyleicosane (PME or PMI), which is an irregular tail-to-tail linked isoprenoid characteristic of methanogenic/methanotrophic (AOM consortia) archaea, was not found in these samples.
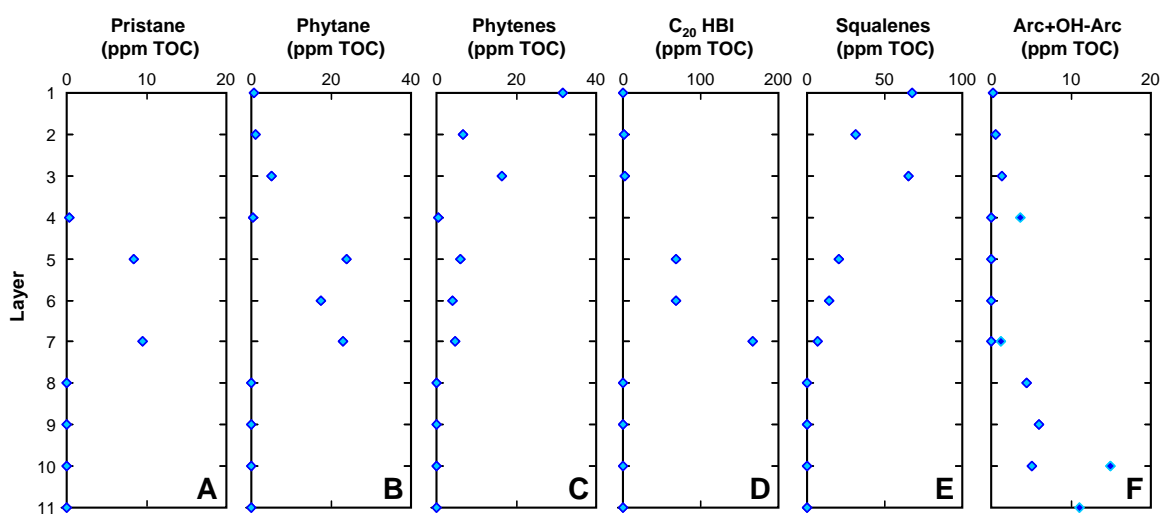
Figure 4.8. P4n5 abundance profiles from extractable IPLs of A) pristane; B) phytane; C) Sum of phytene isomers; D) C_{20} highly branched isoprenoid (HBI—Yon's compound); E) Sum of squalene isomers; and F)

Archaeol (Arc; light blue filled) and tentative hydroxyarchaeol (OH-Arc; dark blue filled). All units in ppm TOC.

Tricyclic terpenes

Tricyclic terpene isomers, tentatively identified based on elution position and published literature spectra, elute after sterenes in the hydrocarbon fraction. The major compound is $C_{20:1}$ (5 isomers) with minor contributions from $C_{20:2}$ and possibly $C_{21:1}$. These are absent in layer 1, with a small amount (4.2 ppm TOC) in layer 2, with maximal concentrations in layer 6 (40 ppm TOC), and decline in layer 7. In layer 8 and below, these compounds were not detected (Figure 4.10A; Appendix Table A4.4c).

Sterols

Sterols as intact polar lipids are present primarily as dehydrated functionalised alcohols (stanols such as C_{27} cholestanol, C_{28} ergostanol, C_{29} stigmastanol, and C_{30} 24-*n*-propylcholestanol), but also exists as (partially) reduced sterenes and steranes (Figure 4.9; Appendix Table A4.4d). In P4n5, sterols (referring to C_{27}-C_{30} stanols) are low in layers 1 and 2, only becoming prominent in layer 3, where stigmastanol reaches 773 ppm TOC – the most abundant extractable sterol throughout the whole mat core (Figure 4.9C). The general carbon number trend for sterols is C_{29}>C_{28}>C_{27} with some minor switches between C_{27} and C_{28} abundances in the top two layers, although layer 6 has a slightly higher amount of C_{28} sterol than C_{29}. Reduced sterols, as steranes and sterenes, are absent/very low in layers 1 and 2 and increase with depth from layer 3 onwards, with maximal concentrations in layers 6 and 7 (Figure 4.9F). In samples after layer 7 (i.e., layers 8-11), sterols are found in the unresolved complex mixture (UCM) and

identification /quantification becomes more difficult. After layer 9, sterenes/steranes have essentially disappeared as free hydrocarbons. C_{30} 24-*n*-propylcholestanol remains fairly constant and low in abundance throughout the core, showing maximum concentrations in layer 3 (Figure 4.9D). Diagenetic steric acid, sterenes, and steranes have low concentrations in the top surface layers and increases downcore to maximal concentrations at layer 6 and 7, followed by a decrease to low values up to layer 11 (Figure 4.9F). The percentage of C_{29} sterols (to total C_{27}-C_{30} sterols) increases slightly with depth, from 25.7% in layer 1 to 42.2% in layer 7. *Dunaliella salina*, a halophilic green microalga that synthesises abundant C_{29} sterol and β-carotene, is not a major source organism in these ponds. Thus, although algal C_{29} phytosterols are the dominant pseudohomologue of the C_{27}-C_{30} series and likely derived from the most abundant algal genus, *Nannochloropsis*, the variety of C_{27}-C_{30} sterols must be derived, in part, from the degradation products due to grazing nematodes at the mat surface (Chitwood *et al*., 1985; Farmer, 1992; Robertson *et al*., 2009).
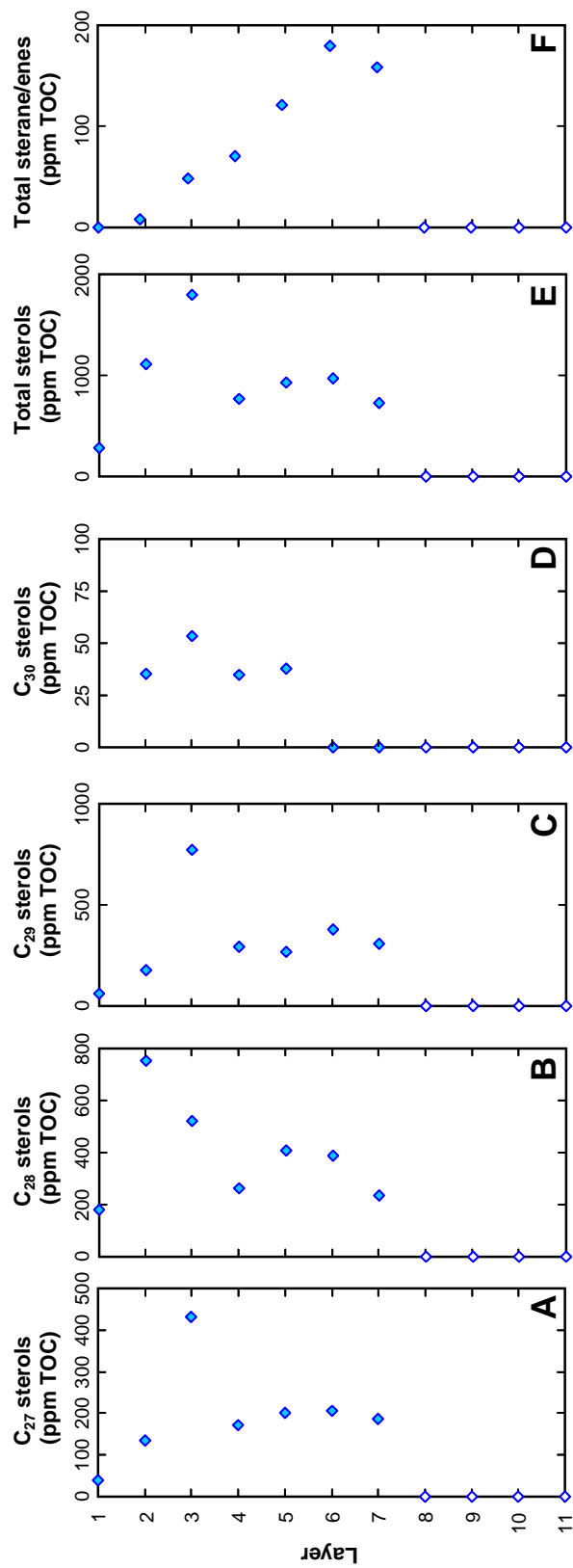
Figure 4.9. P4n5 abundance profiles from extractable IPLs showing sterol distributions throughout the core. A) C_{27} cholestanol in ppm TOC; B) C_{28} ergostanol in ppm TOC; C) C_{29} stigmastanol in ppm TOC; D) C_{30} n-propylcholestanol in ppm TOC; E) Total sterol concentration in ppm TOC; and F) Total sterane/enes concentration in ppm TOC with depth. Open diamonds represent layers in which sterols were difficult to recover due to large unresolved complex mixture (UCM).

131

Tetrahymenol (gammaceran-3β-ol), likely biosynthesised by heterotrophic ciliates living at the anoxic/oxic interface at the water column grazing on purple sulfur bacteria (PSB), is the tetracyclic triterpenoid biological precursor of the biomarker gammacerane. It is often used as a proxy for water column stratification or to indicate hypersalinity (e.g., ten Haven *et al*., 1985; ten Haven *et al*., 1989; Philp *et al*., 1989; Sinninghe Damsté *et al*., 1995). Some methylated homologues of tetrahymenol have also been reported in *Bradyrhizobium* species (Bravo *et al*., 2001). In P4n5, tetrahymenol (Figure 4.10A; Appendix Table A4.4c) has been detected in the upper anoxic layers, probably produced by PSB in this instance (Welander *et al*., 2009). The concentration of tetrahymenol is lower in layer 1 (9.6 ppm TOC) and increases significantly in layer 3, to 44 ppm TOC. Concentrations of tetrahymenol in layers 4 through 7 return to values similar to layer 2, with a marked decrease in layers 9 and 10. 2MeTOH are low (average 3 ppm TOC) in layers 1 through 3, with a significant increase in concentrations to 49.5 ppm TOC in layer 4 (Figure 4.10B). Intermediate values follow in layers 5 through 7, and 2MeTOH was not detected in layer 8 through 11.

Hopanoids

In contrast to the sterols, extractable and detectable hopanoids are much less abundant (Appendix Tables A4.4e-4.4f). Hopanoids are present as the extractable *biological* bacteriohopanepolyol (BHP) and diplopterol/diploptene, in addition to the extractable *diagenetic* products including hopanols, hopanoic acids, hopanoates, hopenes,

and hopanes. BHP is absent in layers 1 and 2, and first appears in layer 3. The maximum

concentration is found in layer
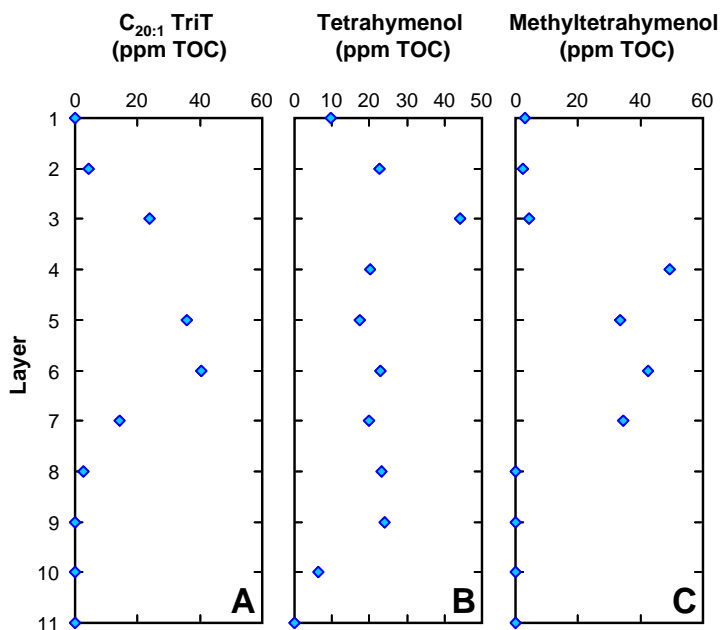
Figure 4.10. P4n5 abundance profiles from extractable IPLs of A) $C_{20:1}$ tricyclic terpene isomers (tentatively identified); B) Tetrahymenol and C) Methyltetrahymenol. All units in ppm TOC.

4 and declines to below detectable limits with depth below layer 5. Diploptene (Figure

4.11E) possess low concentrations throughout the entire core, with maxima (17.5 ppm

TOC) in layer 6, suggesting that this mid-core layer is an active zone of hopanoid

biosynthesis. The sum of the diagenetic hopane products (Figure 4.12B) is low in the

surface layers and increases to 48 ppm TOC in layer 6, with a sharp decline in layers 8

through 11, going from ~36 ppm TOC in layer 7 to ~10 ppm TOC in layer 8.
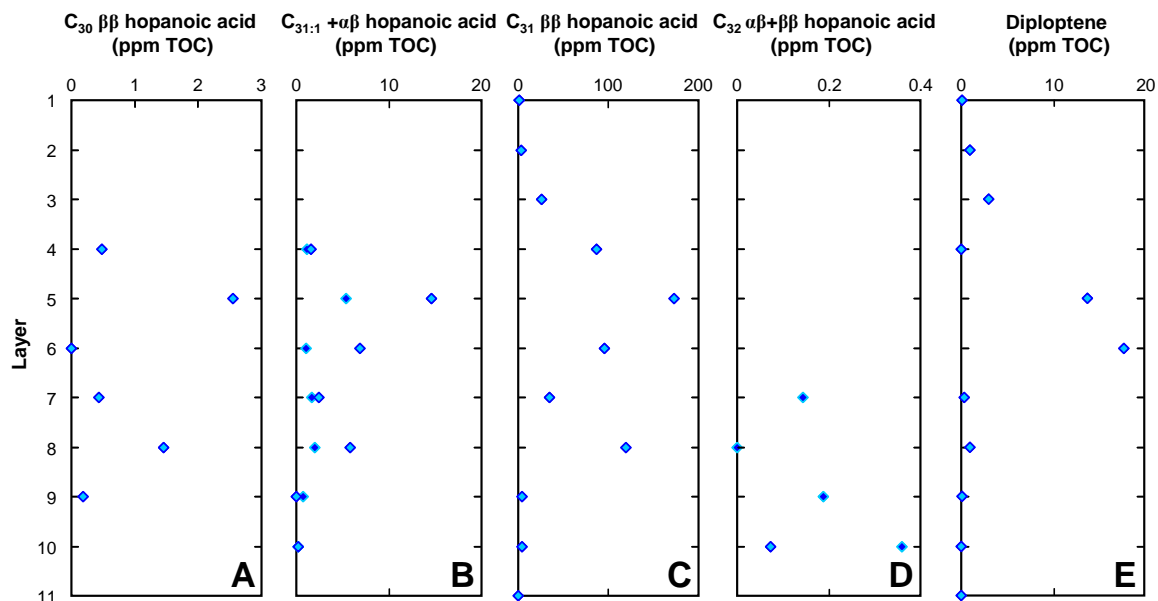
Figure 4.11. P4n5 abundance profiles from extractable IPLs of C_{30}-C_{32} hopanoic acids and diploptene; A) C_{30} $\beta\beta$ hopanoic acid; B) $C_{31:1}$ (dark blue filled) and C_{31} $\alpha\beta$ (light blue filled) hopanoic acids; C) C_{31} $\beta\beta$ hopanoic acid; and D) C_{32} $\alpha\beta$ (dark blue filled) and $\beta\beta$ (light blue filled) hopanoic acid; and E) Diploptene. All units in ppm TOC.
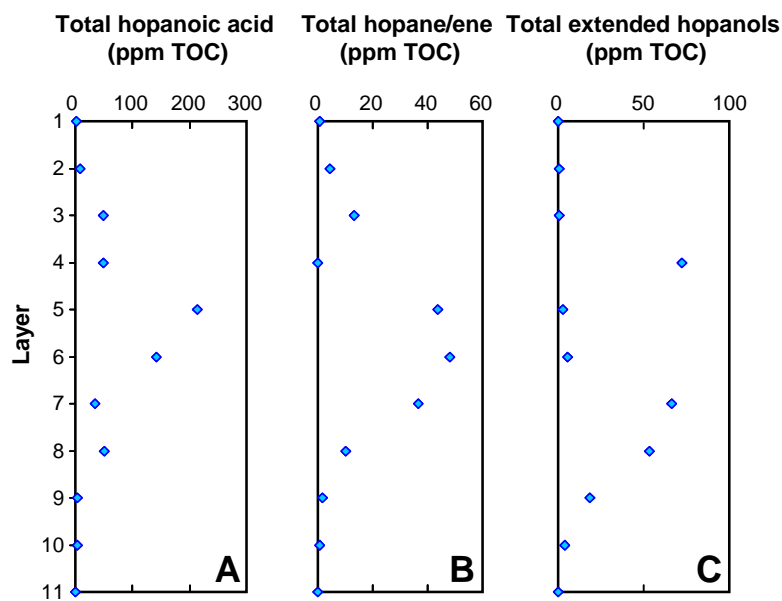
Figure 4.12. Concentration of total extractable hopanoids in ppm TOC in P4n5. A) Hopanoic acids; B) diagenetic hopanes/hopenes; and C) extended (C_{31}-C_{35}) hopanols.

134

Methylhopanoids (2Me and 3Me)

2α-methylhopanoids and 3β-methylhopanoids have been reported as biomarkers from cyanobacteria and type I microaerophilic methanotrophic bacteria, respectively. However, the taxonomic affinity of the former is tenuous due to occurrences of 2α-methylhopanoids from anoxygenic proteobacteria (e.g., Rashby *et al.*, 2007). In P4n5, 2α-methyl-hopanoids (2Me) are low in the surface and middle of the core, with only the layer 10 and 11 showing extractable C_{31} ββ 2αMe (Figure 4.13). On the other hand, 3β-methylhopanoids are very rare in the extractable lipid fraction, besides from gypsum mat crust samples in a higher salinity pond from GN (Jahnke *et al.*, 2014) as 3-methylhopanol. Layers 10 and 11 show minor concentrations of C_{31} ββ 3βMe (Figure 4.13; Appendix Table A4.4f).
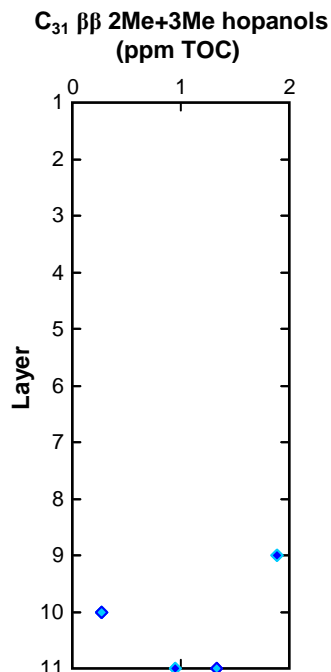
Figure 4.13. Concentration (ppm TOC) of C_{31} ββ 2-methylhopanol (dark blue filled) and C_{31} ββ 3-methylhopanol (light blue filled) in P4n5.

4.1.3 Kerogen-bound saturated biomarkers

Hydropyrolysates of up to 1.5 g of mat layer residues yield a small fraction of aliphatic (alkane and alkene) and aromatic hydrocarbon signal with the majority of the pyrolysate containing polar hydrocarbons. In P4n5, the saturated and aromatic

hydrocarbon fractions increase slightly with depth with a corresponding decline in the polar hydrocarbon yields.

Maximum polar hydrocarbon yield is 94.7 wt% in layer 1 coincident with the lowest saturated hydrocarbon yield of 0.26 wt%. Layer 8 possesses the highest saturated hydrocarbon yield, but also generated equal amounts of aromatic and polar hydrocarbons. It is expected that the active upper layers would have lower saturated hydrocarbon yields due to being in the early diagenetic window stage. In P5AB however, there is no significant trend in downcore fraction yield profiles with layers 1 through 8 exhibiting similar but low fraction yields for saturated and aromatic hydrocarbons (sats between 0.7-9 mg and aros between 2.7-11.2 mg). Although values are similar, saturated hydrocarbons show a general trend toward higher values with depth with maxima at layer 7 and decline in layer 8. Aromatic hydrocarbon yields show an initial decrease with depth up to layer 5 and increase up to layer 7 before declining in layer 8. Polar hydrocarbons dominate the pyrolysate products with little variation (average 90 wt% ± 4.4 wt%).

Alkanes

During the HyPy experimental procedure, fatty acids (either free or bound carboxylic acids) and alcohols are reduced to *n*-alkanes and *n*-alkenes possessing the same carbon number (Love *et al*., 2005). Linear *n*-alkanes from C_{15}-C_{43} are preserved in mat layer samples and display an even-over-odd predominance (EOP; e.g., Figure 4.14), gauged by the carbon preference index for samples in both P4n5 and P5AB. Carbon preference index (CPI) was calculated for all samples, defined as (Marzi *et al*., 1993):

$$CPI = [\Sigma_{odd}(C_{21-33}) + \Sigma_{odd}(C_{23-35})]/[2\Sigma_{even}(C_{22-34})]$$

CPI and OEP (odd-over-even carbon number preference) ratios are used as a rough indicator of *n*-alkane sources. Immature and/or terrestrially-derived organic matter tend to have a pronounced OEP for long chain (nC_{20}-nC_{35}) *n*-alkanes and CPI > 1. Ancient organic matter derived from a marine source tend to have no carbon number preference for *n*-alkanes, with slight EOP pattern from hypersaline environments or evaporitic source rocks (e.g., Peters *et al*., 2005) with no significant terrestrial input. Modern marine organic matter has EOP due to reduction of fatty acids and alcohols. All layers have a CPI < 1 (average 0.68 for both cores), with fairly constant values downcore for P4n5 and a slight decreasing trend for P5AB (0.8 in layer 1 and 0.3 in layer 8). Relative abundance of *n*-alkenes were more prominent in P5AB layer pyrolysates compared to P4n5. The most abundant short-chain (nC_{16}-nC_{20}) alkanes range from nC_{16}, nC_{18}, or nC_{20} (with the mode at nC_{20}), and long-chain (nC_{21}-nC_{34}) is nC_{24}, though this varies a little with depth. The most abundant saturated hydrocarbons in both cores are dominated by the isoprenoid phytane in most cases. Exceptions, in P4n5, include nC_{20} in layer 3, nC_{27} in layer 4, nC_{24} in layer 10, and nC_{22} in layer 11. For P5AB, the most abundant hydrocarbon that is not phytane, include nC_{17} in layer 1, nC_{20} in layer 6, and C_{35} ββR hopane in layer 7.
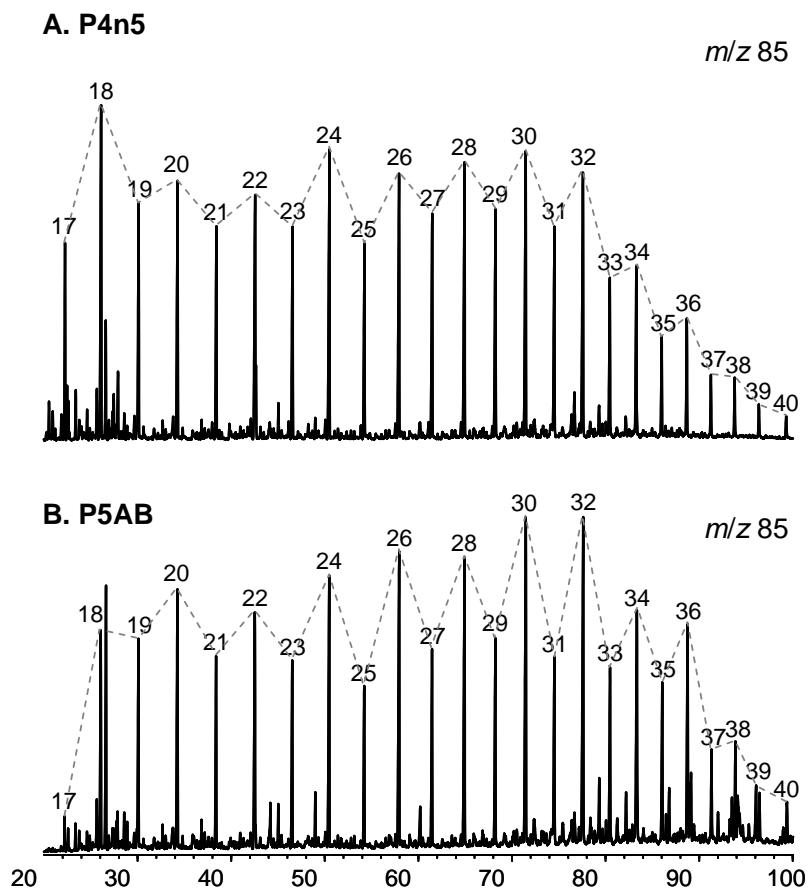
Figure 4.14. Partial *m/z* 85 ion chromatograms of kerogen-bound biomarkers from layer 7 of A) P4n5 and B) P5AB showing even-over-odd predominance of *n*-alkanes. Labelled peaks are *n*-alkanes with carbon number indicated above.

Isoprenoids

Regular acyclic head-to-tail isoprenoids are found in mat layers from both cores. These include a variety of C_{14}-C_{25} regular isoprenoids, dominated by phytane and abundant phytene isomers, as pyrolysis usually generates phytanes, phytenes, and phytadienes in large quantities. Additionally, pristane (and pristene) are present but in lower abundance, hence phytane is likely sourced from archaeal biphytane. Phytane and the six phytene isomers (Figure 4.15) can also be sourced from anoxic degradation

138

products of chlorophylls (chlorophyll phytols) and should be preserved through S-binding (sulfur binding). In this case, the source of phytane could be mixed from chlorophyll degradation or archaeol, however the presence of regular C_{25} isoprenoid (iC_{25}) may suggest the major precursor of phytane in the samples is archaeol. Pristane/phytane (Pr/Ph) ratios provide a simple measure of the redox conditions of the depositional environment, based on chlorophyll degradation pathways, although some source considerations are required when using this proxy. Plots of Pr/Ph show consistently low values for both cores (all values < 0.4 for P4n5 and < 0.2 for P5AB; Figure 4.16A). Log cross-plots of Pr/nC$_{17}$ and Ph/nC$_{18}$ to understand the relationship between kerogen type and redox place all samples from both cores in the marine Type II/reducing kerogen field.
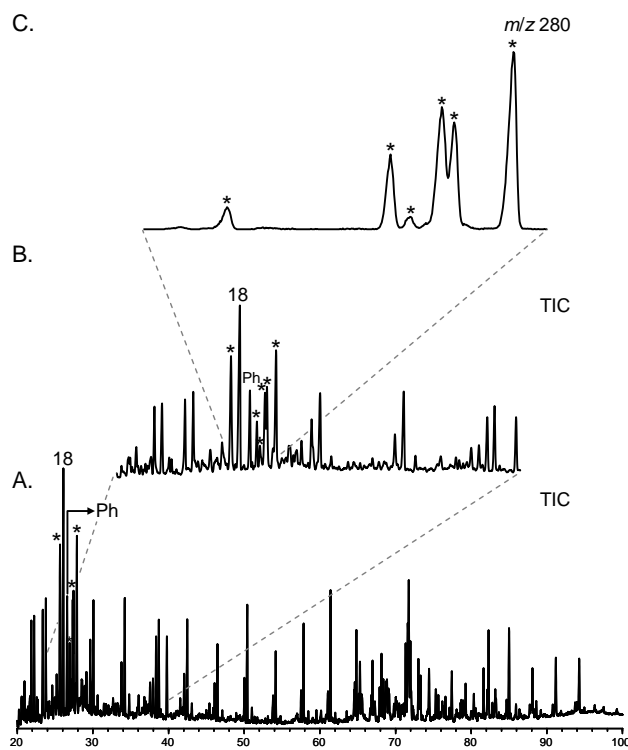
Figure 4.15. Total and partial ion chromatograms of kerogen-bound biomarkers from P5AB layer 3 showing dominance of phytane and phytenes in A) TIC and B) magnified TIC 20-40 mins; and C) m/z 280, with asterisks representing phytene.

Regular iC_{18}-iC_{30} isoprenoids are commonly found in halophilic archaea (Grice *et al*., 1998; Love *et al*., 2005). Regular iC_{25} (as a ratio of the average integrated areas of nC_{22} and nC_{23}, the two *n*-alkanes that it elutes between) increases with depth, with a very similar trend in P4n5 and P5AB. In P4n5, regular iC_{25} is first detectable in layer 6 with steady increase up to layer 9 followed by decreases in layers 10 and 11. In P5AB, regular iC_{25} is present in all layers, with lower relative concentrations in layers 1 through 3, increasing through layer 4 and with maximal relative concentration in layer 8 (Figure 4.16B). Figure 4.17 shows the partial ion chromatogram (*m/z* 183) of layer 7 in P5AB where regular iC_{25} elutes between nC_{22} and nC_{23}. Regular isoprenoids of iC_{30} and higher are present in the high molecular weight (HMW) region of the chromatograms but are sometimes hard to identify accurately due to the high number of compounds and coelution with compounds in the polycyclic biomarker region.

Irregular acyclic tail-to-tail linked isoprenoids include methanogenic/methanotrophic archaeal biomarkers such as crocetane (iC_{20}) and pentamethyleicosane (PMI, iC_{25}), squalane, and the carotenoid lycopene (iC_{40}). Crocetane and PMI are hard to separate due to coelution with phytane and regular iC_{25}, respectively. Although close inspection of characteristic ion fragments between regular iC_{25} and PMI can often distinguish the two compounds, performing coinjections with authentic standards or compound-specific carbon isotopes (in the case of crocetane and phytane, separating them out on a β-CYDEX column) is usually required to confirm the identity of the two compounds. PMI was not found in the IPL fraction and comparison of the mass spectrum of iC_{25} was enough to confirm that it was indeed regular iC_{25} and not

PMI. However trace quantities of crocetane was tentatively identified in P4n5 layer 7 from the IPL hydrocarbon fraction.

Squalane, the hydrocarbon skeleton of the former polyenic, squalene, is the major irregular acyclic tail-to-tail isoprenoid found in these samples. It is biosynthesised by all three domains of life however, in sedimentary organic matter, it is largely derived from archaea (Grice *et al*., 1998). In both P4n5 and P5AB, squalane (as a ratio of the average integrated areas of nC_{26} and nC_{27}, the two *n*-alkanes that it elutes between) increases from layer 1 to 4 and then decreases in P4n5 with depth. In P5AB, the squalane ratio increases again to a second maxima in layer 7 before declining in layer 8 (Figure 4.16C). Figure 4.17 shows the partial ion chromatogram (*m/z* 183) of layer 7 in P5AB where squalane elutes between nC_{26} and nC_{27}.

The main irregular head-to-head acyclic isoprenoid found in both ponds is acyclic biphytane—derived from archaeal ether lipids (Schouten *et al*., 1998). Acyclic biphytane is reported as a ratio of the average integrated areas of nC_{35} and nC_{36}, the two *n*-alkanes that it elutes between (Figure 4.17). In P4n5, the ratio of acyclic biphytane decreases from layer 1 to 3 and then increases up to layer 6. Layers 7 through 10 show lower values followed by a large jump in layer 11. In P5AB, acyclic biphytane increase from layer 1 to 3 and steadily decreases up to layer 7. In layer 8, there is a marked increase in the relative concentration of acyclic biphytane (Figure 4.16D). All isoprenoid data can be found in Appendix Tables A4.5a, 4.5b.
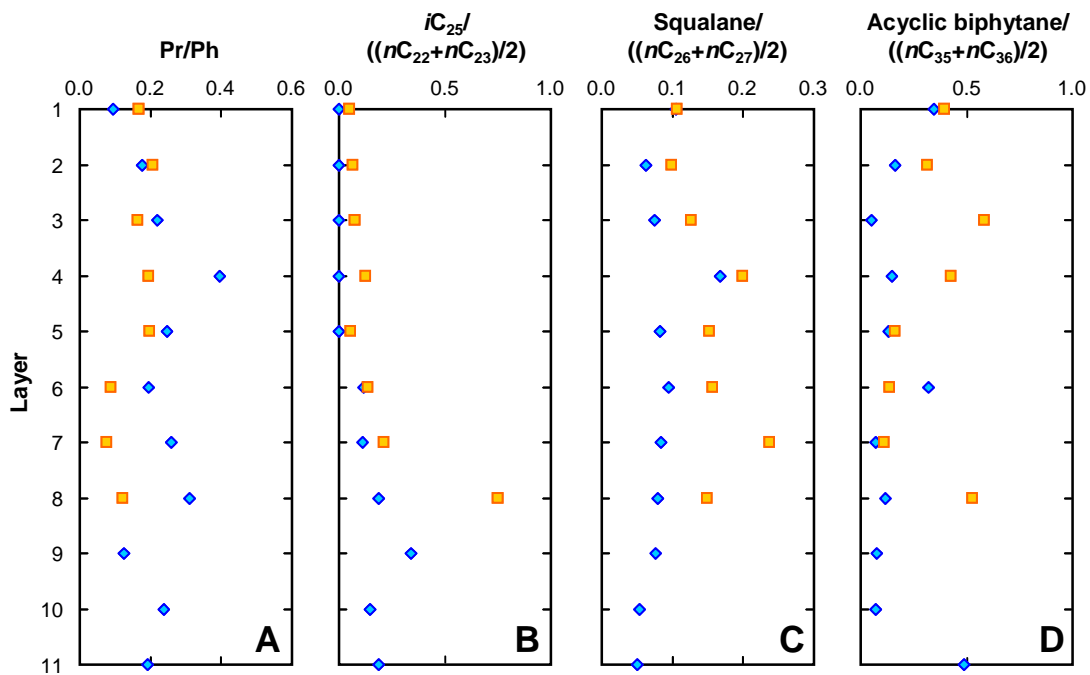
Figure 4.16. Relative abundance of kerogen-bound isoprenoids; A) Pr/Ph ratio; B) Regular C_{25} isoprenoid (iC_{25}); C) Squalane; and D) Acyclic biphytane; in P4n5 (blue diamonds) and P5AB (orange squares).
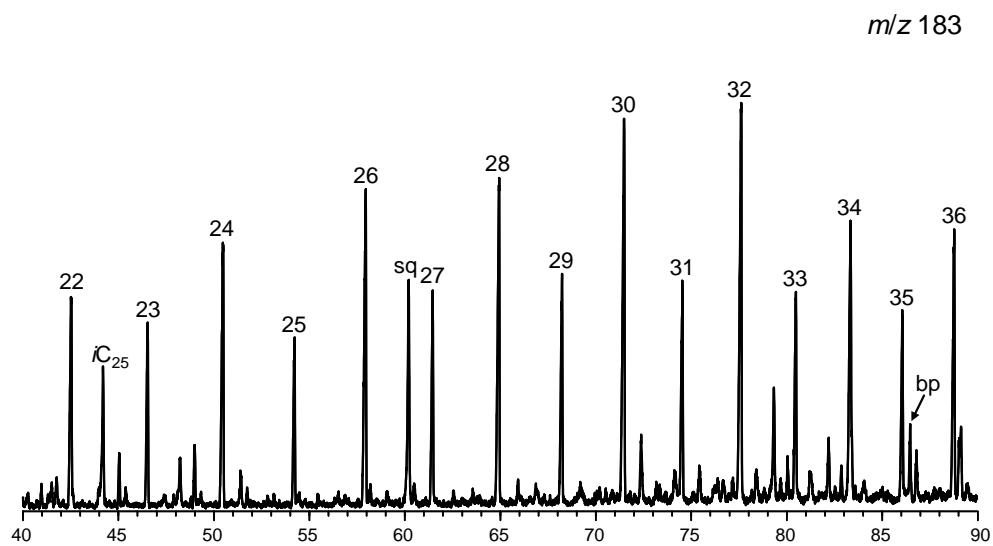
Figure 4.17. Partial m/z 183 chromatogram of P5AB layer 7 showing the dominance of kerogen-bound (L to R) regular iC_{25} isoprenoid, squalane (sq), and acyclic biphytane (bp). Labelled peaks are n-alkanes with C number indicated.

Carotenoids (*m/z* 125)

Carotenoids have been reported to be associated with GN microbial mats previously (Palmisano *et al*., 1989) and are produced by phototrophic organisms to cope with the consequences of photosynthesis. A variety of cyanobacterial and diatom carotenoids and pigments were found in microbial mats from Pond 5 in a previous study (Palmisano *et al*., 1989), e.g., myxoxanthophyll, zeaxanthin, β-carotene, γ-carotene, echinenone, fucoxanthin, and bacteriochlorophylls *a* and *c*. Even though they are rarely preserved in the geological record due to rapid remineralisation and destruction because of their reactive conjugated polyenic core, some lower layers (7 and 8) in P5AB show evidence for rearranged or partial fragments of carotenoids/carotanes possessing the 1,1,3-trimethylcyclohexyl moiety, diagnostic of *m/z* 125 and *m/z* 123 of 1,1,3-trimethylcyclohex-1-enyl. These elute in the high molecular weight region of the chromatogram and are not evident in any layers from P4n5 (Figure 4.18). Compounds are not well resolved due to the abundance of peaks and possible coelution, but peaks with fragment ions 125 and 554, 558, and 560, were found. Additionally, saturated carotane breakdown fragments (Lee & Brocks, 2011), C_{22}, C_{32}, and C_{35}, were also tentatively identified in layer 7 and 8 of P5AB. This is probably due to a difference in source organisms primarily controlled by salinity, as it has been demonstrated that increased carotenoid concentrations were found in a higher salinity pond in GN (Pond 8; ~16-18% salinity; Palmisano *et al*., 1989), derived from haloarchaea and halobacteria. Although there is a purple layer in P5AB (around layer 2), we did not see any evidence for bound okenone/okenane in these samples. Additionally there are five compounds potentially

isomers or part of a homologous series with a M+ molecular ion of 530 eluting between $n\text{C}_{37}$ and $n\text{C}_{39}$. They feature a prominent cluster of ions ranging from 333-336 with maximum fragment ion at 334. There are six additional compounds with dominant 333-336 ion fragment clusters that do not possess M+ of 530. Figure 4.18 is a partial ion chromatogram of m/z 85, 125, and 333 showing the elution of these compounds in P5AB layer 7. Molecular ion of 530 would indicate this compound(s) has a $\text{C}_{38}\text{H}_{74}$ composition (i.e., a C_{38} hydrocarbon possessing 2 double bond equivalents; Appendix Figure A4.1). Since it appears prominently in the m/z 125 trace where we would be expecting to find carotane-derived compounds, then perhaps the m/z 125 points to the β-carotane head group (1,1,3-trimethylcyclohexyl). This can be ruled out for some of the compounds because the 125 fragment ion is not abundant. Some long-chain mono-, di-, and trimethylalkanes have been reported previously from cyanobacterial mats (Kenig *et al.*, 1995), although the overall abundance of short chain mono- and dimethylalkanes in these mats is very low. This unusual series of compounds is only found in layer 7 and 8 of P5AB and requires further source and structural characterisation.
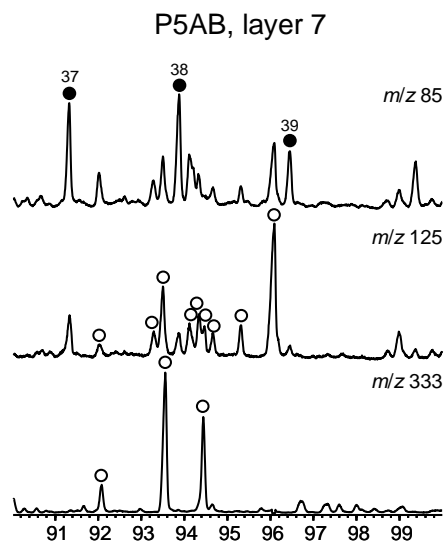
Figure 4.18. Partial *m/z* 85, 125, and 133 ion chromatograms showing the elution position of unknown peaks in the kerogen-bound fraction of P5AB layer 7. Filled circles represent n-alkanes with carbon number indicated and open circles represent the unknown potentially homologous series of compounds.

Steranes, sterenes, diasterenes (m/z 217, 215, 257 and 358→217 to 414→217)

Sterane isomers βααR and αααR from C_{26}-C_{30} were found in most mat layers from P4n5 and P5AB, dominant in the C_{27}-C_{29} range (Figures 4.19A-C; Appendix Tables A4.6a-4.6b, A4.7). Minor C_{26} norsteranes and C_{30} *n*-propylcholestanes are not further discussed or used in calculation of ratios involving total steranes. The dominant pseudohomologue in both cores is C_{29} (Figure 4.20E). In both cores, the concentration of total steranes (in ppm TOC) increases from layer 1 with maximum values at layer 7 (42 ppm TOC for P4n5 and 66 ppm TOC for P5AB) before decreasing to 1.5 ppm TOC in layer 11 of P4n5 and 27 ppm TOC in layer 8 of P5AB (Figure 4.20D).
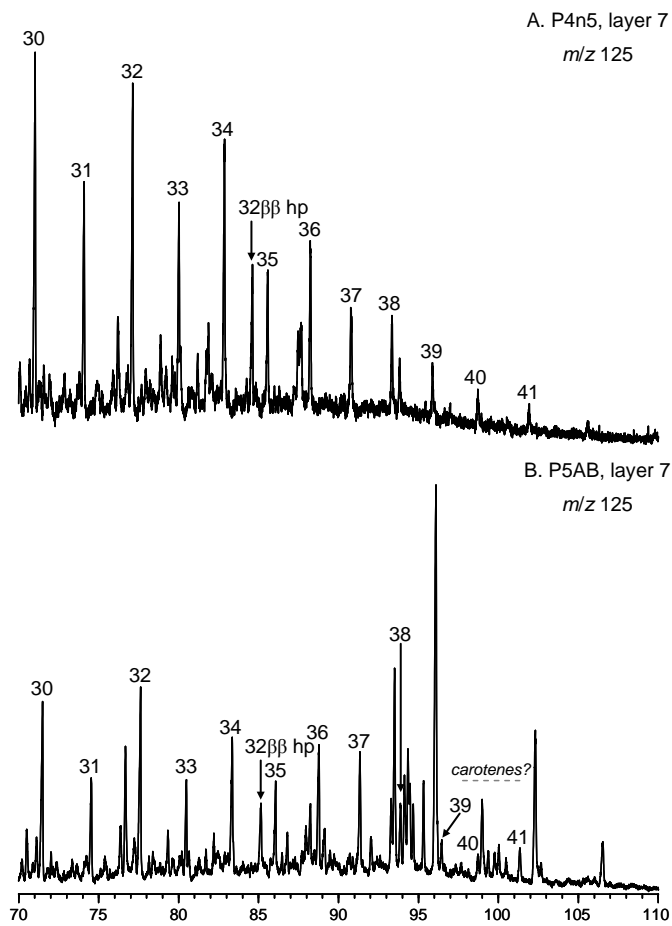
Figure 4.19. Partial *m/z* 125 ion chromatograms showing potential kerogen-bound carotenoid/carotene fragments from A) P4n5 layer 7; and B) P5AB layer 7. Labelled peaks with numbers are *n*-alkanes and C_{32} ββR hopane.
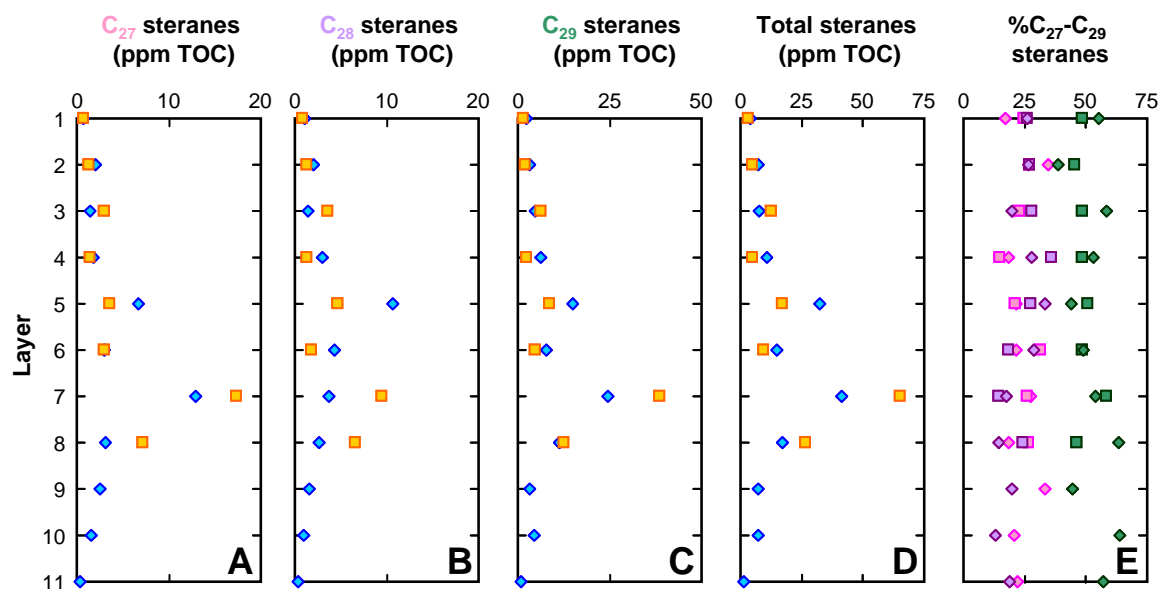
Figure 4.20. Abundance profiles of kerogen-bound steranes from P4n5 (blue diamonds) and P5AB (orange squares). A) C_{27} steranes; B) C_{28} steranes; and C) C_{29} steranes; D) Sum of C_{27}-C_{29} steranes; and E) Percentage of C_{27} (pink), C_{28} (purple), and C_{29} (green) with the diamonds and squares representing P4n5 and P5AB, respectively. Units for A-D in ppm TOC. Sterane isomers used are βααR and αααR.

Sterenes, steradienes, and diasterenes (Figure 4.21) and their various isomers are metastable intermediates formed during chemical transformation of sterols to steranes (Love *et al*., 2005). They arise from the oxidation and subsequent dehydration of sterols with some double bond isomerisation, during the early stages of diagenesis in the water column or at the sediment-water interface (Mackenzie *et al*., 1992). Δ^2-sterenes form through the dehydration of stanols in sediments during early diagenesis and isomerise to form the more stable Δ^4 and Δ^5 isomers (Brassell *et al*., 1984). Sterenes and steradienes and diasterenes with mass fragments *m/z* 215 and *m/z* 257 respectively, were detected for C_{27}-C_{29} αααR in P4n5 and P5AB layers 1 through 8. Sterenes prominently appear in layer 3 (Δ^4-sterene and Δ^5-sterene) eluting before the saturated αααR isomer with the highest

observed in layer 8. The dominant positional isomer is Δ^4-sterene for the C_{27} homologue. Sterenes are absent in pyrolysates from layer 9-11 of P4n5 and layer 8 of P5AB. Diasterenes and steradienes (as C_{27}-C_{29} 13(17)- and $\Delta^{4:22}$ and $\Delta^{5:22}$ isomers, respectively) were also detected, in trace amounts in layer 1 with increasing abundance going down core. This series of unsaturated isomers is only found in immature sediments (Amo *et al*., 2007) and likely captures the diagenetic progression of sterols through the mat. In P5AB, sterene doublets were most prominent in layer 6 (Figure 4.22B) but show isomer differences compared to those found in P4n5 layer 8 (Figure 4.22A). Even though diasterenes are formed during diagenesis they are not readily hydrogenated to diasteranes during HyPy (Love *et al*., 2005). Overall, sterenes and diasterenes can contribute to the large pool of kerogen-bound sterols (Figure 4.21, Figure 4.22).
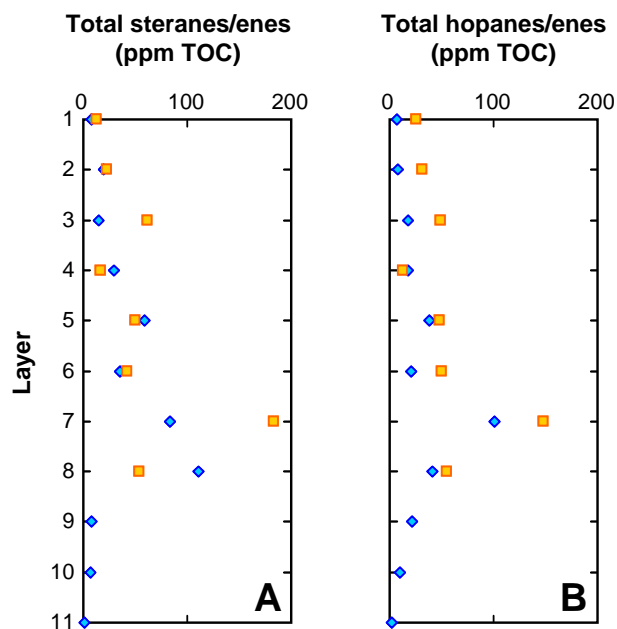
Figure 4.21. Abundance profiles of kerogen-bound A) total steranes/enes (sum of all C_{27}-C_{29} sterane, sterene, steradiene, and diasterene isomers) and B) total hopanes/enes (sum of all C_{27}, C_{29}-C_{35} αβR, βαR, ββR hopanes and C_{27} hop-13(18)-ene, C_{29} hop-13(18)-ene, and C_{30} hop-17(21)-ene.
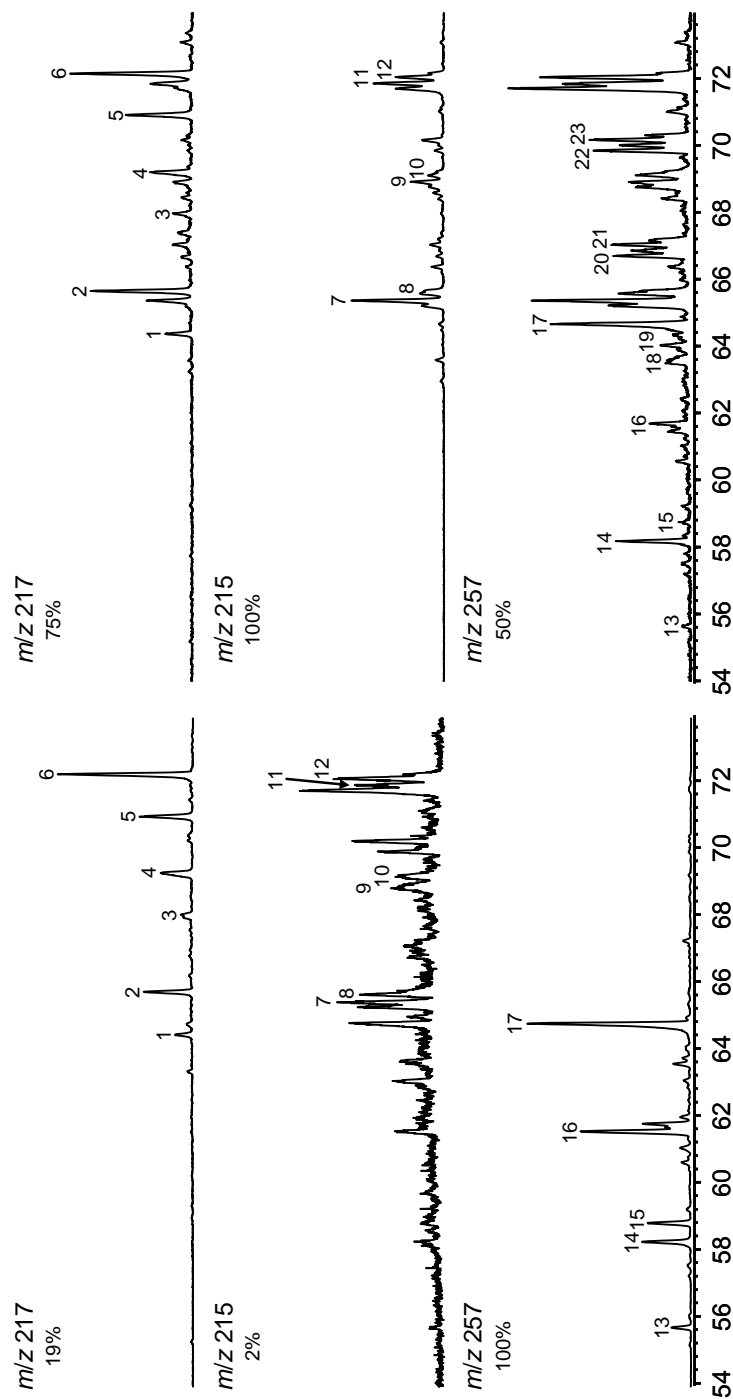
Figure 4.22. Example of kerogen-bound sterane (*m/z* 217), sterene (*m/z* 215), and diasterene (*m/z* 257) distributions in pyrolysates from A) P4n5 layer 8, and B) P5AB layer 6. Labelled peaks are compounds assigned in Table 4.4. Note the difference in steradiene isomer distributions between the two ponds in the bottom panel.

149

Table 4.4. Peak identifications of compounds numbered in Figure 4.22 (in trivial names): Steranes (m/z 217), sterenes (m/z 215), diasterenes and steradienes (m/z 257).

Peak number	Compound class	Compound
1		C_{27} βααR cholestane
2		C_{27} αααR cholestane
3	Steranes	C_{28} βααR ergostane
4		C_{28} αααR ergostane
5		C_{29} βααR stigmastane
6		C_{29} αααR stigmastane
7		C_{27} ster-4-ene (Δ^4)
8		C_{27} ster-5-ene (Δ^5)
9	Sterenes	C_{28} ster-4-ene (Δ^4)
10		C_{28} ster-5-ene (Δ^5)
11		C_{29} ster-4-ene (Δ^4)
12		C_{29} ster-5-ene (Δ^5)
13		C_{27} dia-13(17)-sterene ($\Delta^{13(17)}$)
14		C_{27} dia-13(17)-sterene ($\Delta^{13(17)}$)
15	Diasterenes	C_{28} dia-13(17)-sterene ($\Delta^{13(17)}$)
16		C_{28}+C_{29} dia-13(17)-sterene ($\Delta^{13(17)}$)
17		C_{29} dia-13(17)-sterene ($\Delta^{13(17)}$)
18		C_{27} αααR stera-4,22-diene ($\Delta^{4:22}$)
19		C_{27} αααR stera-5,22-diene ($\Delta^{5:22}$)
20	Steradienes	C_{28} αααR stera-4,22-diene ($\Delta^{4:22}$)
21		C_{28} αααR stera-5,22-diene ($\Delta^{5:22}$)
22		C_{29} αααR stera-4,22-diene ($\Delta^{4:22}$)
23		C_{29} αααR stera-5,22-diene ($\Delta^{5:22}$)

Hopanes and hopenes (m/z 191 and 370→191 to 482→191)

All hopane, hopene, and methylhopane concentrations for P4n5 and P5AB can be found in Appendix Tables A4.8a-4.8f. C_{27} Tm isomers (370→191). The dominant C_{27} trisnorhopanes are the 17α(H)-22,29,30-trisnorhopane (Tm or 17(α)Tm) and its 17(β) isomer, 17(β)Tm (17β(H)-22,29,30-trisnorhopane). Ts (18α(H)-22,29,30-trisnorneo-hopane) is absent from all kerogen pyrolysates, as expected, as it does not get bound into kerogen during diagenesis. 17(α)Tm and 17(β)Tm are pentacyclic triterpanes that are

likely derived from formerly functionalised hopanoids. The relative concentration of $17(\alpha)$Tm in P4n5 (as $17(\alpha)$Tm/$17(\alpha)$Tm+$17(\beta)$Tm) increases with depth reaching its maximum concentration at layer 7 before decreasing through to layer 10 and increasing again at layer 11. In P5AB, $17(\alpha)$Tm increases steadily with depth, with maximum concentration in layer 8. The absolute concentrations of C_{27} hopanes (sum of both isomers) increases with depth in both cores, to a maximum at layer 7 (17 ppm TOC in P4n5 and 33 ppm TOC in P5AB layer 6) with return to lower values in layers 11 and 8, respectively (Figure 4.23A).

There are 3 major and 1 minor hopene isomers identified in these layers based on comparison of mass spectra and relative elution positions (Bishop *et al*., 1998; Huang *et al*., 2010); C_{27} hop-13(18)-ene, C_{29} hop-13(18)-ene, and C_{30} hop-17(21)-ene, with the C_{27} homologue being the dominant of the three. The minor hopene isomer, C_{30} hop-22(29)-ene (diploptene) coelutes with $C_{32}\beta\alpha$R hopane (moretane) and this double peak consequently yields a mass spectrum containing fragment ions characteristic of both compounds, C_{32} $\beta\alpha$R with M+ 440, 425, 369, and 281, and diploptene with M+ 410, 395, 367, and 299. Another compound that also probably coelutes with these two hopanes/enes is a C_{33} hopene, with M+ of 452 (Appendix Figure A4.2).

C_{28} bisnorhopanes (384→191). The C_{28} bis- and trisnorhopanes are absent from all kerogen hydropyrolysates as—similar to Ts—they do not get bound into kerogen during diagenesis.

C_{29} norhopanes (398→191). C_{29} norhopanes are cracking products from C_{30} hopane during pyrolysis, thus the methyl group at C-30 is lost. The profiles of C_{29} αβ, βα, and ββ are near identical to profiles observed for C_{30} αβ, βα, and ββ hopanes both in terms of relative abundance and downcore trends (P4n5: m = 1.3, R^2 = 0.99; P5AB: m = 0.99, R^2 = 0.86; Figure 4.23B).

C_{30} hopanes (412→191). Figure 4.22C shows the diagenetic C_{30} hopane profiles (sum of αβR, βαR, and ββR isomers) from diplopterol/diploptene show an increase with depth from P4n5 layer 1 to a maximum at layer 7 (89 ppm TOC) followed by a decrease in concentration to layer 11 (0.7 ppm TOC). In P5AB the absolute concentrations are, on average, 7 times lower than P4n5. The 3 uppermost layers show variable concentrations and layers 4 (1.2 ppm TOC) through 7 (11.7 ppm TOC) show an increasing trend followed by a decrease in layer 8 (6.7 ppm TOC).
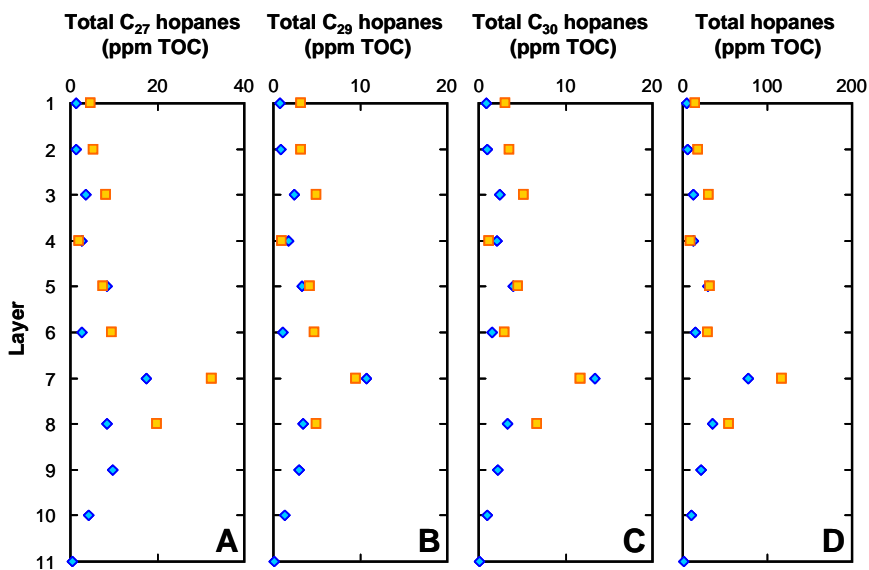
Figure 4.23. Abundance profiles of kerogen-bound A) Total C_{27} hopanes; B) Total C_{29} hopanes; C) Total C_{30} hopanes; and D) Total hopanes (sum of C_{27}, C_{29}-C_{35} αβR, βαR, and ββR hopanes). P4n5 are represented by blue diamonds and P5AB by orange squares. All units in ppm TOC.

Gammacerane (412→191) and methylgammaceranes. The relative concentration of gammacerane (calculated relative to the integrated area of C_{30} ββ R hopane), likely the diagenetic equivalent of tetrahymenol, shows an increasing trend with depth in both cores, with slightly higher relative abundances in P5AB compared to P4n5 (Figure 4.24; Appendix Table A4.9). Additionally, due to the presence of methyltetrahymenols in the extractable lipid fraction, we searched for methylgammaceranes and dimethylgammaceranes (426→205 and 440→205, respectively), which have not been unambiguously identified in any ancient rock or oil, but potentially both are present in Q Oils (Cambrian) of North Oman (Love, unpublished results), for which the source rocks are saline, marginal marine facies. In the chromatograms, there are very small peaks that are potentially methylgammacerane and dimethylgammacerane with similar relative elution positions compared with those tentatively identified in Q oils from North Oman. Since these have not been identified unambiguously, we cannot say with confidence that these are present in these samples without further structural characterisation.

Gammacerane/C_{30} hopane
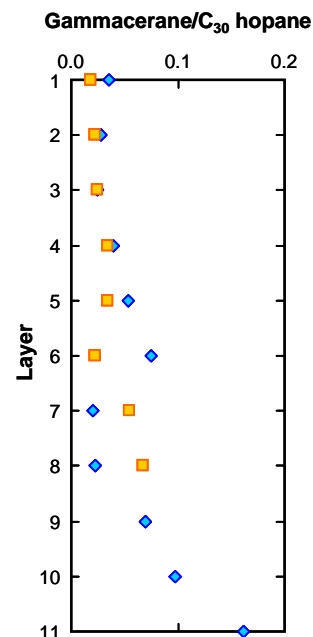
Figure 4.24. Profile of the relative abundance of kerogen-bound gammacerane/C_{30} hopane in P4n5 (blue) and P5AB (orange). C_{30} hopanes are the sum of C_{30} αβR, βαR, and ββR hopane isomers.

Extended homohopanes (426→191 to 482→191). Homohopanes are a homologous series of C_{30} hopane with an addition to the BHP side-chain (C_{31} to C_{35}). Usually the extended side-chain is only preserved if it is able to be bound by sulfide linkages under suitable conditions for preservation, otherwise is it vulnerable to cracking

during diagenesis. Extended hopanes show similar concentration profiles with depth for C_{31}-C_{35}, with a muted response in terms of the layer 7 spike in concentration for C_{31} (in P5AB) compared to the profiles observed in C_{32}-C_{35}. P4n5 extended hopanes of C_{31}-C_{33} show and steady increase from layer 1 to maximum values at layer 7 and decline to layer 11. C_{34} and C_{35} hopanes of layer 8 show similarly high values before declining in layer 9. The general trend in P4n5 shows a decrease in concentrations from layers 1 to 3 followed by an increase in layer 7 before decline to lower values in layer 8. The relative abundance of extended hopanes shifts markedly from layer 7 to layer 8 in P4n5 and from layer 6 to layer 7 in P5AB, to an increase in C_{32}-C_{35} hopane recovery (Figure 4.24 and discussed in more detail in Section 4.3.4).

Methylhopanes (496→205)

Methylated hopane homologues with methylation at C-2 or C-3 are reported from cyanobacteria or proteobacteria and type I microaerophilic methanotrophs, respectively. C-2 methylhopanes (2β-methylhopanes) elute slightly before the ββR hopane isomer carrying one less carbon number. The C_{30} (412→191 transition) and its corresponding C_{31} 2β-methyl (426→205) cannot be resolved due to coelution, which is true for all samples. C_{31}-C_{35} 2β-methylhopanes can be resolved through their individual ion transition channels, with increasing difference in elution time between ββR hopane and 2β-methylhopane with increasing carbon number. A plot of the 2β-methylhopane index (2MeHI) calculated as a percentage of 2β-methylhopane/(2β-methylhopane + ββR hopane) and concentrations are shown in Figure 4.26A and Figure 4.25B, respectively

(Appendix Table A4.8e, 4.8f). C_{31}-C_{35} 2β-MeHI generally show higher values in layer 1 (with consistently higher values in P4n5 than P5AB), with decreasing values to layer 3. Layers 4 through 8 show constant values for C_{31} and C_{32} and decreasing for C_{33}-C_{35}. In P4n5 layers 9 and 10, all homologues show an increase in relative 2MeHI except for C_{34} where 2β-methylhopane was not detected. 3βMeHI (for which αβR and ββR isomers are identified) is slightly more complicated due to the coelution of isomers with moretanes (βαR hopanes) and αβR hopanes. The two homologues that do not have this problem, C_{31} and C_{36}, show not detectable or low abundances in the surface layers with increases with depth in both cores (Figure 4.26C). Figure 4.26D shows the concentration of total 3β-methylhopanes in both cores. The most prominent increase occurs in layer 9 and 10 of P4n5 (similar to 2MeHI). If the source of 3β-methylhopanes is purple non-sulfur bacteria, their absence in the surface layers is consistent with the absence of anoxygenic phototrophs in the surface while becoming more prominent with depth.
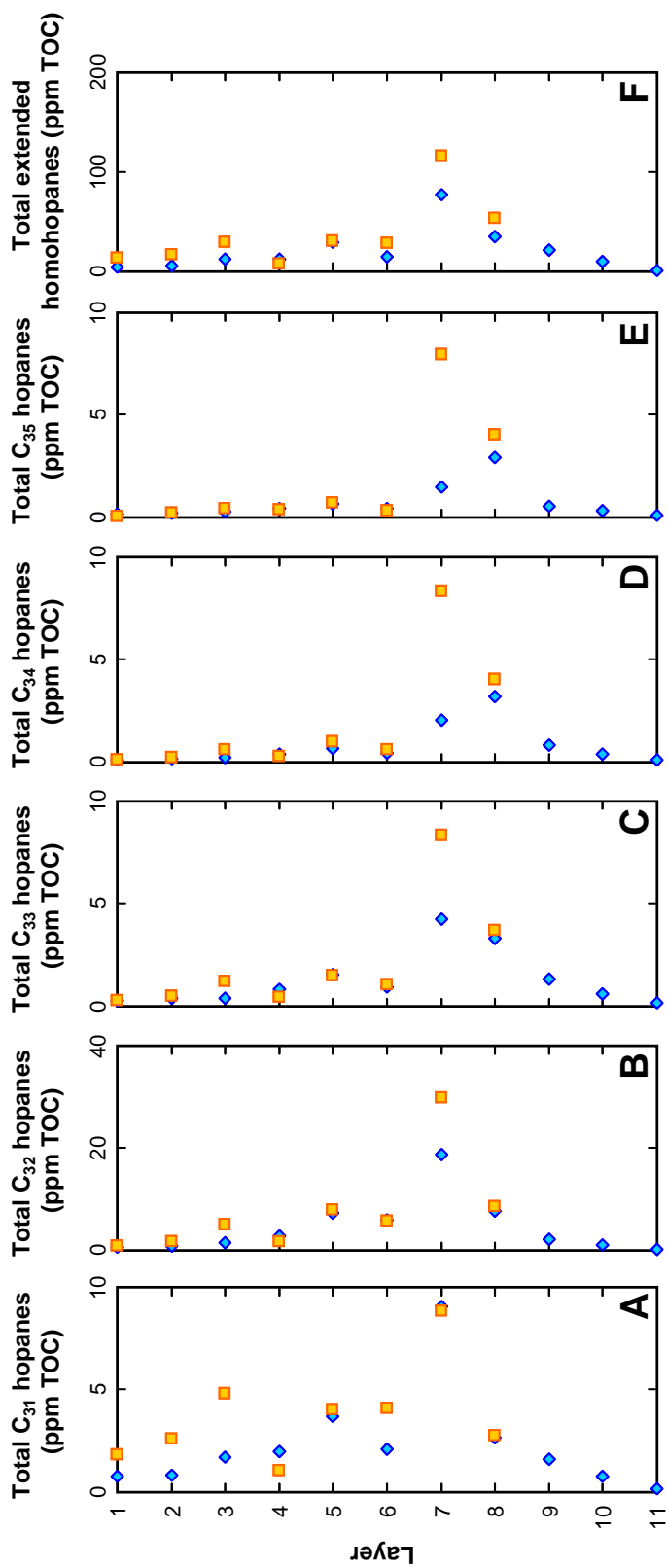
Figure 4.25. Abundance profiles of kerogen-bound extended homohopanes of P4n5 (blue) and P5AB (orange): A) C_{31}; B) C_{32}; C) C_{33}; D) C_{34}; E) C_{35}; and F) Sum of C_{31}–C_{35}. Isomers used are αβR, βαR, and ββR. All units in ppm TOC.
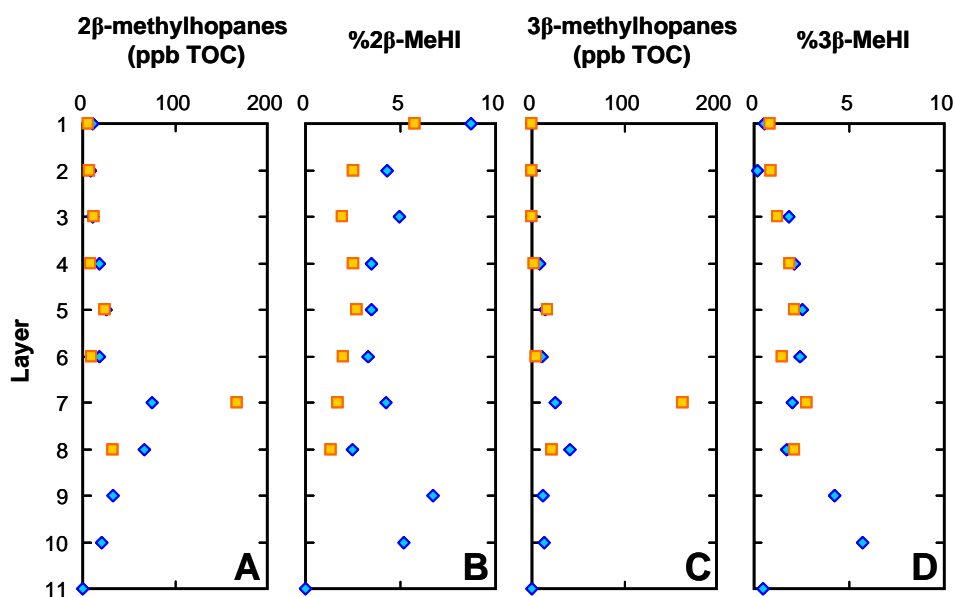
Figure 4.26. Kerogen-bound methylhopane abundance profiles for P4n5 (blue) and P5AB (orange) showing A) Sum of 2β-methylhopanes (C_{31}-C_{36}); B) 2β-methylhopane index (2β-MeHI) calculated as 2βMe/2βMe+ββ hopane × 100; C) Sum of 3β-methylhopanes (C_{31}-C_{36}); and D) 3β-methylhopane index (3β-MeHI) calculated as 3βMe/3βMe+ββ hopane × 100. Concentrations are in ppb TOC.

Assessment of polycyclic biomarker inputs

 Bulk ratios of steranes to hopanes provide a rough gauge into eukaryotic (steranes) *versus* bacterial (hopanes) source inputs into preserved organic matter. Ratios were calculated using the sum of the integrated areas of C_{27}-C_{29} βααR and αααR steranes and C_{27} 17(α)Tm and 17(β)Tm, C_{29}-C_{35} αβR, βαR, and ββR hopane isomers in MRM partial ion mass chromatograms and quantified using 50 ng of d4 internal standard. The Phanerozoic average for sterane/hopane ranges between 0.5-2, which is consistent with the values reported in all layers here (Figure 4.27). Layers 2 and 5 have values >1, with all other layers <1. Values increase and decrease non-systematically throughout the core,

with maxima in layers 2, 5, and 11 and minima in layers 3, 7, and 9. Sterane/hopane values in P5AB are lower compared to values in P4n5, especially in the top two layers. However, the trend is similar with an initial decline from layer 1 through 4, a slight increase to layer 6, followed by a decline to layer 8. Layers 7 and 8 have almost identical values to layer 7 and 8 of P4n5.

4.1.4 Kerogen-bound aromatic biomarkers

Polyaromatic hydrocarbons (PAHs)

Polyaromatic hydrocarbons (PAHs) are usually products of reactions that occur during enhanced thermal maturity of organic matter, especially in thermally mature to overmature rocks and coals and principally arise from three different sources; pyrogenic, petrogenic, or diagenetic (Iqbal *et al.*, 2008). In this instance, reactions occurring during early diagenesis are responsible for the suite of PAHs found bound within the proto-kerogen of these samples, likely from cyclisation and rearrangement of aromatic carotenoids. A wide variety of non-volatile PAHs were identified based on their mass spectra and relative elution positions from 3-ring to 6-ring isomers and their variously alkylated homologues. These include 1) 3-ring PAHs such as fluorenes and methylfluorenes, and aromatic heterocyclic compounds including carbazoles and methylcarbazoles, and 2) regular 3- to 6-ring PAHs such as phenanthrenes and
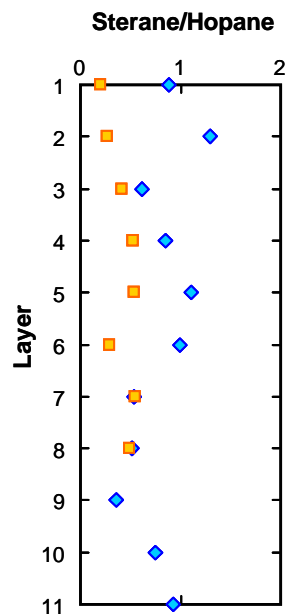
Sterane/Hopane

Figure 4.27. Kerogen-bound sterane /hopane ratio for P4n5 (blue) and P5AB (orange) with depth. Steranes calculated as the sum of C_{27}-C_{29} βααR and αααR isomers and hopanes as sum of C_{27}, C_{29}-C_{35} αβR, βαR, and ββR isomers.

158

methylphenanthrenes, anthracenes and methylanthracenes, binapthyls and phenylphenanthrenes, chrysenes and methylchrysenes, triphenylene, benzoanthracenes, dibenzoanthracenes, methylbenzoanthracenes, fluoranthene, pyrene and methylpyrenes, benzopyrenes, perylene, benzofluoranthenes, and coronene and methylcoronenes. Figure 4.28 shows an example of the variety of PAHs found in some of these layers, in this case P4n5 layer 8. P4n5 showed abundant and persistent PAHs in all layers, whereas P5AB has predominantly the lower molecular weight PAHs in all layers with the higher ring systems only dominant in the surface layers and not at depth. The distribution of cyclopenta-containing PAHs in layer 8 of P4n5 shows a slightly more rearranged/altered distribution than what it usually expected from immature kerogens. We observe greater abundance of fluoranthene [10] compared to pyrene [11], lower abundance of perylene [15], and greater abundance of indeno[1,2,3-cd]pyrene [20] where in immature kerogens benzo[g,h,i]perylene [21] usually dominates. Upper surface layers of P4n5 where the progression of 3-ring to 6-ring PAHs is most prominent and persistent throughout the core, show slightly less rearranged/mature distribution of PAHs, tracking the alteration of PAHs during diagenesis.
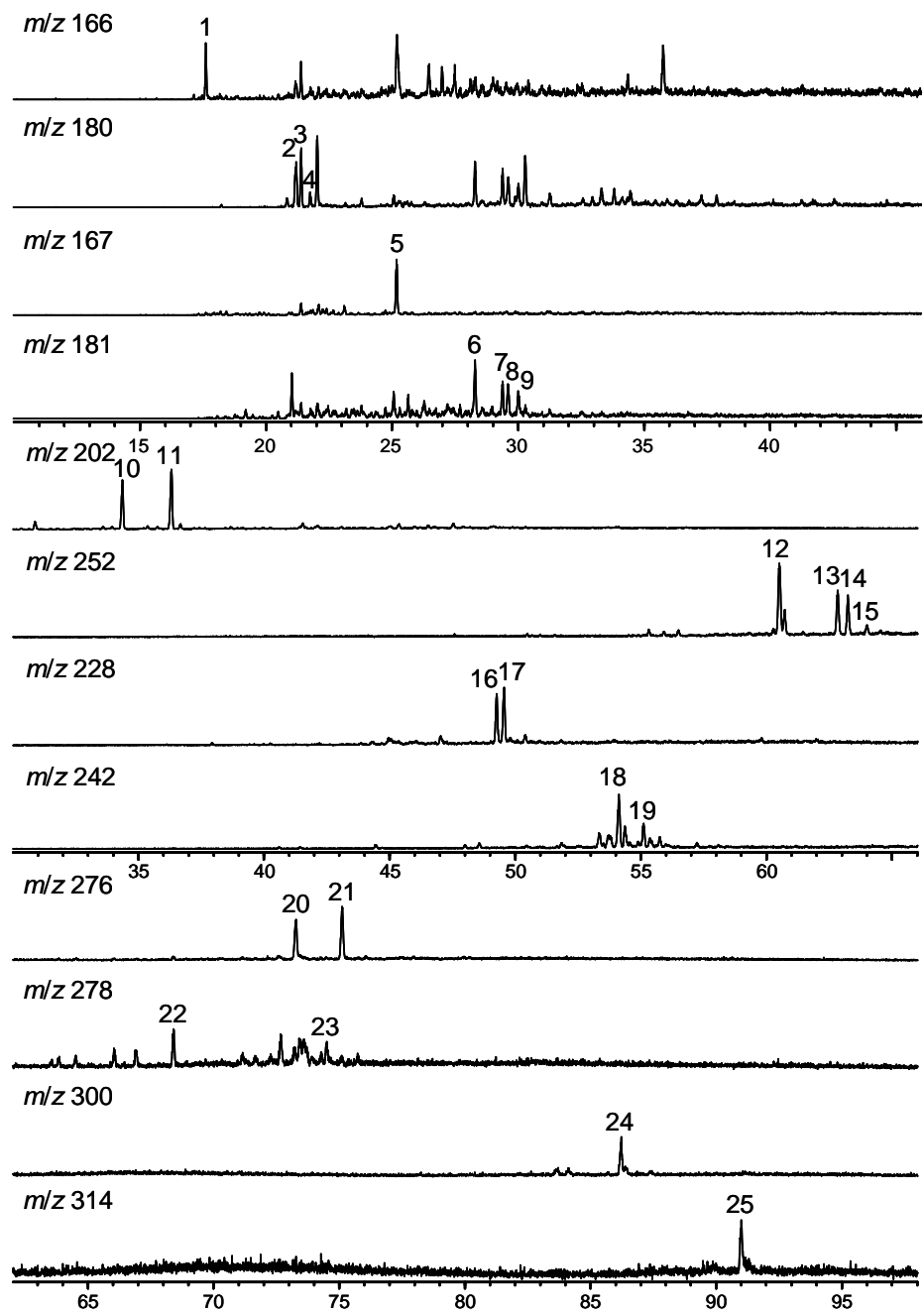
Figure 4.28. Partial ion chromatograms of representative kerogen-bound PAHs from P4n5 layer 8. Peak identifications as follows: [1] fluorene; [2] 2- and 3-methylfluorene; [3] 1-methylfluorene; [4] 6-methylfluorene; [5] carbazole; [6] 1-methylcarbazole; [7] 3-methylcarbazole; [8] 2-methylcarbazole; [9] 4-methylcarbazole; [10] fluoranthene; [11] pyrene; [12] benzo[k]fluoranthene; [13] benzo[e]pyrene; [14] benzo[a]pyrene; [15] perylene; [16] benzo[a]anthracene; [17] chrysene; [18] 6-methylchrysene; [19] 1-methylchrysene; [20] indeno[1,2,3-cd]pyrene; [21] benzo[g,h,i]perylene; [22] dibenzo[a,j]anthracene; [23] picene; [24] coronene; and [25] methylcoronene.

160

Arylisoprenoids

Arylisoprenoids are the diagenetic fragmentation products of aromatic carotenoids such as isorenieratene, chlorobactene, or okenone (Summons & Powell, 1987). They can also be generated as intermediates from the cyclisation and rearrangement reactions of aliphatic carotenoids such as β-carotene (Koopmans *et al*., 1997; Sinninghe Damsté *et al*., 1997). Unless aromatic carotenoids can be sequestered through S-binding, they are readily cyclised and rearrange when pyrolysed. In full scan mode, aryl isoprenoids are below detectable limits, however, a large peak in the *m/z* 133 fragment ion channel could correspond to a C_{29} aryl isoprenoid, possessing characteristic 133/134 Da fragments as well as M+ of 400 Da.

Aromatic terpenoids

The cyclohexyl rings on steroids and hopanoids can be cyclised during diagenesis and preserved in sedimentary organic matter (Liao *et al*., 2015). This can occur in a single ring of the terpenoid and even up to 3 (steroids) or 4 (hopanoids) rings. Although the MSD instrumentation was not sensitive enough to resolve aromatic hopanoids (in addition to the often large UCMs present in this fraction), aromatic steroids are found in some samples where a decent resolution was attainable. The main aromatic steroids found are C_{29} A-ring monoaromatic steroids (in *m/z* 211 from full scan chromatograms) with minor C_{27} (second most abundant) and C_{28} (minor) psuedohomologues. The dominant positional isomer in all cases is the 4-methyl (minor 1-methyl) isomer. These were most prominent in P5AB layer 7 (Figure 4.29), with all three homologues detectable

in layers 3-8 and none detected in P4n5. Ring C monoaromatic and triaromatic steroids were not detected in kerogen pyrolysates.
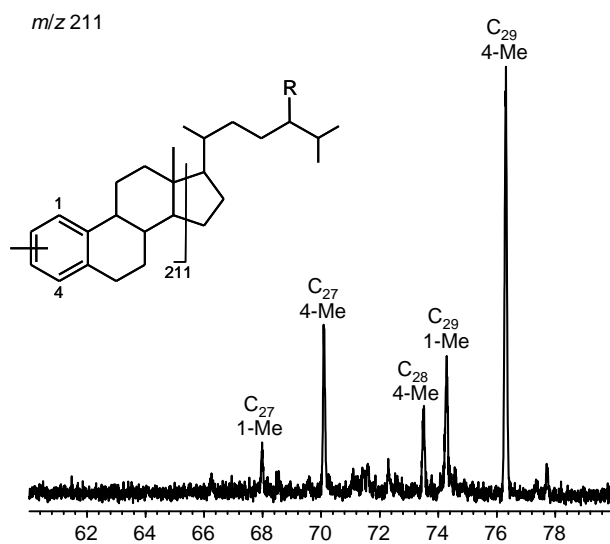
Figure 4.29. Partial *m/z* 211 ion chromatogram showing the presence of kerogen-bound A-ring monoaromatic steroids in P5AB layer 7. C_{27} (methyl-19-nor-cholestan-1,3,5(10)-triene), C_{28} (methyl-19-nor-ergosta-1,3,5(10)-triene), and C_{29} (methyl-19-nor-stigmasta-1,3,5(10)-triene) 1-methyl and 4-methyl isomers. R = H (C_{27}); Me (C_{28}); and Et (C_{29}).

4.1.5 Facies changes captured by extended hopane side-chain preservation

The transition from layer 7 to layer 8 in P4n5 occurs with a change in lithology from gelatinous mat textures rich in EPS to the first appearance of a coarse, gravelly texture. In P4n5, layer 7 shows C_{32} $\beta\beta R$ hopane as the dominant hopane homologue, with lower relative abundances of C_{33}-C_{35} $\beta\beta R$ (Figure 4.30). Layer 8 shows an increase in C_{34} and C_{35} $\beta\beta R$ hopanes. A similar profile is also seen in the transition between layer 6 and layer 7 for P5AB (Figure 4.29). This result suggests that the lower portion of this core where the transition between higher abundances of extended hopane side-chain binding indicates a facies that is more saline or sulfidic, as these conditions promote the preservation of the extended side-chain (particularly C_{35}) during diagenesis (Farrimond *et al*., 2003). In this scenario, we should observe more abundant archaeol (we see an increase in both extractable free archaeol (Figure 4.8F) and kerogen-bound biphytane (Figure 4.16D) in layers below 7 compared with those from above) and less abundant eukaryotic sterols after layer 7, which is also the case. Importantly to note, P5AB was collected 9 years after P4n5, the timing difference of which represents roughly one typical sedimentary layer (in thickness, assuming average sedimentary and organic accumulation and degradation rate). The years that this zone of enhanced preservation of the extended hopane side-chain likely represents a time period in which the pond experienced higher salinity or sulfidic conditions which allowed better preservation of intact C_{32}-C_{35} $\beta\beta$ hopanes.
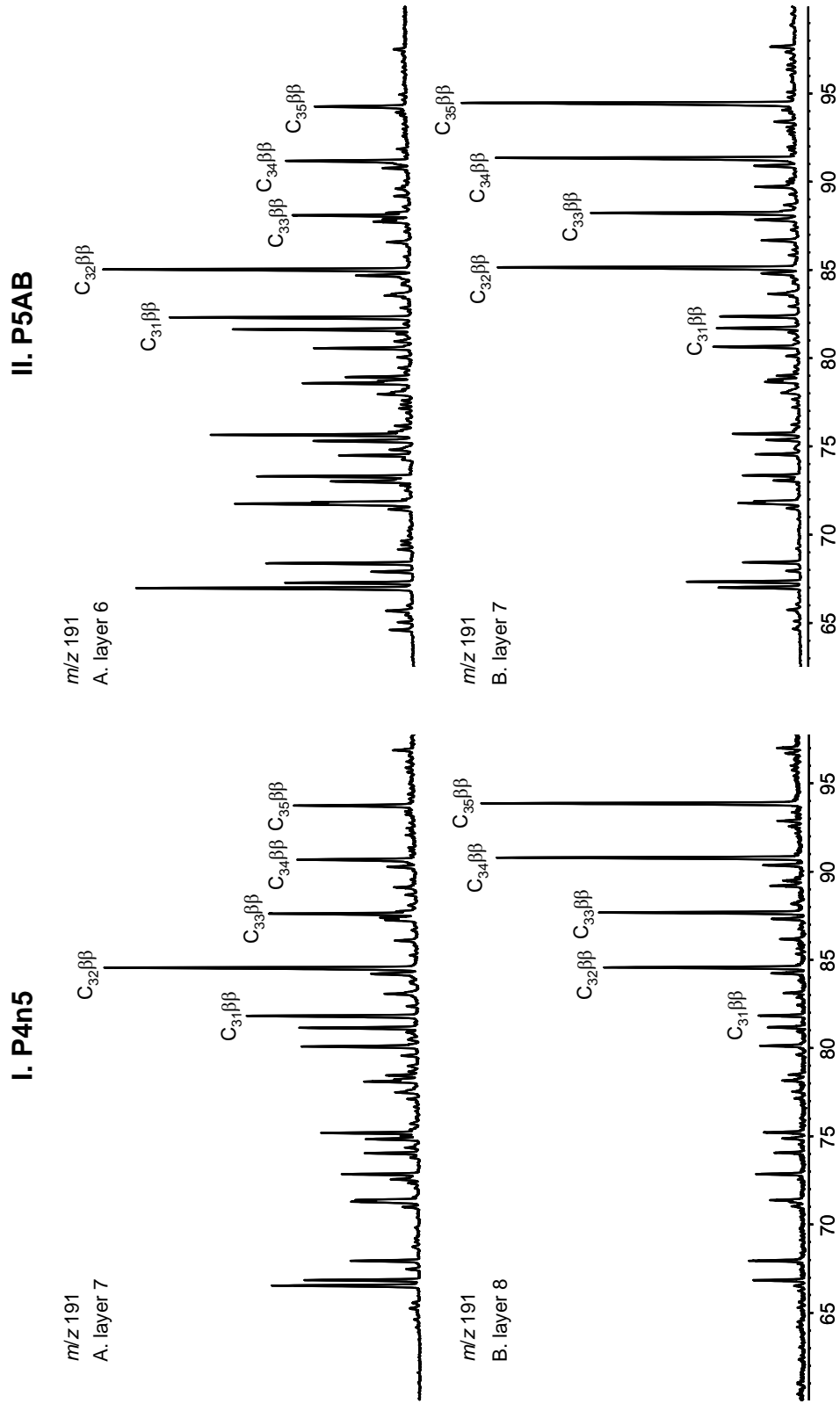
Figure 4.30. Partial ion chromatograms (*m/z* 191) showing the differences of kerogen-bound extended homohopanes of I: P4n5 A) layer 7 and B) layer 8; and II: P5AB A) layer 6 and B) layer 7.

4.1.6 Effect of salinity and microbial population on the incorporation of lipids during kerogen formation

All three domains of life are represented in these microbial mats. The results of conventional extractable lipids and their kerogen-bound hydrocarbon equivalents directly reflect the changing microbial populations with depth. Even with a small increase in salinity (going from 9-9.1 wt% to 11.2 wt% between the two cores), there are shifts in microbial population discernible through visual inspection of the cores (Figure 4.3), for example, the P5AB exhibits a discrete purple layer of PSB not evident in P4n5. Additionally, with the slight increase in salinity, the dominant surface primary producers switches from being dominated by orange surface layer cyanobacteria and diatoms and the green filamentous cyanobacterium, *Microcoleus chthonoplastes*, to carotenoid-producing (purple colouration) photoautotrophs and other halotolerant cyanobacterial species, potentially *Halospirulina*, *Phormidium*, and *Euhalothece*. Although we are yet to characterise the IPL composition of the higher salinity at site P5AB, it is immediately apparent changes in the bacterial population with depth are a reflection of the free and bound lipids with depth from P4n5.

The surficial layers (layers 1, 2, and 3) are dominated by cyanobacteria, exhibiting high concentrations of nC$_{17}$ and nC$_{17:1}$, highest total FAME recovery, abundant phytane, as well as maximum concentrations of stigmastanol (C$_{29}$ stanol) and tetrahymanol. Layer 3 is also marks the first appearance of BHP. These three layers would constitute the most active layers, and supported by kerogen-bound biomarkers, are

directly sequestered into kerogen as they are being biosynthesised. Layers 1, 2, and 3, are thin layers (only a few mm thick, representing about one to two years of organic deposition), so layer 4 is first layer of substantial thickness that is comprised of biomass directly biosynthesised from the upper active mat layer (more description in Chapter 5).

Layer 4 contains maximum concentrations of 10Me18:0, a marker for sulfate-reducing bacteria and maximum 2-methyltetrahymenol (2MeTOH), a methylated compound biosynthesised by the purple non-sulfur bacteria (PNS; *Bradyrhizobium* species), but potentially closely related to *Rhodopseudomonas palustris* (Bravo *et al*., 2001). This is consistent with the surface mat layer being underlain by a microaerophilic and anaerobic anoxygenic phototrophic layer if 2MeTOH is, indeed, being biosynthesised by PNS. This layer of filamentous anoxygenic phototrophs (FAPs) that is dominated by species such as *Chloroflexus* and *Chlorothrix*, but also include green sulfur bacteria, *Chlorobium*, purple sulfur bacteria, *Chromatium*, colourless sulfur bacteria, *Beggiatoa*.

Moving further into the mat, layer 5 and 6 possess the highest concentrations of tricyclic terpenes, specifically five isomers of $C_{20:1}$ (as $C_{x:y}$, where x indicated the number of carbon atoms and y indicates the number of unsaturations) based on comparisons with previously published literature (Greenwood *et al*., 2000). Although there is no definitive biological source organisms for tricyclic terpenoids (terpanes), their abundance in *Tasmanites*-sourced oils led some to believe they are biosynthesised by *Tasmanites* prasinophyte algae (e.g., Tappan, 1980). They have also been found as pyrolysate products from another genus of prasinophyte, *Leiosphaeridia*, thus their presence in

environmental samples cannot be due solely to *Tasmanites* (Dutta *et al*., 2006). There is a decline in tricyclic terpenoids by layer 7.

The lower portions of layer 7 marks the mineralogical transition of previously EPS-dominated mat layer to a texture that is coarse and filled with noticeable gravel-sized particles. As discussed above, layer 8 shows more prominent side-chain BHP preservation, acyclic biphytane, and gammercane coupled with lower abundances of eukaryotes sterols, overall pointing to a more saline and sulfidic facies. Layer 9 marks the first appearance of vinyl ether dimethylacetals, sourced from Gram-positive anaerobic bacteria, *Clostridia*. These dimethylacetals show maximal concentrations at layers 10 and 11. This is in concert with sulfate reduction and fermentation processes in the lower sedimentary portions of the microbial mat, with some *Clostridia* species known to ferment glycerol. Although we do not have comparisons of IPL from P5AB, the molecular profiles of kerogen-bound biomarkers show subtle differences reflecting an increase in salinity. Overall differences that support this include lower sterane/hopane ratios, higher hopenes, higher 3β-methylhopanes, lower Pr/Ph ratios, higher isoprenoids such as regular iC_{25}, squalane, and acyclic biphytane possibly derived from halophilic archaea. This is most prominent in the lower mat layers (particular layers 6, 7, and 8) in P5AB which show evidence for bound carotenoids.

The major geochemical differences in P4n5 and P5AB are that P5AB, the higher salinity core, shows a greater source inputs from archaea (Figure 4.16) with more abundant phytane, regular C_{25} isoprenoid, squalane, and biphytane. Although IPLs for

P5AB have not been analysed yet, we expect to find more free archaeol and hydroxyarchaeol. Due to being at slightly elevated salinity, P5AB shows some evidence for carotenoids, either as rearranged products or potentially hydrocarbon fragments. The high molecular weight region of layer 7, in particular, shows an abundance of compounds with 558 and 560 ions, as well as the characteristic m/z 125 fragment. Despite some distinct differences, most of the geochemical and bound lipid biomarker trends are quite similar with depth, especially for steranes and hopanes.

Here we present a microbial community structure model based on data from this study and previously characterised sections from GN showing the differences between the two cores (Figure 4.31). The main point of this figure is to highlight that the microbial mats are not homogenous and organic matter is not solely derived from primary productivity at the surface. Even though salinity exerts a greater control on the populations at the surface, there are distinct trends with depth.
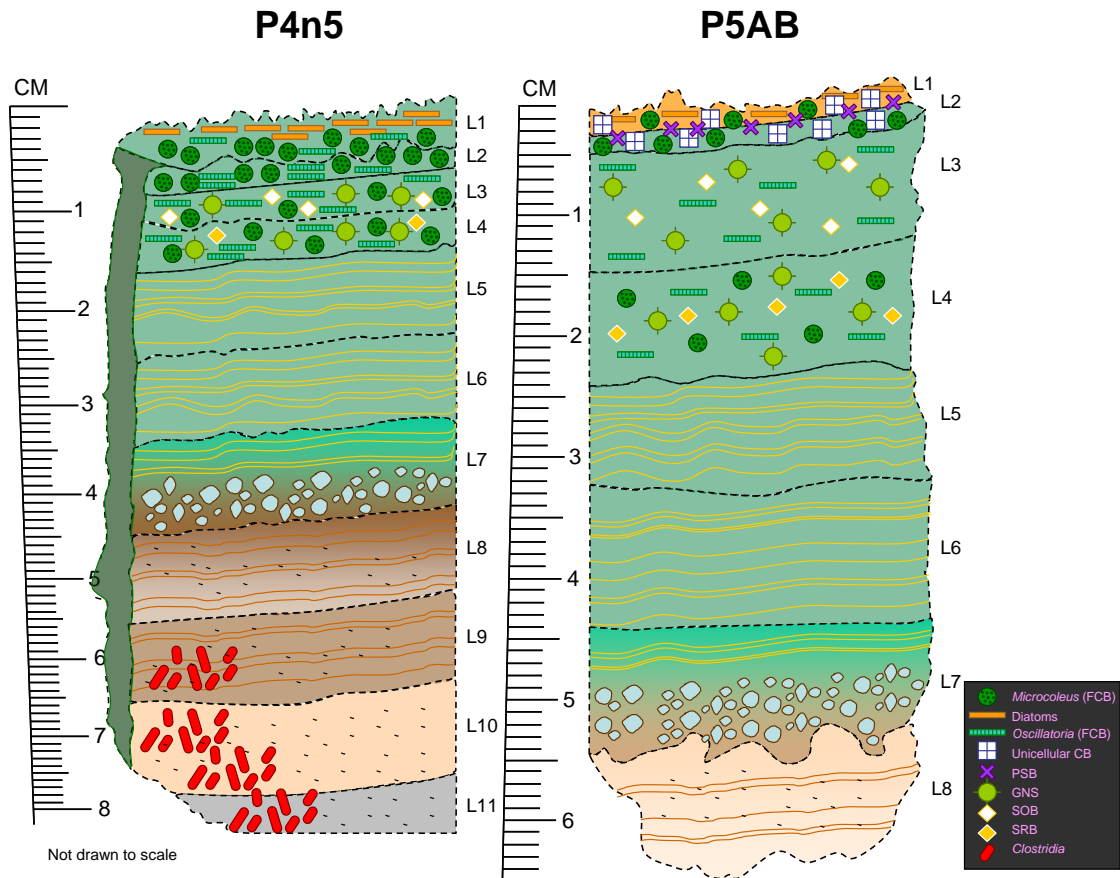
Figure 4.31. Microbial community structure model of A) Pond 4 (P4n5) and B) Pond 5 (P5AB) from Guerrero Negro, Baja California, Mexico. Microbial communities are not drawn to scale. Legend on the right: green dotted circles = *Microcoleus chthonoplastes* (FCB); orange bars = diatoms; blue/green striped bars = *Oscillatoria* (FCB); FCB = filamentous cyanobacteria; white squares with blue crosses = unicellular cyanobacteria; purple crosses = purple sulfur bacteria (PSB); green squares = green non-sulfur bacteria *Chloroflexus* (GNS); white diamonds = sulfide oxidising bacteria (SOB) *Beggiatoa*; yellow diamonds = sulfate reducing bacteria (SRB); and red rods = Gram-positive anaerobic bacteria *Clostridia*. Yellow lines represent gelatinous EPS matrix with filamentous anoxygenic phototrophs and fermenters extending to these zones. Brown lines represent sedimentary layers with particulate (grey) gravel and shell fragments interspersed.

5. Investigating the 'mat-seal hypothesis' and implications for the ancient record

Organic matter preserved in the Proterozoic has different organic geochemical characteristics compared to organic matter preserved in Phanerozoic rock samples. This is largely as result of the evolution and succession of primary producers in the oceans that are a direct reflection of secular trends that indicate prokaryotic communities being dominant in the early stages of the Proterozoic before a rise in eukaryotic organisms and complex animals as biological and environmental evolution progressed. In the Proterozoic, organic matter is generally characterised as exhibiting the following features: low pristane and phytane, high unresolved complex mixtures (UCMs), abundant mono- and dimethylalkanes, and non-detectable or low abundances of eukaryotic steranes (Pawlowska *et al.*, 2013).

A study published in 2013 by Pawlowska and colleagues hypothesised that the characteristic organic matter composition, even from well-preserved and syngenetic Proterozoic samples from shallow marine environments, is a reflection of non-actualistic taphonomic preservation which was termed the 'mat-seal hypothesis'. This hypothesis states that when microbial mats dominated a vast majority of Proterozoic shelves, the geochemical features described above are due to preferential preservation of organic matter derived from the benthic/heterotrophic lower layers of the microbial mat, as the incoming planktonic signal from photoautotrophs is remineralised rapidly due to highly oxidising conditions at the mat surface. Hence, the surface layers created a mechanical *sealing* effect that had profound implications for the fate and transfer of organic matter

from the site of production into the sedimentary record. This mat-sealing effect was 'broken' with the consequent rise of bioturbating/burrowing organisms in the Ediacaran/Cambrian—'Cambrian substrate revolution', although recent studies suggests this didn't occur significantly until the early Paleozoic (Tarhan *et al*., 2014; Tarhan *et al*., 2015) such that younger, Phanerozoic organic matter preserves a geochemical signature derived from primary producers such as planktonic bacteria and algae, as they are able efficiently export organic matter through faecal pellet sedimentation. Phanerozoic rocks exhibit lower UCMs, mono- and dimethylalkanes, and higher eukaryotic steranes, however the low abundance of steranes in older sedimentary rocks could be a result of primary ecological absence rather than a taphonomic mat-seal effect. Additionally, high UCMs in the Proterozoic could be derived from diagenesis of a long-lived dissolved organic matter (DOM) pool from planktonic production (e.g., Lee *et al*., 2015), rather than being solely sourced from benthic production, as that would require the primary mode of production on the deep seafloor to be chemosynthetic.

A more recent study looked at the kerogen-bound lipid fraction of modern calcifying microbial mats (oldest investigated layer has a ^{14}C age of 1,440 years BP) from a lacustrine hypersaline setting to investigate the validity of the mat-seal effect. They found that although lipid fatty acids were transformed during diagenesis, their fatty acid acyl hydrocarbon moieties did not get incorporated into proto-kerogen. Additionally supported by high hopane/sterane ratios in the deeper portion of the mat, they use this as evidence to show that there was a taphonomic mat-seal effect on the preservation of organic matter (Blumenberg *et al*., 2015). The aim of this geochemical study was to

solely address the fate of organic matter produced in the surface layer and track its transformation and/or incorporation into kerogen during diagenesis, thus the microbial community containing source organisms responsible for generating the molecular profiles below the photosynthetically active layers was not characterised or addressed. While it is appreciated that this was beyond the scope of this investigation—which solely sought to confirm or deny the features of the mat-seal hypothesis—this is important factor to consider because microbial mat compositions are inherently heterogeneous and therefore inputs derived from lower layers—not just the surface—also need to be considered. Hopane/sterane ratios, which provide a first order assessment of the contributions of bacterial to eukaryotic inputs into preserved organic matter, reach very high values at the base of the mat (~100). However, the layer directly above it shows a value closer to the surface of the mat (~3). To understand the high value at the base of the mat, it would be helpful if the authors provided some representative chromatograms or indicated which hopane and sterane isomers were used to calculate these ratios.

Since comprehensive studies of modern microbial mats looking at both the extractable and non-extractable lipid profiles is rare, this could provide a unique opportunity to compare these two microbial mat settings to gain a deeper understanding of the fate and transformation of microbial lipids during sedimentary diagenesis. It would be especially beneficial in this instance because it would be comparing a higher temporal resolution to one that extends back to ~1,500 years BP. Since these two sites are so different, it would contrast a lacustrine setting with carbonate matrix and slow sediment accumulation rates to a marine setting with upper layers dominated by EPS and lower

layers consisting of sand, silt, gravel, and gypsum/sulfidic black mud with rapid sedimentation rates. It is difficult to assess or compare molecular profiles of this study with our results when the only chromatogram they show represents about the first 30-45 mins of one layer of one treatment (HyPy fraction). Technicalities aside, these sorts of comparative studies to understand what happens to organic matter after it leaves the biosphere and enters the geosphere are the foundations that provide analytical and interpretative frameworks for understanding the dynamics and evolution of microbial ecosystems.

The study presented here also investigated the kerogen-bound lipids of modern marine microbial mats to see whether polycyclic biomarkers such as steroids and hopanoids (and their diagenetic geolipids steranes and hopanes) were efficiently remineralised at the mat surface and did not get incorporated *via* natural vulcanisation reactions into proto-kerogen during diagenesis. For one of the cores, we compared these kerogen-bound lipids to extractable intact polar lipids, which show similar increasing concentration of sterols/steranes and hopanoids/hopanes with depth. The major findings of this study indicate that sterols (steranes) and hopanoids (hopanes) are rapidly incorporated into kerogen very early during diagenesis and are not efficiently degraded in the surface of the microbial mat. The observation of this rapid binding into kerogen on such short timescales as 20-40 years is remarkable and expected to increase over time. A study by Farrimond and colleagues (2003) showed that the %bound hopanes (as a percentage of total free and bound hopanes) increases with depth over tens to hundreds of years. Figure 4.32 shows the %bound of steranes (Figure 4.32A) and hopanes (Figure

173

4.32B) from P4n5, showing the same increasing trend with time (Figure 4.32; Farrimond *et al*., 2003). The absolute abundance of each compound class is likely reflecting the source contribution of precursor organisms to the overall pool of organic matter. The geochemical profiles of steranes and hopanes are similar to one another which indicate that the timing of incorporation into kerogen was similar and the mat sediments did not preserve one terpenoid preferentially over the other. Additional evidence from chemolysis experiments (expanded upon in detail in Chapter 5) indicates that even though strong oxidative treatment, which may be similar to those experienced at photosynthetically-active microbial mat surfaces, on pre-extracted residues removes a large portion of sterols, steranes can be still recovered in small amounts that were bound in macromolecular phases (Appendix Table A4.10 and Appendix Figure A4.3).
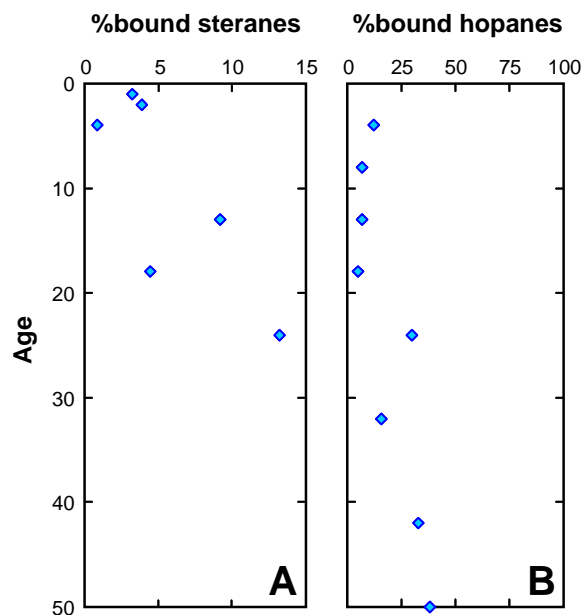
Figure 4.32. Downcore trends of A) %bound steranes (calculated as a percentage of the sum of total free sterols/steranes/sterenes and total bound steranes/sterenes), and B) %bound hopanes (calculated as a percentage of the sum of total free hopanoic acids/hopanes/hopenes and total bound hopanes/hopenes).

Overall, there may be some merit to the mat-seal hypothesis and it is likely that the signatures preserved reflect, to some degree, a taphonomic bias. However the statement that none of the eukaryotic organic matter produced in the surface ocean gets preserved during diagenesis is exaggerated and an example from the modern record which we believe is reflecting actualistic taphonomy comes from the dataset that we present here.

6. Conclusions

This study investigated the distribution of lipid biomarkers *via* catalytic hydropyrolysis on pre-extracted IMOM residues in two microbial mat cores from two well-studied salt ponds of differing salinity—P4n5 and P5AB. Catalytic hydropyrolysis of kerogen is a proven analytical technique that is rapid and generates abundant saturated pyrolysate products from the bound biomarker pool without altering the structures or stereochemistries of the products (e.g. Love *et al*., 1995, 1996, 1998). Additionally, for P4n5 (the lower salinity core), we compared the bound lipid biomarkers to the extractable intact polar lipid composition. Molecular profiles from the two pond environments were significantly different and reflect the contributions of different photosynthetic and respiratory microbial communities to the preserved organic matter, for example the higher salinity pond shows evidence of greater archaeal inputs as well as kerogen-bound carotenoids/carotenoid rearranged products or fragments. Our results indicate that lipid binding into IMOM *via* strong covalent linkages occurs very early during sedimentary diagenesis (Farrimond *et al*., 2003). A variety of polycyclic biomarkers classes, such as

steranes and hopanes, can be sequestered and preserved within the mat sediment IMOM beneath the extant photosynthetic layers through geological time. Ultimately, these bound lipids will be regenerated as recognisable *free* biomarker hydrocarbons during catagenesis of sediments after protracted burial and maturation; meaning that significant taphonomic bias with respect to preservation of steroid or other biomarker classes is unlikely during intervals of Earth history when benthic organic mat inputs are pronounced.

References

Amo, M., Suzuki, N., Shinoda, T., Ratnayke, N. P., and Takashi, K. 2007. Diagenesis and distribution of sterenes in Late Miocene to Pliocene marine siliceous rocks from Horonobe (Hokkaido, Japan). *Organic Geochemistry* 38(7), 1132-1145.

Bebout, B. M., Carpenter, S. P., Des Marais, D. J., Discipulo, M., Embaye, T., Garcia Pichel, F., Hoehler, T. M., Hogan, M., Jahnke, L. L., Keller, R. M., Miller, S. R., Prufert-Bebout, L. E., Raleigh, C., Rothrock, M., and Turk, K. 2002. Long-term manipulations of intact microbial mat communities in a greenhouse collaborator: simulating Earth's present and past field environments. *Astrobiology* 2, 383-402.

Bishop, A. N., Love, G. D., Mcaulay, A. D., Snape, C. E., and Farrimond, P. 1998. Release of kerogen-bound hopanoids by hydropyrolysis. *Organic Geochemistry* 29(4), 989-1001.

Bligh, E. G., Dyer, W. J. 1959. A rapid method of total lipid extraction and purification. *Canadian Journal of Biochemistry and Physiology* 37, 911-917.

Blumenberg, M., Thiel, V., and Reitner, J. 2015. Organic matter preservation in the carbonate matrix of a recent microbial mat – is there a mat-seal effect? *Organic Geochemistry* 87, 25-34.

Brassell, S. C., McEvoy, J., Hoffmann, C. F., Lamb, N. A., Peakman, T. M., and Maxwell, J. R. 1995. Isomerisation, rearrangement, and aromatisation of steroids in distinguishing early stages of diagenesis. *Organic Geochemistry* 6(11), 11-23.

Bravo, J-M., Perzl, M., Härtner, T., Kannenberg, E. L., and Rohmer, M. 2001. Novel methylated triterpenoids of the gammacerane series from nitrogen-fixing bacterium *Bradyrhizobium japonicum* USDA 110. *European Journal of Biochemistry* 268, 1323-1331.

Canfield, D. E., and Des Marais, D. J. 1993. Biogeochemical cycles of carbon, sulfur, and free oxygen in a microbial mat. *Geochimica et Cosmochimica Acta* 57, 3971 3984.

Chitwood, D. J., Lozano, R., and Lusby, W. R. 1986. Recent developments in nematode steroid biochemistry. *Journal of Nematology* 18, 9-17.

Conte, M. H., Madureira, L. A. S., Eglinton, G., Keen, D., Rendall, C. 1994. Millimeter scale profiling of abyssal marine sediments: role of bioturbation in early sterol diagenesis. *Organic Geochemistry* 22(6), 979-990.

Des Marais, D. J., Cohen, Y., Nguyen, H., Cheatham, M., Cheatham, T., Munoz, E. 1989. Carbon isotopic trends in the hypersaline ponds and microbial mats at Guerrero Negro, Baja California Sur, Mexico: Implications for Precambrian stromatolites. In: *Microbial Mats – Physiological ecology of benthic microbial communities* (eds. Cohen, Y., and Rosenberg, E.), American Society of Microbiology, Washington DC, 191-203.

Des Marais, D. J. 1991. Microbial mats, stromatolites, and the rise of oxygen in the Precambrian atmosphere. *Paleogeography, Paleoclimatology, Paleoecology* **97**, 93-96.

Des Marais, D. J., D'Amelio, E., Farmer, J. D., Jorgensen, B. B., Palmisano, A. C., Pierson, B. K. 1992. Case study of a modern microbial mat-building community: the submerged cyanobacterial mats of Guerrero Negro, Baja California Sur, Mexico. In: *The Proterozoic Biosphere: A multidisciplinary study* (eds. Schopf, J. W., and Klein, C.), Cambridge University Press, New York, 325-334.

Des Marais, D. J. 1995. The biogeochemistry of hypersaline microbial mats. In: *Advances in Microbial Ecology* (ed. Jones, J. G.), Plenum, New York, 251-274.

Des Marais, D. J. 2003. Biogeochemistry of hypersaline microbial mats illustrates the dynamics of modern microbial ecosystems and the early evolution of the biosphere. *Biological Bulletin* **204**, 160-167.

Des Marais, D. J. 2010. Marine hypersaline *Microcoleus*-dominated cyanobacterial mats in the saltern Guerrero Negro, Baja California Sur, Mexico. In: *Microbial Mats* (eds. Seckbach, J., and Oren, A.), Cellular Origins, Life in Extreme Habitats and Astrobiology (COLE) Series, Springer, **14**, 401-420.

Dutta, S., Greenwood, P. F., Brocke, R., Schaefer, R. G., and Mann, U. 2006. New insights into the relationship between Tasmanites and tricyclic terpenoids. *Organic Geochemistry* **37**, 117-127.

Farmer, J. 1992. Grazing and bioturbation in modern microbial mats. In: *The Proterozoic Biosphere: A multidisciplinary study* (eds. Schopf, J. W., and Klein, C.), Cambridge University Press, New York, 295-297.

Farrimond, P., Love, G. D., Bishop, A. N., Innes, H. E., Watson, D. F., Snape, C. E. 2003. Evidence for the rapid incorporation of hopanoids into kerogen. *Geochimica et Cosmochimica Acta* **67**(7), 1383-1394.

Goldfine, H., and Panos, C. 1971. Phospholipids of *Clostridium butyricum.* IV Analysis of positional isomers of monounsaturated and cyclopropane fatty acids and alk-1'

enyl ethers by capillary column chromatography. *Journal of Lipid Research* **12**, 214-220.

Greenwood, P. F., Arouri, K. R., and George, S. C. 2000. Tricyclic terpenoid composition of Tasmanites kerogen as determined by pyrolysis GC-MS. *Geochimica et Cosmochimica Acta* **64**, 1249-1263.

Grice, K., Schouten, S., Nissenbaum, A., Charrach, J., and Sinninghe Damsté, J. S. 1998. Isotopically heavy carbon in the C_{21} to C_{25} regular isoprenoids in halite-rich deposits from the Sdom Formation, Dead Sea Basin, Israel. *Organic Geochemistry* **28**(6), 349-359.

ten Haven, H. L., de Leeuw, J. W., and Schenck, P. 1985. Organic geochemical studies of a Messinian evaporitic basin, northern Apennines (Italy) I: Hydrocarbon biological markers for a hypersaline environment. *Geochimica et Cosmochimica Acta* **49**, 2181-2191.

ten Haven, H. L., Rohmer, M., Rullkötter, J., and Bisseret, P. 1989. Tetrahymanol, the most likely precursor of gammacerane, occurs ubiquitously in marine sediments. *Geochimica et Cosmochimica* Acta **53**, 3073-3079.

Houghton, J., Fike, D. A., Druschel, G., Orphan, V. J., Hoehler, T. M., and Des Marais, D. J. 2014. Spatial variability in photosynthetic and heterotrophic activity drives localised $\delta^{13}C_{org}$ fluctuations and carbonate precipitation in hypersaline microbial mats. *Geobiology* **12**(6), 557-574.

Huang, X., Wang, C., Xue, J., Meyers, P. A., Zhang, Z., Tan, K., Zhang, Z., and Xie, S. 2010. Occurrence of diploptene in moss species from the Dajiuhu Peatland in southern China. *Organic Geochemistry* **41**(3), 321-324.

Iqbal, J., Overton, E. B., and Gisclair, D. 2008. Sources of polyaromatic hydrocarbons in Louisiana rivers and coastal environments: principle component analysis. *Environmental Forensics* **9**, 310-319.

Jahnke, L. L., Stan-Lotter, H., Kato, K., Hochstein, L. I. 1992. Presence of methyl sterol and bacteriohopanepolyol in an outer-membrane preparation from *Methylococcus capsulatus* (Bath). *Journal of General Microbiology* **138**, 1759-1766.

Jahnke, L. L., Embaye, T., Hope, J., Turk, K. A., Van Zuilen, M., Des Marais, D. J., Farmer, J. D., Summons, R. E. 2004. Lipid biomarkers and carbon isotopic signatures for stromatolite-forming microbial mat communities and *Phormidium* cultures from Yellowstone National Park. *Geobiology* **2**, 31-47.

Jahnke, L. L., Orphan, V. J., Embaye, T., Turk, K. A., Kubo, M. D., Summons, R. E., Des Marais. D. J. 2008. Lipid biomarker and phylogenetic analyses to reveal archaeal biodiversity and distribution in hypersaline microbial mat and underlying sediment. *Geobiology* **6**, 394-410.

Jahnke, L. L., Turk-Kubo, K. A., Parenteau, M. N., Green, S. J., Kubo, M. D. Y., Vogel, M., Summons, R. E., and Des Marais, D. J. 2014. Molecular and lipid biomarker analysis of a gypsum-hosted endoevaporitic microbial community. *Geobiology* **12**, 62-82.

Knoll, A. H. 1985. A paleobiology perspective on sabkhas. In: *Hypersaline Ecosystems The Gavish Sabkha* (eds. Friedman, G. M., and Krumbein, W. E.), Springer Verlag, Heidelberg, 407-425.

Koga, Y., Morii, H. 2007. Biosynthesis of ether-type polar lipids in Archaea and evolutionary considerations. *Microbiology and Molecular Biology Reviews* **71**(1), 97-120.

Koopmans, M. P., de Leeuw, J. W., Sinninghe Damsté, J. S. 1997. Novel cyclised and aromatised diagenetic products of β-carotene in the Green River Shale. *Organic Geochemistry* **26**(7-8), 451-466.

Lee, C., Brocks, J. J. 2011. Identification of carotane breakdown products in the 1.64 billion year old Barney Creek Formation, McArthur Basin, northern Australia. *Organic Geochemistry* **42**, 425-430.

Lee, C., Love, G. D., Fischer, W. W., Grotzinger, J. P., and Halverson, G. P. 2015. Marine organic matter cycling during the Ediacaran Shuram excursion. *Geology* **43**(12), 1103-1106.

Ley, R. E., Harris, J. K., Wilcox, J., Spear, J. R., Miller, S. R., Bebout, B. M., Maresca, J. A., Bryant, D. A., Sogin, M. L., Pace, N. R. 2006. Unexpected microbial diversity and complexity of the Guerrero Negro hypersaline microbial mat. *Applied and Environmental Microbiology* **72**(5), 3685-3695.

Liao, J., Lu, H., Sheng, G., Peng, P., and Hsu, C. S. 2015. Monoaromatic, diaromatic, triaromatic, and tetraaromatic hopanes in Kukersite Shale and their stable carbon isotopic composition. *Energy Fuels* **29**(6), 3573-3583.

Love, G. D., Snape, C. E., Carr, A. D., Houghton, R. C. 1995. Release of covalently bound alkane biomarkers in high yields from kerogen *via* catalytic hydropyrolysis. *Organic Geochemistry* **23**(10), 981-986.

Love, G. D., Snape, C. E., Carr, A. D., Houghton, R. C. 1996. Changes in molecular biomarker and bulk carbon skeletal parameters of vitrinite concentrates as a function of rank. *Energy & Fuels* **10**, 149-157.

Love, G. D., Snape, C. E., Fallick, A. E. 1998. Differences in the mode of incorporation and biogenicity of the principle aliphatic constituents of a Type I oil shale. *Organic Geochemistry* **28**, 797-811.

Love, G. D., Bowden, S. A., Jahnke, L. L., Snape. C. E., Campbell, C. N., Day, J. G., Summons, R. E. 2005. A catalytic hydropyrolysis method for the rapid screening of microbial cultures for lipid biomarkers. *Organic Geochemistry* **36**, 63-82.

Mackenzie, A. S., Brassell, S. C., Eglinton, G., Maxwell, J. R. 1982. Chemical fossils: the geological fate of steroids. *Science* **217**, 491-504.

Marzi, R., Torkelson, B. E., and Olson, R. K. 1993. A revised carbon preference index. *Organic Geochemistry* **20**, 1303-1306.

McKirdy D. M., Kantsler A. J. 1980. Oil geochemistry and potential source rocks of the Officer Basin, south Australia. *Australian Petroleum Exploration Association Journal* **20**, 68-86.

Nübel, U., Garcia-Pichel, F., Clavero, E., Muyzer, G. 2000. Matching molecular diversity and ecophysiology of benthic cyanobacteria and diatoms in communities along a salinity gradient. *Environmental Microbiology* **2**(2), 217-226.

Oehler D. Z., Oehler J. H., Stewart A. J. 1979. Algal fossils from a late Precambrian, hypersaline lagoon. *Science* **205**, 388-390.

Orphan, V. J., Jahnke, L. L., Embaye, T., Turk, K. A., Pernthaler, A., Summons, R. E., Des Marais, D. J. 2008. Characterisation and spatial distribution of methanogens and methanogenic biosignatures in hypersaline microbial mats of Baja California. *Geobiology* **6**, 376-393.

Palmisano, A. C., Cronin, S. E., D'Amelio, D., Munoz, E., Des Marais, D. J. 1989. Distribution and survival of lipophilic pigments in a laminated microbial mat community near Guerrero Negro, Mexico. In: *Microbial Mats: physiological ecology of benthic microbial communities* (eds. Cohen, Y., and Rosenberg, E.), American Society for Microbiology, Washington DC, 138-152.

Pawlowska, M. M., Butterfield, N. J., and Brocks, J. J. 2013. Lipid taphonomy in the Proterozoic and the effect of microbial mats on biomarker preservation. *Geology* **41**, 103-106.

Peters, K.E., Walters, C.C., and Moldowan, J.M. 2005. *The Biomarker Guide*, 2nd edition: Cambridge University Press, Cambridge.

Philp, R. P., Li, J., and Lewis, C. A. 1989. An organic geochemical investigation of crude oils from Shanganning, Jianghan, Chaidamu, and Zhungeer Basins, People's Republic of China. *Organic Geochemistry* **14**(4), 447-480.

Rashby, S. E., Sessions, A. L., Summons, R. E., and Newman, D. K. 2007. Biosynthesis of 2-methylbacteriohopanepolyols by an anoxygenic phototroph. *Proceedings of the National Academy of Sciences of the United States of America* **104**, 15099 15104.

Robertson, C. E., Spear, J. R., Harris, J. K., and Pace, N. R. 2009. Diversity and stratification of Archaea in a hypersaline microbial mat. *Applied and Environmental Microbiology* **75**, 1801-1810.

Schidlowski, M., Gorzawski, H., and Dor, I. 1994. Carbon isotope variations in solar pond microbial mat: role of environmental gradients in steering variables. *Geochimica et Cosmochimica Acta* **58**, 2289-2298.

Schinteie, R. 2011. Ancient life at the extremes: molecular fossils and paleoenvironmental contexts of Neoproterozoic and Cambrian hypersaline settings. Ph.D dissertation, *The Australian National University*.

Schinteie, R., and Brocks, J. J. 2014. Evidence for ancient halophiles? Testing biomarker syngeneity of evaporites from Neoproterozoic and Cambrian strata. *Organic Geochemistry* **72**, 46-58.

Schouten, S., Hoefs, M. J. L., Koopmans, M. P., Bosch, H-J., and Sinninghe Damsté, J. S. 1998. Structural characterisation, occurrence and fate of archaeal ether-bound acyclic and cyclic biphytanes and corresponding diols in sediments. *Organic Geochemistry* **29**(5-7), 1305-1319.

Shen, Y., and Buick, R. 2004. Antiquity of microbial sulfate reduction. *Earth-Science Reviews* **64**, 243-272.

Sinninghe Damsté, J. S., Kenig, F., Koopmans, M. P., Köster, J., Schouten, S., Hayes, J. M., and de Leeuw, J. W. 1995. Evidence for gammacerane as an indicator of water column stratification. *Geochimica et Cosmochimica Acta* **59**(9), 1895 1900.

Sinninghe Damsté, J. S., Baas, M., Koopmans, M. P., and Geenevasen, J. A. J. 1997. Cyclisation, aromatisation, and expulsion reactions of β-carotene during sediment diagenesis. *Tetrahedron Letters* **38**, 2347-2350.

Spear, J. R., Ley, R. E., Berger, A. B., Pace, N. R. 2004. Complexity in natural microbial ecosystems: The Guerrero Negro experience. *Biological Bulletin* **204**(2), 168-173.

Summons, R. E., and Powell, T. G. 1987. Identification of aryl isoprenoids in source rocks and crude oil: Biological markers for green sulphur bacteria. *Geochimica et Cosmochimica Acta* **51**(3), 557-566.

Summons, R. E., Jahnke, L. L., Hope, J. M., Logan, G. A. 1999. 2-Methylhopanoids as biomarkers for cyanobacterial oxygenic photosynthesis. *Nature* **400**, 554-557.

Tappan, H. 1980. The paleobiology of plant protists. W. H. Freeman & Co., San Francisco, CA.

Tarhan, L. G., and Droser, M. L. 2014. Widespread delayed mixing in early to middle Cambrian marine shelfal settings. *Paleogeography, Paleoclimatology, and Paleoecology* **399**, 310-322.

Tarhan, L. G., Droser, M. L., Planavsky, N. J., and Johnston, D. T. 2015. Protracted development of bioturbation through the early Paleozoic Era. *Nature Geoscience* **8**, 865-869.

Welander, P. V., Hunter, R. C., Zhang, L., Sessions, A. L., Summons, R. E., and Newman, D. K. 2009. Hopanoids play a role in membrane integrity and pH homeostasis in *Rhodopseudomonas palustris* TIE-1. *Journal of Bacteriology* **191**, 6145-6156.

Wieland, A., de Beer, D., Damgaard, L. R., Kuhl, M., van Duschotten, D., and Van As, H. 2001. Fine-scale measurement of diffusivity in a microbial mat with nuclear magnetic resonance imaging. *Limnology & Oceanography* **46**(2), 248-259.

CHAPTER FIVE

Investigating the nature of covalent bonding of bound lipids in microbial mat proto-kerogens *via* sequential chemolysis and hydropyrolysis

ABSTRACT

Insoluble macromolecular organic matter (IMOM) is a significant component of marine sediments and plays a large role in the preservation of organic matter in both modern and ancient environments. In modern marine unconsolidated sediments, IMOM—also known as proto-kerogen—is a complex polymeric matrix containing bound lipids, carbohydrates, proteins biosynthesised by living organisms in the water column and in the shallow subsurface. IMOM is able to sequester a wealth of biogeochemical information that is often overlooked during routine analysis of extractable lipids. Due to its complex, aggregate-like structure, IMOM is typically difficult to structurally characterise without fragmenting to yield molecular building blocks after covalent bond cleavage of various covalent bond types. We performed catalytic hydropyrolysis (HyPy) on pre-extracted IMOM residues treated under three different chemical regimes that target different covalent bond types with varying degrees of specificity and efficiency. IMOM residues were prepared from two mat-sediment cores of differing salinity, collected from hypersaline microbial mats from Guerrero Negro, Baja California, Mexico. Two sediment layers from two microbial mat cores were analysed in this study, with one representing an upper active mat layer dominated by an extracellular polymeric substances (EPS) matrix, the other constituting a deeper sedimentary layer. Despite the

extractions and chemical treatments removing large portions of free and bound lipids, HyPy of pre-treated residues released significant quantities of hydrocarbon and non-carbohydrate soluble products, even after the most aggressive chemical treatment (periodate oxidation). These results provide strong inferences about the mode of chemical binding of sterols (through stronger ether or sulfide linkages on the A-ring) and hopanoids (weaker ester linkages predominantly as C_{31} and C_{32} hopanoic acids; C_{35} bacteriohopanepolyols bound in through multiple alcohol groups in the side-chain) into proto-kerogen, but indicate that binding occurs strongly and at the very earliest stages of diagenesis. Proto-kerogen binds sterols and hopanoids into the macromolecular matrix with good preservation of isomeric and stereochemical configurations, and not all of the IMOM-bound lipid biomarker pool is accessible to chemical reagents through steric hindrance. EPS and cyanobacterial sheath material could play an important role in the sequestration of bound sterols and hopanoids during early diagenesis of benthic mat sedimentary organic matter.

1. Introduction

Proto-kerogen—also known as insoluble macromolecular organic matter (IMOM)—forms in unconsolidated sediments during the very earliest stages of diagenesis. Proto-kerogen is a complex macromolecular matrix of lipids, proteins, and carbohydrates derived from the organisms living in the water column (Figure 5.1). A significant portion of the kerogen matrix can be derived from recalcitrant algal

biomacromolecules composed of polymethylenic chains with linear or isoprenoid carbon skeletons and cross-linked ether bridges through selective preservation (Michaelis & Albrecht, 1979; Goth *et al*., 1988). Kerogen represents the dominant mass fraction of the total sedimentary organic matter and is able to sequester and preserve indigenous biosignatures at the time of deposition due to being recalcitrant and immobile during the thermal evolution of organic matter. Macromolecular organic matter—such as kerogens, resins, and asphaltenes—are difficult to characterise due to being structurally complex and insoluble in typical organic solvents. Selective chemical degradation techniques have, in the past, proven effective at releasing constituents bound with the macromolecular matrix by targeting different carbon-sulfur and carbon-oxygen bond types (e.g., Schaeffer *et al*., 1995; Höld *et al*., 1998; Schaeffer-Ries *et al*., 1998; Kribii *et al*., 2000; Xiong *et al*., 2007), and allow for the analysis of GC-amenable functionalised lipids or their hydrocarbon equivalents. However, most reagents used in chemical treatments of solids are sterically bulky and have restricted access to reactive bonds within the macromolecular matrix due to steric hindrance, which often results in low overall soluble product yields (Mycke & Michaelis, 1986; Mycke *et al*., 1987; Michaelis *et al*., 1990).

Other structurally complex components of microbial mat organic matter are the cellular and membrane components of prokaryotes. Prokaryotes have a variety of membrane configurations (Šmarda *et al*., 2002 and Figure 5.2); with the most complex being Gram-negative bacteria and cyanobacteria. The cell envelope of cyanobacteria typically contains the following layers (in order from inner-most to outer-most): a plasma

186

(inner) membrane composed of α-helix structural domains; peptidoglycan polymer of cross-linked sugars and amino acids; periplasmic space; outer membrane (OM) composed of β-barrel structural domains; surface layer (S-layer); and extracellular polymeric substances (EPS, including mucilage/capsular/sheath material) on the surface (Figure 5.2). This is particular relevant because the uppermost active microbial mat layers would be dominated by this material
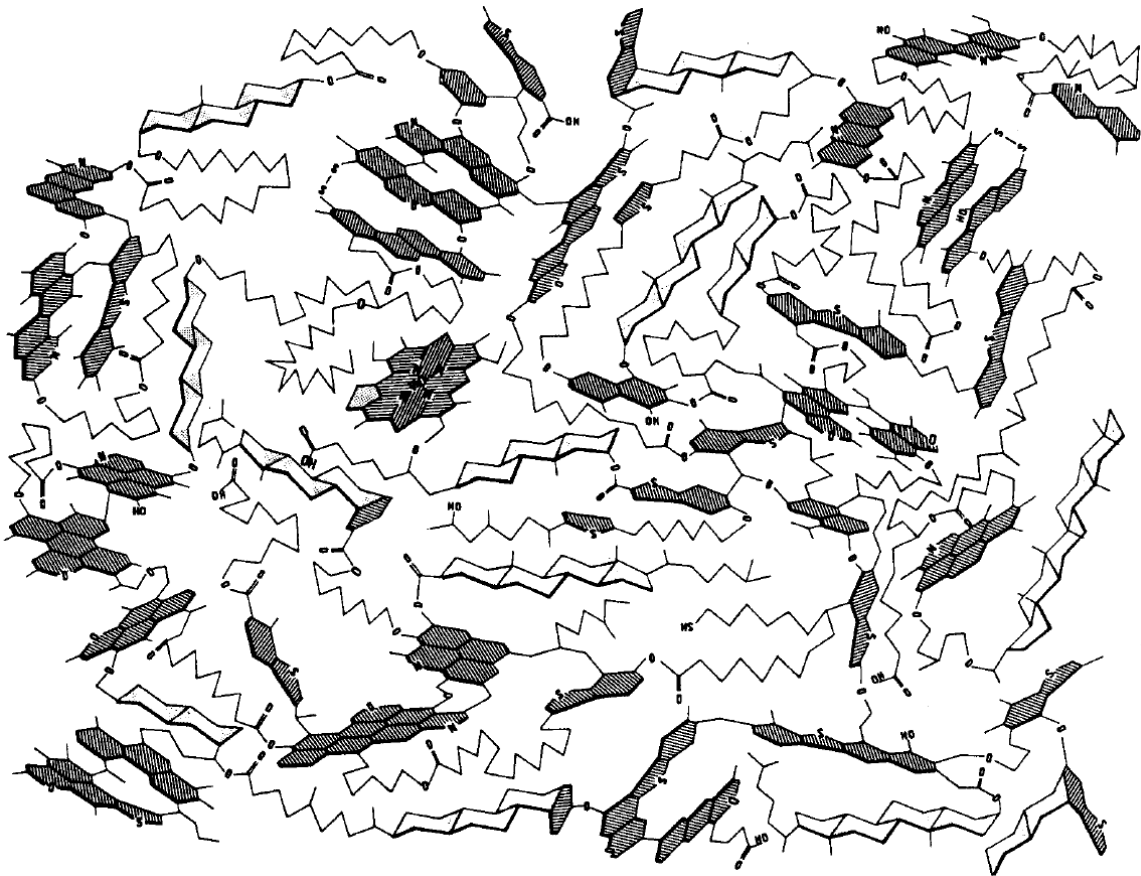
Figure 5.1. Chemical representation of the structure of macromolecular kerogen matrix (Type II) during the early stages of diagenesis (Papoular, 2001). Shaded clusters represent aromatised structures with functional side groups labelled.
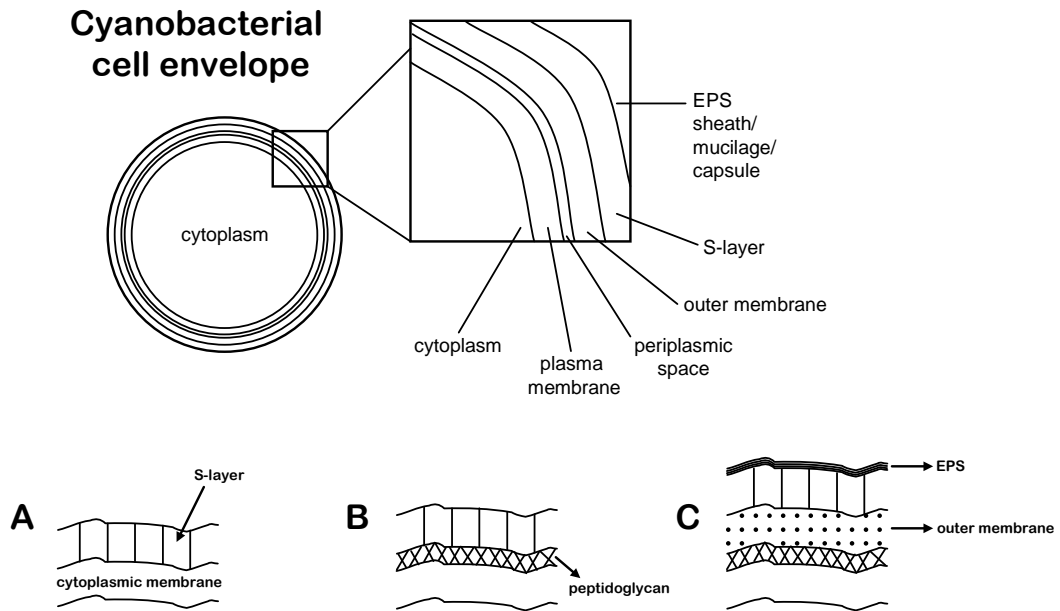
Figure 5.2. Generalised graphical representation of prokaryotic cell membrane components (not drawn to scale, adapted from Šmarda *et al*., 2002). A) Most archaea have S-layers on top of cytoplasmic membranes; B) Gram-positive bacteria and some archaea have an additional peptidoglycan layer separating the S-layer from the cytoplasmic membrane; C) Gram-negative bacteria and cyanobacteria have an outer membrane between the peptidoglycan layer and the S-layer. Additionally cyanobacteria have an EPS layer above the S-layer containing ordered carbohydrate fibrils that assist in gliding and motility (also see schematic above).

Structural elucidation of kerogen and the binding of lipids into the macromolecular matrix of kerogens have been studied for many decades. Selective chemical degradation techniques (chemolysis) have been used with varying degrees of aggressiveness to target specific covalent linkages. Chemically aggressive techniques, such as reduction using nickel boride (NiB) or hydroiodic acid (HI) and stepwise oxidation using sodium dichromate ($Na_2Cr_2O_7$) or potassium permanganate ($KMnO_4$), are able to release degradation products from kerogen in high yield, but reveal little information about the mode of binding, chemical groups remaining, or nature of the oxidation sites. Instead, it is more beneficial for structural characterisation to utilise sequential or selective oxidation, especially with the use of phase transfer catalysts (PTCs) to increase the reactivity of immature kerogens to hydrolysis (Amblès *et al*., 1996).

The most common ways to make the macromolecular matrix accessible are through hydrolysis, oxidation (stepwise or selective), and reduction. Specific examples that have been used previously include deuterium-labelled reagents (Richnow *et al*., 1992), catalytic hydrogenolysis-acetylation (Mycke *et al*., 1987), ruthenium tetroxide oxidation (RuO_4; Boucher *et al*., 1991), boron tri-bromide/chloride/fluoride cleavage (Chappe *et al*., 1980; Amblès *et al*., 1996; Schwarzbauer *et al*., 2003), periodate oxidation (Rohmer *et al*., 1984) acid methanolysis and tetramethylammonium hydroxide (TMAH; Sudgen & Abbott, 2002), and alkaline methanolysis (also known as base hydrolysis or saponification) (Razvigorova *et al*., 2008).

In addition to releasing bound lipids and making the macromolecular matrix easily accessible to conventional analytical techniques, selective chemical degradations also provide specific information regarding the type of covalent bond. Examples include the distinguishing between ether and ester moieties (Dragojlović *et al*., 2005), identification of linear, branched, isoprenoid, carotenoid, hopanoid, and steroid moieties bound through di- or polysulfide bridges (Kohnen *et al*., 1991; Adam *et al*., 1992; Kohnen *et al*., 1993), porphyrins bound to kerogen *via* ester bonds released as mono- and di-acid porphyrins (Huesby & Ocampo, 1997), and $17\alpha(H)21\beta(H)$- and $17\beta(H)21\alpha(H)$-hopanoic acids bound *via* ether linkages (Kribii *et al*., 2001).

Diagenesis of organic matter can occur in the water column and at the sediment-water interface as well as deep into the sediment over long timescales. During diagenesis, chemical reactions such as oxidation, reduction, sulfurisation, allomerisation, cyclisation, methyl migration, chain fragmentation, ring opening, and aromatisation can occur. Several of these reactions may produce metastable intermediates that can get preserved in kerogen during diagenesis (e.g., Ocampo & Repeta, 2002). To investigate the structure and binding of polycyclic terpenoid membrane lipids into proto-kerogen, we present the hydrocarbon profiles of two microbial mat layers from two cores (Pond 4 near 5 (P4n5) and Pond 5A near 5B (P5AB)) that were treated with under three different selective chemical degradations listed in order of moderate to efficient: 5% trichloroacetic acid (TCA), acid methanolysis (AM), and periodate treatment (PT). Additionally, a pre-extracted control (UC) sample was processed concurrently to monitor the effect of each treatment on original pre-extracted residues. These chemically treated residues were

catalyst-loaded, pyrolysed, and analysed for their hydrocarbon content. The layers chosen represent an active layer (layer 4; L4 - depth 9-15 mm; depth 14-24 mm) and a sedimentary layer (layer 7; L7 – depth 25-35 mm; depth 44-54 mm) from P4n5 and P5AB, respectively. Depths are reported as relative to the top of the surface layer (0 mm), e.g., layer 1 is 0-2 mm in both cores.

2. Geological setting

The geological setting from where these samples were collected is previously described in Section 2 of Chapter 4. Briefly, the Guerrero Negro (GN) system of thirteen evaporitic ponds is located in Baja California Sur, Mexico. The pond system is fed locally by Laguna Ojo de Liebre and benthic marine hypersaline microbial mats are dominant in ponds 4 through 6. The P4n5 core (9-9.1% salinity) was taken from Pond 4 near 5 (Figure 4.2A) and sub-divided into 11 layers (Figure 4.2B). Layers 1 through 4 range from 2-6 mm in total thickness, whereas layers 7 through 11 are 10 mm thick. The P5AB core (11.2% salinity) was taken from Pond 5A near 5B (Figure 1) and sub-divided into 8 layers. Layers 1 and 2 are 2 mm thick and layers 3 through 8 are 10 mm thick. Samples were collected and lyophilised. In preparation of sample residues, mat layers were sectioned, freeze-dried, and powdered. Layer 4 was chosen to represent the 'active' microbial layer as it is the first layer of significant thickness that yields a large quantity of total lipid extract (TLE) derived directly from microbial primary production (mainly cyanobacterial) of active microbial activity from layers 1-3 and dominated by an EPS

matrix. Layer 7 was chosen to represent a 'sedimentary layer' of the mat as it marks the first appearance of the coarse-grained gravelly sand texture and the transition from previous gelatinous material dominated by cyanobacterial EPS.

3. Materials & Methods

Sample collection information and description of each layer from both cores is previously described in Section 3.1 of Chapter 4.

3.1 Carbon content and bulk isotopes

Carbon content and bulk isotopes were acquired according to methods already outlined in Section 3.3 of Chapter 4. Where material permitted, we measured the isotopic composition and organic carbon content of pre-extracted residues following chemolysis. In this instance, we compared values for the pre-extracted control for layers 4 and 7 of both P4n5 and P5AB, with additional comparison to periodate treatment (the strongest chemical treatment) for P4n5 layer 4 and P5AB layer 7 to understand what the maximum recovery is likely to be. Based on these end-member values and the weights of recovered residues pre- and post-treatment, we estimated the TOC content of pre-extracted residues following each chemical treatment for quantification purposes.

3.2 Lipid extraction

Intact polar lipids (IPLs) were extracted from freeze-dried mat layers using a modified Bligh-Dyer (B-D) method, outlined previously in Section 3.3.1 of Chapter 4. The residue after B-D extraction was divided into four fractions for subsequent chemical treatments, the pre-extracted control (PC) being the B-D residue (Figure 5.3).
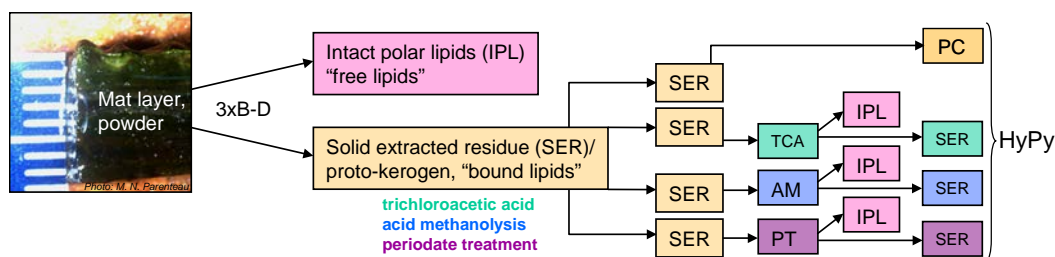
Figure 5.3. Schematic showing distribution of sample residue and chemolysis extraction procedure.

3.2 Chemolysis

3.2.1 Pre-extracted control (PC). To test the effect of three different chemical treatments on the selective incorporation/preservation of biomarkers in proto-kerogen residues, we selected layers 4 and 7 from the P4n5 and P5AB core and performed the following chemical procedures: trichloroacetic acid (TCA) precipitation, acid methanolysis (AM), and periodate treatment (PT) *via* periodate oxidation. The treatments are listed in order of chemical aggressiveness, from least to most aggressive. All chemical treatments were performed by Linda Jahnke in the Exobiology Division laboratories at NASA Ames Research Centre. A pre-extracted control (PC) was

processed concurrently. Residues from these treatments were catalyst loaded and pyrolysed using the same methods as described previously (Sections 3.3.2 and 3.4.2 of Chapter 4).

3.2.2. Trichloroacetic acid (TCA) precipitation. This treatment, reported to disrupt archaeal membranes to effectively recover archaeal tetraether lipids, is a mild acidification procedure to dissociate the lipid and protein complexation and the mildest treatment of the three. Dried B-D residue was placed into a glass centrifuge tube with 4 ml of 5% trichloroacetic acid (TCA) and extracted with 5 ml of MeOH:chloroform (2:1, v/v). Extraction proceeded according to methods outlined in Section 3.3.1 of Chapter 4 and residue for HyPy was recovered through centrifugation, placed into the freezer, and lyophilised.

3.2.3. Acid methanolysis (AM). Acid methanolysis removes polar head groups (archaeol), hydrolyses ester bonds and vinyl ether bonds (dimethylacetals) to release bound fatty acids (FAs; both ester and amide-FAs, contrast alkaline methanolysis releasing only ester FAs), fatty acid methyl esters (FAMEs), and hopanoic acids. Additionally AM targets mono- and dialkyl glycerol ethers (MAGEs and DAGEs) and tetraether lipids. For this treatment, dried B-D residue was placed into a centrifuge tube and suspended in 5 ml of MeOH containing 0.125 ml concentrated HCl (0.3 N). Sealed tubes were heated at 85°C for 5 h. Tubes were then removed from the heating block, cooled, with 10 ml DI water added and neutralised with 7 N potassium hydroxide (KOH) at 85°C for 5 h. Samples in tubes were extracted with hexane:DCM (4:1, v/v) by

vigorous agitation using a Vortex mixer. This procedure resulted in a heavy emulsion in the hexane-DCM upper layer, particularly for samples from P5AB. Centrifugation generated an upper emulsified layer, a water layer, and a small pellet of solid residue. Further recovery of this residue required removal of the upper emulsified layer and continued washing with fresh water. After four repeated washing cycles, no further material was recovered by centrifugation from the emulsified upper layer however, an additional material that floated between the water and hexane-DCM gradually formed a distinct layer. Pellets recovered from the lower water phase and the emulsified upper 'floating' layer were frozen and lyophilised. Lyophilised pellet material from the lower water phase were pyrolysed to see if any lipids are associated with this solvent-insoluble phase (herein referred to as the acid methanolysis hydrophobic residues, or AM-H). Both P4n5 layer 4 and P5AB layers 4 and 7 had this occur during acid methanolysis, though only enough material was recovered from the P5AB layers to perform any further analysis.

3.2.4. Periodate treatment (PT). Treatment involving periodate oxidation of the residue targets the vicinal diol functionalities of the side chain of bacteriohopanepolyols (BHPs) and is the most chemically aggressive of the three. The procedure used here is a modification of the one outlined in Rohmer *et al*., 1984. Dried B-D residue was placed into a glass centrifuge tube with 3 ml of tetrahydrofuran (THF):water (8:1, v/v) with 300 mg of sodium periodate. Small magnetic stirrer bar was placed into the tube and samples were stirred at room temperature for 1 h. 10 ml of DI water was placed into the tube and released lipids were extracted with hexane:DCM (4:1, v/v) using a Vortex mixer. This

lipid extraction step was repeated up to 4 times, with each supernatant collected and combined. The water phase was centrifuged to recover the residue, washed with DI water, centrifuged to consolidate, frozen, and lyophilised.

3.3 Kerogen preparation

Pre-extracted proto-kerogen residues were prepared according to methods outlined in Section 3.4.2 of Chapter 4, including catalyst loading, experimental conditions of hydropyrolysis, and pyrolysate extraction (Table A4.3-4.5).

3.4 Gas Chromatography-Mass Spectrometry (GC-MS) and Metastable Reaction Monitoring (GC-MS-MRM)

Samples were analysed using the same methods and run conditions as reported in Section 3.4.2 of Chapter 4.

4. Results

Three different chemical treatment residues alongside a pre-extracted control were pyrolysed and analysed to determine which compounds are selectively retained and/or released during the chemical treatment compared to the lipids in the residual fraction for layer 4 – more representative of organic matter derived from an active mat

layer and layer 7 – more representative of organic matter derived from a sedimentary mat layer of P4n5 and P5AB. Fraction yields for all samples can be found in Appendix Tables A5.1-5.5. Although the intact polar lipid (IPL) fraction is yet to be analysed, it is expected that the material removed from each treatment will correspond to the covalent bond types and functional groups that each treatment targets. The following sections compare the profiles of layer 4 to layer 7 for each treatment, starting first with P4n5. Since the treatments preferentially target the polycyclic biomarkers, especially the hopanoids, and IPL results are not reported here, the focus of the following section will be on the profiles of kerogen-bound steranes and hopanes (Appendix Table A5.6).

Carbon content and isotopes

As described in Section 3.1 earlier, to provide a semi-quantitative idea of product yields following hydropyrolysis of pre-extracted chemically-treated residues, we have measured TOC content (in wt%) of the two end-member treatments; pre-extracted control and periodate treatment (the other fractions did not have enough remaining material for direct analysis). Given the periodate treatment removes the most (organic) material and trichloroacetic acid and acid methanolysis have similar and intermediate yields between the PC and PT end-members, we used the average organic carbon content of PC and PT. Recorded weights pre- and post-treatment were also used as a guide for indirectly calculating (estimating) TOC. There is no difference in $\delta^{13}C$ values pre- and post-chemical treatment.

4.1 Pond 4 near 5 (P4n5)

4.1.1 Pre-extracted control

Full scan chromatograms of layer 4 and layer 7 shows greater relative abundance of both *n*-alkenes, sterenes, and steradienes in layer 4, with layer 7 chromatogram dominated by hopane assemblages (Figure 5.4, Figure 5.5.A). Layer 4 also yields higher concentrations of total steranes (sum of C_{27}-C_{29} βααR and αααR; L4: 84 ppm TOC; L7: 52 ppm TOC) compared with layer 7, although layer 7 has 8 times the concentration of total hopanes (sum of C_{27} 17αTm, 17βTm, C_{29}-C_{35} αβR, βαR, and ββR hopanes; L4: 19.5 ppm TOC; L7: 160 ppm TOC).

4.1.2 Trichloroacetic acid (TCA) precipitation

TCA precipitation treatments of both layer 4 and 7 show a decrease in total steranes, to similar total concentrations (L4: 32 ppm TOC; L7: 29 ppm TOC). However, in looking at the total hopane recovery, there is a decrease observed in layer 7 (77 ppm TOC) but little change in layer 4 (21 ppm TOC) compared with the pre-extracted control, in fact there is a slight increase (Figure 5.4B). MRM chromatograms show while there is a reduction in extended hopane side-chain values in layer 7, C_{35} ββR hopane is slightly elevated in layer 4.

Figure 5.4. Full scan total ion chromatograms (TIC) of aliphatic hydrocarbons release by HyPy of pre-extracted P4n5 A) layer 4 and B) layer 7. Labelled filled circles are *n*-alkanes, open circles are *n*-alkenes, grey squares are steranes, and grey diamonds are hopanes.

4.1.3 Acid methanolysis (AM)

AM procedure formed an emulsion on the final step while recovering the residue pellet (see Section 3.2.3 in the methods, with further discussion below) of layer 4 only. Material recovered from the emulsion was insufficient to perform any further analyses. Overall, chromatographic profiles for layers 4 and 7 are similar to TCA profiles, with layer 4 showing similar concentrations of total steranes to TCA, but layer 7 shows lower values. Layer 4 shows similarly elevated total hopane concentrations (21 ppm TOC) while layer 7 stays on the downward trend from previously higher values in TCA and PC treatments. We observe a reduction in the extended hopane side-chain of C_{31} $\beta\beta R$ and C_{32} $\beta\beta R$, particularly for layer 7 (Figure 5.5C, Figure 5.6C).

4.1.4 Periodate treatment (PT)

Besides C_{31} and C_{32} hopanes in AM, PT recovered the lowest yields in steranes and hopanes of all three treatments, as expected. Despite the strong chemical oxidation, small quantities of total steranes (L4: 2.1 ppm TOC; L7: 2.8 ppm TOC) and total hopanes (L4: 7.2 ppm TOC; L7: 20.7 ppm TOC) were detected. Although hopanes in layer 4 did not appear to be affected by the chemical treatments thus far (unlike layer 7), a noticeable reduction in C_{33}-C_{35} hopanes is observed after performing PT (Figure 5.5D, Figure 5.6D).

Figure 5.5. Partial *m/z* 191 ion chromatograms of hopanes released by HyPy from P4n5 layer 4 of A) pre-extracted control; B) trichloroacetic acid; C) acid methanolysis; and D) periodate treatment. Isomers are represented by circles, squares, and diamonds representing αβR, βαR, and ββR, respectively. Asterisks represent hopene isomers. Relative abundance (%) normalised to C_{32} ββ (22R) hopane in PC (A).

201

Figure 5.6. Partial *m/z* 191 ion chromatograms of hopanes released by HyPy from P4n5 layer 7 of A) pre-extracted control; B) trichloroacetic acid; C) acid methanolysis; and D) periodate treatment. Isomers are represented by circles, squares, and diamonds representing αβR, βαR, and ββR, respectively. Asterisks represent hopene isomers. Relative abundance (%) normalised to C_{32} ββ (22R) hopane in PC (A).

4.2 Pond 5A near 5B (P5AB)

4.2.1 Pre-extracted control

It is immediately evident from the full scan chromatograms of layer 7 the increase in the high molecular weight polycyclic biomarker region where the sterane and hopane homologues elute (Figure 5.7). Layer 4 pre-extracted control shows remarkably low total steranes (4.5 ppm TOC) and hopanes (8.5 ppm TOC), which is the opposite for P4n5 steranes, though in concert with the P4n5 trend in hopanes. Pyrolysates of layer 4 predominantly generated short-chain *n*-alkanes, with little to no alkenes, whereas layer 7 is dominated by hopanes (117 ppm TOC) and to a lesser degree, but still significant quantities of steranes (65 ppm TOC).

4.2.2 Trichloroacetic acid (TCA) precipitation

TCA full scan chromatograms are similar for both layers, except that layer 7 is once again dominated by hopane assemblages. TCA treatment recovered the greatest total concentration of steranes and hopanes for both layer 4 and 7, even higher than PC. Layers 4 and 7 yield 33 ppm TOC and 83 ppm TOC, respectively, for steranes and 43 ppm TOC and 128 ppm TOC, respectively, for hopanes (Figure 5.8, Figure 5.9).
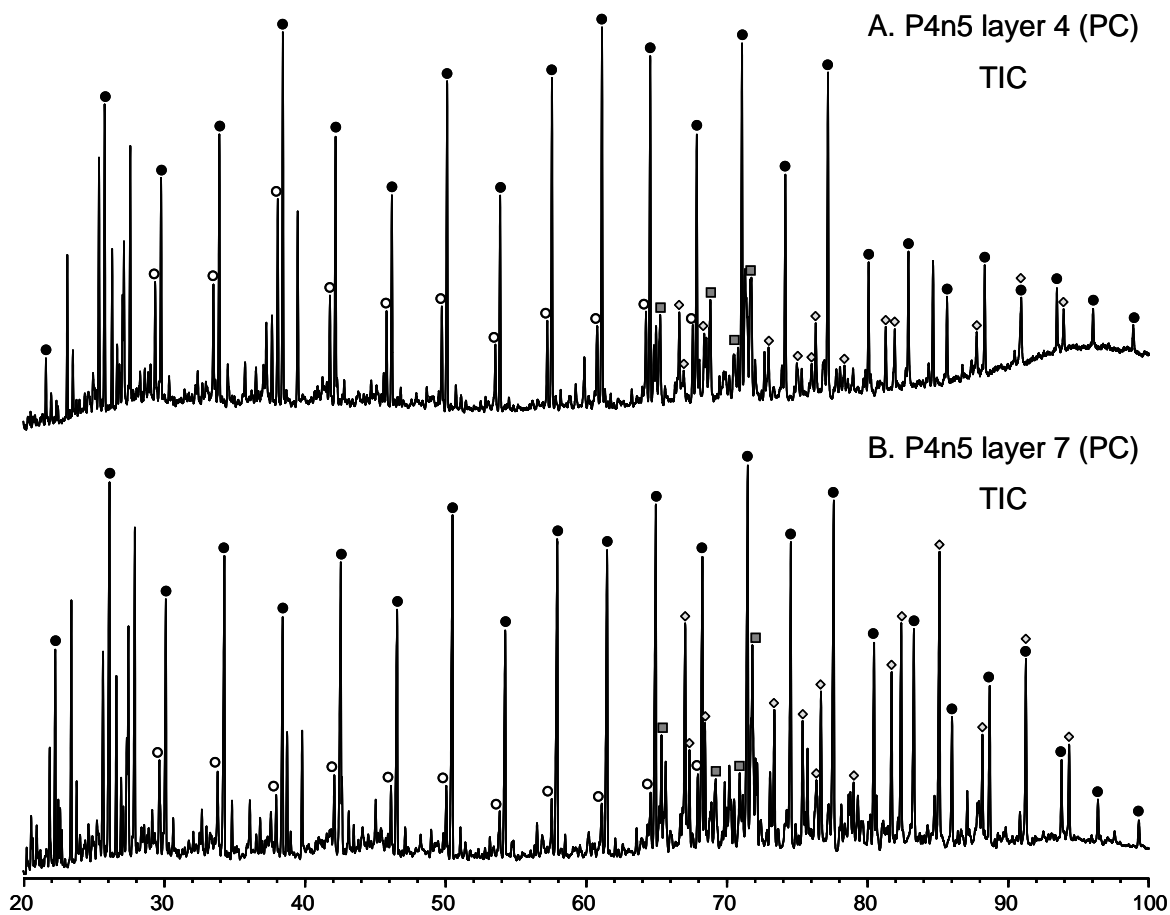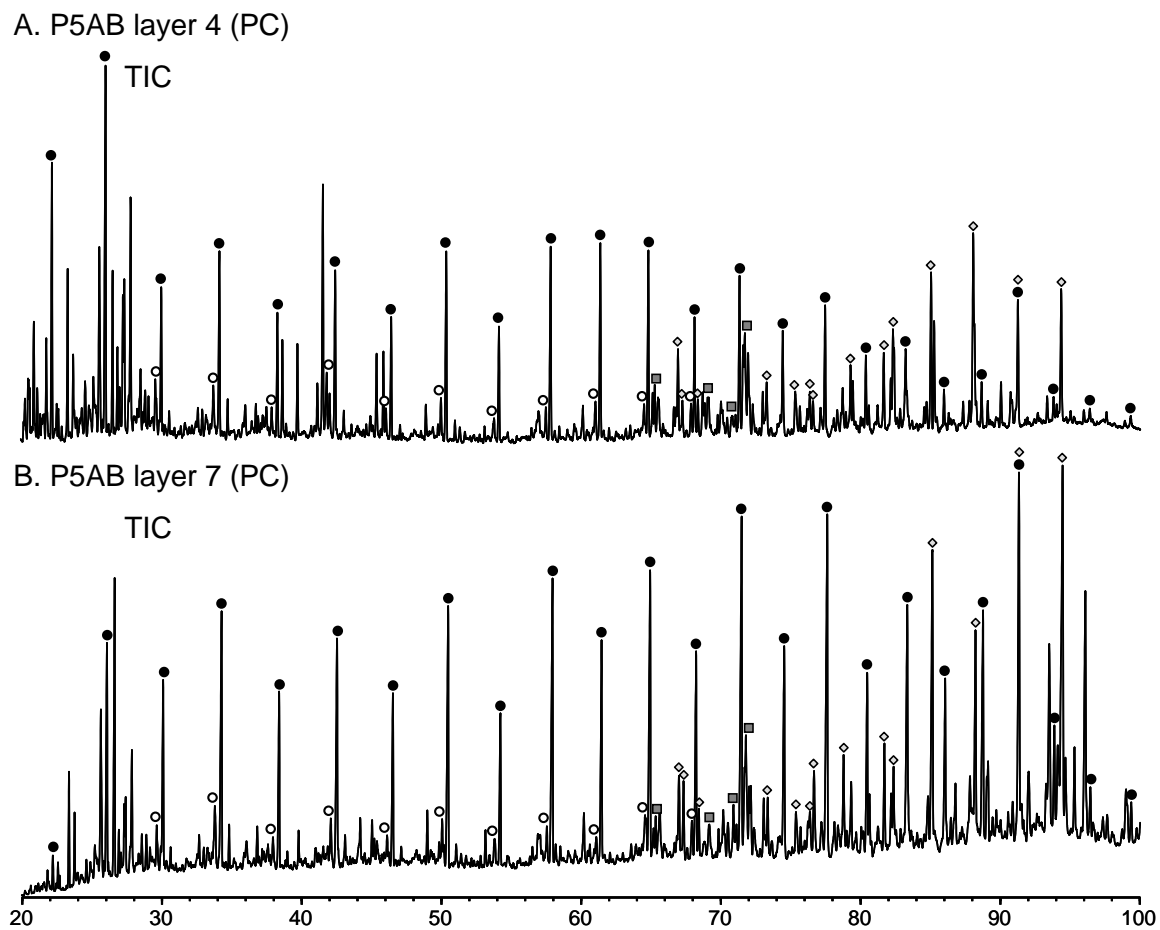
Figure 5.7. Full scan chromatograms (TIC) of aliphatic hydrocarbons generated by HyPy of pre-extracted P5AB A) layer 4 and B) layer 7. Labelled filled circles are *n*-alkanes, open circles are *n*-alkenes, grey squares are steranes, and grey diamonds are hopanes.

4.2.3 Acid methanolysis (AM) and hydrophobic residues (AM-H)

Acid methanolysis generated two phases upon completion of the treatment—a solid residue and an emulsion that was recovered from the interphase, termed 'hydrophobic residue', since it was insoluble in the hexane-DCM phase. The major phase for both layers was the solid residue (AM) with ~50% of the dry weight of the solid residue being the hydrophobic residue (AM-H). Both AM residues generated saturated hydrocarbons dominated by *n*-alkanes with overall lower amounts of steranes and hopanes. Layer 4 and 7 AM have similar total sterane yields (19 ppm TOC and 22 ppm TOC, respectively), and hopanes (41 ppm TOC and 70 ppm TOC, respectively. Figure 5.10C, Figure 5.11C). AM hopanes profiles show a reduction in total C_{31} and C_{32} hopanes. HyPy of AM-H yielded strongly coloured pyrolysate products (more so than AM pyrolysates). Full scan chromatograms show visible steranes and hopanes, whereas these were absent in AM samples (Figure 5.8, 5.9). Quantification of steranes and hopanes by MRM reveal the AM-H treatment yielding significantly more polycyclic biomarkers than any other treatment, including the pre-extracted control. This is true of every sterane and hopane homologue in AM-H. In the case of total hopane concentration for layer 7 AM compared with AM-H, AM-H generated an order of magnitude more total hopanes than AM.
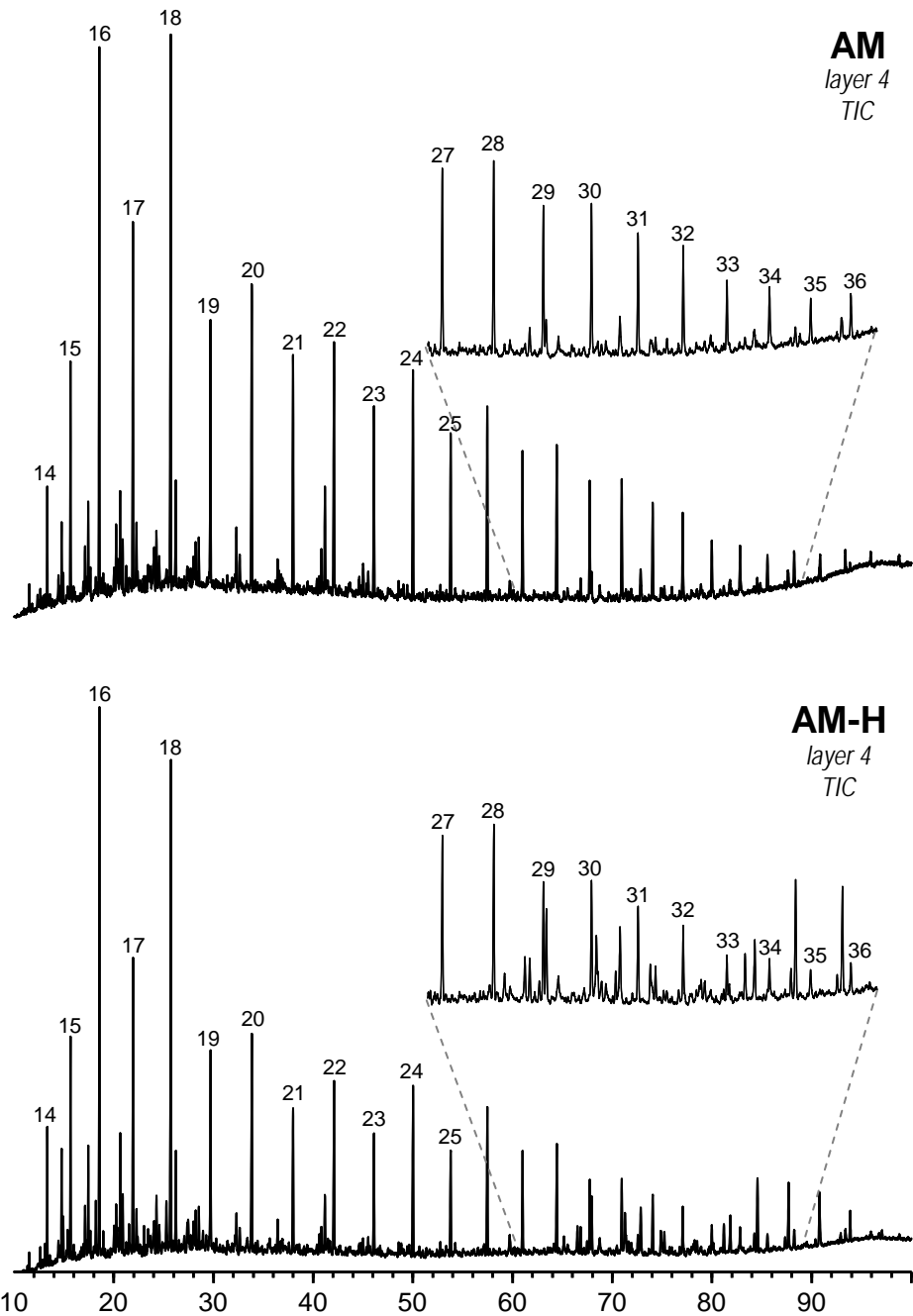
Figure 5.8. Total ion chromatograms (and magnified insets; 60-90 mins) of aliphatic hydrocarbons profiles generated by HyPy of P5AB layer 4 AM (above) and AM-H (hydrophobic residue, below) showing more prominent peaks from polycyclic biomarkers in AM-H compared to AM.
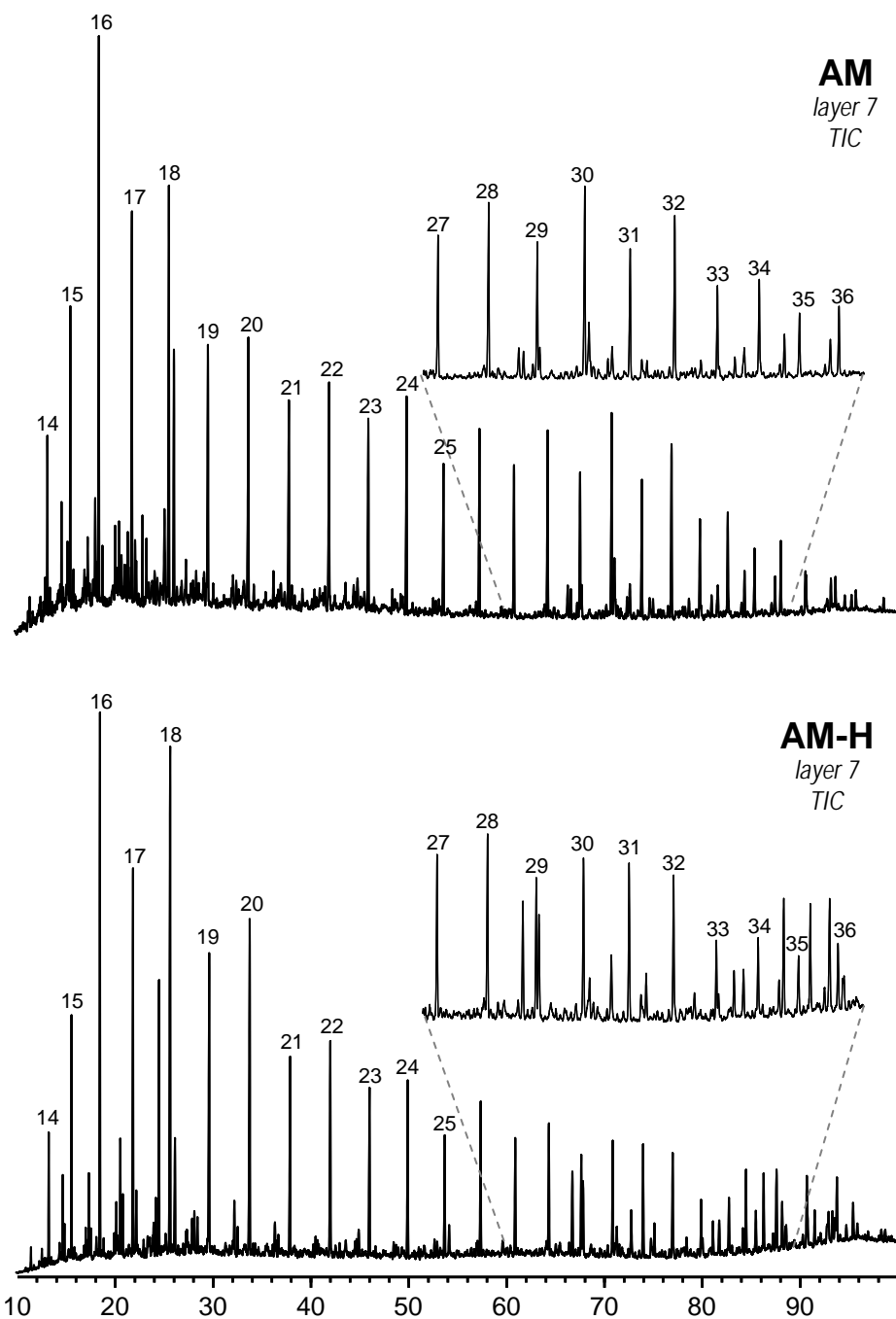
Figure 5.9. Total ion chromatograms (and magnified insets; 60-90 mins) of aliphatic hydrocarbon profiles generated by HyPy of P5AB layer 7 AM (above) and AM-H (hydrophobic residue, below) showing higher relative abundances of polycyclic biomarkers in AM-H compared to AM.

4.2.4 Periodate treatment (PT)

Full scan chromatograms after periodate treatment are dominated by *n*-alkanes. There are very low concentrations of total steranes in both layer 4 and 7 (0.9 ppm TOC and 1 ppm TOC, respectively) with slightly higher recovery of hopanes (10 ppm TOC and 22 ppm TOC, respectively). PT hopane profiles show a reduction in total C_{33}-C_{35} hopanes (Figure 5.10D, Figure 5.11D) which is the same result observed in the P4n5 treatments for both layers.
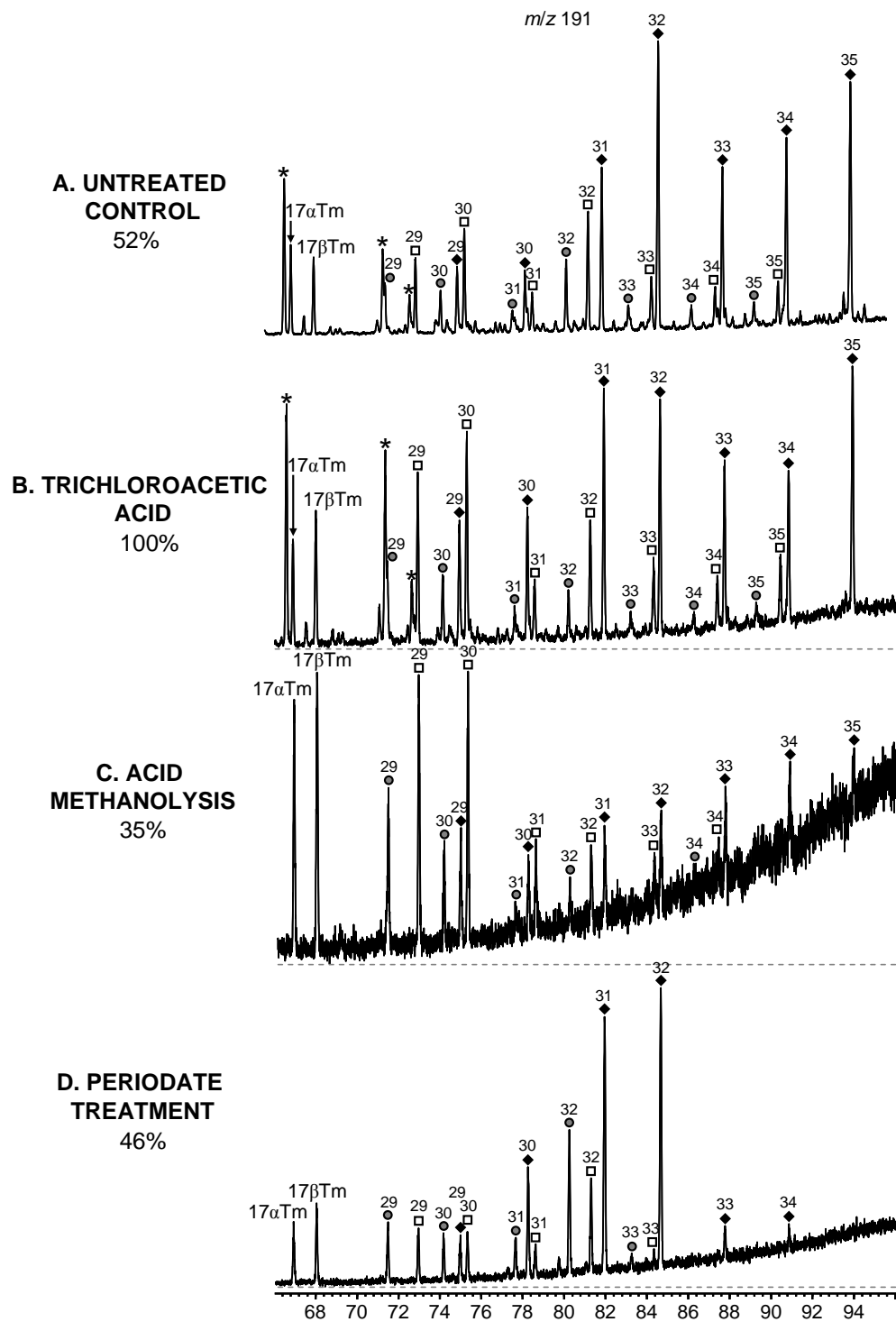
Figure 5.10. Partial *m/z* 191 ion chromatograms of hopanes released by HyPy from P5AB layer 4 of A) pre-extracted control; B) trichloroacetic acid; C) acid methanolysis; and D) periodate treatment. Isomers are represented by circles, squares, and diamonds representing αβR, βαR, and ββR, respectively. Asterisks represent hopene isomers. Relative abundance (%) normalised to C_{32} ββ (22R) hopane in PC (A).
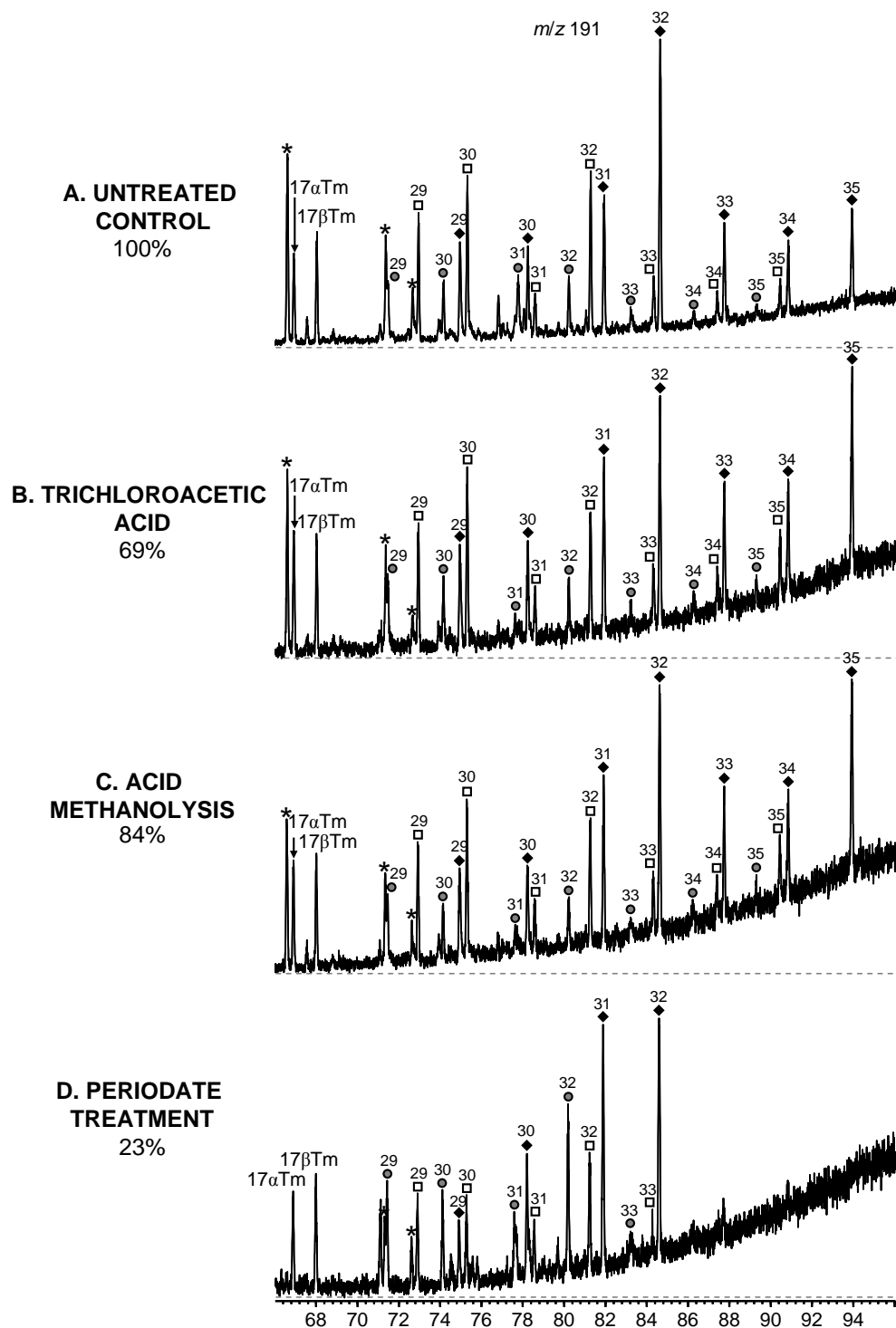
209

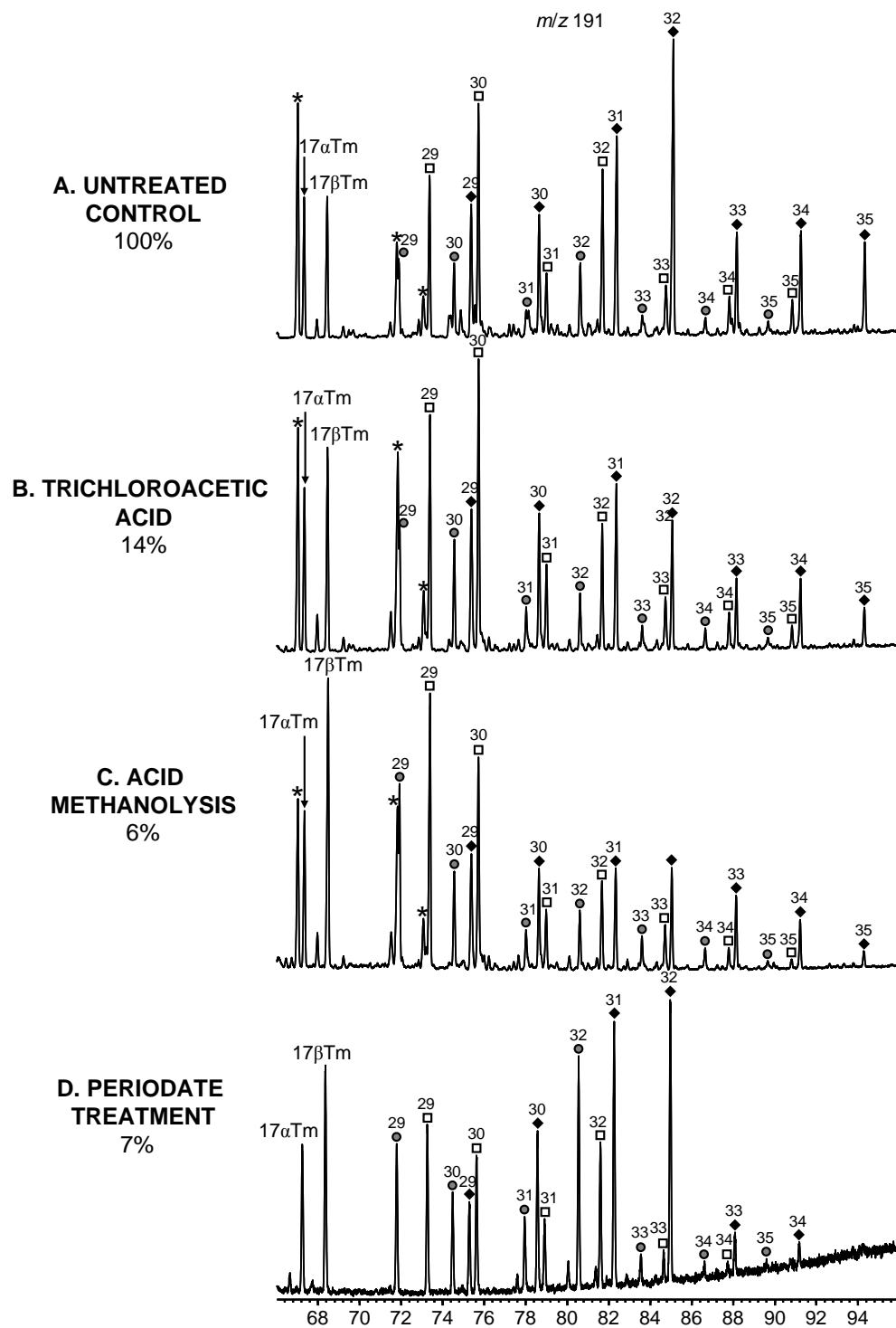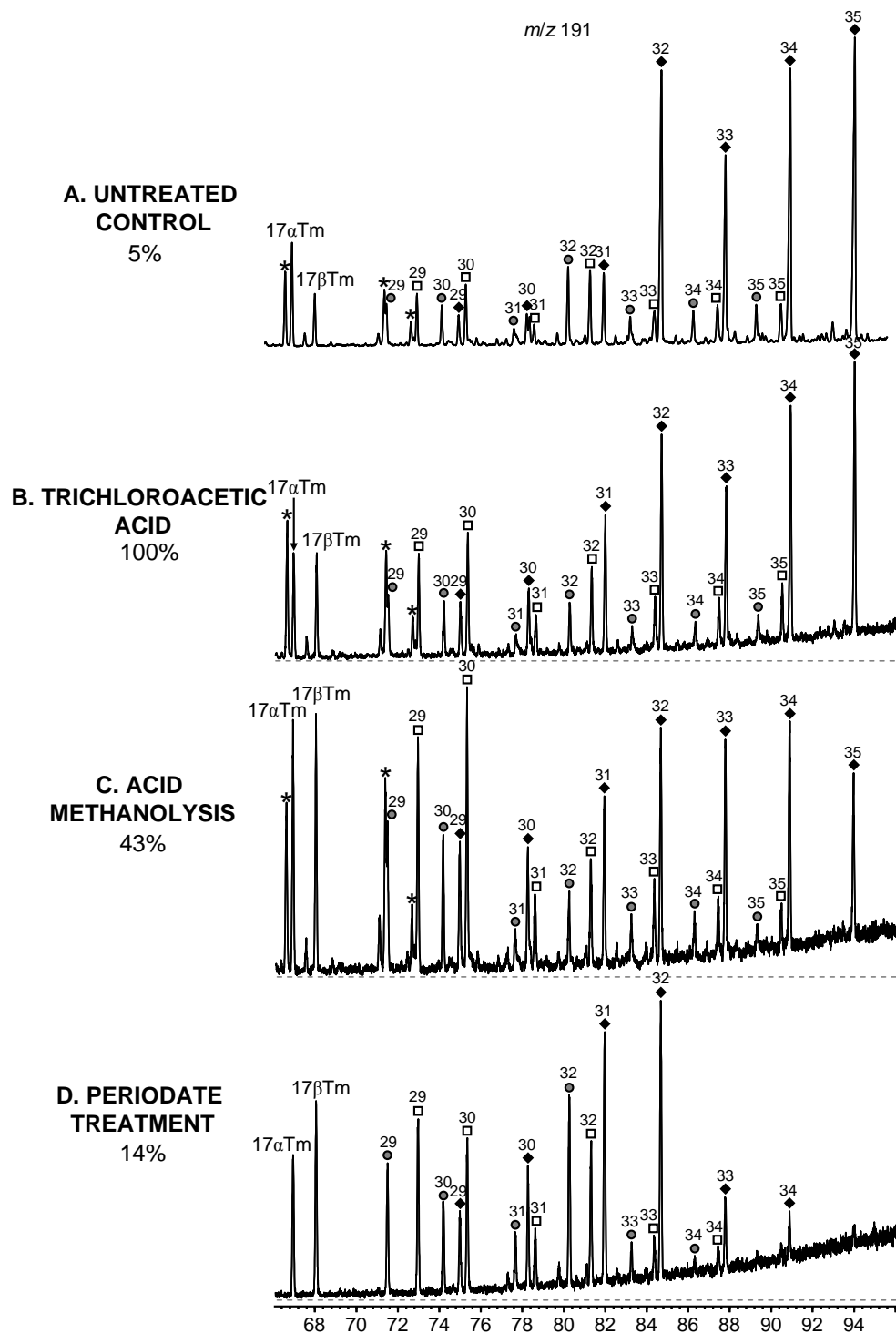**Figure 5.11.** Partial *m/z* 191 ion chromatograms of hopanes released by HyPy from P5AB layer 7 of A) pre-extracted control; B) trichloroacetic acid; C) acid methanolysis; and D) periodate treatment. Isomers are represented by circles, squares, and diamonds representing αβR, βαR, and ββR, respectively. Asterisks represent hopene isomers. Relative abundance (%) normalised to C_{32} ββ (22R) hopane in PC (A).

210

5. Discussion

5.1 Mechanism of steroid and hopanoid binding into IMOM

Catalytic hydropyrolysis of chemically-treated residues provide strong evidence for the rapid incorporation of polycyclic biomarkers such as steranes and hopanes into macromolecular fractions during early diagenesis. These results indicate that sterane and hopane skeletons may be strongly linked and progressively sequestered during diagenesis, as even after conventional lipid extraction and chemical treatment, solid recovered kerogen residues still release hydrocarbons in appreciable quantities. In P4n5, the concentration of total steranes released by HyPy decreases significantly following harsher chemolysis treatment, with no preference for carbon number. Even though periodate oxidation was used to target the extended hopanepolyol side-chain, and carbohydrate structures more generally, it also proved effective at fragmenting kerogen-bound sterols as only relatively low quantities were recovered by subsequent HyPy treatment for each layer in both cores in comparison with the pre-extracted controls. Steroids and their diagenetic hydrocarbon equivalents, steranes, are primarily bound into kerogen through strong ether or sulfide linkages on the A-ring. Trichloroacetic acid and acid methanolysis procedures are milder treatments that mainly target weak ester bonds. The overall decline in C_{31} and C_{32} hopanes from the hydropyrolysates is consistent with these treatments targeting the major hopanoid acids derived from BHP, which are C_{31} and C_{32} hopanoic acids (Bennett & Abbott, 1999; Farrimond et $al.$, 2003). Finally, periodate treatment is used, and has been in the past, to recover large amounts of BHP, as

it particularly targets the vicinal diol functional groups of the BHP extended sugar side-chain. This is consistent with our results showing a reduction in the relative abundance of C_{33}-C_{35} hopanes released by HyPy compared with lower hopane carbon numbers after periodate treatment had been performed.

5.2 The role of EPS on kerogen formation

Extracellular polymeric substances (EPS) are high molecular weight substance mixtures excreted by both eukaryotic and prokaryotic microorganisms. Biofilms are mixtures of EPS, dissolved organic and inorganic particles, and colloids. A large portion of EPS consists of complex carbohydrates, but can also contain proteins, glycoproteins, lipids, glycolipids, phospholipids, exopolymeric saccharides, nucleic acids, and humic acids (Flemming *et al*., 2007). It has been well-documented that EPS plays an important role in mineralisation, specifically carbonate formation, in microbial ecosystems. The surface of EPS contains carboxyl and hydroxyl groups that are able to bind cations such as Ca^{2+} and inhibit the formation of calcium carbonate (Kawaguchi & Decho, 2002). EPS can also enhance calcium carbonate precipitation by providing diffusion-limited sites that create alkalinity gradients in response to microbial processes (Pentecost, 1985; Braissant *et al*., 2007).

EPS, not unlike kerogen, is a complex network of cross-linked, high molecular weight constituents. Different forms of EPS, such as slime, sheath material, and capsule (Flemming & Wingender, 2010) have discrete biochemical and physical properties for

example, sheath material is a heteropolysaccharide which is much more structured than slime. Sheath is proximal to the outer membrane/S-layer, followed by capsular EPS, slime EPS, and soluble (released) EPS which is secreted into the environment. Other membrane-associated features of bacteria include peptidoglycans (dominantly of Gram-positive bacteria but also present in smaller amounts in Gram-negative bacteria) and the lipopolysaccharide (LPS) three layered structure situated in the outer leaflet of the outer membrane comprising lipid A, core oligosaccharide and O-antigen. LPS is an endotoxin characteristic of Gram-negative bacteria. These features play a critical role in the preservation of lipids and studies of their physiological and biochemical behaviour has not only yielded novel methods to circumvent complications with their isolation and purification but also significant advances in the way they are bound to other membrane constituents. For example, isolating and chemically treating different components of EPS such as the sheath material and LPS have yielded bound carotenoids and hopanoids (Böhm *et al*., 1995; Komaniecka *et al*., 2014; Silipo *et al*., 2014), the latter of which could be associated with detergent-resistant membranes (Sáenz, 2010).

There appears be multiple factors that influence the overall HyPy yields of the pre-extracted control for layers dominated by an EPS matrix, as layer 4 from both P4n5 and P5AB ponds show significantly lower total yields compared to the same layer residues post-chemical treatment. Layer 7 of P5AB also shows decreased yields for the pre-extracted control, which may be related to the other two. Layer 4 was chosen because it represents an active layer that has a gelatinous matrix dominated by EPS, whereas layer 7 has more of a sedimentary matrix where most of the EPS has already been

degraded. However, in P5AB layer 7, we are seeing similar relative yields of polycyclic biomarker as in layer 4. Examining textures and noting that P5AB has increased salinity may be the first step in understanding why this is the case. It has been experimentally demonstrated that salinity has an effect on the total amount of EPS (both loosely- and tightly-bound) and this increases with increasing salinity (Wang *et al*., 2013). The increase in salinity switches the microbial population from dominantly filamentous *Microcoleus* (with minor *Phormidium* and *Oscillatoria*) to being dominated by *Phormidium*, *Oscillatoria*, and unicellular cyanobacteria. Higher EPS content in P5AB makes the dissection and layer separation more difficult due to its jelly-like consistency. This increased EPS content may not have been efficiently removed from layer 7, hence similar displaying profiles to layer 4. Considering all of the above observations, it is likely that the washing procedure and extraction of intact polar lipids (IPL) removed significant portions loosely-bound EPS containing bound sterols and hopanoids which reflect the relative lower yields for the pre-extracted control samples.

Although washing procedures (e.g., Klock washing was performed on both cores; Klock *et al*., 2007) removes some loosely-bound EPS-related cellular material such as slime and capsular material, it does not remove sheath material. We noted that acid methanolysis generated a heavy emulsion that could only be recovered through sequential washing, phase partitioning, and organic solvent extraction. The formation of this insoluble 'hydrophobic' material is coincident with the three samples that are associated with higher EPS content and reduced pyrolysate yields of the pre-extracted control. A previous study that performed a chemical treatment similar to acid

methanolysis successfully isolated homoglucan fibrils from *Phormidium* sheath material (Hoiczyk, 1998), indicating chemical constituents of sheath material are able to be accessed by this type of chemical treatment. In light of this observation, a smaller portion of sterols and hopanoids could have been loosely bound to slime or capsular EPS while greater portions were sequestered through strong covalent binding into the resistant phases of EPS, such as sheath material, which could then have been released during acid methanolysis.

The exact nature and origin of this 'hydrophobic residue' material needs further structural and chemical investigation and therefore the above described scenario is associated with some uncertainty. But if it is indeed sheath or remnant accumulated sheath material this could have implications for lipid biomarker preservation, especially when organic matter is dominated by producers that frequently synthesise and discard sheath material and/or in environments where the preservation of sheath material is enhanced, e.g., in saline or hypersaline environments.

6. Conclusions

Selective chemical degradations and subsequent hydropyrolysis (HyPy) of recovered pre-extracted mat/sediment residues yield significant quantities of hydrocarbon and non-hydrocarbon products from covalent bond cleavage. We find that even with a harsh chemical oxidation technique such as periodate oxidation, HyPy of kerogen releases saturated polycyclic biomarkers with the composition reflecting the predicted mode of covalent binding. Geochemical profiles of steranes and hopanes, derived from formerly functionalised sterols and hopanoids, respectively, show distinct trends during earlier stages (layer 4) compared with later stages (layer 7) of diagenesis. However their profiles are ultimately derived from the mode of covalent binding into kerogen during diagenesis, which are preserved to a high degree despite exhaustive extraction, chemical treatments, and subsequent hydropyrolysis. Periodate oxidation efficiently releases a large portion of, but not all of, the bound C_{27}-C_{29} steranes and C_{33}-C_{35} hopanes. This suggests that sterols may be associated with binding into EPS or other carbohydrate structures, or are bound within portions of the matrix that contain significant carbohydrate structures. Acidic treatments followed by hydropyrolysis releases abundant hopanoic acids through hydrolysis of weak ester bonds. Therefore, it is not surprising to observe a prominent decrease in C_{31} and C_{32} relative to other hopanes in HyPy following the milder chemolysis steps, which are likely to preferentially target the major C_{31} and C_{32} hopanoic acids, and these are the main findings of TCA and AM treatments.

Additionally, there are notable differences in accessibility of bound lipids to chemolysis in comparison to HyPy for the higher salinity (P5AB) versus the lower salinity (P4n5) core, as well as some peculiarities observed for layer 4 from P4n5. This might be attributable to the relative abundance of EPS and its relation to the formation of insoluble 'hydrophobic' residue during the acid methanolysis treatment. Overall, the results from this study show that selective chemical degradations that target certain biochemical linkages within kerogen or proto-kerogen, greatly enhances our ability to structurally characterise such a complex macromolecular organic matter fraction. It also places important constraints on the role of EPS during kerogen formation and requires that the role of microbial sheath material be examined in greater detail. Future experiments will target the uronic acid composition of EPS-dominated layers to see if differences in composition can provide insights into the role of EPS during sequestration of lipids into insoluble macromolecular organic matter. Catalytic hydropyrolysis is an important technique to investigate how kerogen-incorporated lipid biomarkers will ultimately become preserved and progressively transformed over long diagenetic timescales since a significant pool of lipids can get incorporated into kerogen beneath extant photosynthetic mat layers. On ancient sedimentary timescales, these covalently-linked lipids will be preserved and buried to greater depths until they are ultimately released by catagenesis as hydrocarbon equivalents with increasing thermal maturity. The bound fraction released from sequestration by HyPy opens a window into early diagenesis, chemical taphonomy of benthic mat organics and thus helps us better interpret the ancient biomarker record.

References

Adam, P., Mycke, B., Schimd, J. C., Connan, J., and Albrecht, P. 1992. Steroid moieties attached to macromolecular petroleum fraction *via* di- or polysulfide bridges. *Energy & Fuels* 6, 553-559.

Amblès, A., Grasset, L., Dupas, G., Jacquesy, J-C. 1996. Ester- and ether bond cleavage in immature kerogens. *Organic Geochemistry* **24**(6-7), 681-690.

Bennett, B., and Abbott, G. D. 1999. A natural pyrolysis experiment – hopanes from hopanoic acids? *Organic Geochemistry* **30**(12), 1509-1516.

Böhm, F., Tinkler, J. H., and Truscott, T. G. 1995. Carotenoids protect against cell membrane damage by nitrogen dioxide radical. *Nature Medicine* **1**, 98-99.

Boucher, R. J., Standen, G., and Eglinton, G. 1991. Molecular characterisation of kerogens by mild selective chemical degradation – ruthenium tetroxide oxidation. *Fuel* **70**(6), 695-702.

Braissant, O., Decho, A. W., Dupraz, C., Glunk, C., Przekop, K. M., and Visscher, P. T. 2007. Exopolymeric substances of sulfate-reducing bacteria: Interactions with calcium at alkaline pH and implication for formation of carbonate minerals. *Geobiology* **5**(4), 401-411.

Chappe, B., Michaelis, W., and Albrecht, P. 1980. Molecular fossils of Archaebacteria as selective degradation products of kerogen. *Physics and Chemistry of the Earth* **12**, 265-274.

Dragojlović, V., Bajc, S., Amblès, A., and Vitorovic, D. 2005. Ether and ester moieties in Messel shale kerogen examined by hydrolysis/ruthenium tetroxide oxidation/hydrolysis. *Organic Geochemistry* **36**(1), 1-12.

Flemming, H-C., Neu, T. R., and Wozniak, D. J. 2007. The EPS matrix: The "house of biofilm cells". *Journal of Bacteriology* **189**(22), 7945-7947.

Flemming, H-C., and Wingender, J. 2010. The biofilm matrix. *Nature Reviews Microbiology* **8**, 623-633.

Goth, K., de Leeuw, J. W., Puttmann, W., and Tegelaar, E. W. 1988. Origin of Messel oil shale kerogen. *Nature* **336**, 759-761.

Hoiczyk, E. 1998. Structural and biochemical analysis of the sheath of *Phormidium unicatum*. *Journal of Bacteriology* **180**(15), 3923-3932.

Höld, I. M., Brussee, N. J., Schouten, S., and Sinninghe Damsté, J. S. 1998. Changes in the molecular structure of a Type II-S kerogen (Monterey Formation, U.S.A.) during sequential chemical degradation. *Organic Geochemistry* **29**(5-7), 1403 1417.

Huesby, B., and Ocampo, R. 1997. Evidence for porphyrins bound, *via* ester bonds, to the Messel oil shale kerogen by selective chemical degradation. *Geochimica et Cosmochimica Acta* **61**(18), 3951-3955.

Kawaguchi, T., and Decho, A. W. 2002. A laboratory investigation of cyanobacterial extracellular polymeric secretions (EPS) in influencing $CaCO_3$ polymorphism. *Journal of Crystal Growth* **240**, 230-235.

Klock, J-H., Wieland, A., Seifert, R., and Michaelis, W. 2007. Extracellular polymeric substances (EPS) from cyanobacterial mats: characterisation and isolation method optimisation. *Marine Biology* **152**, 1077-1085.

Kohnen, M. E. I., Sinninghe Damsté, J. S., Kock-van Dalen, A. C., and de Leeuw, J. W. 1991. Di- or polysulphide-bound biomarkers in sulphur-rich geomacromolecules as revealed by selective chemolysis. *Geochimica et Cosmochimica Acta* **55**(5), 1375-1394.

Kohnen, M. E. I., Sinninghe Damsté, J. S., Kock-van Dalen, A. C., and de Leeuw, J. W. 1993. Sulphur-bound steroid and phytane carbon skeletons in geomacromolecules: Implications for the mechanism of incorporation of sulphur into organic matter. *Geochimica et Cosmochimica Acta* **57**(11), 2515-2528.

Komaniecka, I., Choma, A., Mazur, A., Duda, K. A., Lindner, B., Schwudke, D., and Holst, O. 2014. Occurrence of an unusual hopanoid-containing lipid A among lipopolysaccharides from *Bradyrhizobium* species. *Journal of Biological Chemistry* **289**, 35644-35655.

Kribii, A., Lemeé, L., Chaouch, A., and Amblès, A. 2001. Structural study of the Morrocan Timahdit (Y-layer) oil shale kerogen using chemical degradations. *Fuel* **80**(5), 681-691.

Michaelis, W., and Albrecht, P. 1979. Molecular fossils of archaebacteria in kerogen. *Naturwissenschaften* **66**, 420-421.

Michaelis, W., Richnow, H. H., Jenisch, A., Schulze, T., and Mycke, B. 1990. Structural inferences from organic geochemical coal studies. In: *Facets of Modern Biogeochemistry* (eds. Ittekkot, V., Kempe, S., Michaelis, W., and Spitzy, A.) Springer-Verlag, 388-401.

Mycke, B., and Michaelis, M. 1986. Molecular fossils from chemical degradation of macromolecular organic matter. *Organic Geochemistry* **10**, 499-516.

Mycke, B., Narjes, F., and Michaelis, W. 1987. Bacteriohopanetetrol from chemical degradation of an oil shale kerogen. *Nature* **326**, 179-181.

Ocampo, R., and Repeta, D. J. 2002. Isolation and structure determination of two novel C(13^2)—OH bacteriopheophytin *a* allomers from a coastal salt pond. *Organic Geochemistry* **33**(7), 849-854.

Papoular, R. 2001. The use of kerogen data in understanding the properties and evolution of interstellar carbonaceous dust. *Astronomy and Astrophysics* **378**, 597-607.

Pentecost, A. 1985. Association of cyanobacteria with tufa deposits: identity, enumeration and nature of sheath material revealed by histochemistry. *Geomicrobiology Journal* **4**, 285-298.

Razvigorova, M., Budinova, T., Tsyntsarki, B., Petrova, B., Ekinci, E., and Atakul, H. 2008. The composition of acids in bitumen and products from saponification of kerogen: Investigation of their role as connecting kerogen and mineral matrix. *International Journal of Coal Geology* **76**(3), 243-249.

Richnow, H. H., Jenisch, A., and Michaelis, W. 1992. Structural investigations of sulphur-rich macromolecular oil fractions and a kerogen by *sequential* chemical degradation. *Organic Geochemistry* **19**(4-6), 351-370.

Rohmer, M., Bouvier-Nave, P., Ourisson, G. 1984. Distribution of hopanoid triterpenes in prokaryotes. *Journal of General Microbiology* **130**, 1137-1150.

Sáenz, J. P. 2010. Hopanoid enrichment in a detergent-resistant membrane fraction of *Crocosphaera watsonii*: Implications for bacterial lipid raft formation. *Organic Geochemistry* **41**(8), 853-856.

Schaeffer, P., Harrison, W. N., Keely, B. J., and Maxwell, J. R. 1995. Product distributions from chemical degradation of kerogens from a marl from a Miocene evaporitic sequence (Vena del Gesso, N. Italy). *Organic Geochemistry* **23**(6), 541-554.

Schaeffer-Ries, C., Schaeffer, P., Putschew, A., and Maxwell, J. R. 1998. Stepwise chemical degradation of immature S-rich kerogens from Vena del Gesso (Italy). *Organic Geochemistry* **29**(8), 1857-1873.

Schwarzbauer, J., Ricking, M., and Littke, R. 2003. Quantitation of non-extractable anthropogenic contaminants released from Teltow Canal sediments after chemical degradation. *Acta Hydrochimica et Hydrobiologica* **31**(6), 469-481.

Silipo, A., Vitiello, G., Gully, D., Sturiale, L., Chaintreuil, C., Fardoux, J., Lee, H-I., Kulkarni, G., Busset, N., Marchetti, R., Palmigiano, A., Moll, H., Engel, R., Lanzetta, R., Paduano, L., Parrilli, M., Chang, W. S., Holst, O., Newman, D. K., Garozzo, D., D'Errico, G., Giraud, E., and Molinaro, A. 2014. Covalently-linked hopanoid-lipid A improves outer membrane resistance of a *Bradyrhizobium* symbiont of legumes. *Nature Communications* **5**, 1-11.

Šmarda, J., Šmajs, D., Komrska, J., and Krzyžánek, V. 2002. S-layers on cell walls of cyanobacteria. *Micron* **33**(3), 257-277.

Sudgen, M. A., and Abbott, G. D. 2002. The stereochemistry of bound and extractable pentacyclic triterpenoids during closed system pyrolysis. *Organic Geochemistry* **33**(12), 1515-1521.

Wang, Z., Gao, M., Wang, Z., She, Z., Chang, Q., Sun, C., Zhang, J., Ren, Y., and Yang, N. 2013. Effect of salinity on extracellular polymeric substances of activated sludge from an anoxic-aerobic sequencing batch reactor. *Chemosphere* **93**(11), 2789-2795.

Xiong, Y. Q., Wang, Y. Q., and Wang, Y. M. 2007. Selective chemical degradation of kerogen from Nenjiang Formation of the southern Songliao Basin. *Science in China Series D: Earth Sciences* **50**(10), 1504-1509.

CHAPTER SIX

Conclusions and Future Directions

This dissertation presents lipid biomarker and carbon isotopic data that record microbial community structure and carbon cycling in modern and ancient marine environments. Part I of this dissertation's overall focus was on the composition (lipid biomarker and stable isotopic) of organic matter preserved in an organic-rich facies capturing the enigmatic 'Shuram' negative carbon isotope excursion from the late Ediacaran (~635-541 Ma). The two chapters that make up this part of the thesis not only inform the indigenous composition of the preserved organic matter but allow us to identify distinct organic carbon sources. In this instance, we found that at least two organic carbon sources possessing distinct isotopic compositions were decoupled from one another during the Shuram excursion, thus masking the overall isotopic contribution to the bulk organic carbon values and skewing previous perceptions of the overall magnitude of the isotopic excursion in organic matter. Results presented in Part I allow us to hypothesise a scenario in which a reservoir of hydrocarbons (generated from organic matter buried prior to the Shuram excursion) seeped from the subsurface into the ocean during this time period. The trigger for such a global event could have come from enhanced tectonic activity (Pan African orogeny) during this time period, and is supported by preliminary evidence of an increase in thermal maturity in the organic matter contained in rocks from the Eastern European Platform (Pehr & Love, unpublished data). Heterotrophs feeding on this biomass buffered the magnitude of the

222

autotrophic organic carbon signal and as the isotopic buffering capacity waned during recovery of the Shuram excursion, the coupling of the carbonate and organic carbon isotopes resumes.

The study of late Ediacaran organic matter from South Oman informs us of processes that are occurring in modern environments, especially as high abundances of mid-chain monomethyl alkanes (MMAs or X-peaks) in these samples could be derived from a benthic microbial mat environment. Part II of this dissertation investigated the lipids incorporated into the proto-kerogen of benthic microbial mats sourced from the hypersaline ponds of Guerrero Negro, Baja California, Mexico. They represent a marine environment with increasing salinity from seawater to gypsum precipitation. Microbial mats flourish in the intermediate salinities and develop layered intervals representing the photosynthetic and heterotrophic microbial communities within this system.

To understand diagenesis in single cores, we analysed 19 layers (11 from core P4n5 and 8 from core P5AB) for their proto-kerogen-bound lipid profiles and compared the extractable lipids from P4n5. Significant compositional differences in the molecular profiles of proto-kerogen-bound lipid biomarkers was found with small increases in salinity. Proto-kerogen incorporated a wide variety of lipid biomarkers and bind through strong covalent linkages during the earliest stages of diagenesis. The preservation of sterols and hopanoids below photosynthetic layers of microbial mats indicates that significant taphonomic biases associated with lipids derived from surface primary production is unlikely to exist in organic matter that is dominated by benthic mat inputs.

Additionally, to understand the nature of covalent binding, we performed three different selective chemical degradations (chemolysis) and hydropyrolysis (HyPy) on residues representative active and sedimentary layer for both cores. The three selective chemical degradations range from mild (trichloroacetic acid and acid methanolysis) to aggressive (periodate oxidation). We compared the bound lipids from these chemically-treated pre-extracted residues to a pre-extracted control residue for layers 4 and 7 of P4n5 and P5AB (16 treatments in total). The results show that polycyclic biomarkers are rapidly bound into proto-kerogen through strong covalent linkages, as even the harshest chemical treatment—periodate oxidation—was still able to release detectable quantities of lipid biomarkers. Periodate oxidation also efficiently oxidises a large portion of, but not all, sterols as we are able to only recover trace quantities of steranes post-periodate oxidation.

The profiles generated through chemolysis reflect the mode of covalent binding into proto-kerogen; sterols possibly bound into EPS through carbohydrate structures or associated with portions of the matrix that contain carbohydrate structures. Hopanoids are bound into IMOM as weaker ester linkages, predominantly released as C_{31} and C_{32} hopanoid acids *via* acid methanolysis and trichloroacetic acid. Periodate oxidation targets the vicinal diol bonds of bacteriohopanepolyol (BHP) and results following this treatment show a reduction in the C_{33}-C_{35} hopanes. This is consistent with cleavage of extended hopanoid sugar side-chains with adjacent alcohol groups. Overall, we find that sterols and hopanoids in layers that were dominated by an extracellular polymeric substance (EPS) matrix potentially had different binding affinities to different types of EPS- a large

portion is loosely bound to soluble EPS and potentially a similarly large portion is strongly bound to sheath material EPS, although this observation warrants further chemical and structural characterisation.

Future Directions

Part I: Organic matter behaviour during the Ediacaran Shuram excursion

To investigate the oxidation budget and mass balance scenarios of the subsurface petroleum seepage model in order to explain the organic carbon isotope patterns during the Shuram excursion, we plan to use a thermal subsidence model to understand the mechanics of tectonically-driven global expulsion of generated hydrocarbons, and what feedbacks would accompany such a scenario. Unpublished $^{87}Sr/^{86}Sr$ data pointing to an increase in the weathering flux during this time supports this theory. Additionally, to understand source mixing between to different compositions, a two end-member mixing scenario will be set up to understand the contributions and timing of the hydrocarbon seepage release. The numbers generated from isotopic modelling and mass balance calculations will be compared with estimates for natural marine oil seepage (e.g., Wilson *et al.,* 1974; Kvenvolden & Cooper, 2003). To better understand the mechanism driving the subsurface petroleum seepage scenario, the thermal maturity differences in some Eastern European Platform samples, which are likely Shuram equivalent, will be studied in more detail. This will involve Rock Eval pyrolysis screening to determine thermal

maturity, lipid biomarkers, and better age constraints for correlation to Shuram equivalent sections to Oman and other localities.

Part II: Investigating diagenesis and covalent binding in microbial mat proto-kerogens

To complete the story of understanding how lipids are incorporated into proto-kerogen during early diagenesis in microbial mats, we will be comparing the full suite of intact polar lipids obtained under traditional extraction procedures to the pre-extracted residues subjected to catalytic hydropyrolysis for the higher salinity core, P5AB, as was performed on P4n5 (results presented in this study). Since the kerogen-bound lipid composition has already been investigated for P4n5 and P5AB, a more distal and higher salinity pond site that contains microbial mats (P5n6, 13% salinity, water temperature 27.4°C, pH 7.78) could potentially be another target, as one of the results from this study indicates that even small changes in salinity can influence the composition of lipids incorporated into kerogen. Another option would be to investigate mats that grow in P4n1 (Pond 4 near 1) which has been investigated phylogenetically (and also some intact polar lipid analysis) due to harbouring methanogens (e.g., Jahnke *et al.,* 2008; Orphan *et al.,* 2008) and the interest in characterising methane fluxes. Samples from P4n1 core (8-8.2% salinity, water temperature 25°C, pH 8.62) have lower salinity and would most certainly capture a different downcore profile due to different microbial communities.

Additional chemical treatments on extractable mat residues provide information on the sugar and protein composition. More specific chemical treatments such as EDTA washing, BBr_3 cleavage, and hot-phenol extraction will probe deeper into the structural

binding of functionalised compounds associated with cellular complexes. The overall protocol will provide a perspective of community structure in surface and deeper mat layers and provide information related to secondary heterotrophic populations with depth.

Hydropyrolysate results coupled to selective chemical degradations have already provided a lot of useful information on what compounds survive during diagenesis and how they are bound into macromolecular fractions. Since the HyPy procedure is optimised to generate high hydrocarbon yields and minimise structural and isomeric alteration to release products (unlike other chemolysis techniques that have limited reagent access due to steric hindrance resulting in lower product yields), temperature-controlled experiments can be performed to detect different binding strengths of certain molecules. Ester and weak sulfidic linkages in recent sediments break by 320-340°C (Farrimond *et al.,* 2003) while cleavage of strong C—C and C—O bonds occurs mainly in the range 350-520°C under typical catalytic HyPy conditions. Hence we choose 340°C as the cut-off temperature in a scheme to distinguish 'weak' (C—S, ester) from 'stronger' (C—C and C—O) bonds. Previous work using solid-phase model substrates indicated that the more stable C—C and C—O linkages in macromolecules likely remain largely intact under standard HyPy conditions at 340°C and below (Lafferty *et al.,* 1993; Ismail *et al.,* 1995). Sequential HyPy treatments allow us to assess the mode and extent of binding of different biomarker species within organic macromolecules.

Bulk spectroscopic methods, such as solid state ^{13}C-NMR, have proven effective at structurally characterising complex macromolecular fractions (Petsch *et al*., 2001; Cao

et al., 2013; Burdelnaya *et al*., 2014). Future work will investigate nature of covalent bond types in proto-kerogen and how these change with increasing diagenesis, using solid state ^{13}C-NMR.

Pure cell cultures and phylogenetic studies of modern microorganisms have contributed greatly to the understanding of the source organisms responsible for lipid biomarker precursors (e.g., Hayes, 2001; Welander *et al.,* 2010; Sáenz *et al.,* 2012). HyPy can be a powerful tool for the rapid screening of microbial cultures to provide a first order assessment of the composition of released lipids to aid in identification of lipid patterns in environmental samples (Love *et al.,* 2005). For future work in applying the HyPy technique to rapidly screen pure microbial cell cultures, we would select representative eukaryotic and prokaryotic groups that contribute significantly to the biodiversity in these mats.

Overall, this dissertation presents a comprehensive study demonstrating that organic matter contains a diverse composition of hydrocarbon and, using lipid biomarkers and stable isotopes, we can attempt to deconvolute their sources to understand microbial communities and carbon cycle dynamics.

References

Burdelnaya, N., Bushnev, D., Mokeev, M., and Dobrodumov, A. 2014. Experimental study of kerogen maturation by solid-state ^{13}C NMR spectroscopy. *Fuel* **118**, 308-315.

Cao, X., Yang, J., and Mao, J. 2013. Characterisation of kerogen using solid-state nuclear magnetic resonance spectroscopy: A review. *International Journal of Coal Geology* **108**, 83-90.

Farrimond, P., Love, G. D., Bishop, A. N., Innes, H. E., Watson, D. F., and Snape, C. E. 2003. Evidence for rapid incorporation of hopanoids into kerogen. *Geochimica et Cosmochimica Acta* **67**, 1383-1394.

Hayes, J. M. 2001. Fractionation of isotopes of carbon and hydrogen in biosynthetic processes. In: *Reviews in Mineralogy and Geochemistry* (eds. Valley, J.W., and Cole, D.R.), Mineralogical Society of America, **43**, 225–277.

Ismail, K., Mitchell, S. C., Brown, S. D., Snape, C. E., Buchanan, A. C., Britt, P. F., Franco, D. V., Maes, I. I., and Yperman, J. 1995. Silica-immobilised sulfur compounds as solid calibrants for temperature-programmed reduction and probes for the thermal behaviour of organic sulfur forms in fossil fuels. *Energy & Fuels* **9**, 707-716.

Jahnke, L. L., Orphan, V. J., Embaye, T., Turk, K. A., Kubo, M. D., Summons, R. E., and Des Marais, D. J. 2008. Lipid biomarker and phylogenetic analyses to reveal archaeal biodiversity and distribution in hypersaline microbial mat and underlying sediment. *Geobiology* **6**, 394-410.

Kvenvolden, K. A., and Cooper, C. K. 2003. Natural seepage of crude oil into the environment. *Geo-Marine Letters* **23**,140-146.

Lafferty, C. J., Mitchell, S. C., Garcia, R., and Snape, C. E. 1993. Investigation of organic sulfur forms in coals by high temperature reduction. *Fuel* **72**, 367-371.

Love, G. D., Bowden, S. A., Summons, R. E., Jahnke, L. L., Snape, C. E., Campbell, C. N., and Day, J. G. 2005. An optimised catalytic hydropyrolysis method for rapid screening of microbial cultures for lipid biomarkers. *Organic Geochemistry* **36**, 63-82.

Orphan, V. J., Jahnke, L. L., Embaye, T., Turk, K. A., Pernthaler, A., Summons, R. E., and Des Marais, D. J. 2008. Characterisation and spatial distribution of

methanogens and methanogenic biosignatures in hypersaline microbial mats of Baja California. *Geobiology* **6**, 376-393.

Petsch, S. T., Smernik, R. J., Eglinton, T. I., and Oades, J. M. 2001. A solid state ^{13}C-NMR study of kerogen degradation during black shale weathering. *Geochimica et Cosmochimica Acta* **65**(12), 1867-1882.

Sáenz, J. P., Waterbury, J. B., Eglington, T. I., and Summons, R. E. 2012. Hopanoids in marine cyanobacteria: probing their phylogenetic distribution and biological role. *Geobiology* **10**, 311-319.

Welander, P. V., Coleman, M. L., Sessions, A. L., Summons, R. E., and Newman, D. K. 2010. Identification of a methylase required for 2-methylhopanoid production and implications for the interpretation of sedimentary hopanes. *Proceedings of the National Academy of Sciences of the United States of America* **107**, 8537-8542.

Wilson, R. D., Monaghan, P. H., Osanik, A., Price, L. C., and Rogers, M. A. 1974. Natural marine oil seepage. *Science* **184**(4139), 857-865.

APPENDIX

Relative depth (m) in TM-6 samples: 0 m refers to the top of the A5-A6 unit of the Ara Group and 975 m refers to the base of the Masirah Bay Formation of the Nafun Group.

Table A2.1. Fraction yields for TM-6 samples (nm = not measured).

Group (Formation)	Sample	Sats (mg)	Aros (mg)	Pols (mg)	Total yield (mg)
Ara (Athel)	TM6-1	1.1	1.1	7.0	9.2
Ara (Athel)	TM6-2	1.6	1.3	6.1	9.0
Ara (Birba)	TM6-3	nm	nm	nm	nm
Nafun (Shuram)	TM6-4	4.8	3.5	7.8	16.1
Nafun (Shuram)	TM6-5	7.5	6.1	8.9	22.5
Nafun (Shuram)	TM6-6	6.0	3.9	12.1	22.0
Nafun (Shuram)	TM6-7	3.8	2.5	5.7	12.0
Nafun (Shuram)	TM6-8	2.8	2.1	4.4	21.3
Nafun (Shuram)	TM6-9	5.7	4.0	7.4	17.1
Nafun (Shuram)	TM6-10	3.9	2.6	9.2	15.7
Nafun (Shuram)	TM6-11	2.0	1.1	4.4	7.5
Nafun (Shuram)	TM6-12	3.2	2.7	14.3	20.2
Nafun (Shuram)	TM6-13	2.8	2.7	6.1	11.6
Nafun (Shuram)	TM6-14	3.2	3.0	5.4	11.6
Nafun (Shuram)	TM6-15	3.1	2.2	11.9	17.2
Nafun (Shuram)	TM6-16	2.0	0.6	8.0	10.6
Nafun (Shuram)	TM6-17	6.9	1.7	13.4	22.0
Nafun (Shuram)	TM6-18	5.3	2.2	8.1	15.6
Nafun (Shuram)	TM6-19	1.1	0.8	5.0	6.9
Nafun (Shuram)	TM6-20	2.0	0.6	10.4	13.0
Nafun (Shuram)	TM6-21	0.1	0.1	3.9	4.1
Nafun (Khufai)	TM6-22	0.7	0.7	4.2	5.6
Nafun (Khufai)	TM6-23	0.7	1.2	6.3	8.2
Nafun (Khufai)	TM6-24	5.6	3.5	17.8	26.9
Nafun (Khufai)	TM6-25	5.0	3.3	6.9	15.2
Nafun (Khufai)	TM6-26	3.0	2.0	3.3	8.3
Nafun (Masirah Bay)	TM6-27	2.9	1.0	11.4	15.3
Nafun (Masirah Bay)	TM6-28	2.3	1.7	4.9	8.9

Table A2.2a. Carbon content and bulk carbon isotopic data for TM-6. All isotope data in units of ‰VPDB.

Relative depth (m)	Carbonate wt%	TOC wt%	$\delta^{13}C_{carb}$‰ VPDB	$\delta^{13}C_{org}$‰ VPDB	$\Delta^{13}C_{carb-org}$‰
0			2.48	-32.00	34.48
5			2.46		
10			2.60		
15			2.60		
20			2.81		
25			2.59		
30		0.92	2.32		
35			2.52		
40		1.66	2.73		
45			2.64		
50			2.32	-31.56	33.89
55			2.47		
60			2.26		
65			1.72		
70			1.69		
75		0.66	1.88		
80			-2.69		
85			-3.08		
90		14.86	-3.07	-33.88	30.81
100	88.00	4.89	-3.67	-30.10	26.43
105	66.76	1.38	-2.85	-29.39	26.54
110	90.63	5.37	-3.11	-32.36	29.25
115		7.50	-4.41	-33.23	28.82
120		3.48	-2.86	-33.17	30.32
125		0.18	-3.78	-28.81	25.04
130		1.47	1.80	-31.75	33.55
135		2.37	1.21	-32.17	33.38
140		1.88	1.45	-31.66	33.11
145		1.87	1.47	-31.86	33.33
150		0.78	1.42	-31.74	33.16
155		1.78	2.15	-30.46	32.61
160		4.27	3.02	-31.41	34.43
165		3.32	3.22	-28.82	32.05
170			2.65	-30.52	33.18
175			2.35	-31.75	34.10
180			2.35	-32.24	34.58
185			0.17	-31.02	31.19
190		6.83	-0.24	-30.38	30.14
195			0.66	-31.77	32.43
200		10.47	1.77	-32.30	34.07

205		4.37	1.73	-28.52	30.25
210			1.87	-30.16	32.02
215			1.60	-29.86	31.46
220	96.82		1.46	-29.87	31.33
225	95.05		1.36	-30.17	31.53
230	93.12	2.86	-1.04	-29.53	28.49
235	90.43	2.40	-4.67	-33.91	29.24
240	93.20	2.57	0.17	-33.53	33.70
245	83.06	1.02	0.34	-33.14	33.48
250			0.96		
255	74.39	0.56	1.47	-29.61	31.07
260	80.00		0.98	-30.58	31.56
265	80.77	0.58	0.23	-29.98	30.20
270	72.64		-0.54	-31.12	30.58
275	54.17		0.00	-28.31	28.31
280	60.78		-0.13	-32.82	32.69
285	49.50		-2.02	-35.69	33.68
290	40.00		-1.69	-35.80	34.11
295	40.37		-3.44	-32.00	28.56
300	28.57	1.51	-1.11	-37.64	36.53
305	44.23	2.60	-1.95	-39.33	37.38
310	42.96		-1.77	-36.12	34.34
315	47.48		-1.09	-36.52	35.43
320	25.49		-1.23	-33.65	32.43
325	43.94		-0.19	-33.85	33.66
330	30.95		-0.19	-33.86	33.66
335	37.04		-0.85	-33.30	32.45
340	48.94		-0.78	-32.94	32.16
350	54.55	2.40	-5.61	-36.23	30.62
360		2.30			
370	55.00	11.69	-3.25	-38.69	35.44
380	81.74	2.80	-5.27	-35.81	30.54
395	73.74		-0.47	-33.84	33.38
400	84.75		-0.19	-35.14	34.94
410	62.00	1.58	-1.96	-34.40	32.44
420	58.18		-2.74	-34.96	32.22
430	25.49		-3.20	-36.76	33.56
440	32.53		-1.74	-36.87	35.14
460	23.23	2.03	-1.55	-36.13	34.57
480	18.80	11.48	-2.22	-35.70	33.47
495	21.93	8.52	-3.73		
505	21.14	5.85	-3.42	-37.86	34.44
520	23.30	3.49	-3.03		
540	14.93		-3.42	-38.26	35.23

560	13.74	8.88	-3.37	-38.31	34.94
580	24.21	0.96	-2.55	-36.40	33.84
600			-4.11	-36.98	32.88
620	17.13		-4.17	-36.84	32.68
640	18.50	9.88	-3.03	-35.81	32.77
660	13.27		-2.71	-36.23	33.52
680			-2.71		
685		3.90			
700	36.22	1.59	-2.80	-34.88	32.08
710	28.96	5.92	-3.03		
730	38.97		-2.74	-31.31	28.58
735	37.89	2.44	-3.48		
740	34.87		-8.83	-34.33	25.50
745	91.64		-8.16	-33.42	25.26
750	72.09	2.70	-8.02	-32.22	24.20
755	75.63	10.74	-8.28	-34.08	25.80
760	58.67	1.39	-8.27	-33.69	25.42
765	58.04		-8.31		
770	52.57	2.58	-8.49		
775	49.22	12.59	-8.92		
780	51.47		-10.28	-35.20	24.92
785	50.00		-10.31	-34.70	24.39
790			-11.75		
795	56.50	6.59	-12.75		
800	51.89	9.18	-11.28	-36.02	24.74
805	62.83	8.75	-7.00		
810	48.00		-6.61	-36.12	29.51
815	38.15		-3.36	-33.93	
820	64.12	3.07	2.20	-33.62	35.82
825	71.02		3.35	-35.83	39.17
830			3.29		
840			4.42		
845			4.30		
850	90.54		4.57	-33.82	38.38
855	89.69	3.33	4.62	-32.67	37.30
860	84.01	3.38	4.50	-32.69	37.19
865	93.49	3.04	5.13	-33.34	38.47
870	89.50	3.32	4.72	-32.46	37.18
875	90.56	2.70	4.54	-31.98	36.52
880	86.58		4.61	-31.22	35.83
885		7.29			
890	53.57	17.41	3.86		
895		4.90			
905	34.84	2.41	2.14	-31.23	33.37

920	33.43		-0.43	-31.60	31.17
935		9.76	0.39		
950			-4.56		
965			-6.47		
975	31.27	0.70	-6.54	-31.76	25.22

Table A2.2b. Oxygen, sulfur, and nitrogen isotope data for TM-6. All units in ‰.

Relative depth (m)	$\delta^{18}O_{carb}$‰ VPDB	$\delta^{34}S_{CAS}$‰ VCDT	$\delta^{34}S_{pyr}$‰ VCDT	$\delta^{15}N_{org}$‰ vs. air
0	-3.29	41.20	8.73	
5	-3.43			
10	-3.47			
15	-2.70			
20	-2.82			
25	-2.12			
30	-3.71			1.11
35	-3.71			
40	-3.88			
45	-3.57			
50	-3.37		8.49	
55	-3.34	39.60		
60	-3.17			
65	-1.14			
70	-2.91			
75	-0.96			2.48
80	-2.60	39.30		
85	-1.82	39.20		
90	-1.83	41.30	9.90	
100	-1.38	29.70		
105	-3.35	38.90		
110	-3.02	38.20		
115	-4.17	40.70	7.92	
120	-3.59	40.00	7.94	
125	-3.08	40.30	11.90	
130	-4.15	41.10	9.41	
135	-2.94	38.90	8.23	
140	-2.81	39.60	8.84	
145	-2.40	39.70	9.90	

150	-2.74	39.00	7.59	
155	-2.67	39.30	9.25	
160	-2.16	39.70	8.73	
165	-3.22	40.40	10.83	
170	-2.98	38.70	11.38	
175	-3.38	38.90	10.63	
180	-3.38	38.90	5.52	
185	-5.58	39.20	10.24	
190	-6.54	38.90	6.70	
195	-4.19	41.80	10.39	
200	-3.27	39.20	8.76	
205	-1.59	38.30	10.90	
210	-3.10	39.50	9.10	
215	-3.26	39.40	10.35	
220	-2.21	41.80		
225	-3.03	39.80		
230	-1.90	42.40		4.22
235	-3.54			
240	-0.19	42.30		
245	-0.81	41.30		
250	-2.39	39.50		
255	-2.48	40.20		
260	-2.42	39.60		
265	-1.93	40.70		
270	-1.07	40.80		
275	-1.59	39.60		
280	-2.01	40.50		
285	-1.79	44.30		
290	-2.27	34.90		
295	-3.16	37.90		
300	-2.83	27.10		
305	-2.32	18.30		
310	-2.69	39.10		
315	-2.66	38.40		
320	-2.68	31.80		
325	-2.88	33.70		
330	-2.80	31.90		
335	-2.88	38.10		
340	-2.71	33.70		
350	-1.07			
360		27.80		
370	-3.15	27.20		
380	-3.90	31.70		
395	-3.89	36.50		

236

400	-3.67	33.00		
410	-3.29	29.90		
420	-0.36	8.00		
430	-3.01	18.10		
440	-3.50	27.10		
460	-3.85	27.00		3.70
480	-3.93	14.80		3.52
495	-3.71	18.60		3.64
505	-4.29	23.30		3.11
520	-3.37	25.70		2.86
540	-3.35	13.90		3.67
560	-3.98	13.22		3.28
580	-3.76	13.45		4.16
600	-4.02	10.61		
620	-4.00	17.02		
640	-3.89	22.52		
660	-3.56	10.25		
680	-2.71	24.59	-6.16	
685				
700	-4.83	29.46	-2.86	
710	-4.55	25.55		4.04
730	-5.73	-2.80	-7.60	
735	-7.22	20.78	-6.28	2.56
740	-5.34	13.88	-2.45	
745	-5.77	28.54		
750	-6.23	28.21		2.56
755	-5.81	27.21		3.76
760	-7.14	25.88		
765	-6.93	29.56		3.96
770	-6.48	30.56		2.84
775	-6.24	31.85		3.68
780	-6.35	32.21		
785	-5.98	35.13		
790	-7.13	28.61		
795	-6.69	32.17		3.74
800	-6.26	28.84		1.37
805	-4.10	26.27		4.46
810	-4.09	20.58		
815	-6.49	6.86		
820	-6.08	21.47		
825	-6.93	21.68		
830	-6.06	21.85		
840	-7.13	29.30		
845	-6.52	27.49		

850	-6.16	31.86		
855	-7.67	31.31		4.52
860	-7.37	30.59		
865	-7.25	29.49		
870	-7.49	31.82		
875	-8.88	33.04		5.73
880	-8.34	32.16		
885		17.71		
890	-8.42	10.98		5.09
895				
905	-9.16	0.38	-1.85	
920	-8.55	7.28	-2.88	
935	-8.19			
950	-7.78			3.87
965	-8.85			
975	-8.36	15.97	-2.88	

Table A2.3. Bulk organic carbon isotope fractions through TM-6. All units in ‰VPDB.

Relative depth (m)	$\delta^{13}C_{bitumen}$ ‰VPDB	$\delta^{13}C_{kerogen}$ ‰VPDB	$\delta^{13}C_{sats}$ ‰VPDB
30	-32.31		-31.60
75	-30.37	-30.12	-30.27
230	-28.91	-28.30	
350			-35.30
460	-31.76	-35.55	-36.40
480	-33.94	-36.24	-34.14
495	-35.51	-36.72	-36.82
505	-35.94	-37.71	-35.27
520	-31.57	-37.33	
560	-33.78	-36.44	-36.33
640	-34.05	-35.95	-35.60
680	-31.02		-34.06
710	-34.72	-35.33	-34.70
735	-31.36	-30.62	-32.03
750	-33.28	-32.47	-33.40
755	-33.56	-33.01	-33.63
765	-31.33	-33.25	-34.03
770	-31.69	-33.95	-34.55
775	-31.31		-31.45
790	-32.08	-33.50	-34.89
795	-32.21	-32.99	-33.90
800	-31.48	-33.22	
805	-30.12		-33.14
825	-29.97		-33.17
845	-32.11	-33.72	-32.38
855	-32.80	-33.67	-32.29
875	-31.14	-32.54	-32.40
890	-29.96	-30.64	-31.66
935	-31.24	-31.51	-31.50

Table A2.4a. Select lipid biomarker ratios through TM-6. St = sterane, Hp = hopane, 24-ipc = 24-isopropylcholestane, 2MeHI = 2α-methylhopane index, 3MeHI = 3β-methylhopane index, g = gammacerane, Pr = pristane, Ph = phytane.

Relative depth (m)	St/Hp	%2MeHI	%3MeHI	%C$_{29}$ St	%24-ipc/St	γ/C$_{30}$ Hp	Pr/nC$_{17}$	Ph/nC$_{18}$	Pr/Ph
240	0.72	13.30	7.09	74.52	1.80	0.21	0.49	1.68	0.27
300	0.73	4.22	4.75	68.28	0.95	0.05	0.58	0.79	0.74
350	1.00						0.49	1.64	0.25
380	0.60	15.58	10.84	73.93	1.59	0.32	0.32	1.23	0.24
420	0.76	10.92	5.49	78.63	2.34	0.26			
460							0.36	1.33	0.18
480	0.78	12.90	4.71	71.13	1.60	0.20	0.39	1.28	0.27
495							0.32	1.22	0.17
540	0.71	13.45	5.02	76.29	1.31	0.18	0.29	1.06	0.28
							0.26	1.04	0.19
							0.41	1.32	0.23
							0.37	1.13	0.23
685	0.80								
710	0.61	11.16	5.17	75.17	1.43	0.15	0.42	1.14	0.40
							0.47	1.19	0.31
750	0.50	6.50	5.05	64.71	2.25	0.10	0.72	2.41	0.30
							0.89	2.34	0.24
							0.57	1.92	0.20
							0.65	2.08	0.21
							0.51	1.52	0.24
780	0.51	10.64	5.48	71.49	1.42	0.14	0.44	1.61	0.28
							0.49	1.42	0.22
800	0.84	9.70	4.25	71.44	1.72	0.13			
805	0.47	8.79	5.66	70.37	1.44	0.16	0.56	1.28	0.41
810	1.05	9.26	3.46	63.57	2.20	0.14			
820	0.53	9.37	4.97	73.09	1.74	0.14	0.41	0.92	0.49
830	0.43	5.92	4.67	70.89	2.48	0.09	0.38	0.94	0.34
840	0.45	6.53	5.64	70.29	2.17	0.10	0.42	1.07	0.33
							0.35	1.02	0.19
850	0.39	6.29	5.14	70.76	2.45	0.09	0.40	1.19	0.28
							0.50	1.44	0.22
							0.48	1.44	0.21
							0.29	0.68	0.36
895	0.79								
935							0.44	0.69	0.64

Table A2.4b. C_{20}-C_{26} X-peak (MMAs)/n-alkane ratios through TM-6.

Relative depth (m)	X_{20}/nC_{20}	X_{21}/nC_{21}	X_{22}/nC_{22}	X_{23}/nC_{23}	X_{24}/nC_{24}	X_{25}/nC_{25}	X_{26}/nC_{26}
240	0.41	0.42	0.68	0.43	0.83	0.66	0.60
300	0.20	0.20	0.24	0.13	0.29	0.34	0.33
380	0.44	0.40	0.67	0.51	0.43	0.42	0.37
480	0.64	0.81	1.26	0.82	1.52	0.74	0.85
540	0.72	0.70	1.10	0.78	1.65	0.74	0.85
710	0.52	0.53	0.79	0.52	0.93	0.48	0.47
750	0.31	0.37	0.68	0.36	0.72	0.45	0.38
780	0.51	0.59	0.92	0.72	1.23	0.59	0.59
805	0.45	0.47	0.56	0.37	0.63	0.42	0.35
820	0.37	0.40	0.47	0.41	0.60	0.36	0.34
830	0.19	0.25	0.29	0.25	0.30	0.20	0.16
840	0.26	0.31	0.40	0.30	0.41	0.26	0.18
850	0.28	0.36	0.50	0.35	0.50	0.30	0.26

Table A3.1. Compound-specific C_{20} – C_{28} *n*-alkane isotope data for TM-6. All units in ‰ VPDB, nm = not measured.

Relative depth (m)	$n\mathrm{C}_{20}$	$n\mathrm{C}_{21}$	$n\mathrm{C}_{22}$	$n\mathrm{C}_{23}$	$n\mathrm{C}_{24}$	$n\mathrm{C}_{25}$	$n\mathrm{C}_{26}$	$n\mathrm{C}_{27}$	$n\mathrm{C}_{28}$
75	-33.47	-33.50	-33.14	-32.38	-32.36	-32.91	-33.22	-34.05	-33.35
350	-36.13	-35.80	-35.80	-35.71	-35.47	-36.63	-36.45	-35.83	-37.13
480	-37.94	-37.75	-37.45	-37.66	-37.34	-36.71	-36.73	-36.63	-36.91
560	-38.64	-38.53	-38.58	-37.85	-38.42	-38.20	-37.92	-37.71	-38.38
640	-36.15	-36.44	-36.47	-36.20	-35.47	-35.57	-35.98	-36.43	-35.62
680	-36.57	-36.96	-37.04	-37.27	-37.16	-37.66	-37.24	-37.93	-37.37
710	-37.41	-37.30	-37.09	-37.01	-36.26	-35.96	-36.33	-35.96	nm
765	-36.80	-36.88	-36.47	-36.75	-36.59	-37.09	-36.67	-37.32	-36.73
775	-37.47	-37.52	-37.24	-37.12	-36.50	-36.69	-37.01	-36.63	-36.60
795	-37.81	-37.86	-37.10	-36.75	-35.61	-35.97	-36.48	-38.12	-38.08
845	-35.12	-34.83	-34.70	-34.90	-34.05	-34.61	-33.91	-33.88	-33.63
855	-34.16	-34.32	-34.06	-33.77	-33.09	-32.86	-32.72	-32.69	-32.80
875	-33.59	-33.59	-33.50	-33.08	-33.08	-33.34	-33.50	-33.07	-33.04
890	-32.98	-33.88	-33.79	-34.00	-33.70	nm	nm	nm	nm
935	-33.03	-33.42	-32.90	-33.21	-33.11	-33.19	-34.13	-34.66	-34.12

Table A3.2. Compound-specific C_{20} – C_{28} MMA (X-peak) isotope data for TM-6. All units in ‰ VPDB, nm = not measured.

Relative depth (m)	X_{20}	X_{21}	X_{22}	X_{23}	X_{24}	X_{25}	X_{26}	X_{27}	X_{28}
75	-36.26	-35.11	-34.26	-33.14	-33.02	-31.53	-31.33	-32.40	-32.74
350	-37.40	-37.57	-37.67	-38.13	-37.71	-38.80	-40.89	-37.64	-34.89
480	-39.36	-39.09	-38.96	-38.74	-38.58	-38.07	-38.00	-37.64	-38.22
560	-39.15	-39.26	-38.83	-38.81	-38.59	-38.76	-38.99	-39.13	-39.97
640	-36.87	-37.11	-37.32	-37.13	-37.36	-37.04	-37.16	-36.76	-37.27
680	-38.29	-38.63	-38.65	-38.54	-39.06	-38.95	-39.30	-38.01	-38.65
710	-37.94	-37.61	-38.04	-37.68	-37.54	-36.91	-37.02	-37.03	nm
765	-38.24	-38.12	-38.13	-38.32	-38.46	-38.88	-38.67	-38.40	-39.07
775	-39.09	-38.96	-38.60	-38.32	-38.35	-38.38	-39.56	-37.18	-36.57
795	-38.70	-38.29	-38.35	-38.71	-37.92	-37.11	-38.88	-38.50	-40.51
845	-37.09	-37.00	-37.27	-37.59	-36.76	-36.39	-36.41	-36.95	-36.62
855	-35.89	-35.99	-36.01	-36.66	-35.66	-34.93	-35.18	-34.75	-35.87
875	-35.14	-34.75	-36.15	-35.78	-36.21	-35.20	-34.61	-34.76	-35.18
890	-34.72	-34.95	-35.45	-35.23	-35.84	nm	nm	nm	nm
935	-37.17	-36.84	-36.69	-36.15	-36.45	-36.04	-35.68	-35.58	nm

Table A.3.3. Bulk branched/polycyclic ($\delta^{13}C_{br/cyc}$) carbon isotopes and compound-specific pristane ($\delta^{13}C_{Pr}$) and phytane ($\delta^{13}C_{Ph}$) isotopes for TM-6, nm = not measured. All units in ‰ VPDB.

Relative depth (m)	$\delta^{13}C_{br/cyc}$‰ VPDB	$\delta^{13}C_{Pr}$‰ VPDB	$\delta^{13}C_{Ph}$‰ VPDB
350	-33.53		
480	-33.33	nm	-36.42
640	-35.46	-35.89	-36.05
710	-34.42		
750	-33.14		
755	-32.98	-34.34	-34.57
765	-32.11	-35.28	-36.36
775	-31.12	-36.11	-35.24
845	-31.71	-34.60	-33.28
855	-32.05		
875	-32.03		
890	-30.96		

Table A4.1. Experimental conditions and fraction yields for kerogen hydropyrolysis of P4n5 pre-extracted residues.

Layer	Mass (g)	Catalyst (wt%)	Max. H_2 (bars)	Sats (mg)	Aros (mg)	Pols (mg)
1	0.6717	4.8	147	0.1	1.9	35.8
2	0.9662	4.9	145	0.5	4.9	23.2
3	0.8850	5.2	145	0.3	4.3	29.2
4	0.6566	5.0	141	0.5	1.0	21.7
5	1.0504	4.8	146	1.4	2.2	32.9
6	1.2130	5.0	144	0.6	2.7	24.6
7	1.2921	5.3	148	2.4	7.7	31.3
8	1.0393	4.9	145	1.5	1.4	1.6
9	1.6906	4.7	143	1.4	4.7	7.0
10	1.5966	4.9	146	1.0	9.6	5.2
11	1.1084	5.3	145	0.3	0.3	1.4

Table A4.2. Experimental conditions and fraction yields for kerogen hydropyrolysis of P5AB pre-extracted residues.

Layer	Mass (g)	Catalyst (wt%)	Max. H_2 (bars)	Sats (mg)	Aros (mg)	Pols (mg)
1	1.0805	5.0	144	1.0	14.0	124.5
2	1.0140	5.2	146	1.0	5.2	74.7
3	1.1837	5.2	142	1.0	7.9	123.6
4	1.4815	5.5	149	2.8	6.1	78.6
5	1.1712	4.9	147	1.0	2.8	47.3
6	1.3950	5.2	140	1.5	6.0	90.7
7	1.6338	5.3	135	1.6	2.0	14.2
8	1.6098	5.5	139	1.8	0.7	23.2

Table A4.3. Cell densities, carbon content and isotopes through P4n5 and P5AB (nm = not measured).

	P4n5			P5AB		
Layer	Cell density ($\times 10^7$/mm³)	TOC (wt%)	$\delta^{13}C_{org}$ (‰VPDB)	Layer	TOC (wt%)	$\delta^{13}C_{org}$ (‰VPDB)
1	7.6	18.81	-9.86	1	18.09	-9.81
2	4.5	11.67	-10.63	2	11.04	-11.24
3	2.9	10.53	-10.55	3	11.85	-12.07
4	1.6	10.36	-10.79	4	8.94	-11.54
5	0.8	8.52	-10.78	5	8.82	-11.28
6	0.8	8.59	-11.48	6	9.63	-11.83
7	0.5	8.63	-11.81	7	5.97	-12.02
8	0.3	3.37	-8.93	8	1.62	-12.64
9	0.1	3.49	-8.92			
10	0.2	3.43	-8.78			
11	nm	0.30	-8.00			

Table A4.4a. Intact polar lipid (IPL) data for P4n5 – alkanes. FAME = fatty acid methyl esters (units in $\times 10^3$); LCFAs = long-chain fatty acids; and VE diMe-acetals = vinyl ether dimethylacetals; nm = not measured. All units in ppm TOC (µg/g TOC).

Layer	Total FAME	LCFAs	Iso	Anteiso	2Me	Mid-chain branched	Total branched	VE diMe-acetals
1	20.29	110.72	1144.09	398.82	10.71	878.60	2431.03	4.76
2	16.14	87.28	1492.80	492.39	85.97	330.86	1961.74	0.13
3	11.69	484.84	1523.77	847.13	99.90	847.13	3159.43	0.00
4	4.96	188.11	853.38	313.13	212.20	416.37	1796.22	0.00
5	3.06	219.70	386.96	148.83	269.32	191.36	996.47	0.00
6	2.94	407.08	404.19	179.00	409.97	226.64	1131.73	0.00
7	0.74	103.45	114.95	56.04	114.95	56.04	313.23	0.72
8	0.90	197.74	119.23	72.70	26.17	52.34	270.45	0.00
9	0.34	115.82	45.79	32.32	0.00	13.47	91.58	11.26
10	0.50	167.35	81.28	62.16	0.00	21.52	167.35	42.31
11	0.00	0.00	0.00	0.00	0.00	0.00	0.00	nm

Table A4.4b. Intact polar lipid (IPL) data for P4n5 – isoprenoids. HBI = highly branched isoprenoid. All units in ppm TOC (µg/g TOC).

Layer	Pristane	Phytane	Phytenes (sum)	HBIs (sum)	Squalenes (sum)	Archaeol	ArcOH
1		0.60	31.51	0.00	67.50	0.22	
2		1.11	6.74	0.72	31.50	0.51	
3		5.07	16.39	2.01	65.30	1.31	
4	0.31	0.37	0.49			0.00	3.70
5	8.34	23.92	6.04	68.68	20.70	0.00	
6		17.56	3.93	67.96	14.00	0.00	
7	9.55	22.92	4.53	166.56	7.10	0.00	1.20
8	0.00	0.00	0.00	0.00	0.00	4.40	
9	0.00	0.00	0.00	0.00	0.00	6.00	
10	0.00	0.00	0.00	0.00	0.00	5.10	14.90
11	0.00	0.00	0.00	0.00	0.00		

Table A4.4c. Intact polar lipid (IPL) data for P4n5 – terpenoids. TriT = tricyclic terpene. All units in ppm TOC (µg/g TOC).

Layer	TriT ($C_{20:1}$)	Tetrahymenol	Methyl-tetrahymenol
1	0.00	9.63	3.01
2	1.73	22.76	2.22
3	13.09	44.22	4.29
4	0.00	20.05	49.46
5	32.60	17.36	33.43
6	29.59	22.81	42.43
7	16.52	19.88	34.40
8	7.27	23.15	0.00
9	0.00	24.02	0.00
10	0.00	6.28	0.00
11	0.00	0.00	0.00

Table A4.4d. Intact polar lipid (IPL) data for P4n5 – sterols. All units in ppm TOC (µg/g TOC).

Layer	C_{27} sterols	C_{28} sterols	C_{29} sterols	C_{30} sterols	Total sterols	Total steranes/enes
1	39.88	180.13	63.10	0.00	283.10	0.48
2	135.34	751.87	176.37	45.72	1109.31	7.82
3	432.22	523.20	772.54	71.26	1799.22	47.15
4	172.05	263.81	292.49	40.15	768.50	68.82
5	200.99	406.95	269.32	53.30	930.55	117.51
6	205.13	389.47	379.94	0.00	974.53	174.38
7	185.50	234.64	306.62	0.00	726.76	153.74
8	0.00	0.00	0.00	0.00	0.00	0.00
9	0.00	0.00	0.00	0.00	0.00	0.00
10	0.00	0.00	0.00	0.00	0.00	0.00
11	0.00	0.00	0.00	0.00	0.00	0.00

Table A4.4e. Intact polar lipid (IPL) data for P4n5 – hopanoic acids (HA). All units in ppm TOC (μg/g TOC).

Layer	C$_{30}$ ββ HA	C$_{31:1}$ HA	C$_{31}$ αβ HA	C$_{31}$ ββ HA	C$_{32}$ αβ HA	C$_{32}$ ββ HA	Total HA
1				0.70			1.97
2				3.18			7.74
3				25.71			48.21
4	0.48	1.11	1.54	87.06			49.28
5	2.55	5.39	14.60	172.79			213.94
6	0.00	1.05	6.90	95.58			141.41
7	0.43	1.72	2.44	34.92		0.14	34.29
8	1.45	2.04	5.82	119.81		0.00	50.06
9	0.19	0.75	0.00	4.88		0.19	2.73
10		0.19	0.26	4.64	0.07	0.36	3.72
11				0.00			0.00

Table A4.4f. Intact polar lipid (IPL) data for P4n5 – hopanoids. 2βMeHop = 2β-methylhopanol; 3βMeHop = 3β-methylhopanol. All units in ppm TOC (μg/g TOC).

Layer	Diploptene	Extended hopanols	Total hopanols	Total hopanes/enes	2βMeHop	3βMeHop
1	0.48	0.00	2.45	0.73		
2	3.09	0.51	11.34	4.35		
3	7.32	0.41	55.94	13.25		
4	0.01	72.46	121.75	0.01		
5	21.18	2.61	237.73	43.61		
6	34.54	5.41	181.36	48.15		
7	0.34	66.07	100.70	36.64		
8	1.03	53.33	104.42	10.08		
9	0.07	18.38	21.18	1.70	1.89	
10	0.00	3.75	7.47	0.60	0.26	0.26
11	0.00	0.00	0.00	0.00	0.95	1.33

Table A4.5a. Relative abundance of kerogen-bound isoprenoids for P4n5. Pr = pristane; Ph = phytane; $i\mathrm{C}_{25}$ = regular C_{25} isoprenoid.

Layer	Pr/Ph	$i\mathrm{C}_{25}/$ $((n\mathrm{C}_{22}+n\mathrm{C}_{23})/2)$	Squalane/ $((n\mathrm{C}_{26}+n\mathrm{C}_{27})/2)$	Acyclic biphytane/ $((n\mathrm{C}_{35}+n\mathrm{C}_{36})/2)$
1	0.09	0.00	0.11	0.34
2	0.18	0.00	0.06	0.16
3	0.22	0.00	0.07	0.05
4	0.40	0.00	0.17	0.15
5	0.25	0.00	0.08	0.13
6	0.19	0.11	0.09	0.32
7	0.26	0.11	0.08	0.07
8	0.31	0.19	0.08	0.12
9	0.13	0.34	0.08	0.08
10	0.24	0.15	0.05	0.07
11	0.19	0.19	0.05	0.49

Table A4.5b. Relative abundance of kerogen-bound isoprenoids for P5AB. Pr = pristane; Ph = phytane; $i\mathrm{C}_{25}$ = regular C_{25} isoprenoid.

Layer	Pr/Ph	$i\mathrm{C}_{25}/$ $((n\mathrm{C}_{22}+n\mathrm{C}_{23})/2)$	Squalane/ $((n\mathrm{C}_{26}+n\mathrm{C}_{27})/2)$	Acyclic biphytane/ $((n\mathrm{C}_{35}+n\mathrm{C}_{36})/2)$
1	0.17	0.05	0.11	0.40
2	0.21	0.06	0.10	0.32
3	0.16	0.08	0.13	0.58
4	0.19	0.13	0.20	0.42
5	0.20	0.06	0.15	0.16
6	0.09	0.14	0.16	0.14
7	0.08	0.21	0.24	0.11
8	0.12	0.75	0.15	0.53

Figure A4.1. Mass spectra of long-chain alkyl compounds eluting in the high molecular weight (HMW) region in layer 7 of P5AB. Tentative identification as an alkyl branched C_{38} aliphatic hydrocarbon with 2 double bond equivalents (2 DBE); M+ 530 Da, $C_{38}H_{74}$.
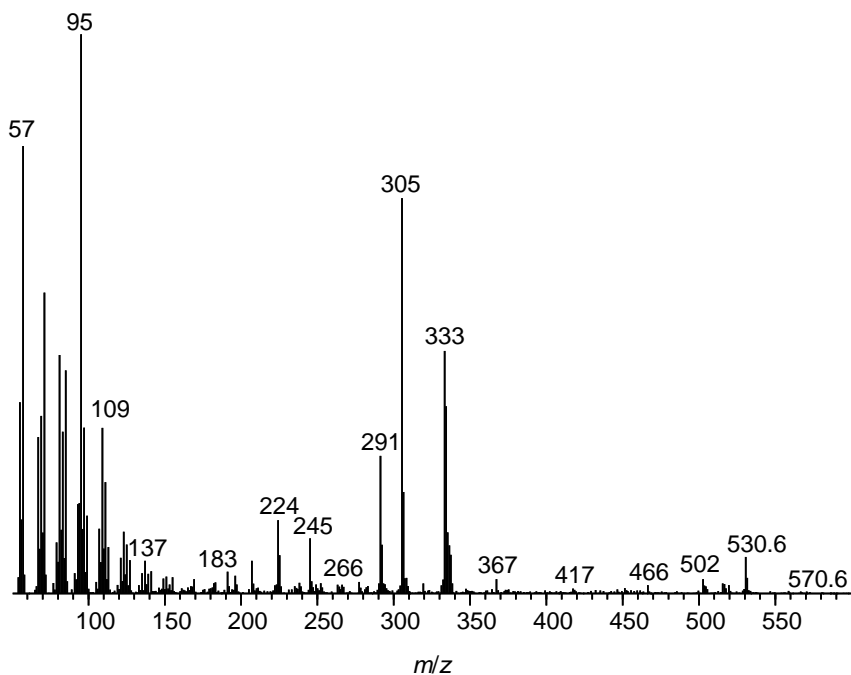

Table A4.6a. Concentration of kerogen-bound steranes and sterenes for P4n5 in ppm TOC (µg/g TOC). Sterenes = sum of the isomers of C_{27}-C_{29} sterenes, diasterenes, and steradienes.

Layer	C_{27} βααR	C_{27} αααR	C_{28} βααR	C_{28} αααR	C_{29} βααR	C_{29} αααR	Total steranes	Total sterenes
1	0.32	0.42	0.26	0.79	0.57	1.88	4.25	3.31
2	0.64	1.40	0.69	1.32	1.21	2.02	7.28	12.56
3	0.46	0.96	0.49	1.00	1.52	3.15	7.57	7.22
4	0.43	1.32	0.79	2.19	1.90	4.30	10.93	18.69
5	1.69	4.96	3.19	7.51	5.17	9.92	32.45	26.69
6	0.69	2.28	1.27	3.00	2.87	4.88	15.00	20.13
7	4.01	8.98	3.19	0.52	12.57	11.98	41.25	42.04
8	0.96	2.12	0.83	1.76	3.14	8.32	17.14	94.13
9	0.56	1.95	0.43	1.08	1.02	2.36	7.40	0.00
10	0.41	1.09	0.30	0.64	1.62	3.00	7.07	0.00
11	0.07	0.23	0.08	0.22	0.24	0.61	1.46	0.00

Table A4.6b. Concentration of kerogen-bound steranes and sterenes for P5AB in ppm TOC (µg/g TOC). Sterenes = sum of the isomers of C_{27}-C_{29} sterenes, diasterenes, and steradienes.

Layer	C_{27} $\beta\alpha\alpha R$	C_{27} $\alpha\alpha\alpha R$	C_{28} $\beta\alpha\alpha R$	C_{28} $\alpha\alpha\alpha R$	C_{29} $\beta\alpha\alpha R$	C_{29} $\alpha\alpha\alpha R$	Total steranes	Total sterenes
1	0.17	0.57	0.22	0.56	0.39	1.07	2.99	9.91
2	0.29	0.99	0.34	0.94	0.62	1.54	4.72	17.75
3	0.69	2.25	0.95	2.60	2.10	4.12	12.72	48.86
4	0.34	1.05	0.36	0.97	0.77	1.51	5.00	12.10
5	1.18	2.45	1.82	2.87	4.16	4.50	16.98	33.12
6	0.70	2.29	0.55	1.20	1.75	2.90	9.38	33.24
7	4.11	13.21	2.88	6.55	15.33	23.21	65.29	118.43
8	1.50	5.74	1.60	4.94	3.21	9.41	26.41	27.59

Table A4.7. Percentage of C_{27}, C_{28}, and C_{29} steranes in P4n5 and P5AB, calculated as a percentage of total C_{27}-C_{29} $\beta\alpha\alpha R$ and $\alpha\alpha\alpha R$ steranes.

	P4n5				P5AB		
Layer	%C_{27} steranes	%C_{28} steranes	%C_{29} steranes	Layer	%C_{27} steranes	%C_{28} steranes	%C_{29} steranes
1	17.16	25.91	55.36	1	24.51	25.95	48.54
2	34.44	26.45	38.42	2	26.84	26.91	45.19
3	20.08	19.75	58.47	3	22.97	27.73	48.51
4	18.43	27.82	52.89	4	14.61	36.13	48.34
5	21.77	33.16	43.94	5	21.27	27.43	50.67
6	21.61	28.84	48.85	6	31.36	18.32	48.71
7	27.54	17.52	53.67	7	26.14	14.23	58.17
8	18.32	14.40	63.35	8	26.61	24.05	46.39
9	33.02	19.91	44.54				
10	20.75	12.97	63.76				
11	22.01	18.99	56.93				

Figure A4.2. Mass spectrum of diploptene (red) coeluting with C_{32} moretane (purple; C_{32} βαR hopane) and possible C_{33} hopene (blue) in P5AB layer 7.
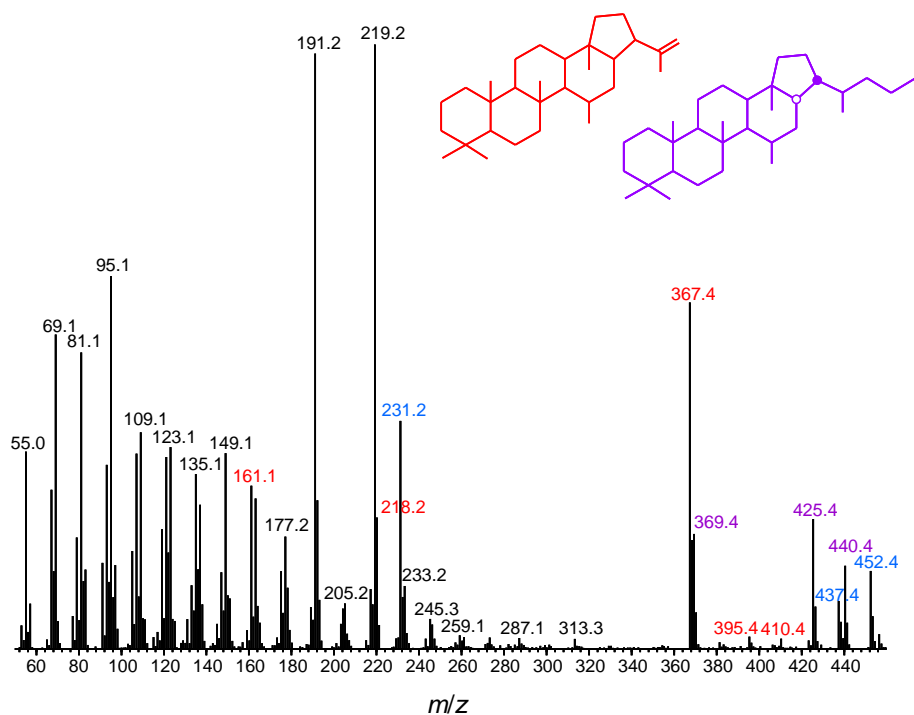

Table A4.8a. Concentration of kerogen-bound hopanes for P4n5 in ppm TOC. C_{27} = 17αTm and 17βTm, C_{29}-C_{35} are sums of αβR, βαR, and ββR isomers. All units in ppm TOC (μg/g TOC).

Layer	C_{27} hopanes	C_{29} hopanes	C_{30} hopanes	C_{31} hopanes	C_{32} hopanes	C_{33} hopanes	C_{34} hopanes	C_{35} hopanes	Total hopanes
1	1.26	0.83	0.90	0.75	0.63	0.27	0.11	0.15	4.89
2	1.39	0.86	1.03	0.84	0.85	0.39	0.19	0.21	5.77
3	3.55	2.42	2.46	1.69	1.55	0.37	0.25	0.27	12.55
4	2.72	1.76	2.09	1.97	2.81	0.84	0.40	0.43	13.02
5	8.41	3.31	4.03	3.68	7.20	1.55	0.68	0.67	29.53
6	2.62	1.07	1.55	2.09	6.06	0.91	0.47	0.44	15.21
7	17.51	10.77	13.37	9.04	18.85	4.27	2.02	1.50	77.33
8	8.43	3.41	3.35	2.68	7.66	3.29	3.23	2.90	34.95
9	9.77	2.97	2.19	1.63	2.25	1.33	0.86	0.54	21.55
10	4.27	1.33	0.97	0.78	1.03	0.59	0.41	0.31	9.70
11	0.42	0.11	0.16	0.15	0.32	0.19	0.11	0.14	1.59

Table A4.8b. Concentration of kerogen-bound hopanes for P5AB in ppm TOC. C_{27} = 17αTm and 17βTm, C_{29}-C_{35} are sums of αβR, βαR, and ββR isomers. All units in ppm TOC (µg/g TOC).

Layer	C_{27} hopanes	C_{29} hopanes	C_{30} hopanes	C_{31} hopanes	C_{32} hopanes	C_{33} hopanes	C_{34} hopanes	C_{35} hopanes	Total hopanes
1	4.71	3.21	3.09	1.87	1.12	0.35	0.14	0.11	14.61
2	5.28	3.25	3.50	2.65	2.03	0.58	0.28	0.26	17.83
3	8.19	4.99	5.20	4.88	5.41	1.28	0.64	0.52	31.10
4	2.04	0.98	1.20	1.11	2.02	0.47	0.31	0.42	8.54
5	7.52	4.20	4.56	4.08	8.22	1.53	1.05	0.76	31.92
6	9.51	4.75	3.01	4.13	5.99	1.10	0.65	0.36	29.51
7	32.55	9.55	11.70	8.91	30.00	8.38	8.40	7.99	117.47
8	19.88	4.92	6.69	2.84	8.81	3.73	4.11	4.08	55.07

Table A4.8c. Ratios of hopene isomers and concentration of total hopenes in P4n5. Hopenes are: C_{27} = C_{27} hop-13(18)-ene; C_{29} = C_{29} hop-13(18)-ene; and C_{30} = C_{30} hop-17(21)-ene. Total hopene concentration in ppm TOC (µg/g TOC).

Layer	C_{27}/17αTm hopane	C_{29}/$n$$C_{30}$	C_{30}/C_{29}ββ hopane	Total hopenes
1	2.24	0.42	1.33	1.70
2	1.37	0.71	0.39	1.80
3	1.55	0.75	0.36	4.99
4	1.51	1.47	0.62	4.51
5	1.05	0.56	0.20	8.60
6	1.66	1.04	0.10	5.32
7	1.37	0.63	0.54	23.55
8	0.23	0.00	0.00	6.27
9	0.09	0.00	0.00	0.00
10	0.33	0.00	0.00	0.00
11	0.00	0.00	0.00	0.00

Table A4.8d. Ratios of hopene isomers and concentration of total hopenes in P5AB. Hopenes are: C_{27} = C_{27} hop-13(18)-ene; C_{29} = C_{29} hop-13(18)-ene; and C_{30} = C_{30} hop-17(21)-ene. Total hopene concentration in ppm TOC (µg/g TOC).

Layer	$C_{27}/17\alpha$Tm hopane	C_{29}/nC_{30}	$C_{30}/C_{29}\beta\beta$ hopane	Total hopenes
1	2.78	1.03	3.05	11.01
2	2.66	1.29	2.31	13.17
3	2.39	1.32	2.04	18.15
4	1.84	0.63	0.77	3.99
5	2.69	0.75	1.07	16.51
6	2.47	0.96	1.01	20.90
7	0.78	0.93	0.30	30.16
8	0.07	0.28	0.07	0.00

Table A4.8e. Methylhopane index (MeHI) and concentration of methylhopanes through P4n5 with units in ppb TOC (ng/g TOC). Concentrations are sums of C_{31}-C_{36} 2β and 3β methylhopanes, respectively. MeHI were calculated as (2βMe/2βMe+$\beta\beta$ hopanes) $\times100$.

Layer	2Me (ppb)	3Me (ppb)	Total 2MeHI	Total 3MeHI
1	11.36	0.00	8.68	0.51
2	7.94	0.00	4.29	0.18
3	11.13	0.00	4.93	1.82
4	18.01	9.03	3.46	2.12
5	25.00	14.99	3.48	2.51
6	18.37	11.36	3.28	2.39
7	75.10	25.75	4.21	2.00
8	66.88	41.64	2.45	1.72
9	32.65	12.40	6.73	4.26
10	20.11	13.06	5.16	5.68
11	0.00	0.00	0.00	0.47

Table A4.8f. Methylhopane index (MeHI) and concentration of methylhopanes through P5AB with units in ppb TOC (ng/g TOC). Concentrations are sums of C_{31}-C_{36} 2β and 3β methylhopanes, respectively. MeHI were calculated as (2βMe/2βMe+ββ hopanes) $\times$100.

Layer	2Me (ppb)	3Me (ppb)	Total 2MeHI	Total 3MeHI
1	6.09	0.00	5.75	0.84
2	7.14	0.00	2.54	0.89
3	11.56	0.00	1.92	1.26
4	8.27	2.62	2.55	1.89
5	24.23	16.46	2.71	2.09
6	9.40	5.35	2.01	1.48
7	167.84	163.21	1.69	2.79
8	33.26	22.05	1.33	2.13

Table A4.9. Concentration of gammacerane through P4n5 and P5AB calculated as gammacerane/sum of C_{30} αβR, βαR, and ββR hopanes.

P4n5		P5AB	
Layer	Gammacerane/ C_{30} hopanes	Layer	Gammacerane/ C_{30} hopanes
1	0.04	1	0.02
2	0.03	2	0.02
3	0.02	3	0.02
4	0.04	4	0.03
5	0.05	5	0.03
6	0.07	6	0.02
7	0.02	7	0.05
8	0.02	8	0.07
9	0.07		
10	0.10		
11	0.16		

Table A4.10. Percentage bound steranes and hopanes calculated as a percentage of free and bound lipids for P4n5; i.e., %bound steranes = (bound steranes/(free sterols + bound steranes))×100. Total steranes includes steranes and sterenes and total hopanes includes hopanols, hopanoic acids, hopenes, and hopanes.

Layer	Age (years)	%Bound hopanes	%Bound steranes
1	1		3.24
2	2		3.89
3	4	7.23	0.89
4	8	4.82	
5	13	5.38	9.16
6	18	3.57	4.48
7	24	24.52	13.18
8	32	13.77	
9	42		
10	50		
11			

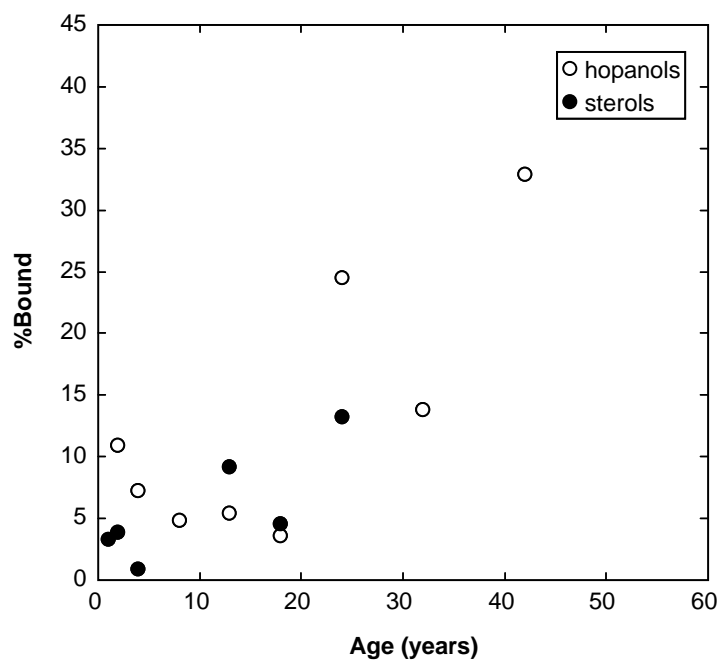**Figure A4.3.** Percentage bound steranes (filled) and bound hopanes (open) as a function of increasing age, in P4n5.

255

Table A5.1. Experimental conditions and fraction yields for kerogen hydropyrolysis of P4n5 layer 4 chemical treatments—PC pre-extracted control; PT periodate treatment; AM acid methanolysis; TCA trichloroacetic acid.

Layer	Mass (g)	Catalyst (wt%)	Max. H_2 (bars)	Sats (mg)	Aros (mg)	Pols (mg)
PC	0.7124	5.2	140	1.9	5.4	51.6
PT	0.7996	5.2	143	0.4	0.4	23.7
AM	0.2726	5.0	143	0.8	2.8	29.2
TCA	0.3446	5.0	143	1.1	4.1	81.2

Table A5.2. Experimental conditions and fraction yields for kerogen hydropyrolysis of P4n5 layer 7 chemical treatments—PC pre-extracted control; PT periodate treatment; AM acid methanolysis; TCA trichloroacetic acid.

Layer	Mass (g)	Catalyst (wt%)	Max. H_2 (bars)	Sats (mg)	Aros (mg)	Pols (mg)
PC	1.0311	4.9	140	3.1	8.0	140.7
PT	1.4561	5.4	138	1.5	12.5	107
AM	1.0188	5.4	133	0.6	3.0	17.7
TCA	1.0362	5.2	137	1.8	6.9	58.6

Table A5.3. Experimental conditions and fraction yields for kerogen hydropyrolysis of P5AB layer 4 chemical treatments—PC pre-extracted control; PT periodate treatment; AM acid methanolysis; TCA trichloroacetic acid.

Layer	Mass (g)	Catalyst (wt%)	Max. H_2 (bars)	Sats (mg)	Aros (mg)	Pols (mg)
PC	1.4815	5.5	149	2.8	6.1	78.6
PT	0.8329	5.3	139	0.5	2.3	53.8
AM	0.1395	5.4	137	0.3	1.0	2.4
TCA	0.3272	5.1	141	0.5	1.4	14.6

Table A5.4. Experimental conditions and fraction yields for kerogen hydropyrolysis of P5AB layer 7 chemical treatments—PC pre-extracted control; PT periodate treatment; AM acid methanolysis; TCA trichloroacetic acid.

Layer	Mass (g)	Catalyst (wt%)	Max. H_2 (bars)	Sats (mg)	Aros (mg)	Pols (mg)
PC	1.6338	5.3	135	1.6	2.0	14.2
PT	1.0304	6.1	137	0.3	1.9	40.2
AM	0.8985	5.2	138	1.3	2.0	9.1
TCA	0.4088	5.1	136	0.7	1.4	9.7

Table A5.5. Experimental conditions and fraction yields for kerogen hydropyrolysis of P5AB layer 4 and 7 hydrophobic residues collected after acid methanolysis treatment.

Layer	Mass (g)	Catalyst (wt%)	Max. H_2 (bars)	Sats (mg)	Aros (mg)	Pols (mg)
L4AM-H	0.0677	5.2	137	0.2	0.2	1.7
L7AM-H	0.0804	6.0	139	0.7	0.5	1.6

Table A5.6. Concentrations of kerogen-bound steranes and hopanes following chemolysis of layers 4 and 7 from P4n5 and P5AB. All units in ppm TOC (µg/g TOC). PC – pre-extracted control; TCA – trichloroacetica acid; AM – acid methanolysis; and PT – periodate treatment.

Core	Layer	Treatment	Total steranes	Total hopanes
P4n5	4	PC	83.97	19.54
		TCA	32.07	20.95
		AM	28.07	21.38
		PT	2.12	7.21
	7	PC	52.32	160.06
		TCA	29.28	76.81
		AM	7.37	44.25
		PT	2.83	20.66
P5AB	4	PC	4.49	8.54
		TCA	33.44	42.68
		AM	19.42	40.51
		PT	0.89	10.21
	7	PC	65.29	117.47
		TCA	82.84	127.61
		AM	21.67	69.57
		PT	1.27	21.94